IIC FILE COPY

(13)

RADC-TR-85-14, Vol II (of two) In-House Report January 1985



PROCEEDINGS OF THE 1984 ANTENNA APPLICATIONS SYMPOSIUM

Sponsored by
ELECTROMAGNETIC SCIENCES DIVISION
ROME AIR DEVELOPMENT CENTER
HANSCOM AFB, BEDFORD MASS. 01731
AIR FORCE SYSTEMS COMMAND

Reproduced From Best Available Copy

APPROVED FOR PUBLIC RELEASE; DISTRIBUTION UNLIMITED

20000811018

ROME AIR DEVELOPMENT CENTER Air Force Systems Command Griffiss Air Force Base, NY 13441



This report has been reviewed by the RADC Public Affairs Office (PA) and is releasable to the National Technical Information Service (NTIS). At NTIS it will be releasable to the general public, including foreign nations.

RADC-TR-85-14, Volume II (of two) has been reviewed and is approved for publication.

APPROVED:

JOHN K. SCHINDLER

Chief, Antennas & RF Components Branch Electromagnetic Sciences Division

APPROVED:

ALLAN C. SCHELL, Chief

Electromagnetic Sciences Division

FOR THE COMMANDER:

JOHN A. RITZ

Acting Chief, Plans Office

If your address has changed or if you wish to be removed from the RADC mailing list, or if the addressee is no longer employed by your organization, please notify RADC (EEAA) Hansoom AFB MA 01731. This will assist us in maintaining a current mailing list.

Do not return copies of this report unless contractual obligations or notices on a specific document requires that it be returned.

SECURITY CLASSIFICATION OF THIS PAGE

ADA 153258

REPORT DOCUMENTATION PAGE						
18. REPORT SECURITY CLASSIFICATION 18		16. RESTRICTIVE MARKINGS				
Unclassified		<u> </u>				
28. SECURITY CLASSIFICATION AUTHORITY		3. DISTRIBUTION/AVAILABILITY OF REPORT Approved for public releace;				
26. DECLASSIFICATION/DOWNGRADING SCHEDULE] Distribution	on unlimite	d.		
A PERFORMING ORGANIZATION REPORT NU	A PERFORMING ORGANIZATION REPORT NUMBER(S)		GANIZATION R	EPORT NUMBER(S) ,	
RADC-TR-85-14 Volume II						
64 NAME OF PERFORMING ORGANIZATION	6b. OFFICE SYMBOL (If applicable)	74. NAME OF MON!	TORING ORGAN	ZATION	,	
Rome Air Development Center	EEA					
6c. ADDRESS (City, State and ZIP Code)		7b. ADDRESS (City, State and ZIP Code)				
Hanscom AFB						
Massachusetts 01731	· **			•	•	
A NAME OF FUNDING/SPONSORING ORGANIZATION	8b. OFFICE SYMBOL (If applicable)	9. PROCUREMENT	INSTRUMENT ID	ENTIFICATION NU	MBER	
Rome Air Development Center	EEA					
Sc. ADDRESS (City, State and ZIP Code)		19. SOURCE OF FU	NOING NOS.	Ţ	,	
Hanscom AFB Massachu:etts 01731		PROGRAM ELEMENT NO.	PROJECT NO.	TASK NO.	WORK UNIT	
11. TITLE (Include Security Classification) Proc		62702F	4600	14	01	
1984 Antenna Applications Sym	posium			<u> </u>	<u> </u>	
	ي بنيون التجريب التجريب					
In-house FROM	COVERED TO	14. DATE OF REPO	y	4	19	
Dages 2/J Chiough boo.	16. SUPPLEMENTARY NOTATION Volume I consists of pages 1 through 27/4: Volume II consists of					
17. COSATI CODES	18. SUBJECT TERMS (C	ontinue on reverse if n	rcemary and ident	ly by block number		
FIELD GROUP SUB. GR.	Phase array ant	ennas,	-Microst	rip antennas		
	Millimeter wave	Reflector antennas				
19. APRICA (Continue on pure of possession	Near-field ante		nts,			
The Proceedings of the 1984 Antenna Applications Symposium is a collection of the state-of-the-art papers relating to phased array antennas, millimeter wave antennas, microstrip and conformal antennas, reflector antennas, and near-field antenna measurement techniques.						
,		•		11 1·1 <u>-</u> 1·	·/	
Veringe de la	-Carlo			9 4	, ,	
Team, 200	ie crip cp			Codi		
			For	e A B	18	
	OUALITY)	P C	10 77 7	9		
		INSPECTED	GRARI TAB ounced	ribut; [labi]	S	
in the second second		ess S C T nno	Tri S	-		
CHHED I IN SI						
			ied		or or	
22a. NAME OF RESPONSIBLE INDIVIDUAL		22b. TELEPHONE NO		22c. OFFICE SYM	IOL .	
Daniel T. McGrath, Capt, USAF	Daniel T. McGrath, Capt, USAF			RADC/EEA		
Daniel T. McGrath, Capt, USAF (617) 861-4036 RADC/EEA D FORM 1473, 83 APR EDITION OF 1 JAN 73 IS OSSOLETE. Unclass if fed						

PREFACE

The Antenna Applications Symposium, held at the University of Illinois' Robert Allerton Park, was cosponsored by Rome Air Development Center's Electromagnetic Sciences Division (RADC/EEA), Hanscom AFB, MA and the University of Illinois, Urbana, IL under contract F19628-84-M-0002.

Contents

Volume I

1

	Wednesday, September 19, 1984
	Session I
	Arrays
1.,	"Considerations for Millimeter Wave, Monolithic Phased Arrays," D. H. Schaubert, D. M. Pozar, K. S. Yngvesson and R. W. Jackson
2.	"The Design of a Thermally Efficient 1:256 Ku-Band Feed Network for a MMIC Phased Array," C. A. Hancik, D. E. Heckaman and E. J. Bajgrowicz
3.	"Characterization of MMIC Devices for Active Array Antennas," J. Smetana, 57 E. Farr and R. Mittra
4.	"Waveguide Slot Array with Csc ² Cos Pattern," J. J. Erlinger and J. R. Orlow
5.	"Sheet Metal Waveguide Forming Technique," P. K. Park and S. E. 113 Bradshaw
6.	"Considerations for Extending the Bandwidth of Arrays Beyond Two Octaves," G. J. Monser

Keynote: "New Antenna Technology," W. T. Patton

Contents

Session II

Microstrip Antennas and Lenses

7.	"Microstrip Monopulse Dipole Array," W. Miccioli, J. Toth, N. Sa and M. Iewis	149
8.	"Theory and Experiment for Infinite Microstrip Arrays," S. M. Wright and Y. T. Lo	171
9.	"Circularly Polarized Microstrip Antennas," Y. T. Lo, B. Engst and R. Q. H. Lee	197
10.	"Radiation and Scattering Performance of Microstrip Antennas Using Exotic Substrates," J. J. H. Wang	219
11.	. "A High-Efficiency, Low-Phase Error Waveguide Lens for a Transform Feed Antenna," D. T. McGrath	
12.	"Computer-Aided Bifocal Dielectric Lens Antenna Design for MM Wave Application," S. Y. Peng	257

Volume II

Thursday, September 20, 1984

Session III

Analysis, Measurements and Auxiliary Devices

- 13. "A Moment Method Solution to Spiral Antenna Radiation," P. Skinner and 275 A. J. Terzuoli
- 14. "Characterization of Dumbbell Slots in Rectangular Waveguide by Method of 291 Moments," P. K. Park and I. P. Yu
- 15. "The Effect of Quantization on the Dynamic Range of Adaptive Processors," 297 A. R. Cherrette, J. F. O'Connor and D. C. D. Chang
- 16. "Antenna Phase Center Movement in UHF Radio Positioning Systems," 311
 J. M. Tranquilla and S. R. Best
- 17. "Approach to a Suitable Directional Antenna for UHF Radio Positioning 341 Applications," J. M. Tranquilla and S. R. Best
- 18. "Four Band Radar Augmentation System for High Performance Targets," 365 H. B. Sefton, Jr
- 19. "Design and Error Analysis for the WR10 Thermal Noise Standard," 393
 W. C. Daywitt

Session IV

Reflector Antennas

20.	Reflector Antennas," V. Galindo-Israel, Y. Rahmat-Samii, W. Imbriale, H. Cohen and R. Cagnon	413
21.	"AUSSAT Ku-Band Space Antenna Subsystem," E. C. Ha, L. G. Clouse, K. A. Simmons, K. Clausing, M. D. Harwood and M. J. Glaser	449
22.	"Controlled Surface Distortion Effects," D. Jacavanco	479
23.	"Null Generation by Phase Perturbations in an Aperture," M. D. Rudisill and A. J. Terzuoli	503
24.	"Analysis of the Cross-Polarization Performance of Alternative Csc ² Doubly Curved Reflector Antenna Geometries-Preliminary Results," T. F. Carberry	517
	Friday, September 21, 1984	
1	Session V	
	Near-Field Techniques	
25.	"Probe Correction for Near-Field Antenna Measurements," A. D. Yaghjian	549
26.	"Optimum Probe Design for Near Field Scanning of Ultralow Sidelobe Antennas," K. R. Grimm	589
27.	"Case Study of Sample Spacing in Planar Near-Field Measurement of High Gain Antennas," R. J. Acosta and R. Q. Lee	613
28.	"Comparison of Measured and Calculated Mutual Coupling in the Near Field Between Microwave Antennas," C. F. Stubenrauch and M. H. Francis	621
29.	"Prediction of Low Sidelobe Antenna Performance in the Presence of Large Scatterers Using RF Field Probe Techniques," J. Wojtowicz, R. Konapelsky, J. Havrilla, R. Vogelsang and K. Ramsey	643
30.	"Extension of Plane-Wave Scattering-Matrix Theory of Antenna-Antenna Interactions to Three Antennas: A Near-Field Radar Cross Section Concept." M. A. Dinallo	665

Paul Skinner, 2D LT, USAF Andrew J. Terzuoli Air Force Institute of Technology Wright-Patterson AFB, Ohio

The method of moments provides a general approach for obtaining an approximate solution to the radiation pattern of a logarithmic spiral antenna. This solution is obtained via a knowledge of the current distribution induced on the antenna by feed excitation. Different methods for modelling a spiral antenna and its feed are discussed in this report, as well as a brief explaination of the implementation of the moment method.

Background

Several attempts have been made to describe the radiation properties of spiral antennas. One of the first was made by Walter Curtis in 1960 (1). He concentrated on the Archimedian spiral. Curtis's approach was to approximate the Archimedian spiral as a series of semi-circles. He assumed a current distribution of the sum of outward and inward travelling waves. He then obtained an exact solution to the radiation of a single semi-circle of thin wire with this distribution, and added the radiated fields for the series. Although this was an exact solution for the slightly distorted Archimedian spiral, it assumed a current distribution which has since been shown to be poor.

In 1964, John Dyson identified an active region on a conical logarithmic spiral antenna (2). This active region is what controls the primary characteristics of the radiated field. He took near field measurements which showed that the radiated near field is very intense over a ____ll

region of the antenna. This was a contradiction to the current distribution assumption Curtis made.

Cheo, Rumsey, and Welch (3) used Maxwell's equations to approach an exact solution for the radiation pattern of an antenna consisting of an infinite number or equally spaced wires in the form of coplanar equiangular (logarithmic) spirals. However, the analytical results they obtained for the current distribution showed a maximum of current on the feed point of the spiral with an amplitude taper as the spiral radius increased. This is a contradiction to the active region which Dyson discovered.

K. K. Mei demonstrated the feasibility of numerically solving an integral equation that modelled the physics of a radiating equiangular spiral antenna (4). He used Hallen's equation (5:79) to solve for the current distribution on the antenna, which he limited to a thin curved wire. Met used the moment method to obtain his solution. However, moment method applications to Hallen's equation have since been shown to converge to incorrect solutions.

The Moment Method

The moment method can be simply described as a mathematical technique used to get an approximate solution to an integral equation. The integral equation will contain an unknown function, which in this study is the radiating current distribution. The first step in the moment method is to write the unknown function as the sum of a weighted set of expansion functions. That is

$$I(\vec{x}^*) = \sum_{n=1}^{K} I_n F_n(\vec{x}^*)$$
 (Eq. 1)

In this form, n is the subscript for the nth expansion function, $F_n(\vec{r}^*)$, and I_n is the nth expansion coefficient, which is unknown.

There are many expansion functions which may be used to represent a current distribution. This study uses the piccewise sinusoidal function, which is given by equation? and sketched below.

$$F_{n}(x) = \begin{cases} \frac{\sin \beta (x - x_{n-1})}{\sin \beta (x_{n} - x_{n-1})} & \text{for } x_{n-1} \leq x < x_{n} \\ \frac{\sin \beta (x_{n+1} - x)}{\sin \beta (x_{n+1} - x_{n})} & \text{for } x_{n} \leq x < x_{n+1} \\ 0 & \text{otherwise} \end{cases}$$

where $\beta = 2\pi/\lambda$ $\lambda = \text{wavelength}$

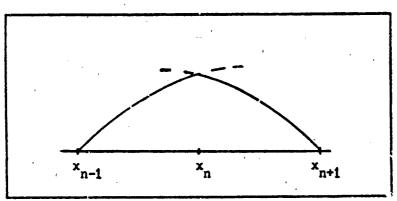


Figure 1. Piecewise Sinusoidal Expansion Function

For the implementation of piecewise sinusoic 1 expansion functions, the antenna structure must be divided into a finite number of subsets. The piecewise sinusoidal function is placed on each adjacent pair of subsets. The sum of the weighted set of piecewise sinusoids can form various complex current distributions, but always insures that the current on the end of the antenna wire goes to zero. To insure that "dips" do not occur in the distribution from too long sinusoids, subsets should be constructed so that

$$x_n - x_{n-1} \leqslant \lambda/4. \tag{71.3}$$

Once the expansion functions are chosen, the summation in equation 1 can be substituted into the original integral equation. In this study, that is the reaction integral equation.

The reaction integral equation is a convenient expression relating the reaction of various fields to each other for many problems. The concept of reaction was developed by V. H. Rumsey in 1954 (6). Rumsey defined the reaction between two electromagnetic sources, a and b, as

$$\langle a,b \rangle = \iiint_{\mathbf{a}} (\overline{E}(b) \cdot \overline{J}(a) - \overline{H}(b) \cdot \overline{K}(a)) dV$$
 (Eq. 4)

where E(b), $\overline{h}(b)$ = electric and magnetic fields radiated by source b $\overline{J}(a)$, $\overline{K}(a)$ = electric and magnetic currents on source a and the integration is done over the volume of source a.

The concept of reaction can be applied with the introduction of testing functions. Testing functions represent currents on subsets of the antenna structure which are allowed to react with other subsets of the structure. As with expansion functions, there are many choices of testing function types. This study uses Galerkin's method, which is the procedure of choosing the same type of function for both expansion and testing functions. Therefore, piecewise sinusoids are used for testing functions. The negative of the reaction between the nth expansion function and the mth testing function forms the mutual impedance between the pairs of subsets on which these functions reside. Since only good conductors (for the antenna structure) will be considered in this study, the magnetic current on the structure can be neglected. Therefore, the mutual impodance between the mth and nth pair of subsets can be written as

$$z_{mn} = -\iiint \vec{F}_n \cdot \vec{F}_n \, dV \qquad (Eq. 5)$$

where $\overline{\mathbb{E}}_{m}$ is the electric field radiated by the ath testing function and

the integration is done over the volume of the nth pair of subsets.

With N total adjacent pairs of subsets on the antenna, an N x N impedance matrix may be constructed to represent the mutual impedances throughout the antenna. This matrix can be multiplied with a current matrix to give a voltage matrix. The current matrix is merely a column vector with the nth entry being the nth expansion coefficient, I_n. The voltage matrix is also a column vector. Each entry in the voltage matrix represents the actual voltage across the a pair of adjacent subsets on the structure. In a radiation problem, these voltage entries can be assumed by specifying a generator model. This study uses delta gap generators for these sources. This gives a voltage entry of exactly zero for each pair of subsets, except for the few in which generators are placed. A voltage may be specified for the entries which contain the generators.

The moment method solution is obtained by solving for the current matrix. This is done by inverting the impedance matrix and multiplying the result with the voltage matrix. The resulting current matrix then gives the coefficients necessary to construct the current distribution with equation 1. Once the current distribution is found, the radiated field can be calculated with the standard radiation integral approach.

Antenna Mcdelling

This study considers three antenna models to simulate a planar logarithmic spiral antenna made of four curved conducting strips which increase in radius as the radial distance increases.

The first model is a simple thin wire model. The equation to describe the median curve in the flat strip was used to derive this model.

Points were calculated at 10° increments and straight segments are a counted

to connect these points and form the model. This is shown below in Figure 2 as a view of a portion of the antenna.

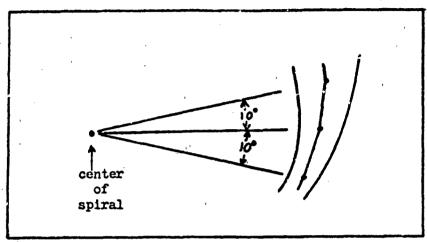


Figure 2. Thin Wire Modelling

Although it may seem more desirable to place piecewise sinusoidal expansion functions over curved wire regments (allowing the model to fit the median curve exactly), this is not practical for implementation of the moment method. It is practical to place the piecewise sinusoids over straight wire segments because the near and far fields radiated by a thin wire with a piecewise sinusoidal current is known exactly (7:368-370). The near field radiated by an adjacent pair of segments must be used to compute the impedance matrix entries.

A two arm antenna was modelled first. This is shown in Figure 3. Segment endpoints were placed 45° apart to give a rough estimate of the radiation pattern. The figure is drawn to actual scale for the antenna modelled. The feed consists of a segment of wire connecting the two feed points. Since the maximum radius of the antenna is about 5 cm, the minimum operating frequency is expected to be about 1 GHz (where the wavelength equals the outer perimeter).

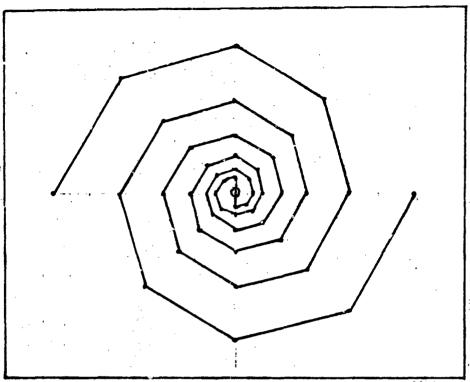


Figure 3. Two Arm Wire Model

The frequency characteristics at the high end of the operating band cannot be explored because the generator used is a corruption of the true feed of an antenna.

Once it was established that the two arm model was giving credible results, a four arm model was developed. The four arm model used segmentation every 10° for more accuracy. Two feeding arrangments were tried with the four arm model. The goal of the different feeds was to produce the sum and difference patterns discussed by Joseph Mosko (8). The sum pattern is simply a large beam centered on the boresight of the antenna. The difference pattern has a null on the boresight, and a maximum about 38° from the boresight, according to the experimentation done by Mosko. In order to generate these patterns, equal amplitude voltages with the phases listed in Table A must be applied to the four feed points.

Table A

Feed Point	Phase for Sum Pattern	Phase for Diff. Pattern
1	, o o	o°
2	90°	180°
3	180°	00
4	270°	180°

The feed points are numbered sequentially in a clockwise manner. To obtain these voltages, the feed models shown in Figure 4 were separately placed in the four arm thin wire model.

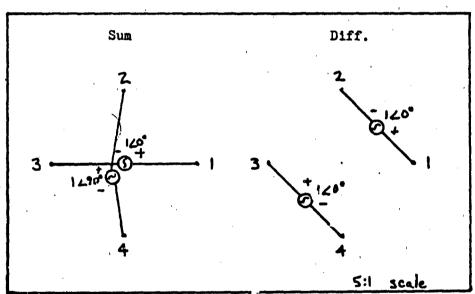


Figure 4. Feed Models for Sum and Difference Patterns

The generator between points 2 and 4 on the sum pattern model is 1 mm above the generator between points 1 and 3, which is in the plane of the four wire arms.

At the time of this writing, the thin wire model has been the only model used to obtain results. However, the authors have considered two other modelling schemes, each of which take into account the possibility of lateral currents developing on the arms of the antenna.

The second antenna model considered is a wire-grid model. This consists of thin wires conforming to the inner and outer edges of the conducting strips (see Figure 2) with straight wire lateral connections every 10°. Implementation of the moment method with this model can use the same piecewise sinusoidal expansion functions used in the thin wire model. The feed structures used in Figure 4 can also be used in this model.

The third antenna model is a quadrilateral patch model. It is formed by placing a conducting patch inside each space created in the wire-grid model. The wire feed models may still be used, but they must be attached to thefirst patch of each arm. This model will probably most closely characterize the actual antenna. The expansion function for the surface patches is more complicated than the piecewise sinusoidal functions for straight wires. A modified piecewise sinusoid is given in equation 6 with the parameters defined in Figure 5.

$$F_n(f^*) = \hat{n} \frac{\sin(\beta 1)}{w \sin(\beta 1)} = \text{surface current density}$$
 (Eq. 6)
 $c = \text{constant}$

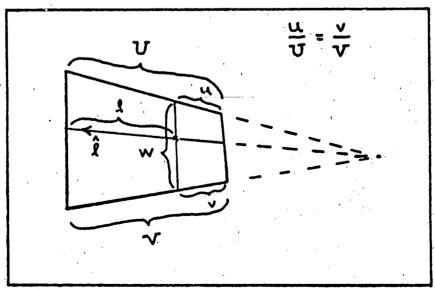


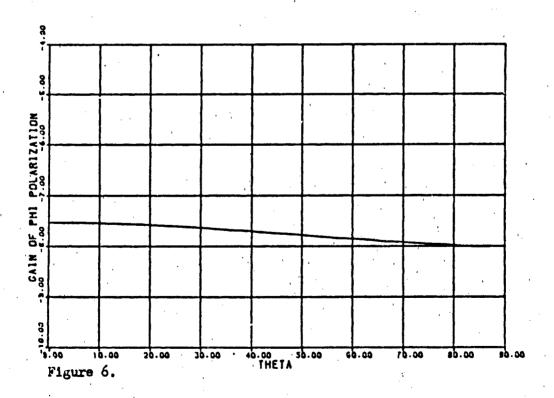
Figure 5. Surface Patch Geometry

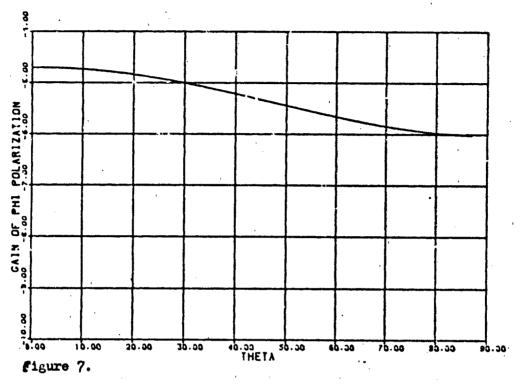
Results

Some computer experimentation has been done with the thin wire model. The authors have used a relatively new code developed by E. H. Newman at the Ohio State University ElectroScience Laboratory. Although the results obtained using this code should be viewed carefully, the early returns seem to indicate the code is working well.

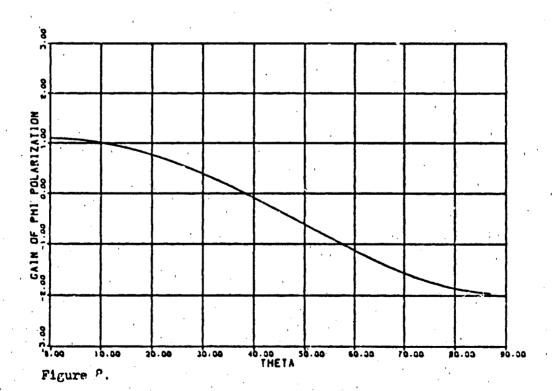
The antenna gain pattern for the two arm model is given in Figures 6 through 11 for different frequencies. The results show the antenna performance drops off at about 1 GHz, which is what we expected. This supports the work of John Dyson, who discovered that the radiating portion of the antenna should be where the circumference equals one wavelength. There is an unexpected drop in gain at 2 GHz. We have no explaination for this.

2-ARM WIRE AMTENNA AT 250 MHZ





2-ARM WIRE ANTENNA AT 1 GHZ



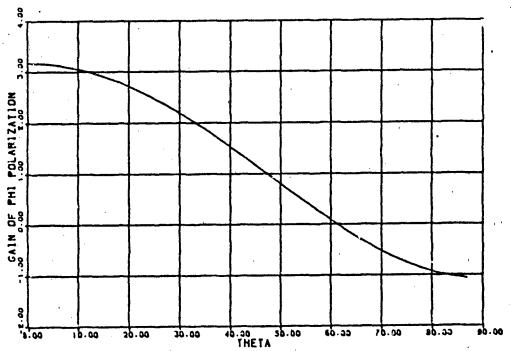


Figure 9.

2-ARM WIRE ANTENNA AT 2 GHZ

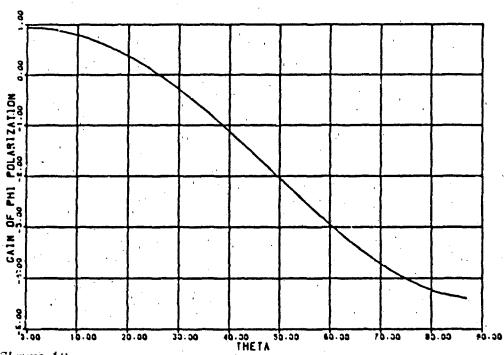
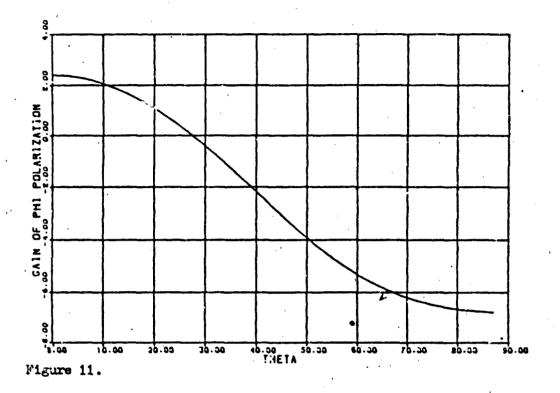
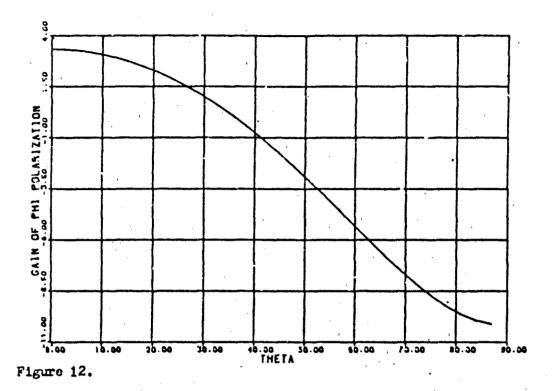


Figure 10.



The pattern at 1.5 GHz is very indicative of what we expected. The maximum gain is a little over 3dB and the beamwidth is about 120°, which is a little larger than most experimental results.

For the sum pattern of the four arm wire antenna, we expect a maximum gain of about 3dB and a beamwidth of around 70°, based on experimentation done by Mosko (8). As seen in Figure 12, this is almost exactly what the computer generated. The maximum gain is 3.37dB and the beamwidth is around 66°. What is particularly interesting about the sum pattern is the currents generated on the antenna. Although we do not have a figure showing the current distribution, we noticed the current reached a maximum amplitude where the circumference of the antenna was almost exactly two wavelengths. According to the work done by Mosko, this is to be expected only for the difference pattern. The sum pattern should have a maximum current where the wavelength equals the circumference.



Problems arose in generating a difference pattern at the time of this writing.

Acknowledgments

The authors wish to sincerely thank Dr. E. H. Newman at the Ohio State University ElectroScience Laboratory for the use of his moment method code. The authors are also indebted to the support of the Electronic Marfare Analysis Branch of the Aeronautical Systems Division at Wright-Patterson Air Force Base, Ohio.

Bitliography

- 1. Curtis, Walter L. "Spiral Antennas," IRE <u>Transactions on Antennas</u> and <u>Propagation</u>: 298-306 (May 1960).
- 2. Dyson, John D. "The Characteristics and Design of the Conical Log-Spiral Antenna," <u>IEEE Transactions on Antennas and Propagation</u>: 488-499 (1965).
- 3. Chec, B.R.S., V.H.Rumsey and W.J.Welch. "A Solution to the Frequency Independent Antenna Problem," IRE Transactions on Antennas and Propagation: 527-534 (November 1961).
- 4. Mei, K. K. "On the Integral Equations of Thin Wire Antennas," IEEE Transactions on Antennas and Propagation: 374-378 (May 1965).
- 5. King, R. W. P. <u>The Theory of Linear Antennas</u>. Cambridge, Mass.: Harvard University Press, 1956.
- 6. Rumsey, V. H. "Reaction Concept in Electromagnetic Theory," Physical Review, 94: 1483-1491 (June 1954)
- 7. Schelkunoff, S. A. and H. T. Friis. Antennas: Theory and Practice.
 New York: John Wiley and Sons, 1952.
- 8. Mosko, Joseph A. "An Introduction to Wideband Two-Channel Direction-Finding Systems," <u>Microwave Journal</u>: 91-105 (February 1984).

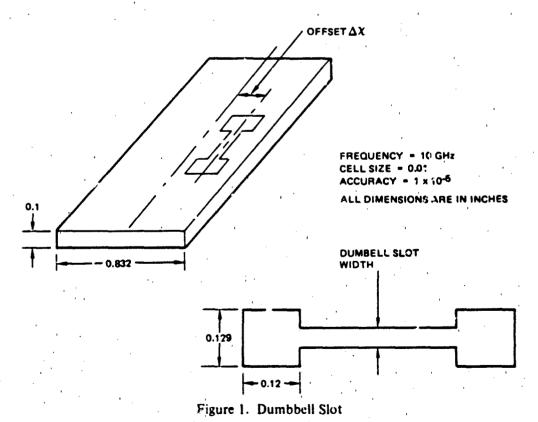
CHARACTERIZATION OF CUMBBELL SLOTS IN RECTANGULAR. WAVEGUIDE BY METHOD OF MOMENTS

P. K. PARK AND I. P. YU

HUSHES MISSILE SYSTEMS GROUP, CANOGA PARK, CA.

ABSTRACT

Dumbbell slots are often used for an array to reduce their resonant length, and hence, their internal and external mutual coupling. The square dumbbell shunt slot shown in Figure 1 is characterized by the moment method. As expected, the resonant length is shorter than a conventional rectangular slot. Also,



changing the width of the dumbbell slot has the same effect as changing the length of the rectangular slot. However, for a small offset such that a part of the dumbbell is across the center line, changing the width of the dumbbell slot has little influence to its admittance.

THEURY

The theoretical analysis of a dumbbell slot on the broadwall of a rectangular waveguide began with an integral equation for the surface magnetic current $J_{\underline{\underline{u}}}$ in the slot.

$$n \times \underline{H}^{1nc}(r) = \underline{j}_{wenx} \int \underline{j}_{ms} (r_0) [\overline{\Gamma}_{h_{zz}}^{(1)}(r)r_0)$$

$$= \underbrace{Dumbbell}_{Slot}$$

$$+ \overline{\Gamma}_{h_{zz}}^{(2)} (r)r_0] ds_0$$
(1)

where

$$\overline{I}_h^{(1)}(rlr_0)$$
 and $\overline{I}_h^{(2)}(rlr_0)$

are the magnetic Green's dyadic in the waveguide and free space respectively, i.e.,

$$\overline{\Gamma}_{h_{ZZ}}^{(1)}(r)r_0) = \left(1 + \frac{1}{k^2} \frac{\partial^2}{\partial z^2}\right) \sum_{m=0}^{\infty} \sum_{n=0}^{\infty} \frac{\epsilon_m \epsilon_n}{2ab}.$$

$$\frac{1}{\sqrt{mn}}\cos\frac{m\pi x}{a}\cos\frac{m\pi x}{a}e^{-\sqrt{mn}|z-z_0|}$$

$$\overline{\Gamma}_{h_{zz}}^{(2)}(r l r_0) = \left(1 + \frac{1}{k^2} \frac{a^2}{az^2}\right) \frac{e^{-jkR}}{2\pi R}$$

Equation 1 is reduced to a matrix equation via the application of the moment method as follows:

$$H^{inc}(r) = \sum_{j=1}^{N} Y_{ij} J_{iqz} i=1, 2, ... N$$
 (2)

whère

$$Y_{11} = Y_{11}^{(1)} + Y_{11}^{(2)}$$

$$\gamma_{1j}^{(v)} = j\omega \epsilon \int \frac{\overline{\Gamma}_{h_{zz}}^{(v)}}{\Gamma_{h_{zz}}} (r_1 lr_0) \psi_j (r_0) dr_0 \quad v = 1.2$$

$$j_{m1} = -\hat{n} \times \underline{E} (r_1)$$

$$\Psi_{j} = \begin{cases} 1/\Delta Aj \\ 0 \end{cases}$$
 if r is on subarea ΔAj

and Y_{ij} is an admittance matrix, J_{mj} and H_i^{inc} are the values of the unknown magnetic current and the incident field, respectively, at discrete sampling points, and Ψ_j is a constant pulse function. The unknown J_{mj} can be found numerically by inverting the matrix Y_{ij} . Assuming the magnetic currents are found, the slot characteristics can be found in terms of the backward and forward scattering coefficients (B_{10}, F_{10}) defined as:

$$B_{10} = \frac{2\frac{\pi}{a}}{\omega \mu_{o} \beta_{10}^{2} ab} \sum_{i=1}^{N} \frac{J_{mz}(i)}{\Delta x_{i} \Delta z} \cos \frac{\pi x}{a} \frac{\sin \pi \Delta x_{i}}{2a}$$

$$\begin{pmatrix} -j\beta_{10}(z_{i} + \Delta z/2) & -j\beta_{10}(z - \Delta z/2) \\ e & -e \end{pmatrix}$$

$$F_{10} = \frac{-2\frac{\pi}{a}}{\omega \mu_{o} \beta_{10}^{2} ab} \sum_{i=1}^{N} \frac{J_{mz}(i)}{\Delta x_{i} \Delta z} \cos \frac{\pi x}{a} \sin \frac{\pi \Delta x_{i}}{2a}$$

$$\begin{pmatrix} -j\beta_{10}(z_{i} + \Delta z/2) & -j\beta_{10}(z - \Delta z/2) \\ -e & -e \end{pmatrix}$$
(3)

The admittance of the shunt slot can be related with the back scattering coefficient as:

$$Y/G_0 = -\frac{2 B_{10}}{1 + B_{10}} \tag{4}$$

NUMERICAL CALCULATION

Computations were performed for a dumbbell shunt slot fed by a rectangular waveguide. A nonstandard X-band waveguide (0.832 x 0.1 inch internal dimensions) with zero wall thickness was chosen to test this approach. Figure 1 shows these general details. The size of the square dumbbell was 0.129 x 0.12 inch and the cell height, 0.01 inch. Dumbbell slot admittance versus slot width is plotted in Figure 2. Regular slot admittance versus slot length is shown in Figure 3.

As expected, a reduction of the resonant length was observed with dumbbell-slots, as illustrated in Figures 2 and 3. Also, the width change of the dumbell slot has the same effect as the length change of the rectangular slot. However, for a small offset, the width change of the dumbbell slot has little influence on the admittance as shown in Figure 2. This phenomenon occurs because the effective dumbbell size is reduced since a part of the dumbbell crosses the center line of the waveguide, and the resonant length variation as a function of slot width is small for a small offset. Experimental results will be presented at the symposium.

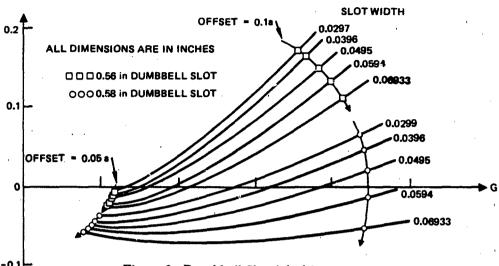


Figure 2. Dumbbell Slot Admittance versus Slot Offset and Slot Width

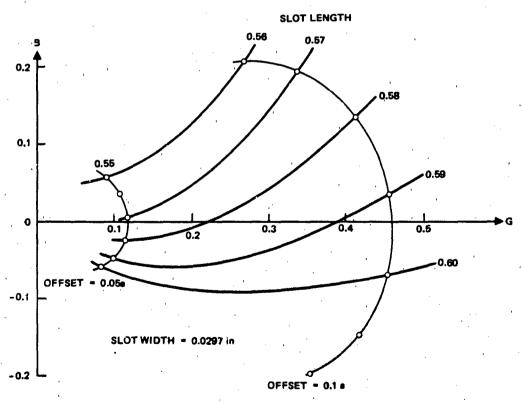


Figure 3. Rectangular Slot Admittance versus Slot Offset and Slot Length

THE EFFECT OF QUANTIZATION ON THE DYNAMIC RANGE OF ADAPTIVE PROCESSORS.

A. R. Cherrette, J. F. O'Connor, and D.C.D. Chang

Antenna Systems Laboratory, Space and Communications Group, Hughes Aircraft Company, El Segundo, California

Abstract

In many adaptive array designs the adaptive algorithm is implemented digitally and the element weighting is quantized. The error incurred when quantizing element weights gives rise to a degradation in the dynamic range performance of an adaptive processor. This phenomenon was studied with an experimental adaptive array that implements the least mean square (LMS) algorithm.

Quantization effects on the dynamic range of the adaptive processor were measured, and a theoretical relationship between quantization and dynamic range is formulated.

1. Introduction

Figure 1 shows a block diagram of the experimental adaptive antenna that was used to study the effects of quantization on dynamic range. The front end consists of an array of up to seven rectangular horns that receive S band signals. The output of each horn is downconverted twice, to 30 MHz, where it is weighted in amplitude and phase. The weighted signals are then summed to form the adapted output signal.

The LMS algorithm is used to modify the channel weights.

This algorithm requires the use of a desired signal. In any real application there is never complete a priori knowledge of the desired signal, but some characteristics such as bandwidth and center frequency may be known. Therefore, as an easily applied criterion, the desired signal is defined as a bandpass filtered

version of the output signal. The output signal and the desired signal are separately correlated with each downconverted horn output, and the result is converted from analog to digital form. A microcomputer performs the LMS calculation and modifies the weight settings.

2. The LMS Algorithm

The basic LMS algorithm takes the form

$$W_{i}(k+1) = W_{i}(k) - \mu \phi_{i}(k) \quad i = 1, M$$
 (1)

where

W_i(k) = weight of the ith element on the kth iteration

 μ = step size or loop gain, a constant controlling stability and rate of convergence (μ > 0)

$$\phi_{\mathbf{i}}(\mathbf{k}) = \int_{\mathbf{t}_{\mathbf{k}}}^{\mathbf{t}_{\mathbf{k}+1}} \varepsilon(\mathbf{k}, \zeta) \, \mathbf{x}_{\mathbf{i}}(\zeta) \, d\zeta$$

= correlator output of ith channel

 $x_i(t)$ = signal output of the ith element

$$\varepsilon(k, t) = \left[\sum_{i=1}^{M} W_i(k) x_i(t)\right] - d(t)$$

d(t) = desired signal

M = number of elements in array

t = time

It can be shown (1) that for μ in the range

$$0 < \mu < \frac{1}{p} \tag{2}$$

where

$$P = \sum_{i=1}^{M} \frac{1}{T} \int_{0}^{T} x_{i}^{2}(\zeta) d\zeta$$

that

$$\frac{\lim_{k\to\infty} |W_i(k)| = 1, M}$$

will converge to the optimum set of adapted weights. Values of μ greater than 1/P will cause $|W_1(k)|$ i = 1, M to increase without bound for $k \to \infty$. Inequality (eq. 2) gives the upper and lower bounds for μ when the variables in eq. 1 are continuous.

In our experimental adaptive array, however, we quantize $W_1(k)$ i = 1, M and $\phi_1(k)$ i = 1, M to 8-bit members. μ is also quantized, but to a 16-bit number, so, for all practical purposes, it can be considered continuous.

If we define the change in weight for the ith horn as

$$\Delta W_{i}(k) = W_{i}(k + 1) - W_{i}(k) = -\mu \phi_{i}(k)$$

then there are two possible ways $\Delta W_{1}(k) = 0$

- 1. $\phi_i(k)$ is so small that when quantized it is zero
- 2. $\phi_1(k)$ is not quantized to zero but μ is so small that $\Delta \ W_4(k) \ \mbox{is quantized to zero}$

When case 1 above holds, the process has usually converged. When case 2 above holds, there is no adaptation. The second case above sets a lower limit on the values μ can assume.

Consider the first iteration of the LMS algorithm

$$W_{\underline{i}}(1) = W_{\underline{i}}(0) - \mu \phi_{\underline{i}}(0) \quad i = 1, K$$

$$\Delta W_{\underline{i}}(0) = -\mu \phi_{\underline{i}}(0) \quad i = 1, M \quad (3)$$

Assume that $\phi_1(0)$ is large (corresponding to a high power jamming signal not yet nulled) let

 $\Delta W_1'(0)$ = the smallest change allowed by quantization for the i^{th} channel with the initial weight of $W_i(0)$

As μ is decreased, it can be seen from eq. 3 that $|\Delta W_{i}(0)|$ will become smaller than the threshold value: $|\Delta W_{i}'(0)|$ for all i. If we pick the value $\mu = \mu_{\rho}$ for which $|\Delta W_{i}(0)| = |\Delta W_{i}'(0)|$, assuming the jth channel is the last channel for which $|\Delta W_{i}(0)| > |\Delta W_{i}'(0)|$ as μ decreases, then μ_{ρ} is the smallest value μ can assume while still allowing the possibility of adaptation. We can now rewrite inequality (eq. 2) with the new lower bound caused by weight quantization

$$\left|\frac{\Delta W_1'(0)}{\phi_1(0)}\right| < \mu < \frac{1}{P} \tag{4}$$

Inequality (eq. 4) gives the range of μ when the weights in eq. 1 are quantized. $W_i(0)$ i = 1, M will not change if

$$\mu < \frac{\left| w_{j}'(0) \right|}{\left| \phi_{j}(0) \right|}$$

and

$$\frac{1_{-m}}{k \to \infty} |W_{i}(k)| \quad i = 1, M$$

will become unbounded for $\mu > 1/P$.

3. Experimental Results

The parameter μ could be set to a fixed value with the adaptive processor's software. Testing was done to determine the allowable range of values μ could assume while maintaining the systems ability to adaptively converge to an optimum set of weights.

When testing, the signal environment consisted of one jamming signal and one desired signal, each with a unique angle of incidence with the array. The locations of the signals were held fixed for all tests. The weight vector was set to the same initial state at the beginning of each run, and values of μ were tested to see if they could make the weight vector converge. After a range of values for μ was found for a particular signal environment, the power of the jamming and desired signals were changed by the same multiplying factor. The adaptive range of μ was then determined at the new power level and the process repeated. Several signal environments were tested at various power levels, and some typical results, are shown in Figure 2.

The values of μ between the two X marks at a particular power are values that cause the weight vector to converge. Values of μ above the upper X mark cause the weight to become unstable, and there is no adaptation when μ is chosen below the lower X mark. Since almost all of the signal power comes from the jammer, the measured values of μ are plotted against jamming signal power measured at the output of the adaptive processor.

With some approximations (see the appendix) the upper and lower bounds or inequality (eq. 4) can be plotted. These bounds are shown in Figure 2 as dashed lines. There is good agreement between theory and experiment for power below -35 dB. The deviation between theory and experiment at higher power is probably due to the effects of the limiters that are placed in the feedback path to increase the dynamic range of the correlators. (2) Their nonlinear characteristics are not accounted for in the derivation.

4. Conclusion

Ideally, an adaptive processor should be able to work for any signal environment, regardless of power levels or incoming signal directions. In the course of testing it was found that incoming signal directions did not affect the system's ability to adapt if the proper choice of μ was made. However, allowable values of μ depend on signal environment power levels as well as weight quantization resolution, as can be seen by the inequality

Province Lineary of Learning Lineary Learning Landson

$$\left|\frac{W_{\mathbf{j}}'(0)}{\phi_{\mathbf{j}}(0)}\right| < \mu < \frac{1}{p}$$

In theory, the dynamic range of the adaptive processor is constant for fixed μ . This can be seen in Figure 2. Horizontal lines (μ = constant) existing between the upper and lower dashed lines are the same length. If the dynamic range of the adaptive processor was large, which it is not in this case for fixed μ , then the system would be able to adapt to varied signal environments without becoming unstable.

A few solutions to the dynamic range problem are to

- 1. Make $W_j'(0)$ very small, which corresponds to fine weight quantization. This increases the dynamic range for fixed μ .
- 2. Search for the proper value of μ . A possible implementation of this would be to start with a very large value of μ and decrease it by $\Delta \mu$ after every x iterations. Eventually μ would reach the proper range, provided $\Delta \mu$ was not too large.
- 3. Calculate μ if $W'_{j}(0)$, $\phi_{j}(0)$, and P are known.

All three solutions will likely add to the time it takes for the system to adapt to the optimum set of weights.

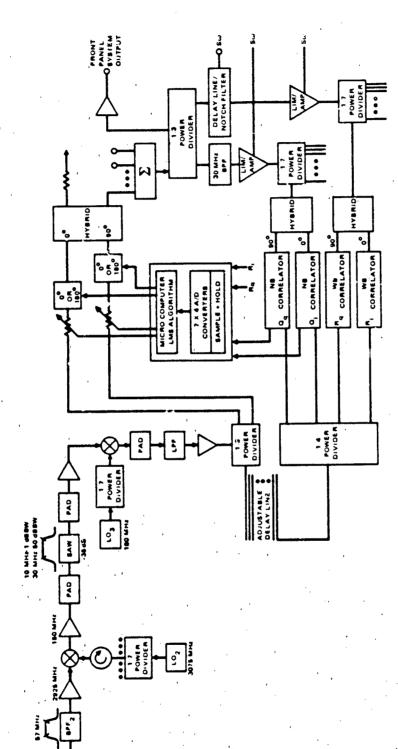


Figure 1. Block Diagram of Experimental Adaptive Array

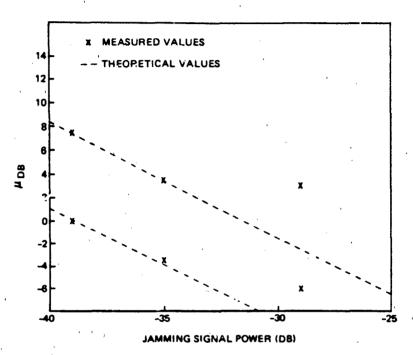


Figure 2. μVersus Power

References

- B. Widrow, P. E. Mantely, L. J. Griffith, and B. B. Goode, "Adaptive Antenna Systems," <u>Proceeding of the IEEE</u>, Vol. 55, No. 12, December 1967, pp. 2143-2159.
- 2. D.C.D. Chang and E. C. Ha, "Limiter Effects on Adaptive Array System," 1982 APS Symposium Digest, Vol. 2, pp. 711-714.

Appendix

Define a reference power level

$$P_{\text{ref}} = \sum_{i=1}^{M} \frac{1}{T} \int_{0}^{T} x_{i}^{2}(\zeta) d\zeta$$

If the amplitude of the signal environment is increased by \sqrt{c} , then assuming the signal power is well above noise power, and perfect system components

$$P = \sum_{i=1}^{M} \frac{1}{T} \int_{0}^{T} cx_{i}^{2}(\zeta) d\zeta = cP_{ref}$$

We can also define a reference correlator output

$$\phi_{i}(0)_{ref} = \int_{t_{k}}^{t_{k+1}} \epsilon(0, \zeta)_{ref} x_{i}(\zeta) d\zeta$$

Since d(t) is a bandpass filtered version of

$$\sum_{i=1}^{M} W_{\underline{i}}(k) x_{\underline{i}}(k)$$

We have, after increasing the signal amplitude by \sqrt{c} .

$$\varepsilon(0, t) = \left[\sum_{i=1}^{M} W_i(k) \sqrt{c} x_i(t)\right] - \sqrt{c} d(t)$$

$$= \varepsilon(0, t)_{ref} \sqrt{c}$$

Hence

$$\phi_{i}(0) = \int_{t_{k}}^{t_{k+1}} c \epsilon(0, \zeta)_{ref} x_{i}(\zeta) d\zeta$$

$$= c \phi_{i}(0)_{ref}$$

Substituting into equality (4)

$$\left| \frac{\mathbf{w}_{1}'(0)}{\mathbf{c}\phi_{1}(0)_{\text{ref}}} \right| < \mu < \frac{1}{\mathbf{c}^{P}_{\text{ref}}}$$

or

$$D_1 < \mu_{dB} + C_{dB} < D_2$$

where

$$D_1 = 10 \log_{10} \left[\frac{W_j^{(0)} \gamma}{\phi_j^{(0)}_{ref}} \right]$$

$$D_2 = 10 \log_{10} \left(\frac{\gamma}{P_{ref}}\right)$$

$$\mu_{dB} = 10 \log_{10} \mu_{\Upsilon}$$

$$C_{dB} = 10 \log_{10} C$$

γ = Dimensional normalizing factor

The upper and lower bounds for $\boldsymbol{\mu}_{\mbox{\footnotesize dB}}$ are, respectively

$$\mu_{dB} = -C_{dB} + D_2$$

$$\mu_{dB} = -c_{dB} + b_1$$

These two equations are plotted as dashed lines in Figure 2. ${\bf D_1} \ \ {\bf and} \ \ {\bf D_2} \ \ {\bf are} \ \ {\bf chosen} \ \ {\bf to} \ \ {\bf best} \ \ {\bf fit} \ \ {\bf the} \ \ {\bf experimental} \ \ {\bf data}.$

ANTENNA PHASE CENTRE MOVEMENT IN U.H.F. RADIO POSITIONING SYSTEMS

J.M. Tranquilla and S.R. Best
Department of Electrical Engineering
University of New Brunswick
Fredericton, N.B., Canada
(506) 453-4561

ABSTRACT

Yagi array configurations such as are commonly used in UHF electronic distance measuring (EDM) systems are analysed to show the antenna phase centre movement for any look angle. It is shown that large phase centre movements may occur within the antenna main-beam pattern and the movement of phase centre is directly related to the angular derivative of the polar radiation pattern. A simple technique is proposed for qualitatively estimating the suitability of any antenna for this type of EDM application and a complete model is presented to evaluate the error introduced for any transmitter-receiver antenna orientation. Extensive results are presented for 7- and 12-element Yagis such as are commonly used in the SYLEDIS UHF Radio Positioning System.

1. INTRODUCTION

The radio positioning systems are becoming increasingly popular in such applications as near off-shore positioning (up to a few hundred kilometers) since they offer the advantage of over-the-horizon capability (which limits microwave systems) and more-or-less terrain conductivity-independent propagation path characteristics (which limits lower-frequency systems). A typical example of a modern (UHF system is the SYLEDIS (SYsteme Ligere de DIStance) which operates at 420-450 MHz with stated accuracy of ± 10 m at maximum range (two to three times line-of-sight). Typical antennas used for maximum range are single and stacked 7 and 12-element Yagis.

The major possible error sources associated with the operation of this system can be categorized as propagation (path and cables), electronic and antenna phase centre. Preliminary field trials suggest that the uncertainty of the location of the antenna phase centre (for both the transmitting and receiving antennas) may be the most significant error contribution and may also be most amenable to analysis.

The phase centre of an antenna is, for example in the case of a transmitting antenna, the apparent source of radiation. In the far-field of the antenna (i.e. several wavelengths) the equiphase contours of the radiating electromagnetic wave

describe concentric spherical shells (or portions of sperical shells over defined angular limits) whose geometric centre is at the phase centre of the antenna. Of course, any "distortion" of the spherical wavefront will lead to a movement of the phase centre. This work considers the phase centre movement as a function of frequency and look angle for a variety of commonly used antennas.

Figure 1 depicts a typical radio positioning application. It is required to measure the distance AB between the beacon (at A) and the interrogator (at B). The transmitting antenna at A is permanently pointed in the direction AA'. The receiving antenna at B is not pointed along BA, but rather along BB' which still has sufficient gain at this off-boresight angle to ensure signal reception. The location of the phase centers C and D of the transmitting and receiving antennas respectively are uniquely defined (for a fixed frequency and a particular antenna) by the angles ϕ_2^* and ϕ_1^* which are the angles between the antennas axes (AA' and BB') and the inter-phase centre line (CD). Of course for each position of the interrogator the phase centers take new positions and hence the angles $\phi_1^{\, \text{!`}}$ and $\phi_2^{\, \text{!`}}$ are different. The distance measured by the equipment in this configuration will be CD which is an erroneous measure of the required distance AB. Thus if A and B are far removed such

that AB is very much larger than the antenna dimensions:

$$AB = AO + BO$$

$$= CO + AC COS(\theta_2 + \phi_2) + DO + BD COS(\theta_1 + \phi_1)$$

$$= CD + AC COS(\theta_2 + \phi_2) + BD COS(\theta_1 + \phi_1)$$
(1)

where the distances AC and BD are functions of the bearing angles ϕ_2^* and ϕ_1^* respectively and must be determined from an analytical model of the specific antennas. Unfortunately in most (if not all) positioning applications the angles ϕ_1^* and ϕ_2^* are never determined and hence corrections cannot be made. The problem is aggravated by the fact that phase centre movement may be a sensitive function of these bearing angles.

2. ANTENNA MODEL AND PHASE CENTRE

Figure 2 shows a Yagi array consisting of a driven element.

a reflector element and several parasitic director elements. The antenna is described mathematically by a system of equations relating the dipole base currents to the dimensions of the antenna. The base terminals of each of the parasitic dipoles may be considered to be short-circuited since the elements are normally constructed of a single piece of metallic rod. The base of the driven element may be modelled by a voltage or current source with source impedance. The voltage equation at the base of the driven dipoles is then

$$V_{T} = Z_{DD}I_{D} + \sum_{n=1}^{N} Z_{Dn}I_{n}, \text{ n an integer}$$

$$v_{T} = Z_{DD}I_{D} + \sum_{n=1}^{N} Z_{Dn}I_{n}, \text{ n an integer}$$
(2)

where N is the number of elements in the array, D is the element number corresponding to the driven element, V_T is the driving voltage at the dipole terminals, Z_{DD} is the self-impedance of the driven element referred to the base, I_D is the driven dipole base current, Z_{Dn} is the mutual impedance between the driven dipole and the n^{th} element in the array referred to the base and I_n is the base current in the n^{th} element. For each of the parasitic elements the voltage equation will be of the same form as (2) with the excitation term on the left-hand side set to zero. Thus we may express the system of voltage equations in matrix form as

V = ZI

from which

$$I = z^{-1}v \tag{3}$$

where Z is the impedance matrix, I is the unknown base current vector and V is the source or excitation vector which is zero except at the driven element where the voltage is arbitrarily set as 1.0 volts. The terms in Z are given by

$$Z_{mn} = -30 \operatorname{csc} \beta h_{m} \operatorname{csc} \beta h_{n-h_{m}}^{h_{m}} \left[\sin \beta (h_{m} - |z|) \right]$$

$$\left[-j \frac{e^{-j\beta r_{1}}}{r_{2}} - j \frac{e^{-j\beta r_{2}}}{r_{2}} + 2j \operatorname{cos} \beta h_{n} \frac{e^{-j\beta r_{0}}}{r_{0}} \right] dz \qquad (4)$$

where the dipole dimensions are shown in Figure 3 and the element current is taken to be the filamentary dominant sinusoidal distribution given by

$$I_{n}(z) = I_{n}^{\text{max}} \sin\beta(h_{n} - |z|)$$
 (5)

where β is the free-space wave number $2\pi/\lambda$. The self impedance terms in (4) are computed by setting dequal to the element radius. Solving (3) for the element base currents thus permits one to compute the far radiation field of the array, thus

$$E = \sum_{n=1}^{N} \int_{-h_n}^{h_n} I_n^{\max} \sin(h_n - |z|) \exp(-jkr)$$

exp(-jk
$$\Sigma$$
 d sin θ sin ϕ) exp(jkz cos θ) exp(jwt) dz (6)

This expression for the electric field is a complex quantity which includes all the phase as well as magnitude characteristics of the field. Let $F(\psi, f)$ be the phase quantity associated with

(6) where ψ is an angular variable which describes the "look angle" or "aspect angle" of the antenna and f is the frequency variable. If there exists an origin vaich reduces $F(\psi, f)$ to a constant then this origin is said to be the phase centre of the antenna. Since this definition of phase centre depends upon polarization and the plane which contains the angular variable ψ , these two quantities must be specified whenever the concept of phase centre is used. In this work the principal θ and ϕ planes (or E and H planes respectively) are of interest.

For most antennas the phase is a function of ψ whatever the origin chosen, but over a limited range of ψ there may exist a point p such that $F(\psi, f)$ is practically constant. If p is chosen as the phase centre for a given aspect angle ψ_p , then the range of ψ for which the fixed point p can be used as the phase centre will depend on the allowable tolerance on F. To find the point p use is made of the evolute of a plane equiphase contour. The evolute is the locus of the centre of curvature of the contour, and the centre of curvature corresponds to the location of an origin which leads to no change in the phase function over an increment $\Delta\psi$. The knowledge of $F(\psi, f)$ as a function of ψ for any origin near the antenna is sufficient to determine the evolute of a far-field equiphase contour.

In the coordinate system of Figure 4, OP = 4 is the distance

from the origin to a point on an equiphase contour S. The ray DP is normal to the tangent line of S at P, therefore DP must pass through the centre of curvature. Using the development of Carrel the displacement of the phase centre can be approximated by

The second belowed the

$$\frac{d_{i}}{\lambda} = -\frac{F(\psi_{i} + \Delta \psi) - F(\psi_{i})}{2\pi[\cos(\psi_{i} + \Delta \psi) - \cos\psi_{i}]}$$
(7)

where ψ_i is a given value of ψ and $\Delta\psi$ is an increment. As $\Delta\psi$ becomes small, equation (7) approximates the derivative of $F(\psi)$ with respect to the variable 2π cos ψ . Once d is found as a function of ψ , rays such as DP can be drawn by setting $\gamma = \psi$. The evolute of the equiphase contour is then the envelope curve of the rays.

We consider the case shown in Figure 5 to illustrate the features of the phase centre movement. Consider the offset distances d_1 , d_2 , d_3 corresponding to observation angles ψ_1 , ψ_2 , ψ_3 respectively and let the rays R_1 , R_2 , R_3 be the distances from d_1 , d_2 , d_3 respectively to the intersections with the evolute contour. Let points A and B be the ray intersections of ray pairs R_1 , R_2 and R_1 , R_3 respectively. If the angular increments between ψ_1 , ψ_2 and ψ_1 , ψ_3 are small then points A and B will be approximately on the evolute. The distance L can be

computed between the intersection of any consecutive ray pairs and the origin and this distance will be a close approximation to the straight line separation between the origin and the phase centre at any observation angle.

$$L_{A} = \sqrt{(x_3 + d_2)^2 + (x_3 tan \psi_2)^2}$$
 (8)

$$x_3 = \frac{\frac{\tan \psi_1}{\tan \psi_2} (d_2 - d_1)}{1 - \frac{\tan \psi_1}{\tan \psi_2}}, d_1 \text{ and } d_2 \text{ negative to left of 0}$$

where the distances L_A , L_B are assigned to correspond to angles ψ_2 and ψ_1 respectively. Thus for any observation angle ψ_1 one may readily locate the phase centre by knowing L_i and the corresponding d_i .

In this work the field is computed at 1 degree angular increments and L is calculated using each successive ray pair.

3. NUMERICAL RESULTS - 12 ELEMENT YAGI

This section describes the radiation characteristics of a 12-element Yagi having dimensions given in Table 1. The computed swept-frequency front and back patterns are shown in Figure 6 from which we select three operating frequencies to illustrate the different types of phase centre behaviour:

frequency point "A" (650 MHz) has moderate front-to-back ratio with shallow sidelobe nulls; frequency point "B" (668.5 MHz) has maximum front-to-back ratio with very deep sidelobe nulls and frequency point "C" (754 MHz) is a resonance which is characterized by scalloping of the main lobe and high side and backlobes. This last point is chosen to illustrate the effects of resonant behaviour and, although the antenna would not normally be operated at its extreme bandedge as in this case, it has been shown 3,4 that similar resonant behaviour may occur thoughout the passband under various conditions. Figure 6 shows the polar H-plane radiation patterns at these three frequencies of interest and Figure 7 presents the distance L as a function

TABLE 1 Yagi Dimensions

Reflector element length $2h_{12} = 23.6$ cm Driven element length $2h_{11} = 21.5$ cm Director element length $2h_1 \rightarrow 2h_{10} = 18.5$ cm

Element radius a = 1.5 mm

No. of elements N = 12

Director element spacing $d_1 \rightarrow d_9 = 9.4$ cm

Driven element-director element spacing d₁₀ = 6.0 cm

Reflector element-driven element spacing $d_{11} = 7.8$ cm

Design frequency = 670 MHz

of angles for these same frequencies.

At 650 MHz and 668.5 MHz the phase centre at boresight $(\phi = 90^{\circ})$ is located approximately 0.6 m back from the front element along the array axis. As the observation angle (4) moves off boresight the phase centre veers off the antenna with the distance, L, from the front element remaining nearly constant with the 3 dB beamwidth of the antenna. As the offboresight angle increases L may rapidly increase to tens or even hundreds of meters. At the resonance frequency (754 MHz) the phase centre distance L varies rapidly even within the 3 dB beamwidth. Of particular importance are the rapid changes in L which correspond to the polar pattern null positions where a cusp normally occurs in the evolute. Upon closer examination we note that the magnitude of L is related to the angular derivative of the polar plot and hence deep nulls, where the angular drivative of the polar pattern is large, are characterize by large values of L (Figure 7). Furthermore, sharp nulls have nearly discontinuous angular derivatives resulting in a cusp in the evolute. When the angular derivative is small such as when the main lobe is very broad and "flat" then value of L is correspondingly small.

4. '.UMERICAL RESULTS - ANTENNAS USED IN SYLEDIS SYSTEM

We consider now 7- and 12-element Yagis which are in use

in the SYLEDIS radio positioning system. Antenna specifications are given in Table 2 and the swept-frequency responses are shown in Figure 8. Polar H-plane radiation plots are also given at the system operating frequency 432 MHz. Since the

TABLE 2 Yagi Dimensions Used in SYLEDIS System

No. of elements N = 7 (or 12)

Reflector element length $2h_7 = 35.0$ cm $(2h_{12} = 25.0$ cm)

Drive a element length $2h_6 = 30.0$ cm $(2h_{11} = 30.0$ cm)

Director element lengths $2h_1 = 27.5$ cm $2h_2 \rightarrow 2h_5 = 30.0$ cm $(2h_2 \sim 2h_{10} = 30.0$ cm

Element radius a = 3.0 mm

Element separation
$$d_1 = 15.5 \text{ cm}$$

 $d_2 + d_5 = 14.5 \text{ cm} (d_2 + d_{10} = 14.5 \text{ cm})$
 $d_6 = 10.2 \text{ cm} (d_{11} = 10.2 \text{ cm})$

antennas are normally vertically polarized in use we consider only angular movements in the H-plane of the antenna. The 7-element array has a ±26° 3 dB beamwidth with a first null 52° off boresight. The 12-element array has a ±16.5° 3 dB beamwidth with a first null at 32° off boresight and a much deeper null at 63° off boresight. A plot of L over one angular

quadrant ($\phi = 0 - 90^{\circ}$) for each antenna is given in Figure 9 from which several observations may be made:

- for a 7-element array L remains nearly constant (approx. 0.4m) over the 3 db beamwidth however for the 12-element array L changes rapidly within a few degrees of boresight;
- ii) both arrays showed large rapid phase centre movements of the order of tens of meters over the quadrant;
- iii) the phase centre of the longer array veers off the antenna more rapidly than for the shorter array due to the sharper main lobe with nulls nearer to boresight;
- iv) although both arrays have well defined nulls off boresight, longer arrays tend to have much sharper nulls
 (hence larger angular derivatives and discontinuities
 in the angular derivative) with corresponding large
 phase centre movements;
- of or both arrays the general features of the "L vs.

 angle" curve can be readily predicted by observing the

 polar radiation pattern and visually estimating the

 relative size of the angular derivative of the plot,

 particularly noting the occurrence of sharp nulls;

vi) regardless of the array length there is no single range correction term which can be of value in field service short of calculating the exact phase centre location for each bearing angle and frequency.

5. ERROR CORRECTION

Phase centre movements inevitably result in errors in distance determinations since the electronic equipment simply gives a readout proportional to the phase centre separation between transmitting and receiving antennas. In practice, an initial "calibration" reading is often taken over a path of known length and the instrument reading is manually "corrected" to give zero error. This same correction is then applied to all subsequent readings and is intended to account for fixed phase delays in cable lengths and electronic circuitry as well as any propagation effects which may be present. It also includes any phase centre displacement which was present in the calibration procedure. Referring to Figure 10(a) we have an interrogation site at A using a directional antenna whose phase centre can be computed for any look angle and a beacon at B which, for simplicity of discussion, is assumed to have zero phase centre displacement for all angles in the observation plane. The following discussion is easily adapted for any combination of interrogator-beacon antennas if this assumption

is invalid. The calibration reading is a measure of the distance B - PC1 (where PC1 is the phase centre at the calibration boresight look angle) and is "corrected" to give the known distance AB. For reasons which will be discussed shortly it is important that the calibration be done at boresight. When the receiver antenna is turned through the angle ξ to a new look angle the instrument reading will change by the amount L' cos n (assuming A and B are far removed) corresponding to the new phase centre location PC2. A plot of L' cos η as a function of ξ (Figure 11) will thus indicate an "error" function normalized to the calibration setup. If the receiver is then moved to another observation site and the same initial calibration is used care must be taken to ensure that the antenna bearing with respect to the survey line is identical to that used in the calibration setup. In order to use the "error function" curve to correct the instrument readings it thus becomes necessary to record the antenna bearing (pointing direction with respect to the survey line) with each reading. If the beacon antenna also exhibits. phase displacement, as would be the case for Yagi arrays which are typically used, then both antenna bearing angles must be recorded and a separate "error function" curve for the beacon antenna must be available. Corrections for phase centre movement must then be applied at both ends of the survey line.

As indicated above the antenna bearing for calibration should be boresight in which case the phase centre lies on the array axis as well as on the survey line (Figure 10(a)). Then, as discussed earlier, the change in instrument reading indicates the distance L' $\cos \eta$. If, however, the boresight angle is not used for calibration (Figure 10(b)) the change in instrument reading corresponding to an angular antenna rotation ξ will be given by L' $\cos \eta$ ' with a resulting different of L'($\cos \eta$ ' - $\cos \eta$). This discrepancy may become significant even when η ' - η is small since L' may become of the order of tens or even hundreds of meters at some angles for the Yagis studied. The following procedure is therefore recommended for obtaining and correcting range data obtained from systems similar to the SYLEDIS system:

- Perform a boresight calibration measurement over a known
 path with known beacon antenna bearing. If the beacon
 antenna exhibits phase centre movement, its "error function"
 curves for both antennas must be used to correct the
 readings.
- For any changes in cabling, antennas or receiver the calibration procedure must be repeated.
- 4. Since the largest range errors occur in the vicinity of antenna pattern nulls, each antenna used in the system should be accompanied by its polar radiation pattern in

order that beam null readings may be avoided.

6. CONCLUSION

An analytical model has been developed to compute the location of the phase centre of Yagi arrays for any antenna look angle and this model has been used to calculate distance error curves for antennas commonly used in the SYLEDIS system. Yagis are shown to be unsuitable for uncorrected use in UHF radio positioning systems where wide beam coverage is required and it is shown that significant phase centre movement may occur even within the main lobe, particularly for long, high-gain Yagis. Recommendations are made for a calibration and operation procedure which would allow phase centre movement corrections to be made. A simple technique for qualitatively evaluating the suitablity of an antenna for radio positioning applications is presented.

7. REFERENCES

- Carrel, R.L. (1961) Analysis and Design of the Log-Periodic
 <u>Dipole Antenna</u>, Technical Report #52, Contract AF33(616) 6079, Antenna Laboratory, University of Illinois, Urbana,
 Illinois.
- Tranquilla, J.M. and Balmain, K.G. (1981) Resonance
 phenomena on Yagi arrays, <u>Canadian Electrical Engineering</u>

 Journal 6 (no. 2): 9-13.

- 3. Tranquilla, J.M. and Graham, G.B. (1982) The development of anomalous responses on single tapered and untapered Yagi antennas as a function of antenna length, Canadian Electrical Engineering Journal 7(No. 1): 18-22.
- 4. Tranquilla, J.M. and Graham, G.B. (1982) Resonance

 phenomena on non-skewed H-plane multiple-Yagi arrays,

 Canadian Electrical Engineering Journal (No. 3): 18-23.

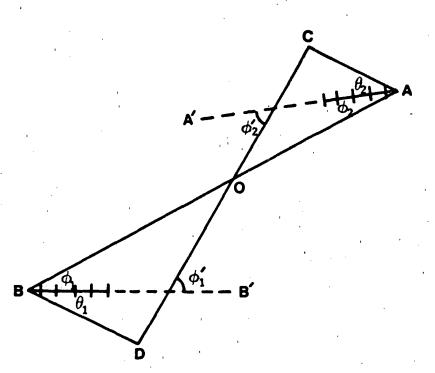


Fig. 1 Typical radio positioning setup with beacon at A, interrogator at B. Phase centres for beacon and receiver antennas are at C and D respectively.

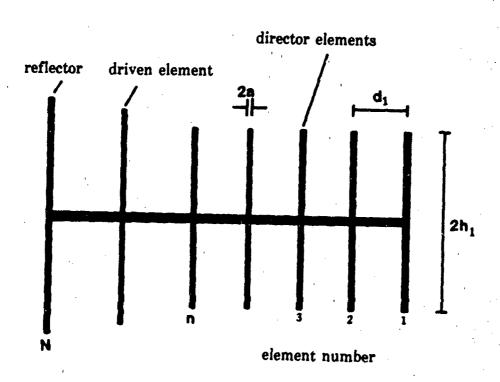


Fig. 2 Yagi array of dipole elements.

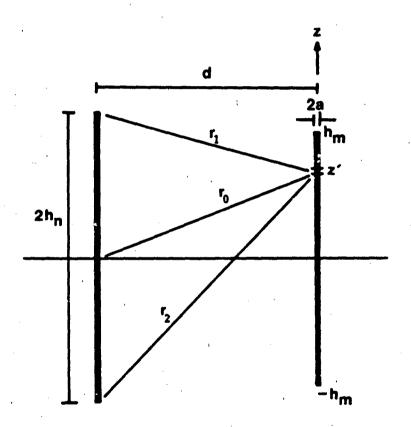


Fig. 3 Geometry for mutual impedance calculation by induced emf me

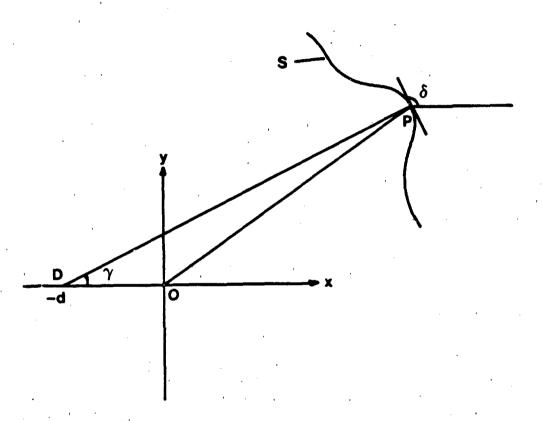


Fig. 4 Coordinate system for phase centre computations (after Carrel [1]).

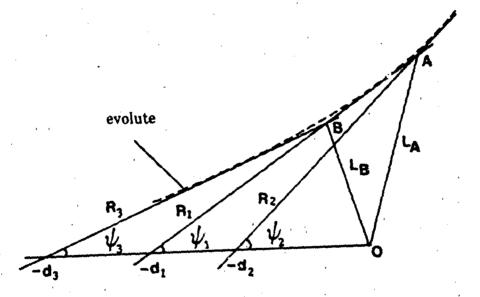


Fig. 5 Geometry for determination of distance from origin to phase centre.

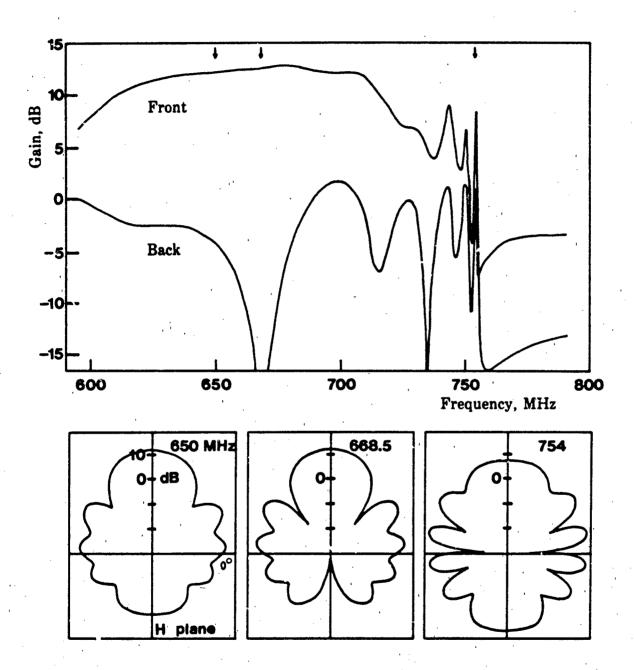
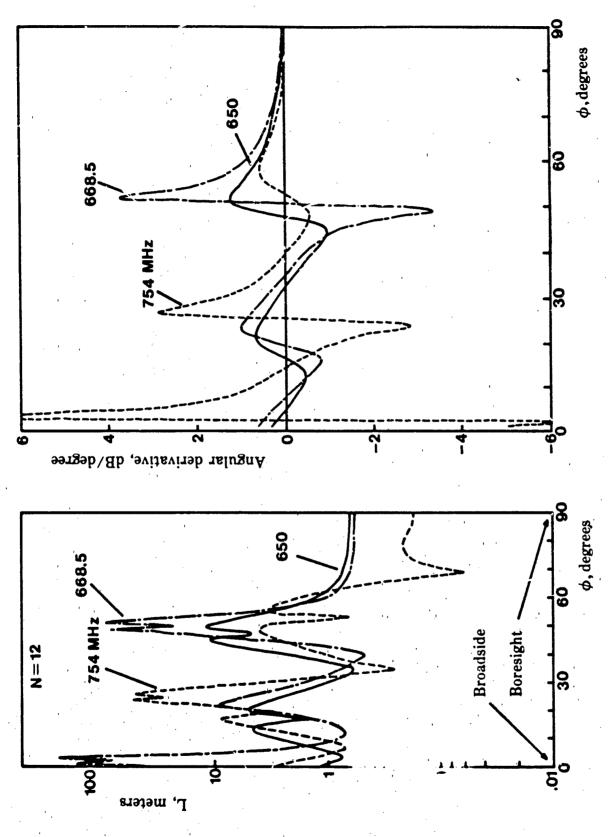


Fig. 6 Calculated swept-frequency radiation pattern for 12-element Yagi and polar patterns at 650 MHz, 668.5 MHz and 754 MHz.



Calculated phase centre distance L and angular derivative of the polar radiation pattern for 12-element Yagi at 650 MHz, 668.5 MHz and 754 MHz. Fig. 7

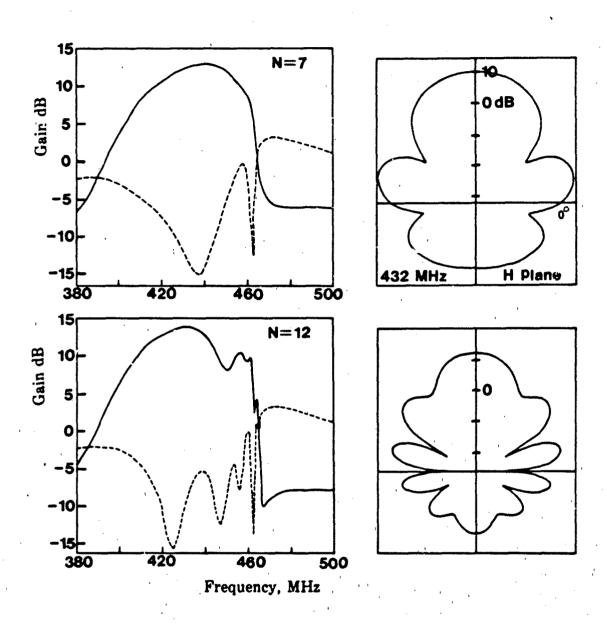


Fig. 8 Calculated swept-frequency radiation pattern for 7 and 12-element Yagi arrays and polar plots for each at 432 MHz.

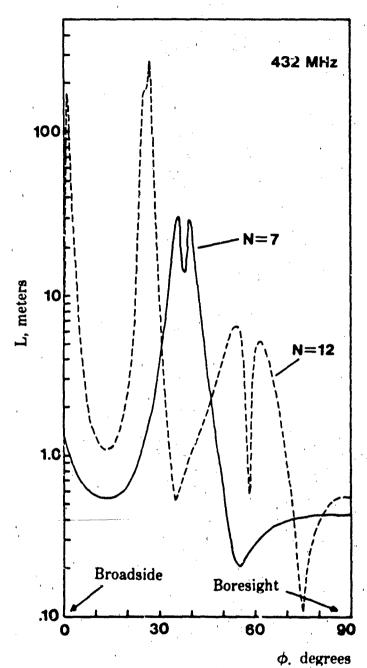


Fig. 9 Computed straight line distance from phase centre to origin for 7 and 12-element Yagi arrays at 432 MHz. Origin is located at the centre of the front director Yagi element.

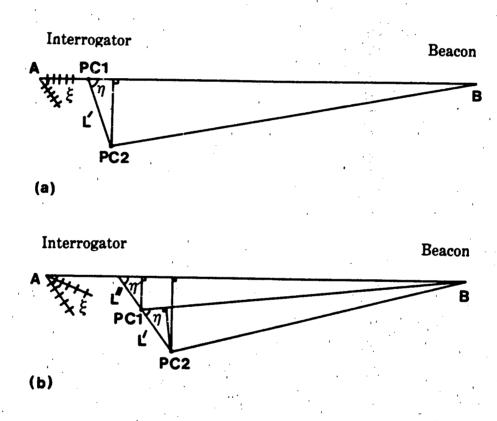


Fig. 10 Error involved in (a) boresight, (b) off-boresight calibration.

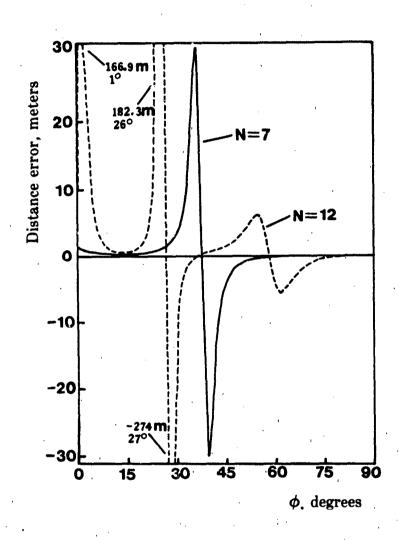


Fig. 11 Computed distance error for 7 and 12-element Yagi arrays at 432 MHz.

APPROACH TO A SUITABLE DIRECTIONAL ANTENNA FOR UHF RADIO POSITIONING APPLICATIONS

J.M. Tranquilla and S.R. Best
Department of Electrical Engineering
University of New Brunswick
Fredericton, N. B., Canada
(506) 453-4561

ABSTRACT

The phase centre properties of log-periodic dipole (LPD) arrays are examined for suitability in UHF radio positioning systems and are compared with phase properties of commonly used Yagi arrays. LPD arrays offer gain nearly comparable to that obtained from short Yagis, exhibit nearly 180° main lobe coverage with no front quadrant nulls, and show very small phase centre movement over the entire front hemisphere.

1. INTRODUCTION

Modern UHF radio positioning systems such as SYLEDIS SYsteme LEgere de DIStance) require beacon transmitters whose antennas have sufficient gain to allow operation to several hundred kilometers. Yagi antennas (either singly or in dual arrays) are commonly used, however, the phase centre movement on high gain Yagis may lead to errors of the order of tens or even hundreds of meters in distance determination 1. High gain Yagis inherently exhibit narrow beamwidth with several sharp nulls in the polar radiation pattern. It has been shown that the phase centre displacement (as a function of observation angle) increases dramatically with the angular derivative of the polar pattern and hence yields maximum distance measurement error in the vicinity of pattern nulls '. Equipment manufacturer recommendations often include the warning that such antennas not be used outside their 3 dB beam pattern which, for single 7- or 12-element Yagis commonly used, restricts the user to approximately 15° or 25° respectively from boresight. This is an impractical restriction since the user would not normally know which of the possibly several beacons were pointed toward him and, therefore, would not know which readings were reliable.

One solution to the problem is to make available to each user the phase centre displacement "correction curves" for each antenna

in the system and to record receiver-beacon antenna bearings with each distance measurement. Data processing using known site coordinates, antenna bearings and phase centre locations could then be used to apply corrections to field readings.

An obviously more desirable solution would be to select or design antennas which exhibit the required gain while also having small phase centre displacement for look angles covering at least the front hemisphere of the antenna. Log-periodic dipole arrays are known to have moderate gain, broad front lobe coverage and a boresight phase centre which follows the so-called active region of the antenna².

This paper considers the phase properties of a typical linear array from which we may infer some basic requirements to produce a stable phase centre. We then consider the case of the commonly used Yagi to illustrate the extent of phase centre movement and its dependence upon array length. Finally, we consider the LPD array and compare the range errors obtained from it at look angles in the principal planes with those obtained from a Yagi array.

2. PHASE PROPERTIES OF LINEAR ARRAYS

Consider an array of z-directed, parallel linear elements lying in the y-z plane as shown in Figure 1. The element spacing is not necessarily uniform and \mathbf{d}_n is the distance along the array line from the \mathbf{n}^{th} element to some convenient reference origin, 0.

The complex current in each element may be represented as I_n and P is an observation point in the far field. The phase dependence of the fields at P due to the nth element is then given by the usual Green's function approximation

$$\phi = e^{-jkr} e^{-jk d_n sin\theta} sin\phi_e^{jkz} cos\theta_e^{j\alpha_n}$$
 (1)

where e jan represents the phase of the driving current in the nth element and $k = 2\pi/\lambda$. Of course, these terms must be subsequently integrated over the element length for the z-directed currents and summed over all elements to give the final field result. Thus the phase of the field, and hence the location of the phase centre are dependent upon the element size, array length and view angle. Ideally, for minimum phase centre movement, the element factor $\exp(jkz \cos\theta)$ and the array factor $\exp(-jkd_n \sin\theta \sin\phi)$ should be as near to unity as possible. For elements near resonance the element factor cannot be adjusted, however, the array factor can be minimized if the array size is reduced and particularly if the dominant array currents are localized to a relatively small portion of the array at the operating frequency. since compact arrays have inherently wide-beamwidth and low to moderate gain we can see the conflicting requirements of phase and gain performance.

Yagis are travelling wave radiators on which an electromagnetic wave is excited at the driven element, guided along the director elements, and launched as a free space wave. The length and spacing of the parasitic director elements adjusts the phase velocity of the wave to nearly match that of free space so that the antenna will radiate efficiently. The gain of the antenna is dependent upon the length of the director guiding structure so that high-gain Yagis have many directors and exhibit several sidelobes and nulls in the polar radiation patterns. Unfortunately, the increased length of the director segment adversely affects the phase properties in (1).

LPD ARRAY MODEL

Figure 2 shows the LPD array with the network representation used by Carrel². Following Carrel's well-known development, we may solve the matrix equation

$$I = (U + Y_F Z_A)I_A$$
 (2)

for the element base current vector $\mathbf{I}_{\hat{\mathbf{A}}}$ where \mathbf{I} is the excitation current vector, $\mathbf{Y}_{\hat{\mathbf{F}}}$ is the feedline admittance matrix, $\mathbf{Z}_{\hat{\mathbf{A}}}$ is the element impedance matrix and \mathbf{U} is the unit vector. Once the element currents are known, the radiated electric field may be computed as

$$E = \sum_{n=1}^{N} \frac{j^n}{\pi} \exp(-jkr) \exp(-jk \sin\theta \sin\phi \sum_{i=1}^{N-1} a_i)$$

$$\frac{I_{n}}{\sin \theta} \left[\cos(kh_{n}\cos\theta) - \cos kh_{n} \right]$$
 (3)

where n-120w ohms and the element current is taken as the dominant sinusoidal mode described by

$$I(z) = I_{n \text{ max}} \sin k(h_n - |z|)$$
 (4)

The expression for the electric field in (3) is a complex quantity which includes all the phase as well as magnitude characteristics of the field. Let $F(\psi, f)$ be the phase quantity associated with (3) where ψ is an angular variable which describes the "look angle" or "aspect angle" of the antenna and f is the frequency variable. If there exists an origin which reduces $F(\psi, f)$ to a constant then this origin is said to be the phase centre of the antenna. Since this definition of phase centre depends upon polarization and the plane which contains the angular variable ψ , these two quantities must be specified whenever the concept of phase centre is used. In this work, the principal and planes (or E and H planes respectively) are of interest.

For most antennas, the phase is a function of whatever the

origin chosen, but over a limited range of there may exist a point p such that $F(\psi, f)$ is practically constant. If p is chosen as the phase centre for a given aspect angle ψ_p , then the range of ψ for which the fixed point p can be used as the phase centre will depend on the allowable tolerance on F. To find the point p use is made of the evolute of a plane equiphase contour. The evolute is the locus of the centre of curvature of the contour, and the centre of curvature corresponds to the location of an origin which leads to no change in the phase function over an increment $\Delta\psi$. The knowledge of $F(\psi, f)$ as a function of ψ for any origin near the antenna is sufficient to determine the evolute of a far-field equiphase contour.

In the coordinate system of Figure 3, OP = r is the distance from the origin to a point on an equiphase contour S. The ray DP is normal to the tangent line of S at P, therefore, DP must pass through the centre of curvature. Using the development of Carrel the displacement of the phase centre can be approximated by

$$\frac{d_{i}}{\lambda} = -\frac{F(\psi_{i} + \Delta \psi) - F(\psi_{i})}{2\pi \left[\cos(\psi_{i} + \Delta \psi) - \cos\psi_{i}\right]}$$
(5)

where ψ_i is a given value of ψ and $\Delta \psi$ is an increment. As ψ becomes small, equation (5) approximates the derivative of F (ψ) with respect to the variable 2π cos ψ . Once d is found as a

function of ψ , rays such as DP can be drawn by setting $\gamma = \psi$. The evolute of the equiphase contour is then the envelope curve of the rays. We consider the case shown in figure 4 to illustrate the features of the phase centre movement. Consider the offset distances d_1 , d_2 , d_3 corresponding to observation angles ψ_1 , ψ_2 , ψ_3 respectively and let the rays R_1 , R_2 , R_3 be the distances from d_1 , d_2 , d_3 respectively to the intersections with the evolute contour. Let points A and B be the ray intersections of ray pairs R_1 , R_2 and R_1 , R_3 respectively. If the angular increments between ψ_1 , ψ_2 and ψ_3 , are small then points A and B will be approximately on the evolute.

The distance L can be computed between the intersection of any consecutive ray pairs and the origin and this distance will be a close approximation to the straight line separation between the origin and the phase centre at any observation angle.

$$L_{A} = \sqrt{(x_{3} + d_{2})^{2} + (x_{3} \tan \psi_{2})^{2}}$$

$$x_{3} = \frac{\frac{\tan \psi_{1}}{\tan \psi_{2}} (d_{2} - d_{1})}{1 - \frac{\tan \psi_{1}}{\tan \psi_{2}}}, d_{1} \text{ and } d_{2} \text{ negative to the } (6)$$

$$1 - \frac{\tan \psi_{1}}{\tan \psi_{2}}$$

$$1 - \frac{1}{\tan \psi_{2}}$$

$$1 - \frac{1}{\tan \psi_{2}}$$

where the distances LA, LB are assigned to correspond to angles

 ψ_2 and ψ_1 respectively. Thus for any observation angle ψ_1 one may readily locate the phase centre by knowing L_1 and the corresponding d_1 .

In this work, the field is computed at 1 degree angular increments and L is calculated using each successive ray pairs.

In electronic distance measurement applications the phase centre movement results in a distance error as described using Figure 5. In Figure 5, the system is boresight calibrated over a known path AB. At the boresight angle, the phase centre of the receiver antenna is located at C along the path AB. The instrument reading is a measure of the separation between antenna phase centres (BC) and the calibration procedure adjusts this reading to give the known value AB, thus accounting for any phase delays in cables and electronic circuitry, propagation effects and phase centre displacement. As the receiver antenna is turned through an angle & from boresight the phase centre moved to C' which may be uniquely defined in terms of the angle wmeasured from the array line. The angle & may thus be computed as the angle between the line joining phase centres C - C' and the path AB. The distance reading, using the same calibration correction described above, will thus be in error by the amount CC' cos & at this off-boresight angle. Of course, for any antenna pointing angle & the new phase centre C' and the corresponding angle

w must be recalculated to give the distance error. In this manner an "error" curve may be produced to show the needed correction at any antenna pointing angle. Care must be taken to ensure that in the initial calibration procedure the antenna is pointed along the path AB (thus ensuring that C lies on AB) or, if this is impractical, that the off-boresight angle be measured and the off-axis phase displacement be taken into account.

4. COMPUTED LPD ARRAY RESULTS

The LPD array parameters are given in Table 1 and were selected to give midband operation at 432 MHz corresponding to a commonly used frequency in the SYLEDIS system. Figure 6 presents the polar H-plane radiation pattern and the computed straight line distance L (from equation (6)) in both the E and H planes. This array gives nearly \pm 90° front beam coverage with very small phase centre movement compared with the performance of 7- and 12-element Yagis (figure 7). It may be noted that for comparison purposed the LPD array length was chosen to be nearly equal to that of the 7-element Yagi.

In Figure 8 the distance error curve for the 10-element LPD array is shown for a 90° front quadrant. Also presented for comparison are the error curves for 7- and 12-element Yagis commonly used in the SYLEDIS system. The improved performance of the LPD array is evident in that the distance error magnitude is

TABLE | LPD Array Parameters

10 element LPD array

 $\tau = 0.92$

 $\sigma = 0.172$

element radius 1.4 mm

longest dipole length 0.395 m

longest element half-wavelength frequency 380 MHz shortest element half-wavelength frequency 805 MHz feedline characteristic impedance Z $_0$ = 200 Ω

6 element LPD array with parasitic director extension

 $\tau = 0.92$

 $\sigma = 0.172$

element radius 1.4 mm

longest dipole length 0.363 m

longest element half-wavelength frequency 413 MHz shortest element half-wavelength frequency 627 MHz feedling characteristic impedance Z_0 = 200 Ω parasitic dipole length 0.239 m parasitic element spacing 0.091 m

less than 4mm out to approximately \pm 60° from boresight and remains less than 2.5m even at broadside angle.

In many positioning applications requiring maximum system range a single antenna does not offer sufficient gain, and even in shorter-distance situations maximum antenna gain is desirable to avoid unnecessary signal loss due to noise. The LPD array, in spite of its excellent phase performance, is not a high gain antenna, however, its gain can be markedly improved by the addition of a parasitic array aboad of the LPD elements. The analysis of such a hybrid array alosely follows that described in this work with the addition of a set of equations in (2) representing the voltage vector of the base of the parasitic elements.

We consider the case of an LPD array similar to that described in Table 1 with the modifications that the longest and three shortest elements are removed to reduce array length. This affects only the array bandwidth which is of no consequence in this application since the resultant operating band leaves the array unchanged at the 432 MHz operating frequency. To this 6-element LPD array we then add up to a 6 parasitic elements whose dimensions are given in Table 1. The polar patterns and distance error curves for several of these hybrid arrays are presented in Figure 9. The effect of the parasitic extension is

to increase the gain (up to 2dB in this case for 6 parasitic elements) and to decrease the beamwidth (from 110° for no elements to 74° for 6 parasitic elements, however, the distance error remains very small (of the order of 1 m. maximum) out to the first nulls on all of the arrays and all of the arrays offer effective front hemispherical coverage which is not available with Yagi arrays. Further addition of parasitic element, however, will lead to the development of front-quadrant nulls and larger distance errors in the vicinity of these nulls.

5. CONCLUSIONS

An analytical model of the log-periodic dipole array has been used to study the antenna phase centre movement and to determine the applicability of this antenna for UHF electronic distance measurement systems such as SYLEDIS. The LPD array distance error is compared with that of 7- and 12-element Yagis and it shown that the LPD array offers much improved phase centre and beam coverage performance.

- 6. REFERENCES
- 1. Tranquilla, J.M, and Best, S.R. (1984) Antenna phase centre movement in U.H.F. radio positioning systems. Submitted for publication in the <u>Journal of the Institute of Navigation</u>.
- 2. Carrel, R.L. (1961) Analysis and Design of the Log-Periodic

Dipole Antenna, Technical Report #52, Contract AF33

(616)-6079, Antenna Laboratory, University of Illinois,
Urbana, Illinois.

3. Kahn, W.K. (1981) Double-ended backward wave Yagi hybrid antenna, IEEE Trans. Antennas and Propagation AP-29 (No. 3) 530-532.

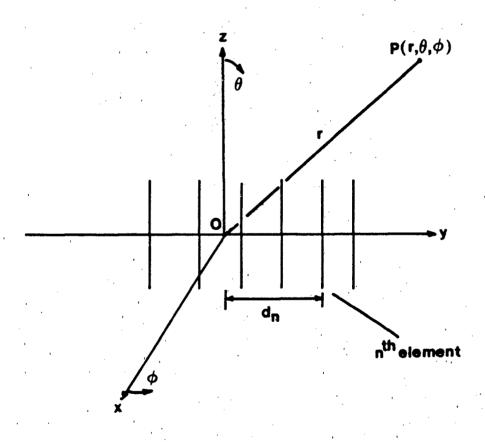
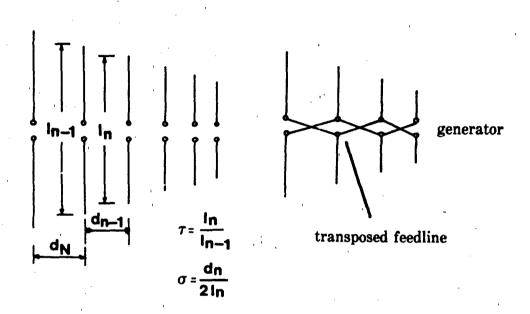


Fig. 1 Array of linear elements lying in y-z plane. An observation point $P(r, \theta, \phi)$ is located in the far field of the array.



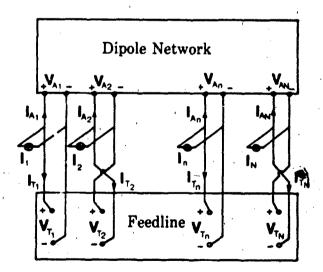


Fig. 2 Details of the LPD array model after Carrel [2] showing the element and feedline arrangement and the connected network model.

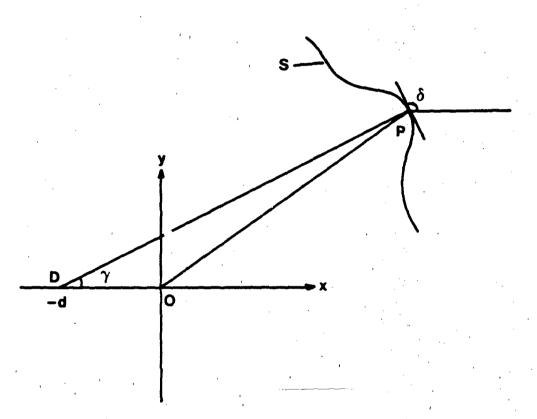


Fig. 3 Coordinate system for phase centre computations (after Carrel [2]).

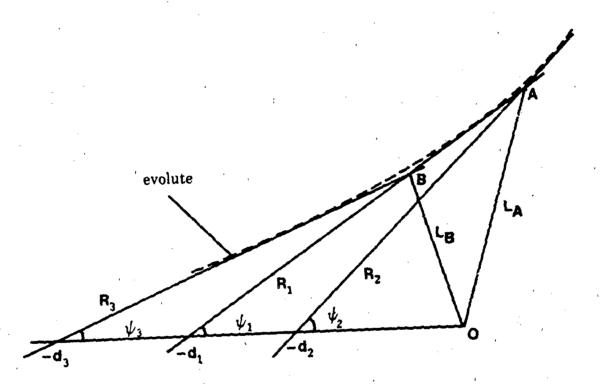


Fig. 4 Geometry for determination of the distance from the origin to the approximate phase centre on the evolute.

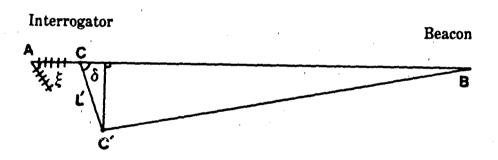
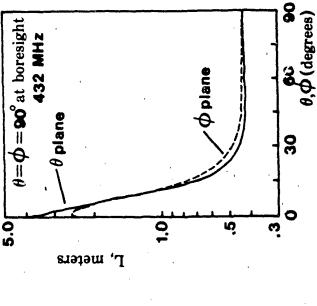
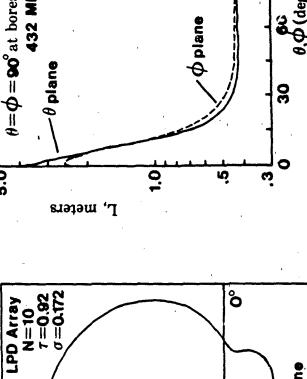
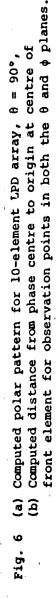


Fig. 5 Distance measurement error involved in boresight calibration.







9

H plane

10 dB

432 MHz

Relative Gain

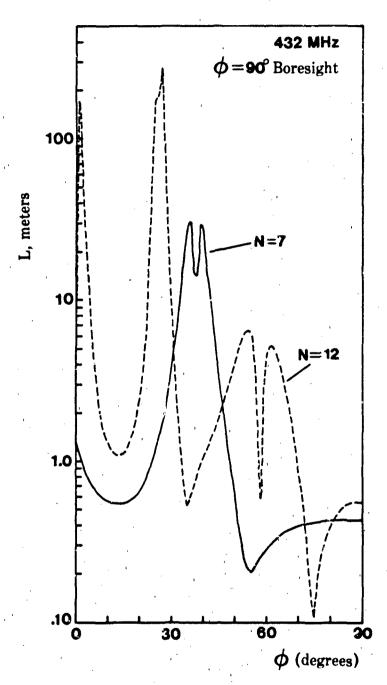
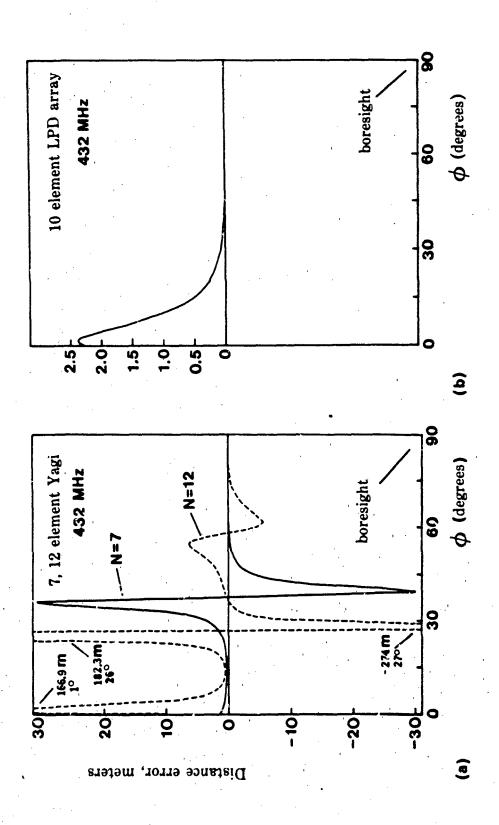
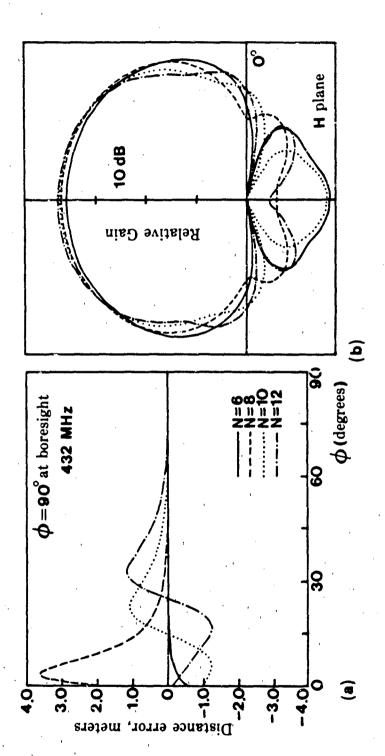


Fig. 7 Computed straight line distance from phase centre to origin at center of front element for 7 and 12-element Yagis at 432 MHz.



.g. 8 Computed distance measurement error for (a) 7 and 12 element Yagis and (b) 10-element LPD array. Error is expressed with respect to the boresight phase centre.



Computed results for a 6-element LPD array with a variable number of parasitic director elements (a) distance measurement error expressed with respect to the boresight phase centre, (b) polar radiation patterns in the ϕ -plane. Fig. 9

FOUR BAND

RADAR AUGMENTATION SYSTEM FOR

HIGH PERFORMANCE TARGETS

HARRY B. SELTON JR.

TECOM INDUSTRIES, INC.
9324 Topanga Canyon Blvd.
Chatsworth. Califfinia

ABSTRACT

Modern day targets, used to exercise radar detection and tracking frequently employ radar augmentation systems to enhance their cross section to simulate a larger vehicle. This results in improved detection/tracking that is closer to operational scenarios. Since detection and tracking radars are frequency optimized systems, the radar augmentation must cover the multiple bands in which these radars operate.

A design was undertaken to provide radar augmentation, for a high performance target, in L. S. C and X bands. This target operates at MACH 3, to 80,000 feet altitude, with flight times to 300 seconds, and experiences stagnation temperatures at the radome in excess of 500° F. Radar cross section levels.

required, were used to define antenna gains and isolation levels.

The completed design consisted of pairs of orthogonal antenna elements highly isolated so that solid state amplifiers could be inserted to provide active augmentation. Crossed dipoles were used at L-Band, yagi's at S-Band, and planar spirals from C-Band through X-Band. Isolation levels varied from 25 dB to greater than 50 dB, over frequency, to achieve the required RCS levels. These isolations were achieved in the presence of a nose tip mounted pitot tube and associated heater wires.

The antenna elements were foamed into a single module for environmental protection and located in an A sandwich radome fabricated using polyimide resin. The radome electrical design was identified as critical to achieving high isolations and preventing pattern breakup. The design also had to meet rigid structural and thermal requirements. The entire antenna/radome nose cone was formally qualified prior to the production of 35 prototypes and subsequent production of annual production purchases.

The design is currently being upgraded for increased bandwidths to encompass additional radars with polarizations changed to all circular to accom-

modate target roll. The module design is being considered as universal for application to other targets.

1.0 REQUIREMENTS

The requirements for the high performance target were contained in a specification control drawing prepared by the target manufacturer. These requirements included both electrical and structural requirements.

1.1 Electrical

The electrical requirements of the radar augmentation system(s) are presented in Table 1-1.

The frequency requirements are presented by generic band and bandwidths. Polarization requirements listed follow the normal polarizations in use by operational radars. Gain levels were not specified but RCS levels were. Although ±45° coverage was specified off the target nose these angles greatly exceeded actual requirements. This in turn was the driver for the 90° beamwidth specified.

The amplitude ripple requirement was a system design goal applied to the composite gain of the transmit antenna pattern gain plus the receive antenna pattern gain.

Power handling of each antenna element had to be

TABLE 1-1
SUMMARY OF AUGMENTATION SYSTEM REQUIREMENTS

Characteristic	Limits			
Banu	L	S	c ⁽¹⁾	X (1)
Bandwidth, %	10.2	6.7	8.8	3.4
Polarization	H	A\#	, . v	V
Gain, dBi Hin. (2)	H/S	M/S	w/s	N/S
Coverage Zone off Nose	-45*	<u>-</u> 45°	<u>+</u> 45°	±45*
Amplitude Ripple, db(3)	3.0	3 0	3.0	3.0
Half Power SW, Nom.	90*	963	9 0*	90*
Isolation, Min. uB	26	40	45	50
Power Handling, Watts CW	1.0,	1.0	2.0	2.0
VSWE Max.	2:1	2:1	2:1	2:1

MOTES: (1) May be serviced by one broadband antenna element for both bands

⁽²⁾ Not speciated. Must be compatible with pattern and BCs requirements.

⁽³⁾ Grain for composite transmit and receive pattern (4.c., System) re onth.

capable of handling a few watts generally derived from a solid state amplifier. Anteuna VSWR levels were required to be less than 2:1 to provide efficient transfer of energy to/from the active amplifiers to be used.

1.2 Environment

The environmental requirements for the high performance target are summarized in Table 1-2. The radome antenna system used for radar augmentation must operate during these conditions.

These harsh requirements led to two early design conclusions. These were: 1) The antenna elements must be foamed in place to survive the robust vibration, shock and moisture (induced via altitude cycling) requirements; and 2) The radome must be constructed using a high temperature resin such as polyimide to survive the expected surface temperature.

2.0 TARGET RADAR CROSS SECTION

Active radar augmentation is achieved by receiving a sample of the radar energy inpurging upon the target via an antenna $G_{\rm E}$, amplifying that RF signal and its modulation(s), and retransmitting the increased signal via an antenna $G_{\rm E}$. It is obvious that the antennas $G_{\rm E}$ and $G_{\rm E}$ must be isolated by

TABLE 1-2

SURBARY OF HIGH PERFORMANCE TARGET ENVIRONMENT

Condition

Limit

Temperature Altitude

MIL-STD-810C, Method 5-4.1, Altitude 0-80,000 feet, Temperature 40°C to +71°C.

Temperature Shock

HIL-STD-810C, Method 503.1, -57°C to +71°C.

Surface Temperature(1)

+296°C for 5 minutes, 57 lbs. at

STA 117.

Random Vibration

HIL-STD-810C, Hethod 514.2, 20-2000 Hz at Wo = .04g²/Hz,

1 bour each axis.

Shock

MIL-STD-810C, Method 516.2, Procedure 1, half sine, 20g peak, 11 msec, 3 pulses each direction,

along each major axis.

Acceleration

HIL-SID-810C, Hethod 513.2, ± 9g in I axis, ± 8g in Y axis,

± 17g in Z exis.

Structural Loads (2)

220 lbs. at STA 118.7.

WOTES: (1) Radome surface

(2) Applied to radome as static test.

an amount greater than the amplifier gain to prevent the familiar "sing around" often observed in amateur acoustic situations.

2.1 Radar Cross Section

The radar cross section taut of an antenna may be defined on boresight as follows:

$$\sigma_{ant} = \frac{g^2 \cdot \lambda^2}{4\pi} = \frac{g_t \cdot g_t \cdot \lambda^2}{4\pi}$$
 (2-1)

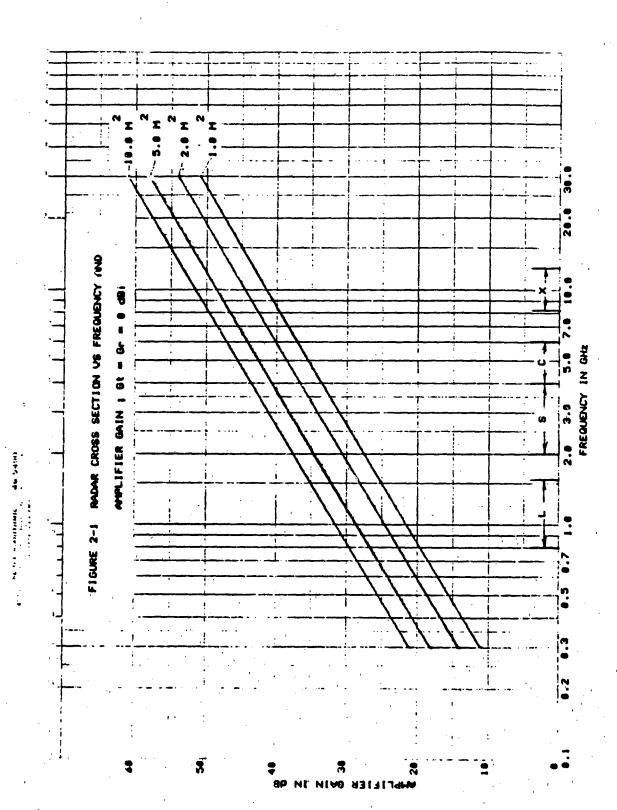
This reduces to:

$$\sigma_{ant} = .08 G_t \cdot G_r \cdot \lambda^2$$
 (2-2)

The total radar cross section of the target $\sigma_{\rm T}$ can be expressed in terms of an amplifier gain which is inserted between the 2 antennas $G_{\rm C}$ and $G_{\rm C}$. Thus we have:

$$\sigma_{\rm T} = \sigma_{\rm ant} \times G_{\rm amp} = .08\lambda^2 \cdot G_{\rm c} \cdot G_{\rm t} \cdot G_{\rm amp}$$
 (2-3)

Figure 2-1 is a parametric plot of this function. It is intuitively obvious that the following equation expresses the stability requirement for active augmentation that gust exist between amplifier gain G_{amp} and inter antenna isolation I_{t-r} to prevent escillations. Expressed in the more familiar



and convenient dB terms we have:

It-r > Gamp

(2-4)

System margins of 3 to 10 dB were established to ensure system stability. Figure 2-1 is based on unity gains (0 dBi) for both G_t and G_r to simplify use. Thus if two 0 dBi gain antennas were used at 300 MHz with a +14 dB amplifier gain a net radar cross section of about +2 dB above a square meter would result. To achieve the same +2 dB re m^2 cross section at 30 GHz would require an amplifier gain of +54 dB and an isolation greater than 54 dB. In the latter example, if the antenna gains were each increased to +10 dBi then the required amplifier gain would be decreased to only 34 dB.

3.0 ANTENNA DESIGN APPROACH

Antenna designs were sought that provided the modest gains required to satisfy the pattern shapes and which were capable of meeting the minimum isolation requirements. Above all, low technical risk solutions were sought.

3.1 Mechanical Constraints

The host target was 13.5 inches in diameter having an ogive radome approximately 24 inches in

length at the tip of which was installed a pitot tube to determine static and dynamic pressures. These pressures were transmitted via high temperature tubing through the antenna volume installed in the base of the radome. Conventional thic walled, carbon loaded, neoprene hoses were found to be unsuitable due to induced pattern ripple resulting from losses/reflections. Thin walled accordian teflon tubing was electrically invisible but collapsed at altitude.

The pitot tube and stainless steel mounting base constituted an axial obstruction. In addition, a pair of No. 16 guage wires had to be routed through the antenna volume to conduct D.C. power to the pitot tube heater for de-icing purposes at altitude. These wires were found to couple strongly to the L- and S-Band antenna fields in a manner that often reduced isolations by 10 to 20 dB. The optimum location of these wires was ultimately determined using empirical methods.

3.2 Mechanical Packaging

Although the entire volume of the radome was available for the augmentation antennas only the aft portion was utilized. The antennas were mounted on a .090 inch thick base plate 8.5 inches in diameter and

the elements foamed with a low density foam into a cylinder approximately 7.2 inches in diameter by 4.5 inches long. A notch was molded into the periphery of the foamed cylinder for passage of the pitot tubes and wires.

The radome incorporated a molded flange of polimide glass inset about 3 inches from the radome base in order to clear canard actuator mechanisms. This flange incorporated captive nutplates for installation of the foamed antenna module.

Figure 3-1 is an external view of the: 1) Ogive radome with tip mounted pitot tube. 2) An unfoamed antenna module, and 3) A foamed (potted) antenna module showing passage ways for the pitot tube hoses.

Figure 3-2 is an interior view into the base of the radome. Visible are the pairs of antenna jacks for L-Band (Jl. J2), for S-Band (J3, J4) and C/X-Bands (J5, J6).

3.3 L-Band Antenna

The antenna configuration selected for L-Band was a pair of orthogonal dipoles operated approximately .02 lambda in front of the aluminum metal base plate. Each dipole was inclined at 45° with respect to target vertical so as to intercept equally either horizontal or vertical polarization. This,

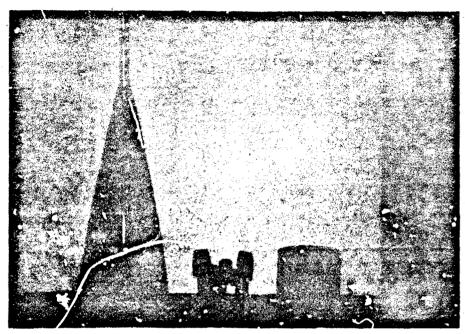


FIGURE 3-1 EXTERNAL VIEW OF RADOME, KNEGTTED ANTENNA ASSEMBLY, AND POTTED ANTENNA MODULE

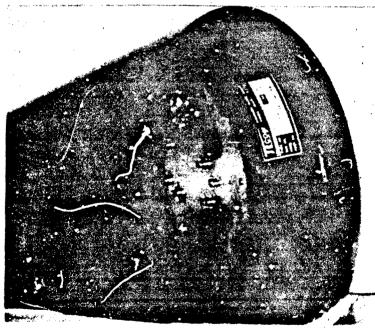


FIGURE 3-2 AFT END OF RADOME BASE SHOWING ANTENNA COAXIAL OUTPUTS AND THE PROVISIONS FOR PITOT TUBES AND HEATER CONNECTIONS

however, does result in a gain loss of 3 dB for both receive and trangel: With nearly coincident phase centers this configuration is capable of isolations of 35 dB with minor adjustment. The presence of the pitot heater wires, coupled strongly at these frequencies, causes reduced isolations.

The dipole elements are fed using standard baluns constructed of 0.141 inch diameter semi-rigid tubing. These elements are clearly visible in Figure 3-1.

3.4 <u>S-Band</u>

Because of the increased isolation required at this band, the antenna elements were separated as much as possible at the edges of foamed 7.2 inch diameter. The elements themselves were orthogonal linear elements, as in L-Band, each inclined 45° with the target vertical so as to receive/transmit either principal polarization (V or H). Because of the anticipated 3 dB gain loss due to polarization each antenna consists of a 5 element Yagi antenna fed by means of .085 inch diameter semi-rigid coaxial tubing. The entire set of 5 elements, including driven element were printed on .020 inch thick 5870 Duroid. These elements show up as the trapezoids in Figure 3-1.

3.5 C/X Bands

At these shorter wavelengths advantage was taken of broadband circularly polarized antenna elements. It was possible to use orthogonally polarized (RHCP and LHCP) unloaded planar cavity backed spirals to cover both these bands. Such an element has a typical bandwidth ratio of 2.5:1 to the 0 dBli points. These elements, as in S-Band are mounted at the maximum diameter available to systemize isolation. The use of orthogonal polarizations contributed 7 to 15 dB to the isolation.

Note that the transfer of the state of the state of the contract of the transfer to the transfer of the transf

The planar spirals show up as the 2 cylinders in Figure 3-1. They are raised off the ground plane by short lengths of .141 inch diameter semi-rigid co-axial cable so as to be in roughly the same aperture plane as the other 2 bands.

4.0 RADOME DESIGN

At the outset of the program TECOM recognized the need to control the radome characteristics because of the electrical influence that would be exerted on antenna performance in terms of both pattern and isolation responses. The success of the program being reported was due in large part to the early decision by the target contractor to merge

system responsibilities for <u>both</u> the augmentation autennas and the radome with a single contractor.

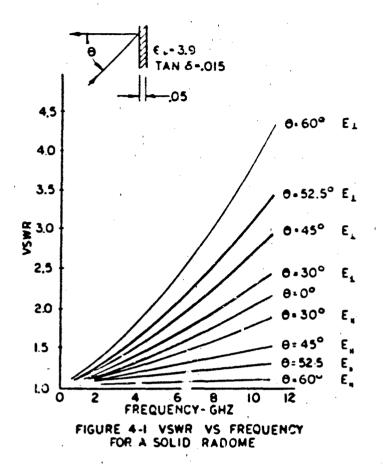
4.1 deflection Levels

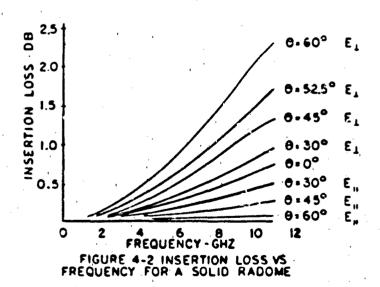
As cited earlier TECOM proposed an A sandwich radome structure that has proven to be successful in the past for broadband coverage over these frequencies. Figures 4-1 and 4-3 present graphically the difference in reflection levels for a solid vs. a sandwich. This is critical as reflection levels contribute adversely to isolation levels.

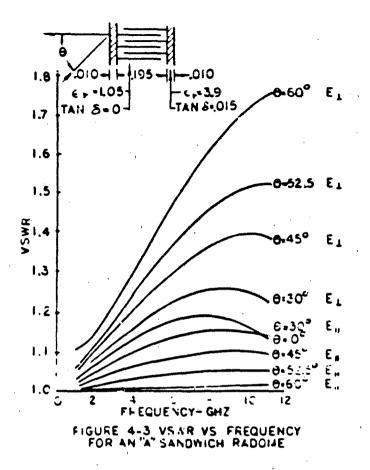
ror example, examine both figures at 10 GHz at an incidence angle of 45° and note the reflection VSWR. For the solid radome that is .05 inches thick (inadequate mechanically) for perpendicular polarization the VSWR is 2.7:1 for a return loss of -6.8 dB or 21% reflection. For a sandwich consisting of .195 inch thick core and .010 inch thick skins at the same frequency and polarization the VSWR is 1.39:1 for a return loss of -15.7 dB or 2.7% reflection. This represents a dramatic improvement of nearly 8:1 in reduced reflection level.

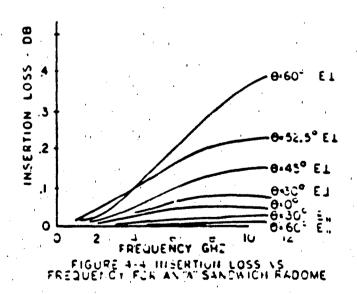
4.2 Transmission Levels

Figures 4-2 and 4-4 in similar fashion show the differences in transmission losses between a solid and sandwich construction. Obviously, from conser-









vation of energy principles, the energy that is reflected is not transmitted. Returning to the same point of 10 GHz and perpendicular polarization we see that the solid radome has a loss of -1.4 dB (72% transmission) vs. for the A sandwich a loss of only -.14 dB (97% transmission). All of the data presented in Pigures 4-1 through 4-4 are the results of flat panel computer runs. Actual measured values are expected to vary somewhat as a result of variations due to unknowns in manufacturing tolerances, exact materials properties and the 2-dimensional model assumed.

4.3 Paprication

Century Plastic was selected to fabricate the radomes of polyimide resin and fiberglass using a female metal mold to hold the outer contour to the precise ogive shape required by the aerodynamicists.

Century Plastics was selected because of their extensive demonstrated skills in the manufacture of other fiberglass products such as radomes, antenna covers and shaped surfaces such as CSC² reflectors.

5.0 ELECTRICAL TEST RESULTS

Based on the initial design, first article testing and subsequent production of prototype units, the

ranger and the second of the

electrical performance of the radoms/antenna four band radar augmentation was established. Radar cross section levels were confirmed via measurements in a government anechoic range as well as through the instrumented flight tests.

5.1 Summary Performance

Table 5-1 is a summary of the electrical performances achieved by the 4 band radar augmentation system.

Note that the achieved bandwidths exceed the requirements particularly for the upper 2 bands. The bandwidth indicated is the least of the isolation, pattern and VSWR - generally restricted by the latter.

Polarization is intrinsic to the element chosen for isolation purposes as discussed previously. Note that the use of circular polarizations for the upper 2 bands avoids gain sensitivity as a function of roll position or polarization.

Gains, in linear terms, meet the system requirements as does coverage. Amplitude ripple at the higher 2 bands suffers from pitot tube blockage and results in pattern scalloping.

Half power beamwidths are as expected for low gain elements such as dipoles and spirals.

The isolation goal of 30 dB at L-Band had a 3 to

TABLE 5-1
SURMARY OF ACTUAL AUGMENTATION SYSTEM PERFORMANCE

Cherecteristic	•.	Li	mita	
Band	L	S	C ⁽¹⁾	X (1)
Bandwidt , %	≈ 12	≈ 8	≈ 55	≈55
Polarization	V/N	V/ 4	A\#\Cb	Y/A/CP
Gais, dBli	+3(2)	+3(2)	+0	+5
Coverage Zone off Nose	<u>+</u> 32*	±32°	±40°	±35*
Amplitude Ripple, db(3)	2	2.5	4	2-6
Half Power SW, Non.	≈ ₆₅ •	≈65•	≈80°	≈ 15°
Isolation, Min. dB	27	43	> 50	> 55
Power Handling, Watts CW	>20	>5	≈ 4 '	≈4
YSWR HAX.	1.9:1	1.6:1	1.7:1	1.6:1

- MOTES: (1) Service by one broadband spiral for both bands.
 - (2) Net gains to principal linear polarizations.
 - (3) Composite pattern using transmit and receive patterns.

4 dB short fall. Exhaustive tests as to pitot tube heater wire locations failed to exceed, in production, isolations better than about 27 dB vs. a revised limit of 26 dB.

Power handling of the selected configuration, based on analyses, exceeded the requirements in all bands.

Measured VSWR data taken on each antenna for each of the prototype units resulted in the maximum values shown with the worst at L-Band and best at X-Band as entered in Table 5-1.

5.2 Radiation Patterns

Radiation patterns taken at boresight, with the radome in place were taken at band centers for the designated frequencies at L-, S-, C- and X-Bands. The patterns follow as Figures 5-1, 5-2, 5-3 and 5-4. Note that for each frequency two patterns are plotted, one for transmit and one for receive. Thus the jack numberings are L-Band (J1, J2), S-Band (J3, J4), C-Band (J5, J6) and X-Band (J5, J6).

The patterns were all taken for azimuth (yaw) cuts at the polarizations noted. Pattern shape indicates zone of coverage, ripple, and combined effects of the pitot tube and heater wire.

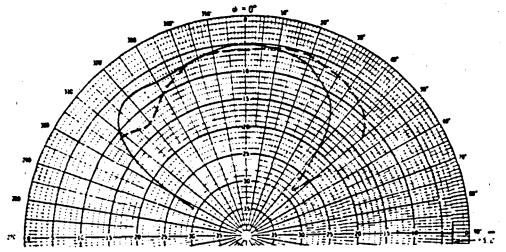


FIGURE 5-1 L-BAND PATTERN FOR HORIZONTAL POLARIZATION AZIMUTH CUT ; J1=---- J2=----

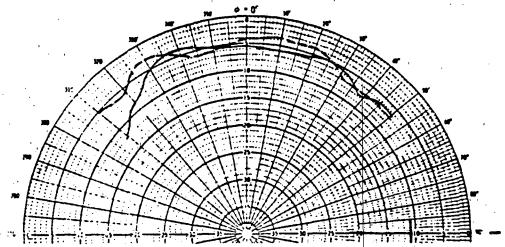


FIGURE 5-2 S-BAND PATTERN FOR HORIZONTAL POLARIZATION AZIMUTH CUT ; J3=--- J4---

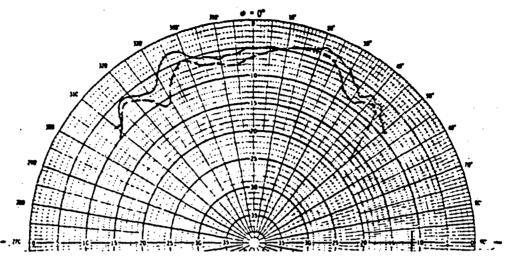


FIGURE 5-3 C-BAND PATTERN FOR VERTICAL POLARIZATION AZIMUTH CUT ; J5---- J4----

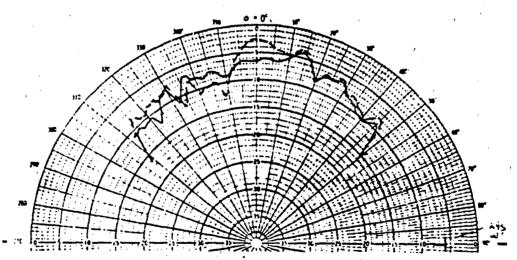


FIGURE 5-4 X-BAND PATTERN FOR VERTICAL POLARIZATION AZIMUTH CUT ; J5---- J4----

5.3 Receive-Transmit Isolations

Each antenna module was tested a minimum of 3 times during the fabrication through acceptance test. These tests occurred at the following stages:

1) After assembly and prior to foaming. 2) Post foaming of the antenna module, and 3) After installation into the radome as the final acceptance testing.

Figures 5-5 through 5-7 are typical plots of isolation measured on the completed assembly with the antenna installed in the radome with pitot bases and heater wires in place - in its final configuration just prior to shipment.

Note that the L-Band isolation, for 10% bandwidth centered as shown, exceeds approximately 28 dB. At S-Band the isolation, for the 7% bandwidth centered as shown, exceeds about 43 dB. For the sweep that covers C- and most of X-Band the isolation exceeds almost 55 dB across the entire sweep.

6.0 FORMAL QUALIFICATION

One of the radome/antenna four band radar augmentation systems was subjected to formal qualification testing prior to subsequent production go-ahead and flight test of prototype units.

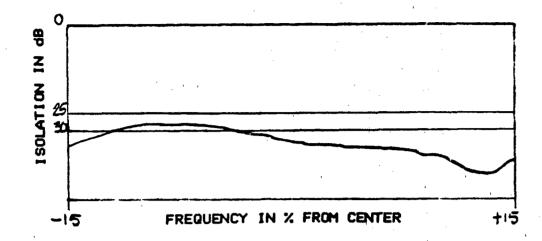


FIGURE 5-5 L-BAND ISOLATION FROM J1 TO J2

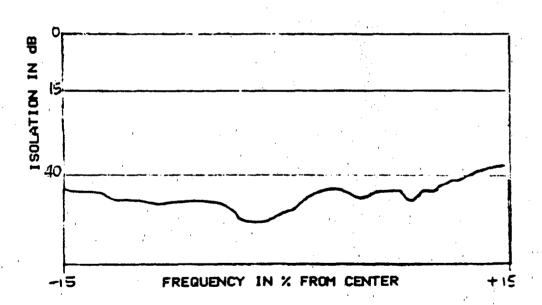


FIGURE 5-6 S-BAND ISOLATION FROM J3 TO J4

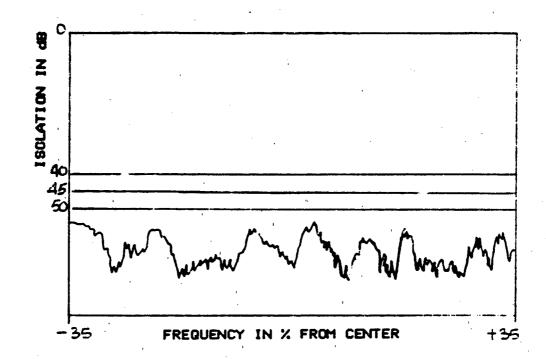


FIGURE 5-7 C THROUGH X-BAND ISOLATION FROM J5 TO J6

6.1 Formal Testing

All tests were conducted in accordance with a contractor approved qualification test plan. Requirements were as stated in Table 1-2 herein.

Pre- and post-testing to electrical requirements were in accordance with the first article provisions of the Acceptance Test Plan.

Once formal qualification to environmental conditions was initiated the tests continued without a

single failure until all tests were completed.

Static load tests were conducted at TECOM with all other tests conducted at Environmental Associates' testing facility.

6.2 Surface Temperature

One test worthy of description was the radome surface temperature test to 296°C. The radome was securely mounted with its axis vertical, pitot tube up, and the tip loaded with a side force.

To one side a 1 meter metal cubical shaped box, lined with 4 inch thick batts of asbestos insulation on each of all 6 faces, was electrically heated to about 300°C. The cube was metal on only 5 sides with no bottom other than the asbestos batting.

When the box reached temperature it was raised over the radome and dropped so that the pitot tube pierced the bottom asbestos batting, exposing the radome to the internal 300°C temperature.

System performance was monitored via continuous measurement of S-Band VSWR for the 300 seconds. S-Band was selected as being most fragile and nearest to the foam surface.

6.3 Qualification Test Report

A formal qualification test report was written and forwarded to the cognizant government agency. It

was subsequently approved.

Copies of this report may be obtained by interested parties having proper clearance and established need to know.

7.0 FUTURE IMPROVEMENTS

A number of improvements are planned to the 4 band radar augmentation meaule as a result of service and industry feedback.

7.1 Polarization

To avoid the possibility of gain drop with target roll to $\pm 45^{\circ}$ (e.g., from slant linear polarization), the polarizations for both L- and S-Bands will be changed to circular polarization.

7.2 Increased Bandwidth

To accommodate additional radars, the S-Band bandwidth will be increased from 6.7% to 21.5%.

The increased bandwidth required at X-Band of 20.8% is already available from the existing antenna which provides continuous coverage from C- through X-Bands.

Design and Error Analysis for the WR10 Thermal Noise Standard

William C. Daywitt
Electromagnetic Fields Division
National Bureau of Standards
Boulder, Colorado 80303

Abstract

This note describes the design and error analysis of a WR10 thermal noise power standard. The standard is designed to operate at the boiling point of liquid nitrogen with a noise temperature accurate to \pm 1 K.

Key words: antenna efficiency; diffraction; error analysis; millimeter wave; noise standard; plane-wave scattering matrix.

1. Introduction

Over the past twenty years, the Electromagnetic Fields Division of the National Bureau of Standards (NBS) has built a number of coaxial and waveguide noise sources $^{1-3}$ consisting of single-mode, uniform transmission lines terminated in reflectionless loads. The accuracy of their calculated noise temperatures are typically 1% which tends to degrade as the operating frequency increases. The basic design is illustrated in figure 1 where the termination and a portion of the transmission line are immersed in a thermal reservoir at temperature T_m , with the

remaining portion of the line leading to the output connector at room temperature T_0 . The temperature distribution T_X of the line is also illustrated where the room-temperature portion of the line has a length 1. Radiation from the termination and the dissipative losses of the line result in a noise temperature

$$T_{n} = T_{m} + \Delta T \tag{1}$$

where, for the idealized distribution shown,

$$\Delta T = (2a'1) (T_0 - T_m).$$
 (2)

The attenuation coefficient a' refers to the line at T_0 , and the equations indicate that only that portion of the line contributes to the excess (in excess of thermal equilibrium conditions) noise temperature ΔT .

The largest source of error in calculating the noise temperature by eq (1) is the attenuation $2a^{\prime}2$, which is usually estimated to an error varying from 10% to 20%. With this large an error, it is necessary to keep the attenuation small (to maintain the error in T_n less than 1%), implying either a small attenuation coefficient a^{\prime} , a short transition length 2, or both. In the microwave frequency range and below, the attenuation can be kept down with relatively simple engineering designs; but as the

frequency increases into the millimeter-wave range, this becomes more of a problem³. In this higher frequency range, surface roughness also plays a bigger role⁴, causing an additional increase in the attenuation.

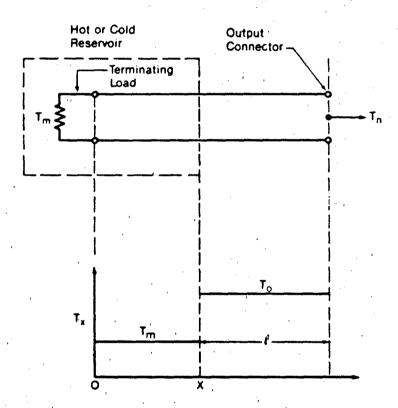


Figure 1. Schematic diagram of a transmission-line type noise standard.

To circumvent the engineering difficulties, it was decided to abandon the transmission-line type of noise standard in favor of a

design incorporating a millimeter-wave horn antenna "looking" at an absorber of known temperature. The resulting antenna noise temperature is close to the measured temperature $T_{\rm m}$ of the absorber, with additional noise contributions from the dissipative antenna losses, and from the antenna side and back lobes. This type of noise source is not new, but its use as a primary reference standard of high accuracy required the successful resolution of two previously unanswered questions: can a useful expression for the noise efficiency (defined in next section) of the antenna with sources in its radiating near field be found; and can the error caused by near-field excess radiation (in excess of thermal-equilibrium conditions) entering the side and back lobes of the antenna be estimated?

The antenna noise efficiency derivation described in the next section and in a previous note⁶ is based upon the plane-wave scattering-matrix (PWSM) theory of antennas⁷. This efficiency, because of reciprocity, reduces to the antenna radiation efficiency. However, in contrast to the usual definition⁸ of the radiation efficiency, the PWSM description reveals enough of the structure of the efficiency to permit a detailed calculation and error analysis of its magnitude. The PWSM formalism is used solely to derive an expression for the antenna noise efficiency and excess noise temperature with the cavity in the antenna

radiating near field, and to show how the efficiency can be evaluated in terms of antenna far-field quantities.

Insights gleaned from the Uniform Theory of Diffraction $(UTD)^9$ are used⁶ to eliminate the angle-dependent components of the noise efficiency. The error incurred from neglecting these contributions to the efficiency is then estimated. The residual, angle-independent part of the efficiency is estimated⁶ by substituting the rectangular waveguide expression for the absorption coefficient, changing the cross-sectional dimensions to conform to the interior dimensions of the horn antenna. The waveguide expression is used because of the nonexistence of pyramidal horn mode equations. An estimate of the error caused by this substitution is also made⁶.

Effects of surface roughness on dissipative loss are reviewed⁶, and an attempt is made to clarify some disagreements found in the literature 10,11 . A modified expression for the corresponding noise efficiency is then determined.

Due to more intense fields in the waveguide portion of the horn, dissipative loss is greater there than in the horn flare. Consequently, the horn waveguide lead is made as short as possible without introducing a significant amount of higher-mode contamination in the antenna noise temperature. The minimum allowable length is determined along with an estimate of the error due to these higher modes.

The UTD is used⁶ to estimate the noise temperature error due to the cavity wall temperature being greater than the temperature of the absorber, and to estimate the effect of multiple reflections between the horn and rear cavity wall. An upper limit to the magnitude of the excess cavity noise is determined, and (by examining multiple reflections between the horn aperture and rear cavity wall) separating the total excess noise into a sum of excess antenna and cavity noises is justified.

2. Antenna noise efficiency and construction of the horn

ジョのでした。 スカル 10mm 大学 大学 10mm できたい 1

The antenna noise temperature T_n is determined from eq (1) with a different excess noise temperature ΔT than that given in eq (2) for transmission-line type noise standards. This new correction temperature has the form

$$\Delta T = (1 - \alpha) (T_0 - T_m)$$
 (3)

for an antenna inside a reflectionless, isothermal cavity. α is the noise efficiency, T_0 is the physical temperature of the antenna, and T_m is the physical temperature of the cavity. An equation for the efficiency, when the cavity is in the radiating near field of the antenna, is derived by use of the antenna scattering matrix and the Clausius statement of the second law of thermodynamics 12. The details of the derivation reveal that the

cavity walls need not be strictly reflectionless, only that no multiple refrections take place between the cavity and the antenna (an important distinction that is utilized in constructing the standard).

One inveresting and useful feature that comes from the derivation is that the efficiency is the same whether the radiating sources (the cavity) are in the antenna near or far field. This result allows the efficiency to be more easily examined with far-field quantities. The result is

$$\alpha = \frac{1}{\Omega_a} \int \left| \frac{r\underline{E}'(\underline{r})}{r\underline{E}(\underline{r})} \right|^2 P_n(\Omega) d\Omega$$
 (4)

In eq (4), Ω_a is the antenna solid angle, \underline{r} is the radius vector from the antenna aperture to the far-field point (r is the magnitude), $P_n(\Omega)$ is the normalized power pattern where Ω stands for the antenna pointing angles, d Ω is the differential solid angle, and $r\underline{E}(\underline{r})$ is the E-field pattern. The prime refers to the real (lossy) antenna, the unprimed quantities belonging to the same antenna with no losses.

Ideally, the pattern ratio in eq (4) could be measured, or calculated from Maxwell's equations, but the measurement is too inaccurate to be useful and the calculation is prohibitively

difficult. However, since most of the loss comes from the waveguide and flare portions of the $horn^6$, the efficiency is easily calculated if losses from the remainder of the horn are neglected. Figure 2 shows an isometric view of the horn designed for the WR10 frequency band (75 GHz to 110 GHz) to take advantage of this situation. Reflections from the waveguide-flare junction,

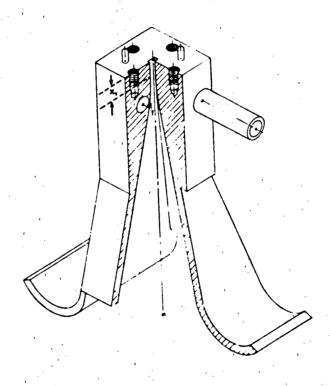


Figure 2. Isometric view of the WR10 horn antenna.

or throat, are minimized by joining the waveguide and flare with a circular arc of sufficiently large radius 13 , beginning at x_1 and ending tangentially on the flared walls. A quarter-round (3 wavelength radius) matching section 14 at the aperture, in addition to a large aperture cross section 15 , minimize the aperture reflections. With multiple reflections interior to the horn eliminated, a wave entering the horn flare from the waveguide maintains its TE_{10} -mode configuration out to the aperture.

Before including the throat taper and the aperture matching section into the design, and after choosing the E-plane aperture dimension, Braun's equations 16 were used to determine the other aperture dimension and the flare angles and lengths to insure approximately equal E- and H-plane beam widths and a simple butt joint at the waveguide-flare junction. The waveguide length x_1 was chosen to minimize the effects of higher modes (generated by radiation incident on the antenna from the cavity) on the antenna noise temperature. Finally, a water jacket was included around the waveguide-throat region to maintain this high-loss area at a constant known temperature.

The calculated horn attenuation neglects the effect of surface roughness on the losses, predicting a loss that is less than the actual value. For an isotropically rough surface, the horn attenuation coefficient increases by a factor K, which is independent of position inside the horn-depending only upon the

roughness of the surface and the operating frequency. Furthermore, it is reasonable to assume that K is independent of temperature. These considerations imply that K can be determined by comparing the measured and calculated (assuming no surface roughness) attenuation for a waveguide section with the same surface roughness as the horn. A picture of the horn with the four waveguide sections and quarter-wave short (94.5 GHz) used to determine K is shown in figure 3. The horn was constructed by machining a stainless-steel mandril to the interior horn dimensions, flashing it with gold, and electroforming copper on top of the gold. After

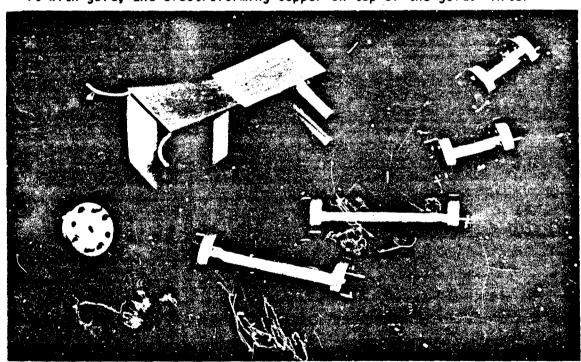


Figure 3. WR10 horn antenna, waveguide sections, and quarter-wave short.

electroforming and machining, the mandril was removed, leaving the horn shown in the figure. The process was repeated to produce the four waveguide sections with the same interior surface roughness as the horn. Then, after determining K for the waveguide section, the efficiency of the horn was calculated from

$$\alpha = e^{-2K \int \mathbf{a}^{\dagger} d\mathbf{z}} \tag{5}$$

where the attenuation coefficient a^i is a function of the dimensions and temperature of the horn at position z along the horn $axis^6$. The integral is performed over the length of the horn.

Figures 4, 5, and 6 show the results of the calculations with K=1. The attenuation coefficient a' for 75 GHz and 110 GHz is plotted as a function of z along the horn axis, with the waveguide flange of the horn at the origin. The waveguide portion of the horn extends from z=0 to z=0.31, where the transition to the flare starts. The aperture and the beginning of the quarter-round matching sections are at z=7.0, and the water jacket extends from the flange to z=3.6. Figure 5 shows the total horn attenuation (the exponent of eq (5) with K=1) as a function of frequency, leading to the excess noise temperature shown in figure 6.

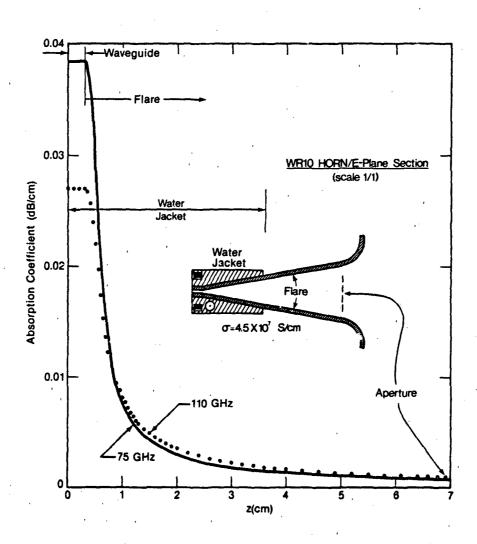


Figure 4. Attenuation coefficient for the WR10 horn antenna.

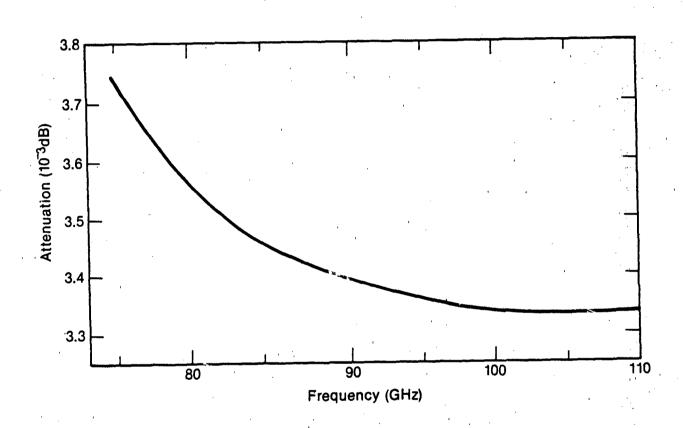


Figure 5. Attenuation versus frequency for the waveguide, throat, and flare portions of the WR10 horn antenna.

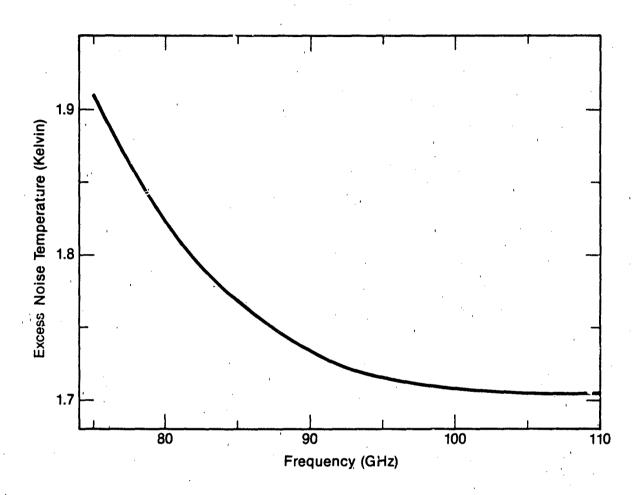


Figure 6. Correction noise temperature for the WR10 noise standard.

3. Construction and operation of the cavity

An assembly drawing of the WR10 noise standard is shown in figure 7. The horn antenna is suspended at the top of the cavity by a yoke (items 18A and 18B) that attaches it to a flexible, beryllium-copper membrane (17) which fits loosely in a holder (7) that allows approximately 8 mm side motion. This motion, with the flexibility of the membrane, permits the horn waveguide flange to be connected to a radiomater without supporting the weight of the entire standard, greatly reducing problems associated with flange misalignment. The cavity consists of the yoke and membrane, the silicon-carbide absorber (13), and the load holder (14). inside cavity walls are polished and gold flashed to reduce thermal radiation from their surfaces. Two radiation shields (6C, 6E) help reduce the amount of external radiation entering the cavity. The bottom portion of the cavity is immersed in liquid nitrogen, allowing the liquid to leak through the bottom of the holder and be absorbed to the silicon carbide. The liquid level is mainlained between the maximum and minimum levels shown in the Millimeter-wave absorber (16) is inserted between the figure. bottom of the load holder and the vacuum flask (12) to absort radiation entering the flask from outside the standard. 3v using this absorber, the radiation temperature¹⁷ of the radiation entering the cavity from the flask area is reduced from

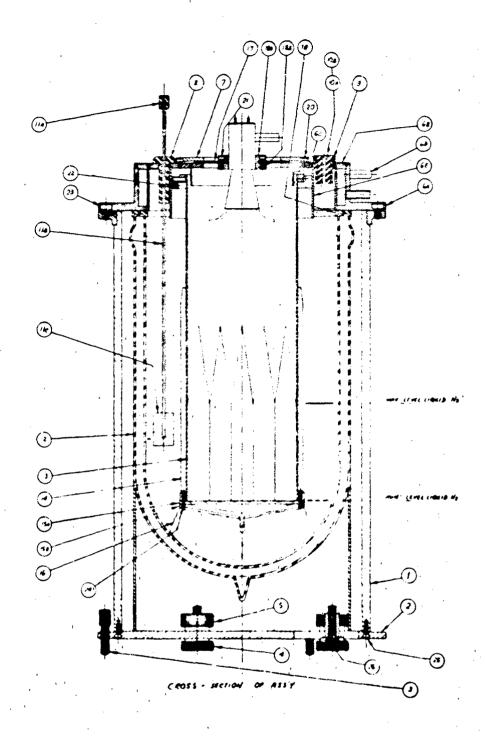


Figure 7: Assembly drawing of the WR10 noise standard.

approximately 300 K to 2 K above the boiling temperature (77 K) of the liquid. Once the flask is filled to the maximum level, it takes approximately seven hours for the liquid to boil down to the minimum usable level. Figure 8 is a photograph of the completed assembly.

The silicon-carbide absorber was manufactured from commercially available grinding-wheel stock (grad P, grit C320, vitrified bond, silicon carbide) by cutting the stock into rectangular shapes and sharpening the ends. The pieces were then fastened together and the assembly ground to form the cylindrical shape shown in figure 9. When inserted in the holder (fig. 10), the cohesive action between the silicon-carbide particles and the liquid nitrogen draws the liquid up into the wedges, allowing the liquid to boil off on the wedge surfaces. With this technique, the temperature of the radiating surface of the absorber is maintained at the boil-off temperature of the liquid nitrogen to within 0.2 K, independent of the level of the liquid in the flask.

4. Results, errors, and conclusions

Equations (1), (3), and (5) are used to calculate the noise temperature T_n of the standard, where T_m is the measured temperature (liquid nitrogen boil-off temperature) of the absorber, T_0 is the temperature of the horn antenna (room temperature), α is the noise efficiency of the horn, K is the

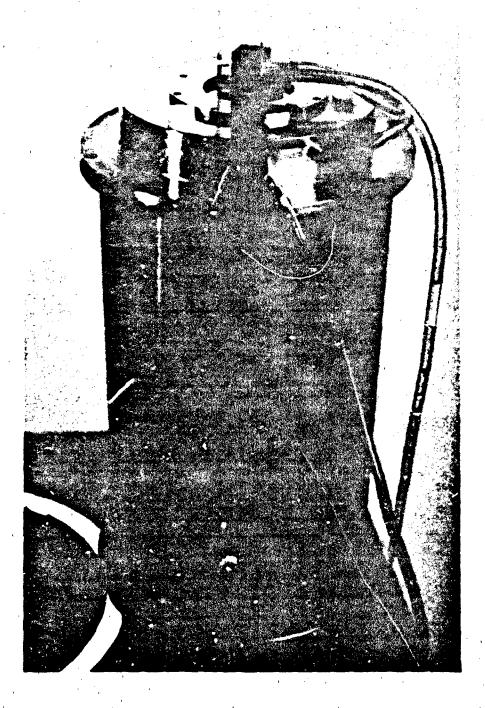


Figure 8. WR10 noise standard.

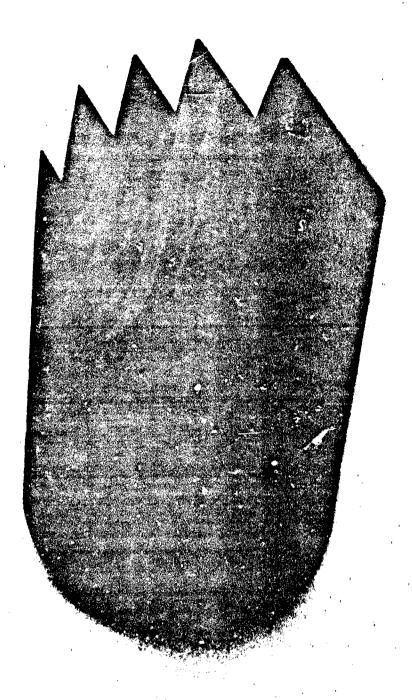


Figure 9. Silicon-carbide absorber.

roughness factor, and a' is the absorption coefficient at position z along the horn axis. Six possible sources of error accompany the use of these equations: (i) higher-mode contamination of the noise temperature, (ii) multiple reflections between the horn and rear cavity wall, (iii) wall temperatures greater than the absorber temperature, (iv) uncertainty in T_m , (v) uncertainty in T_0 , and (vi) uncertainties in the noise efficiency. These sources of error are discussed below and summarized in table 1 along with the resulting errors they produce in the output noise temperature.

The length of the waveguide portion of the horn was chosen to adequately filter out the higher waveguide modes generated in the horn flare by radiation from the cavity incident on the horn. The calculations 6 show, that for 0.31 cm, the residual contamination amounts to no more than + 0.12% of the noise temperature.

Multiple reflections between the back wall of the cavity and the horn affect both the validity and magnitude of the correction noise temperature in eq (3). Calculations⁶ show the discrepancy in the magnitude to be insignificant, indicating that the assumption of a reflectionless cavity in the derivation of eq (3) leads to no larger an error than - 0.05%.

The temperature of the cavity back and side walls varies from room temperature at the top of the cavity (fig. 7) to liquid-nitrogen temperature where the side wall meets the absorber. The elevated wall temperatures cause the noise temperature to be in

excess of the load temperature $T_{\rm m}$. The resulting error 6 is no larger than - 0.10%.

The temperature of the absorber wedges was found to be within 0.1 K (the experimental error) of the liquid-nitrogen boil-off temperature (which was measured with the same thermocouple). When the standard is in use, the absorber temperature is determined by reading the atmospheric pressure (± 1 mm Hg) off a precision barometer and converting to the boil-off temperature (± 0.14 K) via standard vapor-pressure equations 18. Care was taken in constructing the standard to insure a positive flux of nitrogen boil-off gas from the enclosure, preventing contamination of the liquid nitrogen by atmospheric gasses, and allowing the equations to be used to an assumed accuracy of 0.02 K. The total error (0.26 K) in measuring the absorber temperature is the sum of these three errors. This causes an error of less than 0.34% in the noise temperature.

The temperature of the horn, reduced slightly by cooling from the liquid-nitrogen boil-off gas, is determined by circulating room-temperature water through the water jacket (fig. 2). The water temperature is measured before entering the horn by use of a precision (± 1 K) mercury thermometer, and the temperature of the high-loss portions of the horn is depressed no more than 1 K by the boil-off gas. The horn temperature error is, therefore, no

Table 1. Errors in the MR10 (75 GHz - 110 GHz) moise standard

1. Higher modes 2. Multiple reflections between horn & cavity 3. Elevated cavity-wall temperature 4. Uncertainty in T _m 5. Uncertainty in T _m 6.1 Meglecting losses beyond aperture 6.2 Using waveguide loss equation 6.3 Dimensional uncertainties in d 6.4 Uncertainties in d 6.5 Uncertainties in d 6.6 Uncertainties in d 6.7 Uncertainties in d 6.8 Uncertainties in d 6.9 Uncerta		Source of Error	Source Uncertainty	Resulting Percentage Error in Ta
s between horn & cavity 1 temperature	=======================================	igher modes	1	0
t emperature ± 0.26 K ± 2 K ± 1 K ± 2 K ± 2 K ± 2 K ± 1 oss equation = 2 ss = 2 ss = 3 oss equation = 4 oss equation = 5 ss = 5 s	2. #	ultiple reflections between horn & cavity	:	0,0 0.05
ses beyond aperture 1 loss equation 2 L K 2 L K 2 L K 3 L 2 K 3 L 2 K 4 L 2 K 4 L 2 K 4 L 2 K 5 L L C K 5 L L C L C C C C C C C C C C C C C C C		levated cavity-wall temperature	1	+C - 0.10
ses beyond aperture 1 loss equation	÷	ocertainty in Im	± 0.26 K	± 0.34
tes beyond aperture 1 loss equation 2 certainties 1 0.0025 cm 2 5% 1 n K 2 5%		certainty in T ₀	# 2 K	± 0.02
ses beyond aperture F loss equation	5	Kertainties in a		
r loss equation ± 0.0025 cm in dc resistivity curve ± 5s in K ± 5s	•	.1 Meglecting losses beyond aperture		+ 0 + 0 - 0.01
rertainties ± 0.0025 cm In dc resistivity curve ± 58 In K ± 58	•	2 Using waveguide loss equation	· .	* 0.01
In dc resistivity curve ± 5%	•		# 0.0025 cm	* 0.0
* 5\$	•	4 Uncertainties in dc resistivity curve	± 58	± 0.01
	•	5 Uncertainties in K	25	\$ 0.06
	lotal (error (linear sum)		+ 0.5 \$ - 0.7 \$

larger than 2 K, causing an error of less than 0.02% in the noise temperature.

Errors in the noise efficiency fall into two classes: errors due to the approximations leading to eq (5), and errors due to uncertainties in the parameters used in the equation. The first class contains an error due to neglecting dissipative horn losses beyond the aperture⁶, resulting in a noise temperature error less than a negative 0.01%; and an error due to the nonexistence of equations describing pyramidal horn fields⁶ resulting in an error no larger than 0.01%. The parametric errors are due to uncertainties $(\pm 0.0025 \text{ cm})$ in the internal horn dimensions, in the slope versus temperature curve for the dc resistivity of the horn walls $(\pm 5\%)$, and in the roughness factor K. The first two result in noise-temperature errors of less than 0.01% and 0.06%, respectively.

The roughness factor at 297 K was determined by comparing the measured and calculated values of attenuation for the waveguide sections shown in figure 3. Errors in the roughness factor are due to errors (\pm 0.0012 cm) in the measured dimensions of the waveguide sections, and uncertainties associated with the six-port millimeter-wave system¹⁹ used to measure the attenuation. The roughness factor was determined to be 1.14 (\pm 0.05) at 94.5 GHz, with an error no larger than 0.06% in the noise temperature.

The sum of errors in table 1 for the noise-temperature output of the noise standard is within 1%, showing that it is possible to construct a precision horn/absorber type of standard, and, thus, eliminate the engineering problems mentioned in the introduction. Furthermore, this type of standard can be easily duplicated at the higher millimeter-wave bands.

Calculations using the UTD show that, if the yoke and membrane (items 17, 18A, and 18B in fig. 7) are removed from the standard, the noise temperature increases by approximately 0.7%. If, in addition, the aperture-matching quarter-rounds (the curved sections on the horn aperture in fig. 2) are removed from the horn, this figure increases from 0.7% to approximately 3%. Therefore, the yoke and membrane are needed to insure an accurately known noise temperature.



Figure 10. Top view of the cavity.

5. Acknowledgments

The author takes great pleasure in acknowledging the many beneficial contributions from his colleagues in the Electromagnetic Fields Division who unhesitatingly shared their expertise in a number of seminars and many private discussions.

6. References

- 1. Arthur, M. G.; Driver, L. D. A precision HF-noise power measurement system. ISA Transactions, 10: 264 268; 1971.
- 2. Wells, J. S.; Daywitt, W. C.; Miller, C. K. S. Measurement of effective temperature of microwave noise sources. IEEE Trans. on I&M, IM-13: 17 28; 1964 March.
- 3. Daywitt, W. C. WR15 thermal noise standard. Nat. Bur. Stand. (U.S.) Tech. Note 615; 1972 March.
- 4. Tischer, F. J. Experimental attenuation of rectangular waveguides at millimeter wavelengths. IEEE Trans. on MTT, MTT-27, No. 1: 31 37; 1979 January.
- 5. Hansen, R. C. "Aperture Theory," <u>Microwave Scanning</u>
 Antennas, Vol. 1., New York, NY: Academic Press; 1964.
- 6. Daywitt, W. C. Design and error analysis for the WR10 thermal noise standard. Nat. Bur. Stand. (U.S.) Tech. Note 1071, 1983 December.
- 7. Kerns, D. M. Plane-wave scattering-matrix theory of antennas and antenna-antenna interactions. Nat. Bur. Stand. (U.S.) Monogr. 162; 1981 June.
- 8. IEEE standard definitions of terms for antennas. IEEE Std. 145-1973.
- The modern geometrical theory of diffraction. Vol. 1, Electro-Science Laboratory, The Ohio State University; 1982.
- Benson, F. A. Waveguide attenuation and its correlation with surface roughness. Proc. IEE, <u>100</u>, Part III: 85 -90; 1953 March.
- 11. Allison, J; Benson, F. A. Surface roughness and attenuation of precision-drawn, chemically polished, electropolished, electroplated and electroformed waveguides. Proc. IEE, 102B: 251 259; 1955 March.

- 12. Allis, W. P.; Herlin, M. A. Thermodynamics and statistical mechanics. New York, NY: McGraw-Hill Book Company, Inc.; 1952.
- 13. Terzuoli, A. J., Jr.; Peters, L., Jr. VSWR properties of E-plane dihedral corrugated horns. IEEE Trans. on A & P, AP-26, No. 2: 236 239; 1978 March.
- Burnside, W. D.; Chuang, C. W. An aperture-matched horn design. IEEE Trans. on A & P, AP-30, No. 4: 790 796; 1982 July.
- 15. Jull, E. V. Reflection from the aperture of a long E-plane sectoral horn. IEEE Trans. on A & P, AP-20, No. 1: 62 68; 1972 January.
- 16. Braun, E. H. Some data for the design of electromagnetic horns. IEEE Trans. on A & P, AP-4: 29 31; 1956 January.
- 17. Ko, H. C. Antenna temperature and the temperature of electromagnetic radiation. IEEE Trans. on A & P, AP-12: 126 127; 1964 January.
- 18. Jacobsen, R. T.; Stewart, R. B.; McCarty, R. D.; Hanley, H. J. M. Thermophysical properties of nitrogen from the fusion line to 3500 R (1944 K) for pressures to 150,000 PSIA (10343 x 10⁵ N/m²). Nat. Bur. Stand. (U.S.) Tech. Note 648; 1973 December.
- 19. Weidman, M. WR-10 single six-port measurement system. Nat. Bur. Stand. (U.S.) NBSIR 81-1650; 1981 September.

CONSTRAINED OVERLAPPING FEED ARRAYS FOR CONTIGUOUS CONTOUR BEAM REFLECTOR ANTENNAS*

V. Galindo-Israel, Y. Rahmat-Samii, W. Imbriale

Jet Propulsion Laboratory, California Institute of Technology

Pasadena, CA 91109

H. Cohen, R. Cagnon

TRW Systems

Redondo Beach, CA 90278

Abstract:

Contour beam ancennas with contiguous beams generally utilize frequency and/or polarization discrimination between the adjacent beams for isolation purposes. When polariza ion discrimination is not possible and the frequency separation between channels is small, isolation between the adjacent beam feed ports can be achieved with a -3 dB loss in the overlapping feeds. An alternative to this approach, with less loss (~0.5 dB), may be achieved by 'constraining' overlapping feed radiating elements which serve both contiguous beams. If the number of constrained feeds N, is

^{*}The research described in this paper was carried out in part by
the Jet Propulsion Laboratory, California Institute of Technology
under contract with the National Aeronautics and Space Administration, and by TRW Systems.

equal to 2^P (P an integer), then physical realization of the power dividing network is straightforward.

1. INTRODUCTION

Contour beam antennas with very close or contiguous beams . Lerally utilize frequency and/or polarization discrimination between the adjacent beams for isolation purposes. In some situations where polarization discrimination is not possible and the frequency separation between channels is small, isolation between the adjacent beam feed ports can be achieved with a -3 dB loss in the overlapping feeds. An alternative to this approach, with less loss (~0.5 dB), may be achieved by 'constraining' overlapping feed radiating elements which serve both contiguous beams.

The feed array elements radiating into a particular contour beam are excited with relative complex coefficients determined by an optimization procedure. This procedure finds a 'best' fit to the contour beam according to a predetermined 'ost function' which defines quantitatively what 's meant by 'best' fit. Generally, if M feed elements exist, there are 2M (M amplitudes and M phases) real degrees of freedom to 'fit' the 'best' contour beam. If N feeds (and beams) overlap, then (2M - 2N + 2) degrees of freedom can be used instead with no power distribution (Ohmic) loss in the isolation of the two feed ports for each beam. The constraining of the N feeds to only 2 degrees of freedom (1 amplitude and 1 relative phase) permits no power distribution loss,

but it does lead to a slightly inferior pair of contour? The straightforward of constrained feeds N, is equal to 2^P (P an integer), then physical realization of the power dividing network is straightforward. Applications to direct broadcast satellite antennas for the United States, Alaska, and Hawaii demonstrate about a 0.5 dB average loss in gain over the region of the slightly deteriorated contour.

In this paper, we will demonstrate this method by the example of a single polarization DBS (direct broadcast satellite) antenna design. This design utilizes an array of feeds radiating into a paraboloid to produce time zone contour beams over the U.S.

2. DIRECT BROADCAST SATELLITE OVERVIEW

An overview of the direct broadcast satellite objectives should help to clarify how the choices of parameters for the antenna design were made.

In Figure 1, we observe the general objectives of the system. A DBS satellite in equatorial synchronous orbit supplies a down-link to all receivers in a broad geographical area at about 12.5 GHz. The uplink, at about 17.7 GHz, supplies the satellite with communications, television, information, etc. The uplink transmitters may be located at one or more isolated locations as indicated. We will consider an Albuquerque location.

The satellite DBS antenna is therefore required to supply coverage for several contoured areas at 12.5 GHz, and it is

required to supply pencil or spot beams at one or more locations at 17.7 GHz.

Typical continental United States (CONUS) coverage 'contoured' regions are shown in Figure 2. The Alaska and Hawaii spot beams are considered part of the Pacific time zone (PTZ), while Puerto Rico is part of the Eastern time zone (ETZ). The Central time zone (CTZ) generally will be illuminated simultaneously with the ETZ. The Mountain time zone (MTZ) will generally be illuminated simultaneously with the PTZ.

A single antenna design is to be used for all four zones. The ETZ and CTZ will be illuminated when the satellite is located at 101° W. longitude. The MTZ and PTZ are illuminated when the satellite is at 157° W. longitude. A single paraboloid reflector design is to be used for all four zones.

The time zone regions illustrated in Figure 2 are only approximated. Specifications of gain required is actually given for a set of specific locations or cities within a given time zone. However, it is required that the gain coverage supplied by the antenna will vary smoothly between cities in a given time zone.

In order to improve the gain within a time zone and the isolation between the contiguous time zones, the gain coverage is expected to drop off as sharply as possible outside of the time zone. The actual variation of gain that is desired over a particular zone, for example the ETZ, will depend on two principle factors — the rainfall attenuation (statistically) in the local (city) region and the required diameter or gain of the ground receiving antennas. Generally, it is desired to keep the receiving ground antennas as small and inexpensive as possible since large numbers are expected to be installed.

Figure 3 illustrates some of the above considerations for a list of cities in the ETZ. The variation in required gain (of the satellite antenna) over the ETZ, i.e., the ΔΕΙΚΡ (dB), is shown for two cases - 1) a constant diameter ground station of 0.9 meter, and 2) three possible diameters adjustable for each position. A lower and more constant gain correction is required if we permit larger (0.9 meter) ground antennas in those areas with greater rainfall.

A brief study of the effect of the diameter of the spacecraft antenna on ground coverage was also made. If the spacecraft antenna diameter is larger, with resulting smaller beamwidths for the pencil beams which will ultimately comprise the contoured beam, the resolution of the contour beam should be finer. Ultimately, the contour beam will have zero gain outside the prescribed region (ETZ for example) and the ideal maximum gain within the contour. However, as pencil beams are scanned away from the optical boresight of a reflector antenna, the shape, gain,

The deterioration increases with an increasing number of beam-widths scanned away from boresight. Hence, we would expect that the performance of a contour beam antenna utilizing an array feed generating coherent pencil beams would in fact have a peak or optimum performance diameter.

Our tests for results versus diameter were limited to three diameters as illustrated in Figure 4. The more difficult ETZ was used as a test case. A different 'optimized' feed layout was chosen for each case, that is, each larger diameter had a feed array with more feeds or pencil beams composing the ETZ. The gain delta quantity in the figure is

Gain Delta = Gain (Actual) - GC (Gain Correction)

Thus we desire a uniform gain delta of maximum value as an opti-

We observe, in Figure 4, that not all cities have monotonically increasing gain deltas with increasing spacecraft antenna
diameter. In fact, the increase of gain delta is negative for
some cities when the diameter is increased. There are more such
negative increases when the diameter is increased from 2.44 meters
to 2.7 meters than when it is increased from 2.2 meters to 2.44
meters. An optimum diameter may thus be less than 2.7 meters.

These tests were made with beams overlapping at -3 dB and at -4 dB. Generally, a -4 dB overlap will yield the smoothest variation of gain delta within the contour for a triangular lattice of beams. The use of a -3 dB crossover does occasionally permit a better layout of beams to fit the contour with minimum spillover outside the contour. Figure 5 summarizes some results for both beam overlap values and three different reflector diameters for the spacecraft antenna.

3. THE REFLECTOR AND FEED DESIGN

The actual reflector and array feed layout that was chosen for the design was done so with consideration of several additional constraints.

The use of the Intelsat V masterdie, for cost savings purposes, led the chosen reflector diameter to be 2.438 meters or about 101 wavelengths. With the master die and shroud restrictions, the final offset paraboloid chosen is that depicted in Figure 6. The expected feed array is optically clear of the projected aperture of the reflector for all beam scan positions.

The feed array must now be designed with the following considerations. The ETZ and CTZ will be illuminated from the satellite positioned at 101°W. Longitude. The MTZ and PTZ are to be illuminated from 157°W. Longitude. Albuquerque, within the MTZ, is to be used as the source for the 17.7 GHz uplink. Most significantly, a single sense of polarization is to be used for all

zones. Finally, the maximum gain possible is to be obtained at a prescribed set of locations in each zone subject to a prescribed gain correction (see previous section) variation at each location.

Typical of the gain correction requirements is that set of corrections for the ETZ depicted in Figure 7. With the exception of Puerto Rico, the gain is desired to vary by about 1.8 dB over the contour. These gain correction values are inserted into a 'cost function' for the Mini-Max computer program which optimizes the excitation coefficients of the feed array.

The plane of the feed array for each pair of time zones is shown in Figure 6. The normal to the feed plane points to the center of the projected aperture of the reflector. This direction is little different than the angular bisector that is frequently used. It has been shown that this feed array direction is approximately optimum for small displacements of the feed elements from the focal point. 2

The final feed layout chosen is shown in Figure 8. There are a number of significant characteristics to observe.

a) The East/Central (E/C) beams are configured to the left of the Mountain/Pacific (M/P) beams so as to approximately minimize displacement of a feed element from the focal point (particularly for Alaska and Hawaii). This minimizes the worst case beam distortion. The chosen boresight axis indicated on the figure is chosen with this in mind.

- b) A -4 dB beam crossover is chosen for the E/C beams since this crossover can be shown to give approximately the smoothest gain surface in a triangular beam configuration. A -3 dB beam crossover is chosen for the M/P zones, however, since these two zones can be seen to be long and narrow (as viewed from synchronous orbit) relative to the beamwidths available. The -4 dB beam width crossovers thus would lead to greater spillover for the M/P zones. Furthermore, the -3 dB crossover for the M/P zones leads to a single beam overlaying Albuquerque (part of the Mountain beam configuration).
- c) Note that there is a 'line' of feeds for the E/C zones which is common to both zones. Similarly, there is a 'line' of feeds for the M/P zones which is common to both zones. It is a severe constraint on the beam layout to configure these 'lines' of feeds such that there is a minimum spillover beyond the borders of each zone. This constraint is all the more critical since only one polarization is used for all four zones.
- d) The fact that a single polarization is used and that there is a 'line' of overlapping feeds 'u each pair of time zones requires that the feed elements in these 'lines' of feeds be fed as one element. In other words, their relative phase and amplitude have only two degrees of freedom (one amplitude and one phase) even though several feeds are involved. In the E/C array, there are four overlapped feeds so that their complex relative

excitations must be (for orthogonality); Amp (Phase):

1 (67.5 deg), 1 (22.5 deg), 1 (-22.5 deg), 1 (-67.5 deg).

For the M/P zones there are five overlapped feeds so that their relative excitations must be:

1 (72 deg), 1 (36 deg), 1 (0 deg), 1 (-36 deg), 1 (-72 deg).

Although other possibilities do exist, these relative values were found to be optimum since the constrained 'linear' array places a 'linear' beam in an approximately useful location on the CONUS map.

In Figure 8, we note that the 'optimization points' are specified by crosses and triangles (triangles for ETZ and PTZ, crosses for CTZ and MTZ). A triangle designates the location of Albuquerque within the MTZ. It is useful to have Albuquerque, the 17.7 GHz up link, approximately centered within the pencil beam of a feed. This considerably facilitates the design of only one 12.5/17.7 GHz coaxial feed.

While it is possible to use feeds of different sizes, we have found it best to use a fixed, but minimum diameter, feed size for maximum flexibility in laying out a feed array to cover the various contours. The E/C array and M/P arrays are tilted independently to best fit each contour.

The constrained line of feeds for E/C and for M/P shown in Figure 8, are placed in the layout so that there are a mininum number of such feeds. As stated in the introduction, we lose (2N-2) degrees of freedom in obtaining the optimum feed excitation if we have N overlapping feeds. It should be added that the location of the required optimization points (cities) within each zone precludes the possibility of having no overlapped beams in the design.

Some optimization points, other than those initially specified, are needed and added so as to insure a smooth gain function over the contour. They are not depicted in Figure 8. The gain correction for such points is found by interpolation. One such point, for example, is the eastern tip of Cape Cod, Massachusetts.

4. THE OPTIMIZATION PROCEDURE AND CONTOUR PLOT RESULTS

The far-field pattain of the feed array and offset reflector is found with a Jacobi-Bessel (JE) computer program. The JB series coefficients for each feed is computed with a unit excitation coefficient. The field at all optimization points is then computed. A 'cost function' is then devised which requires that the optimization point with the minimum gain delta be maximized (the Mini-Max procedure). Various additional constraints can be placed upon the cost-function.

For example, we may require that the overlapping feeds of Figure 8 be excited with a prescribed relative excitation as

discussed early. Other possibilities include:

- a) amplitude only is permitted to vary,
- b) phase only is permitted to vary,
- c) either amplitude or phase or both are allowed to vary only over discrete steps.

We allowed continuous variation for phase and amplitude.

Another possibility is to constrain the overlapping feeds with an amplitude taper in place of the equal amplitude excitation which we have chosen (see last section). While it is possible to do this, it is not possible to design a power distribution network to do this without loss.

The feed excitation coefficients were optimized 1 for maximum gain delta (with gain correction included) over each time zone under two conditions;

- a) with no relative constraints between the overlapped feeds,
- b) with the relative amplitude and phase constraint imposed on the overlapped feeds.

All feed element excitations were allowed to vary in amplitude and phase (except where constrained). Circular polarization was used.

Figure 9 illustrates the results for the Eastern time zone.

In Figure 9a, the resultant contour plot with the constrained

'line' of overlapped feeds is presented. In Figure 9b, the corresponding result with the unconstrained 'line' of feeds is

presented. Note that the unconstrained array gives a better fit to the zone. There is clearly more spillover for the constrained result. In fact, the worst gain location for the constrained results is as much as 1 dB worse than the worst gain location (not necessarily the same location) for the unconstrained results.

This difference of between 0.5 to 1 dB between the constrained and the unconstrained results was fairly consistent for most of the time zones. Figures 10, 11, and 12 present similar results for the Central, Mountain, and Pacific zones.

Alaska, Puerto Rico, and Hawaii are illuminated by spot beams. The gain results in Figures 9-12 include the spot beams as well as the gain correction considerations discussed earlier. The gain correction imposed varies depending on specific location from -2.1 to +0.5 dB (except for Puerto Rico which is allowed a -5.0 dB gain correction).

The spacing between ear a contour line in Figures 9-12 is one dB, except below -35 dB where the spacing is 5 dB. The -35 dB contour line is drawn more darkly. Note that the gain drops very sharply outside this contour. The -35 dB contour therefore approximately delineates the outside shape of the gain pattern.

Within the contour, the maximum point(s) is indicated by a heavy cross. Note that a gain variation is desired because of the specified gain correction values.

The difference between the constrained and the unconstrained results in the MTZ and PTZ contour patterns is much less than that for the ETZ and CTZ (see Figures 11 and 12). This can be explained by the fact that the constrained feeds radiate a beam which fits approximately into the desired contours.

These results are summarized in Figures 13 and 14. Note that these figures present worst case gain delta (Figure 13) and worst case gain (actual gain - Figure 14). The beams for the M/P region have a -3 dB overlap as discussed earlier, while the E/C region has a -4 dB beam overlap. Also, the M/P region is illuminated from a sateIlite location at -157° (157° W), while the E/C region is illuminated from -101°.

The worst case gain delta values for the constrained excitation cases fall from about 0.1 dB to 0.9 dB below those for the constrained case. The severest drop occurs for the ETZ, which is the most complex shaped contour. Since it is the gain delta which is optimized by the Mini-Max computer program, the worst case actual gain shown in Figure 14 could have a better constrained result than unconstrained result depending upon the gain correction value for the particular worst case gain geographical location.

In Figures 15 through 18, we present the actual final complex excitation coefficients for each feed array - ETZ, CTZ, etc.

The excitations are presented both for the constrained and the

unconstrained cases. The feed locations are presented relative to boresight location in the plane of the feed array (therefore Z = 0. for all feeds). The feed numbers relate to beam numbers shown in Figure 8.

The relative amplitudes and phases of the four constrained feeds in the ETZ, for example, are fixed. The overall phase and amplitude are allowed to vary in the optimization algorithm. other words, two degrees of freedom exist for the eight parameters (four feeds). It is interesting to note that all excitation coefficients of the unconstrained array differ from the constrained array for the ETZ. This difference is not quite as sharp for the CTZ (Figure 16), and less so for the MTZ and PTZ excitation coefficient results (Figures 17 and 18). This appears consistent with the graphical results presented in Figures 9 through 12, and with the worst case results presented in Figures 13 and 14. The differences between the constrained and unconstrained results is greatest for the ETZ and, secondly, for the CTZ. This is reflected in the result that all excitation coefficients changed markedly between the constrained and unconstrained situations for the ETZ.

5. THE POWER DISTRIBUTION NETWORKS

Although this study required no hardware construction, physical realizability was an important consideration.

With a set of beams overlapping for the E/C and M/P regions, the power distribution networks for ETZ input and CTZ inputs must be isolated; and, likewise, the power inputs to the MTZ and the PTZ inputs must be isolated.

While there is sufficient separation between the frequency communication channels for the ground station receivers to distinguish the channels, we have the restriction that the frequency channels are too close for the microwave circuitry to distinguish channels (without adding very expensive and heavy filtering equipment).

In the unconstrained case, we allow the adjacent zones, for example ETZ and CTZ, to be illuminated by orthogonal polarizations. In this case, the inputs to the two zones can be isolated, at one frequency, by utilization of an orthomode transducer (or equivalent) circuitry as shown in Figure 19.

For the constrained feeds, a different network is required because in this case we must not assume that the ETZ and CTZ (for example) are illuminated by orthogonal polarizations. Hence both the frequency and the polarization for the ETZ and the CTZ are assumed identical. As shown in Figure 20, an 'overlapped feeds network' must be developed which will isolate the 'C' (CTZ) input from the 'E' (ETZ) power input ports.

We prefer that this isolation be accomplished without loss. It appears that two choices are available:

- 1) Suffer a -3 dB loss for the four beams/feeds that are overlapped in the E/C region, but thereby allow eight degrees of freedom in the four complex excitation coefficients. This is simply accomplished by using a magic tee (or equivalent) and dissipating the power into the 'matched dissipative load' for both the 'C' and 'E' inputs.
- 2) Constrain the <u>relative</u> amplitudes and phases of the overlapped feeds to prescribed values so that no energy is lost.

We should note that method (1) above may be preferable to method (2) for the ETZ/CTZ since the ETZ, particularly, suffers moderate loss in gain due to the constrained excitation coefficients. Furthermore, a -3 dB loss in only four out of 17 (ETZ) or 16 (CTZ) feeds does not necessarily imply a greater overall loss in gain delta than that obtained by constraining the excitation of the four feeds. On the other hand, there are 5 constrained feeds out of 19 feeds (MTZ) and only 14 (PTZ) which will suffer a -3 dB loss for these two regions. Since the constrained excitation results for these two regions (M/P) do not seem to suffer greatly relative to the unconstrained results (see Figures 11, 12, and 13), method (2) above appears attractive for this pair of regions.

When we constrain the relative excitation of the linearly aligned constrained feeds (see Figure 8), we are in effect constructing a linear array. In a sense, we want two <u>isolated</u> inputs to excite this linear array. A method for doing this which will

also result in two 'orthogonal' beams radiated by this array is discussed in reference 3. For the four feed (E/C) case, we can obtain <u>four</u> isolated inputs and four output beams. We need only <u>two</u> isolated inputs and four output beams.

In Figure 21 we illustrate this power distribution network for the four constrained feeds of the E/C region. The network makes use of hybrid couplers. Each isolated 'beam port' in the figure (A, B, C, and D) generates an orthogonal beam. Since we need only two isolated ports (one for the ETZ and one for the CTZ in this case), we have chosen the two ports with conjugate phases and beams steered a minimum from broadside. One port excites the ETZ while the other excites the CTZ for this case. As discussed earlier, this arrangement requires equal amplitude excitation of all four feeds. Shelton and Kelleher (reference 3) have shown that a lossy network is required for obtaining an unequal amplitude excitation of the four output (feed or beam) ports.

The 'lossless' four port hybrid coupler operation is depicted in Figure 22. There are other physically realizable methods of constructing such a hybrid in stripline or waveguide.

REFERENCES

- 'Improved Wide-Angle Scan Using a Mini-Max Optimization Technique,' IEEE International Symposium on Antennas and Propagation, May 1983, W. Imbriale, V. Galindo-Israel, Y. Rahmat-Samii, R. L. Bruce.
- 'An Efficient Technique for the Computation of Vector Secondary Patterns of Offset Paraboloidal Reflectors,' IEEE Trans. on Antennas and Propagation, May 1979,
 R. Mittra, Y. Rahmat-Samíi, V. Galindo-Israel.
- 'Multiple Beams from Linear Arrays,' J. P. Shelton, K. S.
 Kelleher, IRE Transactions on AP, vol. AP-9, March 1961.

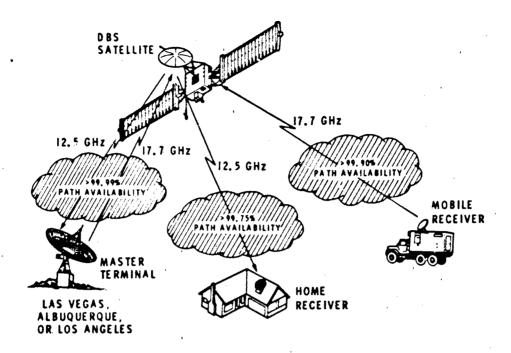


Figure 1. Direct Broadcast System Overview

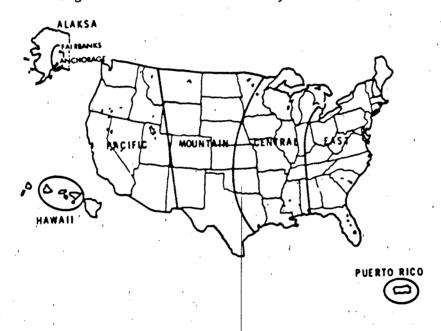


Figure 2. Approximate Conus Zones

спу	RAINFALL	CONSTANT Q 9 M DISH	VARIABLE DISH (0.6, 0.75, 0.9 M)		
	ATTENUATION (dB) (Q, 2%)	ΔEIRP (d8)	DISH SIZE (M)	ΔEIRP (48)	
MIAMI, FLORIDA	4.2	0.0	0.9	0.0	
TAMPA, FLORIDA	40	-0.2	0.9	-0.2	
TALLAHAS SEE, FLORIDA	40	-0.2	L Q.9	-0.2	
PENSACOLA, FLORIDA	3.8	-0.4	0.9	-0.4	
BIRMINGHAM, ALABAMA	3,6	-0.7	0.9	-0.7	
NASHVILLE, TENNESSEE	2.5	-1.9	0.75	-0.6	
INDIANAPOLIS, INDIANA	1.6	-3.0	0.6	0.0	
DETROIT, MICHIGAN	1.5	-3.1	0.6	0.0	
BUFFALO, NEW YORK	1.7	-2.8	0.6	+0.3	
MASSENA, NEW YORK	1.5	-3.0	0.6	+0.2	
CARIBOU, MAINE	1.1	-3.4	0.6	-0.3	
BOSTON, MASSACHUSETTS	2.0	-2.5	0.6	+0.8	
ATLANTIC CITY, NEW JERSEY	1.9	-25	0.6	+0.5	
PORTSMOUTH, NORTH CAROLINA	2.9	-1.3	0.75	0.0	
CHARLESTON, SOUTH CAROLINA	3.9	-0.2	0.9	-0.2	
JACKSONVILLE, FLORIDA	4i	-ā i	0.9	-āi	

Figure 3. Required EIRP Variation - Eastern Service Area

CITY	GAIN OELTA 22 W (dB)	GAIN DELTA 2.438 % (dC)	GAIN DELTA 27 M (dB)	Δ GAIN DELTA 2.438 M — 2.2 M (dB)	Δ GAIN DELTA: 2.7 M — 2.438 M (dB)
MIAMI	34.33	37.03	38.04	0.70	1.01
TAMPA	36.33	34.86	37.15	0.53	0.29
TALLAHASSEE	36.90	36.86	37.79	0.04	0.93
MOBILE	36.32	36.86	37.15	0.54	0.29
BIRM:NGHAM	36.40	32.43	37.47	2.03	0.96
NASHVILLE	36.33	37.86	37.15	1.56	-0.73
INDIANAPOLIS	37.8-	38.00	37.50	0.16	-0.41
DETROIT	36.32	37.86	37.20	1.34	-0.46
BUFFALO	36.86	34.20	37.15	1.54	-1.06
MASSENA	37.15	36.80	36.14	-0.27	1.26
CARIBOU	36.33	36.87	38.08	0.54	2.21
BOSTON	36.02	36.12	30.15	0.10	1.03
ATLANTIC CITY	37.96	37.84	39.20	-0.11	1.44
NEWBERN	36.3	36.87	37.15(1)	0.56	0.28
CHARLESTON, S.C.	37.67	30.22	37.84	1.55	1.58
JACKSONVILLE	37.29	36.82	37.75	1.53	-1.07
NEW YORK	38.19	30.33	39.10	1.14	-0.23
CLEVELAND	37.44	38.02	30.86	0.58	0.84
WASHINGTON	37.80	39.13	30.81	1.24	0.32
PITTSBURGH	37.73	30.54	38.79	0.81	0.25
ATLANTA	37.27	36.93	38.41	-0.34	1.48
CHARLOTTE	37.29	37.31	38.25	0.02	0.94
CHARLESTON, W. VA.	30.22	37.28	30.62	-0.98	2.30
EASTPORT	36.31(1)	36.86(1)	37.16	0.55	0.30
	AVE 37.10	37.74	30.07	AVE 0.84	AVE 0.34

(1)WORST CASE (MINIMUM GAIN DELTA) - COMPUTER RESULT-

Figure 4. Eastern Service Area Antenna Gain Deltas (dB)
Comparison of Results for 3 Aperture Diameters
Using -3 dB Crossover

			BEAMLET OVERLAP AT -3 dB				BEAMLET OVERLAP AT -4 dB				'44
ANTENMA FOCAL DIAMETER LENGTH (M)	FEED SIZE (CM)	NO. OF FEEDS	MIN. GAIN DELTA (dB)	AVG. GAIN DELTA (IBM)	RATIO OF NUMBER OF HIGHEST GAIN DELTA CITIES TO TOTAL (24)	FEED SIZE (CM)	NO. OF FEEDS	MIN. GAIN DELTA (dB)	AVG. GAIN DELTA (dB)	RATIO OF NUMBER OF HIGHEST GAIN DELTA CITIES TO TOTAL (24)	
2.20	2.50	3.33	13	36.31.	37.10	0/24	3.93	11	38.57	37.27	\$/24
2.438	2.460	3.06	16	36.86	37.74	9/24	3.57	14	36.96	37.34	3/24
2.79	2.400	284	17	37.16	38.07	15/24	3.21	14	37.53	37.82	16/24

Figure 5. Summary Comparison of Results - Eastern Service Area - 3 Antenna Apertures

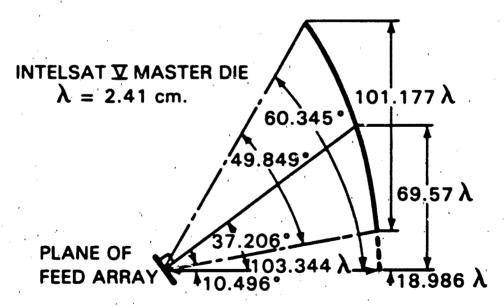


Figure 6. 2.438 Mtr. Reflector Geometry

	· · · · · · · · · · · · · · · · · · ·			
FEED NO.	спу	LONGITUDE	LATITUDE	GAIN CORRECTION (dB)
1	MIAMI/ETZ	-80, 150	25,450	0.0
,	TAMPA/ETZ	-82, 380	27,580	0.2
ز أ	TALLAHAS SEE / ETZ	-84, 300	30,300	0.4
4	MOBILE/ETZ	-88, 050	30,400	0.3
' 5	BIRMINGHAM/ETZ	-86, 550	33,500	0,5
6	NASHVILLE/ETZ	-86, 500	36, 100	0,3
6 7	INDIA NAPOLIS/ETZ	-86, 100	39, 450	-1.0
8	DETROIT/ETZ	-83,050	42, 230	-0.8
9	BUFFALO/ETZ	-78,550	42,520	-0.6
10	MASSENA, N.Y./ETZ	-74, 800	44,900	-0.4
11	CARIBOU, ME/ETZ	-68,000	46, 900	-0.2
12	BGSTON/ETZ	-71,050	42, 200	iQ.3
13	ATLANTIC CITY/ETZ	-74,300	39,300	-1.5
14	NEWBERN, N.C. /ETZ	-77,000	35,000	0.6
15	CHARLESTON, SCIETZ	-80,000	32,800	Q3
16	JACKSONVILLE/ETZ	-81, 400	30, 200	0.6
17	NEW YORK/ETZ	-74,000	40,700	-0.5
18	CLEVELAND/ETZ	-81_410·	41,300	-0.8
19	WASHINGTON, DC/ETZ	-77, 000	38,550	-0.7
20	PITTS BURGH/ETZ	-80,000	40, 260	-0.9
21	ATLANTA/ETZ	-64, 230	33, 450	0.0
22	CHARLOTTE, NC/ETZ	-80,500	35.030	0.2
23	CHARLESTON, WY/ETZ	-81, 400	38, 230	-1.0
24	SAN JUAN, PRIETZ	-66.0	18.0	-i.0

Figure 7. Typical Gain Correction (Eastern Cities)

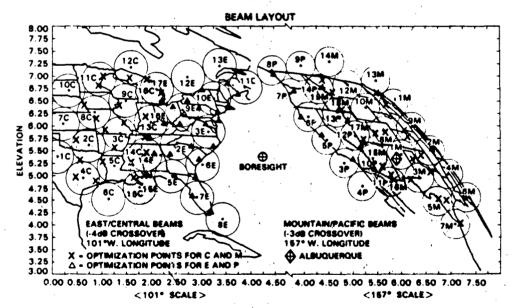


Figure 8. Beam Layout

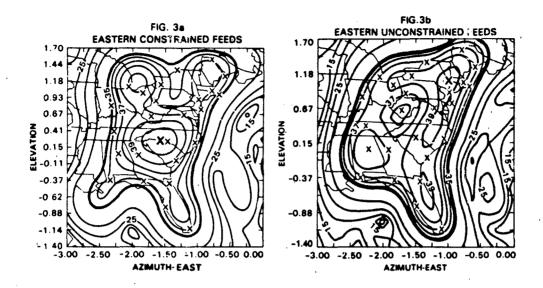


Figure 9. Eastern Constrained Feeds, Eastern Unconstrained Feeds

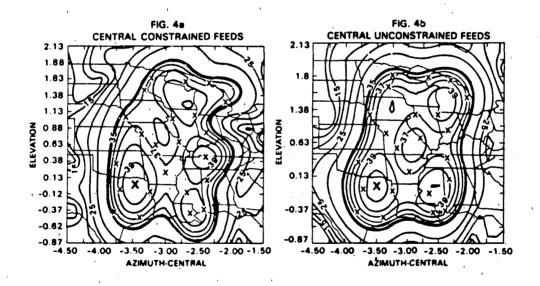


Figure 10. Central Constrained Feeds, Central Unconstrained Feeds

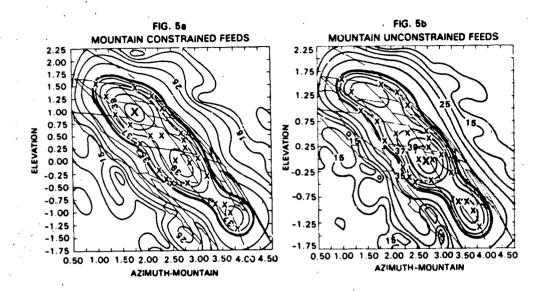


Figure 11. Mountain Constrained Feeds, Mountain Unconstrained Feeds

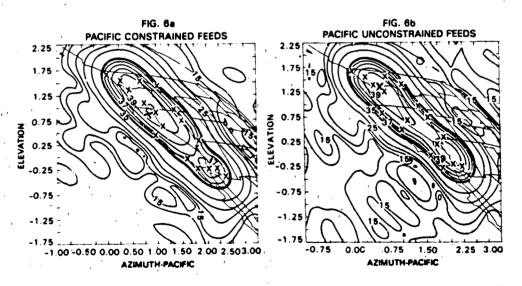


Figure 12. Pacific Constrained Feeds, Pacific Unconstrained Feeds

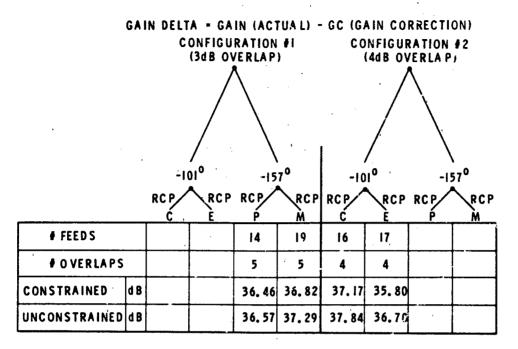


Figure 13. Worst Case Gain - Delta's (dB)

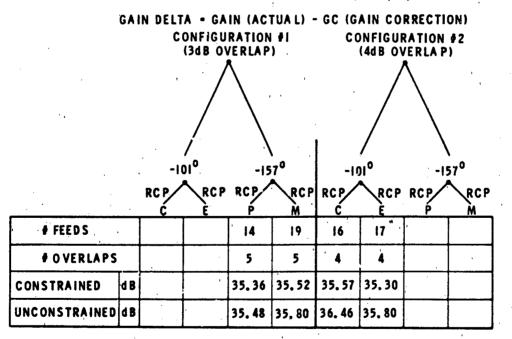


Figure 14. Worst Case Gain (Actual) dB

	FEED LOCATION			ORTHO	AINED AND GONAL TO AL PHS	UNCONSTRAINE		
	X	Y	Z	AMP	PHS	AMP	PHS	
1	-2, 262	4, 852	0,000	0,349	76.7	0,509	37.8	
2	3,557	-0, 553	0.000	1,000	12.5	0.813	25.8	
3	2, 215	-1.029	0,000	0, 628	28, 4	0,951	42.1	
4	0, 874	-1,503	0,000	0, 110	23.2	0, 145	27.9	
4 5	3, 815	0.847	0,000	0, 418	34.8	0,667	-10,4	
6	2,474	0,371	0,000	0,531	27.3	0,787	27.5	
7	2,734	1,769	0,000	0, 680	38.5	0,000	37.6	
8	1,652	2,695	0,000	0, 250	36.7	0,403	28,7	
9	3, 297	-1, 953	0,000	0,478	-66.5	0,887	-39.7	
10	1, 957	-2, 429	0,000	0,586	5.2	0, 895	14.4	
11	0,614	-2, 903	0,000	0, 435	44.0	0,558	24, 9	
12	3.037	-3.351	0,000	0.411	-32.9	0, 462	-14.8	
13	1.697	-3,825	0,000	0, 213	31,3	0, 321	29, 4	
14	4, 897	-0.078	0,000	0,543	67.5	0, 980	16.6	
15	5, 157	1.322	0,000	0,543	22,5	0, 280	20,4	
16	4, 637	-1, 478	0,000	0.543	-22.5	0,653	- 7.6	
17	4,378	-2,876	0,000	0,543	-6 7.5	0,342	- 9.3	

Figure 15. Final Eastern Feed Coefficients

	FEED LOCATION				NINED AND SONAL TO PHS	UNCONS	UNCONSTRAINED	
	X	Y	Z	AMP	PHS	AMP	PHS	
1	8, 662	-0,054	0,000	0, 167	-101.0	· Q. 467	-73,8	
2	7.320	-0,528	0,000	1,000	- 37.7	1,000	-36.8	
	5. 980	-1,004	0,000	0,526	-69.1	0.581	-19.8	
4	7.580	0,872	0,000	0,752	-47.5	0,849	-51.8	
5 6 7	6, 238	0,396	0.000	0.797	-45.4	0, 809	-40.1	
6	6, 497	1.796	0,000	0, 220	-51.9	0, 162	-56.8	
1.	8, 403	-1.452	0,000	0.302	-27.8	0, 259	-52.0	
8	7.060	-1, 926	0.000	0,720	-43, 8	0, 937	-29.5	
7	5.720	-2,400	0.000	0, 946	13.8	0,757	-13.1	
10	8, 143	-2, 852	0.000	0, 132	-109.0	0,055	-71.2	
11	6, 803	-3.326	0.000	0.859	- 25.3	0,832	-40.7	
12	5, 460	-3, 800	.0,000	0, 611	- 5.9	0, 415	0.6	
12 13 14	4, 637	-1.478	0.000	0, 855	-67.5	0, 682	2.5	
	4, 897	-0,078	0,000	0, 855	-22,5	0.997	-48	
15	5, 157	1.322	0,000	0.855	22,5	0, 473	13.8	
16	4:378	-2, 876	0,000	0, 855	67.5	0.790	0.3	

Figure 16. Final Central Feed Coefficients

	FEED LOCATION				AINED AND GONAL TO CIFIC	UNCONS	TRA INED
	X	Υ	Z	AMP	PHS	AMP	PHS
1	-5, 462	-0,080	0,000	0,783	34,1	0,886	- 6,4
2	-6, 687	-0, 252	0,000	0,360	32.7	0.348	15.0
3	-6,225	0, 897	0,000	0,864	32.5	0, 924	-20, 8
4	-7, 450	0,724	0,000	0, 123	-32.0	0, 126	-33, 1
5	-6, 986	1.872	0,000	0, 956	16, 9	1,000	-5l, l
6	-8, 211	1.699	0,000	0.550	-53.6	0, 475	-46,7
7	-7.749	2,848	0,000	0,721	-14, 1	0, 805	-21, 2
8	-4,701	-1.056	0.000	0, 859	21, 2	0,781	13.6
9	-5.926	-1.227	0,000	0, 613	38.6	0,561	-15.7
10	-3.958	-2.031	0,000	1,000	- 5.6	0.946	10,3
11	5.16	-2, 202	0,000	0, 440	5.3	0,544	-54.5
12 .	-3. 178	-3.006	0.000	0,898	-39. 2	0,885	20,0
13	-4, 402	-3, 180	0.000	0,612	- 1.5	0,496	- 2,7
14	-2, 415	-3, 982	0,000	0, 417	<u>-54.5</u>	0,335	<u>43, 2</u>
15	-4, 237	0.093	0.000	0, 685	72.0	0, 624	17.3
16	-4, 998	1,068	0,000	0, 685	36.0	0.819	-19.6
17	-3,477	-0,883	0,000	0, 685	0.0	0.526	46, 4
18	-2.714	-1,858	0,000	0,685	-36.0	0.390	19.6
19	-1, 953	-2,835	0,000	0, 685	-72.0	0,791	28, 8

Figure 17. Final Mountain Feed Coefficients

FEED LOCATIONS			ORTHO	AINED AND GONAL TO NTAIN	UNCONSTRA INED		
	X	Υ	Z	AMP	PHS	AMP	PHS
1	5.714	-5, 868	0,000	1,000	82, 2	0, 963	167.7
2	6,908	3,617	0,000	0, 873	95.1	0, 829	30,5
3	-3, 013	0, 266	0,000	0,579	-38.4	0,054	48.0
4	-3,773	1, 241	0,000	0, 207	-85.1	0, 113	- 33.4
5	-2, 250	-0.711	0,000	0, 533	12.5	0,527	- 12.7
6	-1, 489	-1, 687	0,000	0,788	56.4	0,652	- 13.1
7	-0.726	-2,662	0,000	0,755	45.5	0.768	- 23.8
8	0,035	-3,637	0,000	0,646	86,5	0,583	- 17.6
9	-1, 190	-3.811	0,000	0,518	100,3	0, 497	3.9
10	-4, 237	0,093	0,000	0,646	-72.0	1,000 -	9.3
11	-4, 998	1,068	0,000	0.646	-36.0	0,420	35.2
12 -	-3.477	-0, 883	0,000	0,646	0.0	0,712	- 1.2
13	-2.714	-1, 858	0,000	0,646	36,0	0,645	- 22.5
14	-1, 953	-2, 835	0,000	0,646	72.0	0,566	21.5

Figure 18. Final Pacific Feed Coefficients

UNCONSTRAINED (2 POLARIZATION)

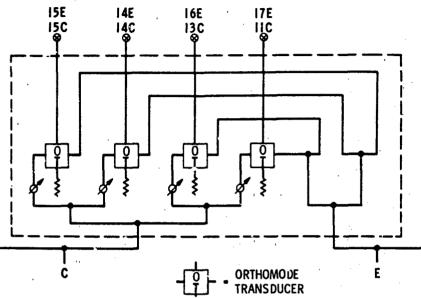


Figure 19. Schematic of Overlapped Feeds Connections (Central - Eastern)

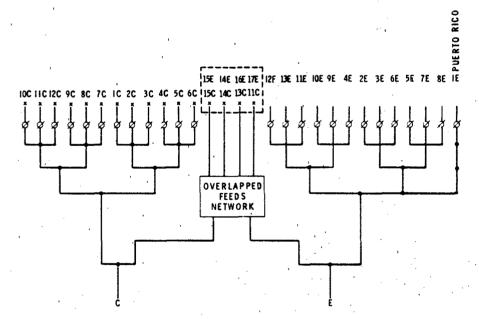
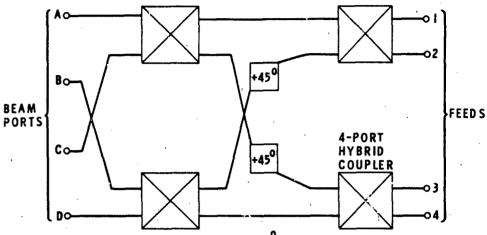


Figure 20. Eastern - Central Distribution

EQUAL AMPLITUDE AT EACH FEED OUTPUT



EXAMPLE I: BEAM PORT A: PHACE = 0° FEED PHASES: I:(0°), 2:(-45°), 3:(-90),4:(-135°)

EXAMPLE 2: BEAM PORT B: FEED PHASES: 1:(+90°), 2:(+45°), 3:(0°), 4:(-45°)

Figure 21. 4 Feed/2 Beam Constrained Isolation Network

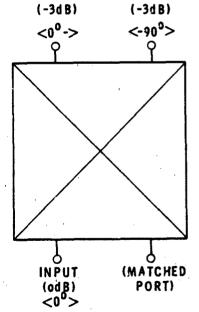


Figure 22. 4 Port 'Hybrid Coupler'

AUSSAT KU, BAND SPACE ANTENNA SUBSYSTEM

E.C. Ha, L.G. Clouse, K.A. Simmons, K. Clausing, M.D. Harwood, and M.J. Glaser

Abstract

The Aussat antenna was designed for the first generation of satellites to be used in the Australian national satellite communications system. The wide range of domestic services to be provided by this system includes direct broadcast, high quality television relays between major cities, digital data transmission, voice applications, and centralized air traffic control services. To meet the stringent requirements imposed by this system, and compatibility with the established Hughes HS 376 bus, an innovative Ku band antenna subsystem has been designed, with ten independent beams for communications and separate beams for command and beacon tracking. The antenna farm consists of three shared aperture pairs, each aperture being reused via polarization diversity, resulting in six offset single reflector systems. There are nine independent feed systems, of which two serve both transmit and receive functions by means of diplexers. The transmitted EIRP is 47 dBW for homestead and communities broadcasting satellite services and 36 dBW for fixed satellite services. The electrical and mechanical design of the subsystem allows for a high degree of flexibility, as demonstrated by the fact that

Hughes was able to meet a new customer requirement to change a beam shape during the final weeks of the flight antenna range testing.

1. Introduction

The Aussat Ku band communication satellite is a 15 channel active repeater system, providing multiple beam coverage (10 shaped beams) for Australia. Each cha. el is 45 MHz wide. The transmit bandwidth extends from 12.25 to 12.75 GHz, while the receive bandwidth extends from 14.00 to 14.50 GHz. Frequency reuse is achieved by linear orthogonal polarization. Eight of the channels (designated transponder A) are received horizontally polarized and retransmitted vertically polarized (see Figure 1). The remaining seven channels (designated transponder B) are received vertically polarized and retransmitted horizontally polarized.

To implement the required multiple beam, dual polarization performance, the Aussat communications antenna system uses six gridded reflectors (three for each polarization) in conjunction with a feed system employing nine beam forming networks and a total of 23 feed horns (excluding tracking feeds). The reflector design incorporates two reflector surfaces in a single aperture. Typical of each shared aperture pair, the front reflector is horizontally polarized, while the rear reflector is vertically polarized.

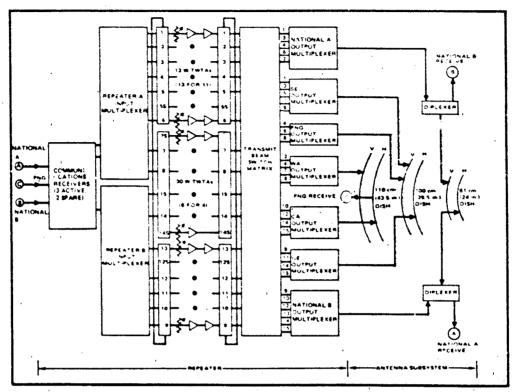


FIGURE 1. AUSSAT COMMUNICATION PAYLOAD

To minimize the depolarization produced when linearly polarized radiation propagates through dense rain, the polarizations are required to be nominally horizontal and vertical at the earth stations across Australia. As the orbital arc is centered on 160° E longitude (east of the Australian mainland), the polarization axes of the vertical and horizontal feed horns and the reflector grids are oriented 45° counterclockwise and clockwise, respectively, from the spacecraft spin axis.

The antenna coverages are shown in Figures 2 and 3. The 61 cm (24 inch) horizontally polarized front reflector is fed by a single feed horn which is diplexed to provide National receive

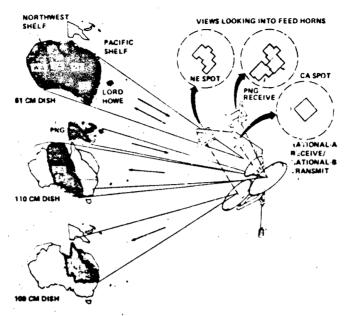


FIGURE 2. FRONT REFLECTORS - HORIZONTAL POLARIZATION

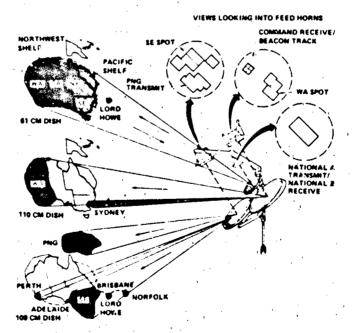


FIGURE 3. REAR REFLECTORS - VERTICAL POLARIZATION

and transmit functions. The 61 cm vertically polarized rear reflector is also fed by a single feed horn which is diplexed to provide additional channels for National receive and transmit functions. The National beams provide coverage of mainland Australia, Tasmania, Lord Howe Island, the Pacific shelf, and the Northwest shelf.

The 110 cm (43.5 inch) horizontally polarized front reflector is fed by two functionally distinct feed arrays. A four-horn array provides transmit coverage of Central Australia. A separate three-horn array provides receive coverage of Papua New Guinea. Sharing the same aperture is a vertically polarized rear reflector which is also fed by two separate feed arrays. A three-horn array provides transmit coverage of Western Australia and the Northwest chelf. The remaining four-horn array is used to provide high gain on-station command coverage (the command omniantenna is also available to receive commands), and to perform beacon tracking.

The 100 cm (39.5 inch) horizontally polarized front reflector is illuminated by a four-horn feed array to achieve coverage of Northeastern Australia. Sharing the same aperture is a vertically polarized rear reflector fed by two distinct feed arrays. A three-horn array is used to provide transmit coverage of Papua New Guinea. Another four-horn array provides transmit coverage of Southeastern Australia, Lord Howe Island, Norfolk Island, Brisbane, Adelaide, and Perth.

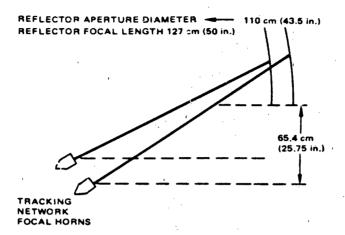


FIGURE 4. TYPICAL SHARED APERTURE REFLECTOR GEOMETRY

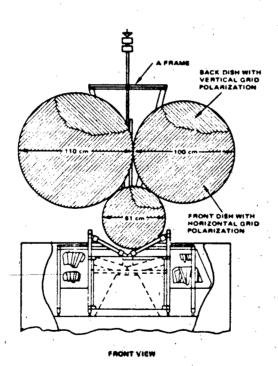


FIGURE 5. AUSSAT SPACECRAFT ANTENNA SYSTEM

2. Electrical Design

Each reflector pair is composed of two orthogonally polarized offset reflectors, one behind the other, sharing the same aperture (Figure 4). Polarization selection for each reflector is achieved by conductive grids on a paraboloidal shell. The front reflector of each reflector pair has its conductive grids oriented 45° clockwise (horizontal polarization) with respect to the spacecraft spin axis (Figure 5). The conductive grids on the surface of the rear reflector are oriented orthogonal to the front reflector grids, when viewed along the boresight of the front reflector. The reflector diameters and focal lengths are identical for each polarization; however, the base of the vertically polarized reflector is offset from the horizontally polarized reflector, permitting focal point separation. This allows the two reflectors to occupy a common aperture, and positions each feed array at its respective focus without physical interference. The front horizontally polarized gridded reflector is essentially RF transparent to the rear vertically polarized gridded reflector.

The sources illuminating the six reflectors are pyramidal horns. Of the twenty-seven pyramidal horns used, four are dielectrically loaded. The dielectric inserts are tapered rexolite slabs attached to the E plane walls. The dielectric inserts provide a more uniform H-plane distribution and, therefore, a

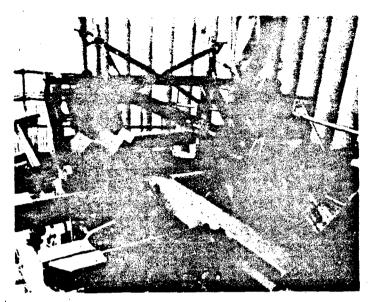


FIGURE 6. AUSSAT FEED HORN LAYOUT

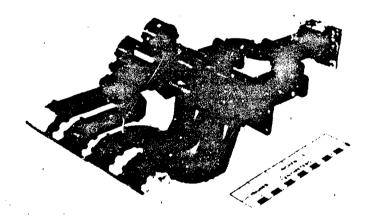


FIGURE 7. TYPICAL FEED NETWORK DESIGN

higher aperture efficiency and wider H-plane secondary beamwidth.

The dielectric inserts were used in the horns providing coverage of Western and Southeastern Australia.

Figure 6 shows the layout for all of the feed horn arrays. The single horn in the foreground of the photograph is one of the horns providing complete coverage of continental Australia. The rack of feed horns on the left rear side illuminates the 39.5 inch diameter reflector pair, while the rack on the right rear side illuminates the 43.5 inch diameter reflector pair.

A typical spot beam feed network is shown in Figure 7. All spot beam networks are single mode networks. Single slot couplers were used to distribute the power among the horns comprising each feed horn array. Trombone sections were used to adjust the phase of the radiation propagating from each horn.

Precision east-west (ΔAz) and north-south ($\Delta E1$) antenna pointing signals are developed from a dedicated set of four tracking feed horns (Figure 8). The same feed system also serves to provide the command link.

The tracking feed horns have difference signal versus sum signal (null) characteristics designed for tracking purposes. These feed horns are excited by approximately equal power and independent phase signals, controlled by adjusting the physical line length between the feeds and the magic tee power summers. Difference outputs from two axis monopulse feed array networks results in signals proportional to angular position from the

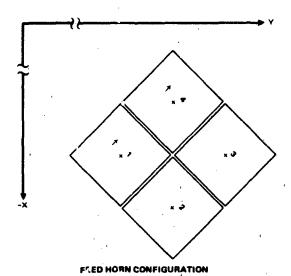
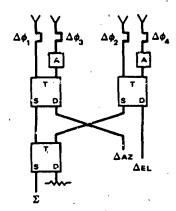


FIGURE 8. COMMAND/TRACK FEED HORN CONFIGURATION



A - ATTENUATOR $\Delta \phi_1 = -38^\circ$ T - MAGIC TEE $\Delta \phi_2 = 0^\circ$ S - SUM PORT $\Delta \phi_3 = -3^\circ$ D - DIFFERENCE PORT $\Delta \phi_4 = -28^\circ$

FIGURE 9. TRACKING FEED COMBINING NETWORK

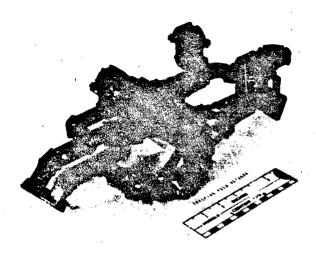


FIGURE 10. TRACKING FEED NETWORK

beacon location (at Sydney). Subsequent combination of the sum and difference signals creates amplitude modulated error waveforms which are detected in the command/track receivers. The receivers' outputs are processed in the antenna position electronics (APE) and the attitude control electronics (ACE) to control the antenna north-south and east-west pointing. A schematic of the tracking feed combining network is shown in Figure 9; a photo of it is shown in Figure 10.

This type of tracking system is capable of controlling the antenna positioning to within $\pm 0.02^{\circ}$ in azimuth and elevation.

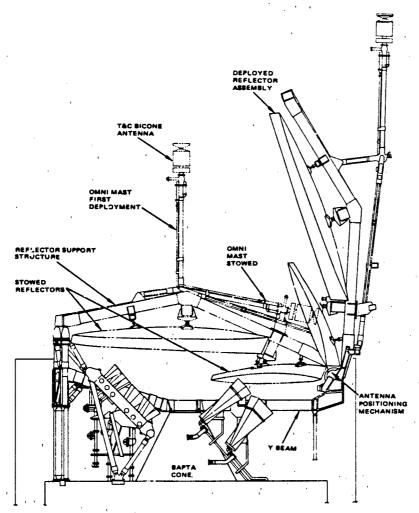


FIGURE 11. ANTENNA SYSTEM

3. Mechanical Section

The decision to incorporate a multiple reflector design produced challenging mechanical requirements with regard to pointing capabilities and thermal stability of the system. Many effects which were previously second order, because the communications and tracking reference patterns were produced by the same reflector, could now have a significant impact on system performance.

The first area of developmental work on the Aussat antenna was the design and mounting of each of the three reflectors (see Figures 11 and 12). With gain slopes as high as 10 dB per degree, coupled with operating frequencies at Ku band, the manufacturing tolerance and thermal stability of each reflector became very significant.

The reflectors are fabricated using techniques developed for the HS 376 product line. Two precisely machined mechanite mandrels were used as the shell forming tools, with each parabolic surface being machined to an accuracy of 0.025 mm (0.001 inch) rms. A low temperature curing epoxy resin system is used to minimize thermal distortion of the part during the curing process.

The major design change was to incorporate a center mounting technique that would provide flexibility to precisely align each reflector on the test range while meeting the requirements of thermal stability, strength, and stiffness.

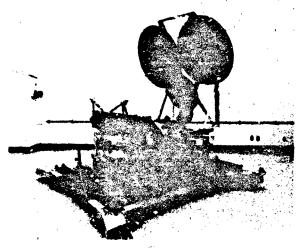


FIGURE 12. FULL UP ANTENNA FARM PRIOR TO RANGE TEST

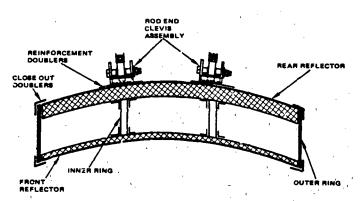


FIGURE 13. SECTION VIEW OF REFLECTORS

Each reflector is attached to the support structure with three spherical bearing rod ends spaced about the reflector inner rings. The rod ends negate any thermal stress between reflector and support structure, while the attachment to the inner rings provides a natural hard point. As with previous designs, local reinforcement was provided at the attach points (see Figure 13). Both the rod end and clevis attaches to the rear of the reflector assembly and utilizes low expansion materials. Fine adjustment can be made by angular rotation of the rod end bearing relative to its bracket. Boresight adjustments of 0.005° were easily obtainable. Once optimum boresighting was achieved on the test range, each reflector attachment assembly was permanently secured for flight.

To confirm that the reflector and attachment assemblies will not induce unacceptable distortions during orbit, a comprehensive thermal distortion test was performed. The reflector test setup consisted of the Kl flight 110 cm (43.5 inch) reflector attached to a quartz plate, using flight rod end attach fittings (see Figure 14).

The test setup was instrumented with 60 thermocouples and 52 linear variable differential transformers (LVDTs) to measure displacements. The test was performed in a thermal-vacuum chamber to simulate both hot and cold bulk temperatures, as well as

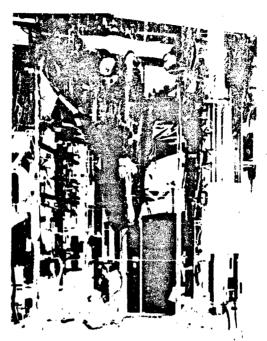


FIGURE 14. THERMAL MECHANICAL TEST OF FLIGHT REFLECTOR



FIGURE 15. BARE ANTENNA STRUCTURE

thermal gradients. Results from the test were analyzed and found to have no significant degradation of antenna performance.

The next major developmental work for the Aussat antenna was to design a stable structure to attach all three reflectors and feeds. This structure had many constraints with regard to strength, stiffness, weight, and most important of all, thermal stability.

The purpose of the support structure is to support and constrain the antenna during launch and provide a stable platform to maintain the feed horn to reflector geometrical relationship in orbit. Loads from the antennas are reacted through the antenna support structure into the spacecraft. The structure, shown in Figure 15, illustrates the deployed configuration less feeds and reflectors. The common use of composite materials, primarily graphite, and hollow bonded subassemblies provides for low weight while maintaining the necessary strength. The use of composites also provides excellent dimensional stability with temperature variations.

The reflector support structure (see Figures 1i and 16) provides a common support for each of the three dual reflectors and the T&C antenna and its linkage. The complete system is attached to the antenna positioning mechanism. The primary design objective is to maintain the relative alignment of the three reflectors under operating environmental conditions. Materials



FIGURE 16. REFLECTOR SUPPORT STRUCTURE WITH ASSEMBLY FIXTURE

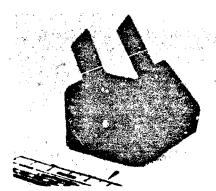


FIGURE 18. THREE SOCKET FITTING



FIGURE 17. GRAPHITE APM FITTING

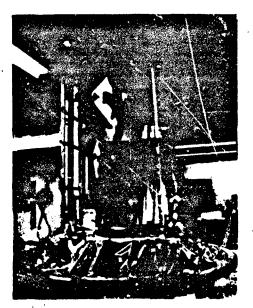


FIGURE 19. INSTRUMENTED REFLECTOR SUPPORT STRUCTURE PRIOR TO THERMAL MECHANICAL TEST

and configuration were chosen for minimum thermal distortion and maximum stiffness of the structural assembly.

Because of the stringent requirement of this structure, several graphite fittings were developed to replace metallic fittings typically used (see Figures 17 and 18). These innovative fittings were made using high strength graphite fabric with epoxy resin. They successfully reduced weight while improving the thermal stability of the structure.

Again, to ensure that the reflector support structure would not produce unacceptable distortions during orbit, a comprehensive thermomechanical test was performed. This test was meant to provide a means to bound the pointing error contribution due to differential distortion between the three dishes. The reflectors were replaced with thermally stable quartz plates, and the entire structure was instrumented (see Figure 19).

Mirrors were used to measure the quartz plate rotation during the test of the reflector support structure. The quartz plates, which were used to simulate the flight reflectors, were also instrumented with LVDTs to provide a coarse backup check of the mirror results. Further, a series of targets were installed to measure system growth in the plane of the reflectors.

Test results showed that the reflector support structure was extremely stable and met all requirements, with regard to pointing budget allowance.

4. Measured Test Results

The antenna measurements were performed under clear weather conditions on a far field range. All antenna tests included proper modeling of the spacecraft structure to simulate an in-orbit operating condition (i.e., thermal blanket, reflector sunshields, horn covers, and aluminum ring simulating a portion of the solar panel were present). All antenna gains were referenced to a gain horn standard calibrated by the National Bureau of Standards. A carefully calibrated waveguide switching network was used to switch between various test ports to ensure repeatability.

To ensure proper alignment of the transmitter polarization to the conductive grids on the reflector under test, the transmitter was rotated until it was orthogonally polarized to the reflector grids. This was achieved when the measured crosspolarization null attained a minimum magnitude. The transmitter was then rotated back exactly 90° ro align the transmitter polarization to the reflector grids.

The various Aussat coverage regions are shown in Figures 20 through 25. In each case, the darkened region(s) represent secondary zones, while the white regions represent primary zones.

The transmit and receive coverage requirements are shown in Tables 1 and 2, respectively. These gain requirements were

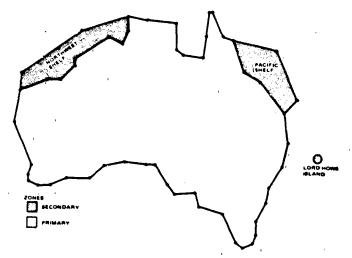


FIGURE 20. NATIONAL BEAM COVERAGE

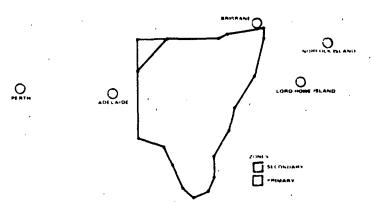


FIGURE 21. SOUTHEASTERN SPOT BEAM COVERAGE

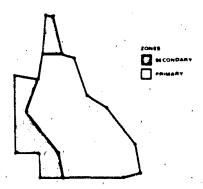


FIGURE 22. NORTHEASTERN SPOT BEAM COVERAGE

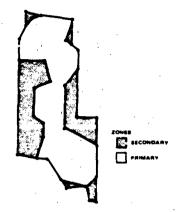


FIGURE 23. CENTRAL AUSTRALIA SPOT BEAM COVERAGE

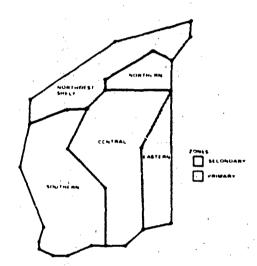


FIGURE 24. WESTERN AUSTRALIA SPOT BEAM COVERAGE

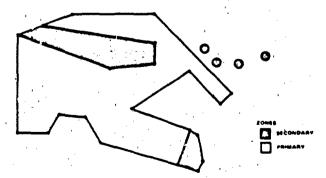


FIGURE 25. PAPUA, NEW GUINEA (PNG) COVERAGE

derived from EIRP and G/T contract specifications assuming the predicted repeater performances.

TABLE 1. TRANSMIT GAIN COVERAGE REQUIREMENTS

	Transmit Antenna Gain		
Region Coverage	Spot Beams,* dB	National A and B, dB	Papua, New Guinea, dB
80% Primary	34.0	_	-
95% Primary	,-	27.1	_
100% Primary	31.0	26.1	32.0
Secondary	29.0	22.1	25.0

^{*}Spot beams are comprised of northeast, central, western, and southeastern Australia coverage beams.

TABLE 2. RECEIVE GAIN COVERAGE REQUIREMENTS

	Receive Antenna Gain		
Region Coverage	National A and B,	Papua, New Guinea, dB	
95% Primary	26.9	26.7	
100% Primary	25.9	25.7	
Secondar	21.9	23.7	

Figures 26 through 36 show one representative copolarization gain contour plot for each coverage beam. All copolarization gain contours are plotted with superimposed coverage maps (as

viewed from the satellite at orbital locations 156°E, 160°E, and 164°E) expanded by the indicated printing errors. For National Australia, as well as the spot beam gain contour plots, only the primary coverage spec contours are numbered (represented by darkened contour(s) in each case). Also shown are the peak gains of the contours, the test frequency at which the contours were measured, and the pointing errors incorporated into the maps.

The crosspolarization performance in the far field of the antenna system is due principally to two mechanisms. The first is the nature of the grid reflectors, which employ finite thickness grids and are subject to manufacturing tolerances. The crosspolarization performance over the copolarized service area is due predominantly to non-ideal reflecting grid geometry.

The feed horns are the second source of far field crosspolarization impurity. For the case of the horizontally polarized feed, the impure field components (vertically polarized) pass through the front horizontal grid reflector and reflect off the rear vertical grid reflector. However, the rear reflector defocuses these impure vertical components because the horizontally polarized feed is widely offset from the focus of the rear vertically polarized reflector. Thus, far field crosspolarization (vertical) caused by horn impurity is not focused into the principally polarized (horizontal) coverage area. Similarly

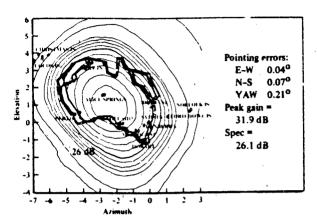


FIGURE 26. NATIONAL A TRANSMIT (VERTICAL)

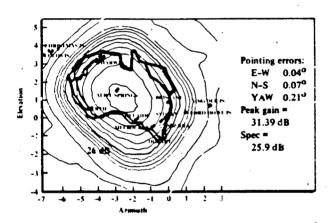


FIGURE 27. NATIONAL B RECEIVE (VERTICAL)

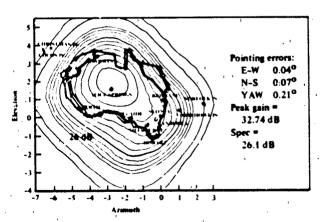


FIGURE 28. NATIONAL B TRANSMIT (HORIZONTAL)

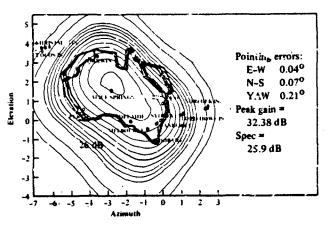


FIGURE 29. NATIONAL A RECEIVE (HORIZONTAL)

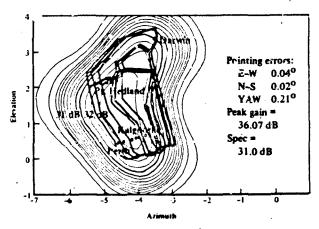


FIGURE 30. WESTERN AUSTRALIA SPOT BEAM

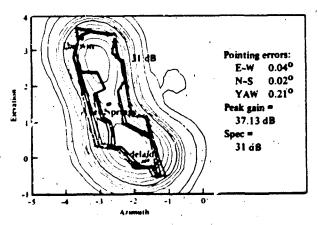


FIGURE 31. CENTRAL AUSTRALIA SPOT BEAM

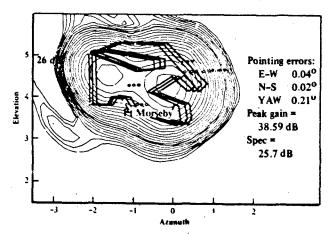


FIGURE 32. PNG RECEIVE SPOT BEAM

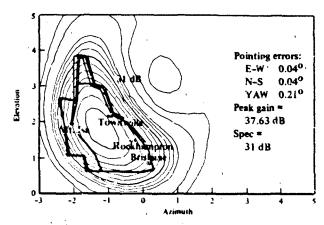


FIGURE 33. NORTHEASTERN AUSTRALIA SPOT BEAM

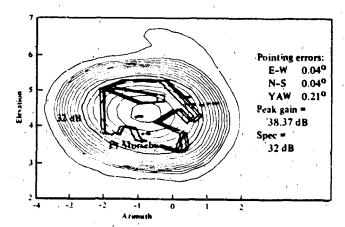


FIGURE 34. PNG TRANSMIT SPOT BEAM

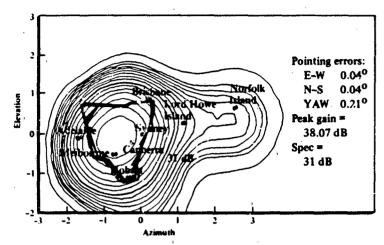


FIGURE 35. SOUTHEASTERN AUSTRALIA SPOT BEAM

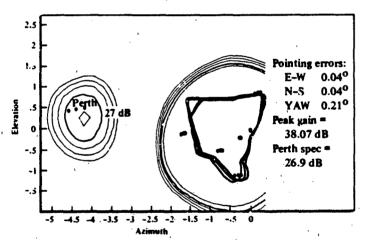


FIGURE 36. SOUTHEASTERN AUSTRALIA SPOT BEAM (CONTINUED)

this effect applies to the crosspolarized components of the vertically polarized feed.

Figure 37 illustrates the crosspolarization performance of the WA spot beam. The crosspolarization due to feed impurities has been defocused to the south of Australia. The crosspolarization isolation exceeds 36 dB over the primary service areas.

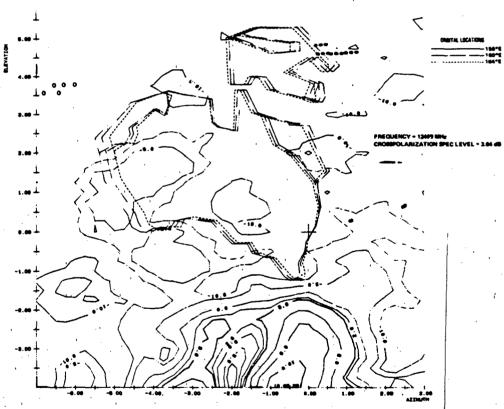


FIGURE 37. WESTERN CROSSPOLARIZATION PERFORMANCE

5. Conclusion

The Aussat antenna has met all flexible beam shaping, pointing, thermal stability, and other mechanical requirements. The electrical design is relatively simple, allowing for short assembly/test times. Built into both the electrical and mechanical designs are flexibilities to adjust the beam shaping and beam pointing in the antenna system. As a result of innovations added to the many standard features of the Hughes HS 376 line of spacecraft antenna systems, the Aussat antenna system represents an important milestone in the history of Australian telecommunications.

CONTROLLED SURFACE DISTORTION EFFECTS

DANIEL JACAVANCO
EM Technology Applications Section
EM Techniques Branch
Electromagnetic Sciences Division
Rome Air Development Center
Hanscom AFB, MA 01731

ABSTRACT

Results of a theoretical and experimental study of a technique that controls the level of the sidelobes in the far field pattern of a horn fed paraboloid are presented. The reflecting surface is intentionally distorted by mounting small circular disks on the dish and adjusting their height while monitoring the energy in the field at a specific angle. Patterns measured before and after show (a) localized sidelobe control on the order of 25 dB, (b) little main beam distortion, and (c) acceptable overall sidelobe degradation. A theoretical model of a collapsed circular aperture containing the illumination due to the horn feed is used. The resulting aperture distribution is composed of three parts-the amplitude across the dish, and the amplitudes across each of the two disks. A computer subroutine duplicates the manual process of adjusting the disk position while monitoring the energy in the far field. There is good agreement between theory and experiment.

2. INTRODUCTION

A novel technique is described for placing fixed nulls in the far field radiation pattern of a horn-fed paraboloid. Small disk shaped moveable reflectors are mounted on rods that protrude through the reflector surface and allow the height above the dish to be controlled from the rear. See Figure 1. Single nulls can be placed in the radiation pattern using two disks and show cancellation up to 25 dB with minimum perturbation to the overall antenna response.

One might say that this technique is a solution looking for a problem. The potential applications are somewhat special. One use might be for urban communication systems or point-to-point telephone links which rely on reflectors exclusively. In these instances, single fixed nulls could be effective in reducing specular reflections from large buildings or in reducing the effects of unintentional jamming upon total system noise due to the proliferation of microwave antennas in the urban environment. Given future NASA plans for direct broadcast satellites and the attendant need for a receiving antenna on every roof, there could be a need for a simple, inexpensive, fixed nulling technique as described herein.

The remainder of this paper will describe the theoretical model used to predict the nulling performance of two disks mounted on a paraboloid, six feet in diameter. Experimental results are

given which generally show good agreement with theory.

Cancellation up to 25 dB, along with the very important minimum distortion of the overall far field pattern, is in evidence.

Finally, some preliminary results of placing two nulls in the far field pattern using three disks is given.

THEORY

When a small moveable disk is mounted on the inner surface of a paraboloid, the resulting amplitude and phase distribution of the electric field in the aperture plane is driven asymmetric about boresight. From a theoretical standpoint, this means that obtaining the far field through the usual Fourier Transform calculation is difficult because the amplitude and phase distribution is not of closed form. For this reason, it was decided to model the antenna performance in the azimuthal plane in which all the measurements were made, by collapsing the aperture over the vertical plane.

Thus, for the purposes of pattern computation, the reflector and its asymmetric aperture distribution is modeled as an electrically equivalent, horizontally disposed linear array of elements. The amplitude and phase assigned to each of these elements are calculated from the combination of the feed horn E and H-plane patterns. When the aperture is collapsed mathematically, this linear array will contain the amplitude effects of feed blockage, multiple disks, surface error, and the

circular aperture due to the paraboloid itself.

The first step in the collapsing procedure is to measure the feed horn E and H-plane patterns. The measured patterns are reproduced in Figure 3 and show an edge taper of -21 dB in the azimuth (H-plane) and a -17 dB taper in the vertical (E-plane). The patterns are then sampled at a collection of points denoted by the heavy dots in Figure 2. In this sampling procedure, one can simply read off the values of the measured feed pattern at the desired sample points or, alternately, match the measured patterns by a polynomial and let the computer calculate pattern values at the desired points. This latter method was easier for large paraboloids and was adopted. Fifth order polynomials were found to satisfactorily describe the measured feed patterns in each plane with an accuracy of + 0.1 dB in amplitude. Using these sampled values, the field distribution at all other points in the aperture plane of the reflector, such as those represented by the 91 x 91 matrix of small dots in Figure 2, can be generated by multiplication.

In Figure 2, the large circle is the outline of the 6-foot paraboloid, the smaller circle containing the rectangular projection of the outline of the feed horn, is the aperture blockage region, and the two, small, off center circles are the aluminum disks.

The next step is to collapse the vertical field points on to

a horizontal line, at a discrete number of equispaced points that correspond to the locations of the elements in our hypothetical linear array. A one-fifth wavelength element spacing was chosen as a trade between accuracy and computation time. Obviously, the closer the spacing, the more accurately the computed array distribution represents the reflector fields. In collapsing the reflector aperture field in the vertical dimension, the computer calculates the product of one horizontal field value with all the corresponding vertical field values at a horizontal point corresponding to an array element location. If the computed point lies on the reflector, or on a disk, it is retained for pattern calculation. If the point lies in a blockage region, and never contributes to the pattern, the value is discarded. In this way, three separate linear array amplitude distributions are arrived at, one each representing the reflector and the two disks. The technique is general enough to account for any number of disks, positions and sizes.

A uniform phase distribution is assigned to the array to produce a broadside mainbeam. Also added to this phase were the measured reflector surface errors and an additional phase perturbation due to the disks. To maintain consistency between the vertical collapsing used in the computer model and actual far field measurements of the paraboloid, pattern measurements were made in the azimuthal plane which contains the centers of the two

が、日本の人が大きなない。これはないでは、一般ななななななない。これではないないは、これななななななない。これなるないではなっていました。

disks and the feed horn.

The largest error in the collapsing scheme is probably in the estimate of the individual disk gain. The small number of product-points, approximately 16 for a 1 wavelength diameter disk, is small compared to the 8281 points in the 91 x 91 element matrix. Small disks, on the order of 1 to 2 wavelengths in diameter, are used for the purpose of nulling in this experiment, so as to minimize the effect of the disks upon the overall radiation pattern of the paraboloid.

我们是是这个人的,也是是这种的的,也是不是这个人的,也是是一个人的,也是是一个人的,也是是一个人的,也是一个人的,也是一个人的,也是一个人的,也是一个人的,也是

In order to show that the computer code that collapses the aperture works properly, two standard antenna configurations were analyzed using this technique. When, an 18 wavelength square aperture with uniform illumination assumed to be generated by a hypothetical feed horn is employed, and the aperture field collapsed as described above, Figure 4 is the computed far field pattern. The plot in Figure 4a with the accompanying expanded plot Figure 4b shows the expected -13.2 dB first sidelobe and a mainbeam width of 3.36 degrees, characteristic of a square aperture. If, instead of a square aperture, an 18 wavelength circular aperture with uniform illumination is used, the resulting far field pattern is given in Figure 5. The plot shows the expected -17.6 dB first sidelobe and a mainbeam width of 3.89 degrees.

Thus, with the confidence in the computer code exhibited by

the results in Figure 4 and 5, the predicted far field pattern of the six foot diameter paraboloid was calculated. (see Figure 6a). In collapsing the aperture, the measured feed horn patterns were used, the blockage was modeled by a circle, eight inches in diameter and the surface error was included. No disks were assumed to be in place. The measured pattern, given in Figure 6b shows reasonable agreement in the main beam, first sidelobe and the average far-out sidelobes.

4. EXPERIMENT

Figure 7 shows the small effect that positioning the two disks close to the surface of the reflector has upon the performance of the paraboloid. The two plots represent the case 'before' and 'after' the disks are added. Minimum changes in these measured patterns are evident. The disks used in this experiment were 5 and 8 inches in diameter, positioned at 3 and 12 inches from the center of the paraboloid. As a test of where, in the sidelobe region, one should expect nulling, the combined area of both disks, compared to the area of the paraboloid, can be calculated. This ratio of disk area to dish area is expressed in dB. Thus, in this case, one could expect nulling in sidelobes lower than -17.6 dB. This calculation however, ignores the taper over the disks due to the feed horn. When this is accounted for, the gain of the two disks, relative to the reflector, is calculated to be -14.6 dB. Thus, it is reasonable to expect

nulling to be possible at angles greater than ± 5 degrees in the paraboloid pattern, where there is sufficient disk gain to match the gain in the dish. The plot in Figure 8 is the initial pattern of the dish with the two disks flush with the surface. The collection of large dots represent the levels to which the power received was driven by manually adjusting the penetration of the disks. Each dot represents one particular positioning of the two disks. Note than one can control location as well as the value of the pattern cancellation. Upwards of 25 dB cancellation was achieved at some locations y moving the 5 and 8 inch diameter disks. The paraboloid was first moved to a specific angular position, and the disks adjusted, one at a time, until no further cancellation was possible. Nulling was attempted every two degrees in the far field over two broad angular sectors.

No claim is made as to the uniqueness of the final position of the disks. One might argue however, that a 'global' null was reached at those angular positions where the pattern response was driven to the noise level of the receiver (-60 dB). A 'local' rull is claimed at those angles where (a) the -60 dB level was not achieved or (b) multiple combinations of positions of the two disks achieved similar, but not equal cancellation.

The asymmetric nulling performance evidenced in Figure 8 can be explained in the following way. Over the range of angles +6 to +42 degrees the two disks were not shadowed by the feed support

structures and good nulling performance is seen. Over the few negative angles where nulling was tried, the disks were completely shadowed by the feed. The poor nulling performance observed cannot be explained by aperture blockage because no angular dependence of blockage is included in the model used, i.e., the center section of the aperture plane is simply subtracted out and produces an error effect over a broad range of angles, principally manifested by a filling in of the first sidelobe and null. The specific reflective properties of the metal tripod, adjustable feed horn mounting ring and the pyramidal feed horn and their influence on this technique will be the subject of future work.

The solid line in Figure 9a, 10a, and 11a is the measured pattern of the paraboloid after nulling was accomplished at -40, +9, and +15 degrees. The dashed plot is the initial pattern before nulling. The large dot in each case represents the initial value in the pattern before the two disks were moved in order to produce a null. Overall, the integrity of the main beam has been maintained and aside from a few sidelobes that increase a few dB, there appears to be no unacceptable pattern distortion.

The final position of the two disks, after nulling, is given in tabular form below after converting distance moved to phase shift.

TABLE 1

NULL POSITION	5" DISK	8 DISK	
DEGREES	INCHES/DEGREES	INCHES/DEGREES	
-40	0.8/160	1.45/290	
+9	2.5/140	1.83/6	
+15	0.7/140	0/0	

Figures 9b, 10b, and 11b are the computer predicted patterns based on an algorithm that duplicates the manual process of nulling with the disks, one at a time. The final phase shift assigned to each of the disks by the computer nulling subroutine is given in Table 2.

TABLE 2

NULL POSITION

DEGREES 5" DISK DEGREES		8" DISK DEGREES	
-40	312	186	
+9	186	341	
+15	312	357	

A number of reasons can be given for the lack of agreement between Table 1 and Table 2. The principal problems in the experiment are (a) scattering from the feed support structure (b) accuracy in measuring the penetration distance of the disks, (c) accuracy in measuring the position of the null, and (d) disk-disk coupling and stray reflections.

The principal shortcomings of the theoretical model include (a) a lack of a description of the diffraction pattern of the disks, (b) simplified ray tracing to describe disk movement, (c) lack of a description of cross-polarization effects, (d) simplified aperture blockage model, (e) poor match of feed horn patterns, and (f) errors in measuring the paraboloid surface.

It is not clear at this time which of these effects dominate.

A more accurate model is under development along with diffraction measurements of the individual disks.

An interesting experiment was performed using three disks on the surface of the 4-foot diameter paraboloid. It was assumed that the three degrees of freedom afforded by this combination would allow positioning of two nulls simultaneously. In order to do this, two different S-band sources, separated by 6 degrees in the horizontal were located in the far field. The output of the antenna was filtered so that each signal could be monitored simultaneously. The antenna was positioned so that a sensible amount of power was received at each frequency. At that point, the sources were located at +28 and +34 degrees. Three aluminum disks, 3, 5, and 9 inches in diameter were located 4, 8, and 16 inches from the center of the paraboloid.

The three disks were adjusted, one at a time while the received energy at the two frequencies was monitored. A modest amount of cancellation at both frequencies was measured

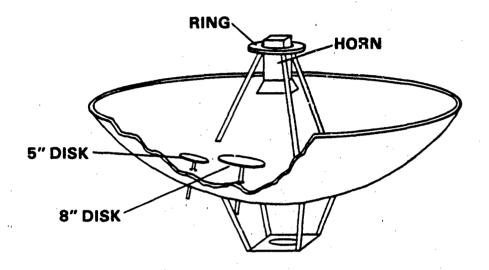
simultaneously. Figure 12a is a plot of the antenna pattern at 3.2 GHz before and after adjusting the disks for a total of 14 dB cancellation. Figure 12b is a plot at 3.4 GHz, which shows the 6 degree offset angle and a total cancellation of 10 dB. No theoretical model has been developed to describe the performance using three disks.

5. CONCLUSION:

Preliminary results have been given for a combined theoretical and experimental effort to modify the far field pattern of a horn fed paraboloid. Single and double nulls have been placed in the antenna power pattern by adjusting the position of small aluminum disks, mounted on the reflector surface. Cancellation up to 25 dB and acceptable distortion of the overall antenna pattern have been measured. The conclusion reached by this effort is that minor modification to a reflector surface can produce significant control in the far field pattern of a horn fed paraboloid.

6. ACKNOWLEDGEMENT:

The author is indekted to Mr. Mark Karan for skillful computer programming and Mr. James Kinney for invaluable assistance in the measurements.



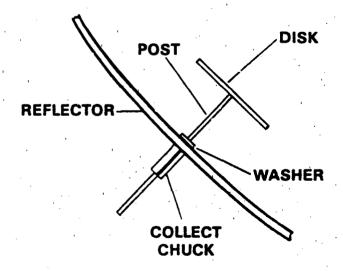


Figure 1

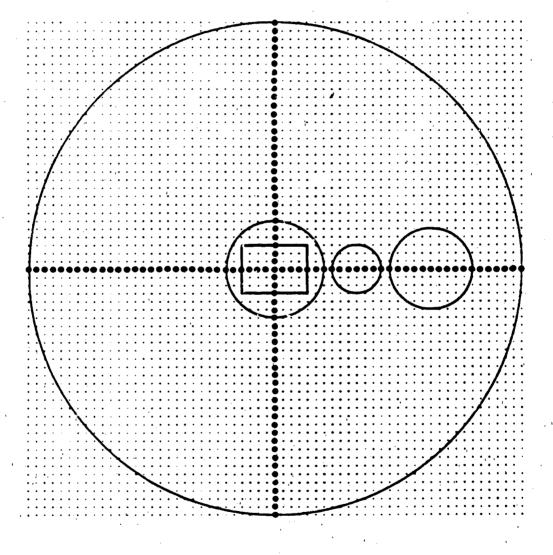
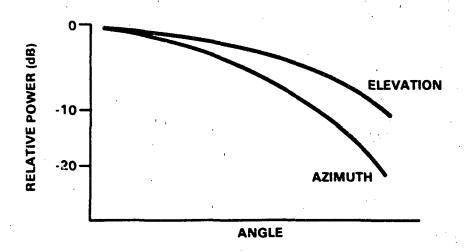


Figure 2



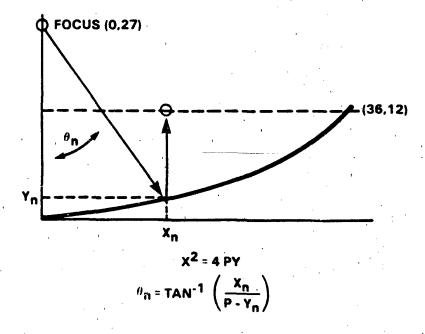
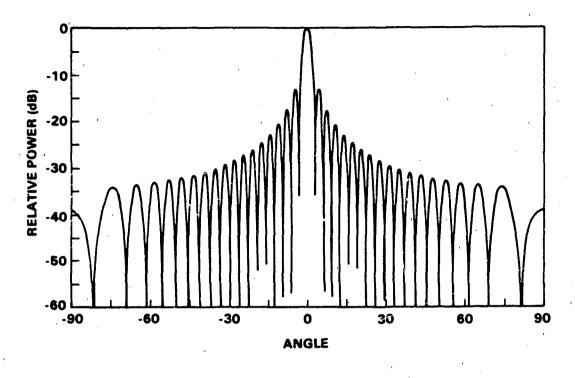


Figure 3



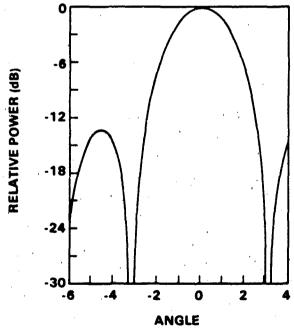
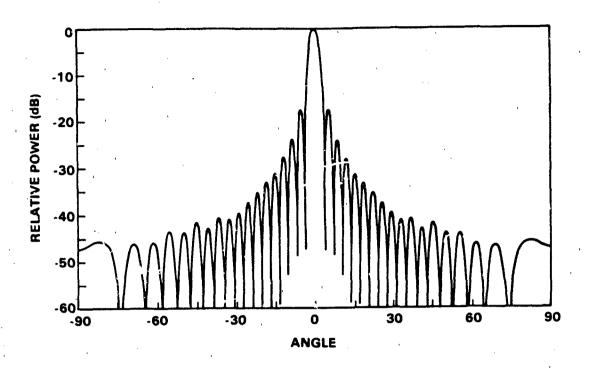


Figure 4



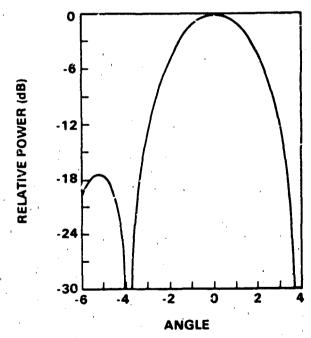
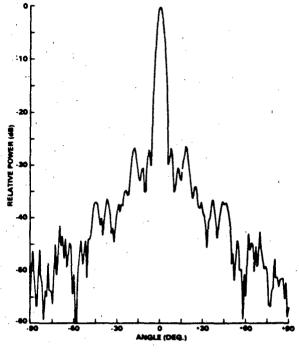
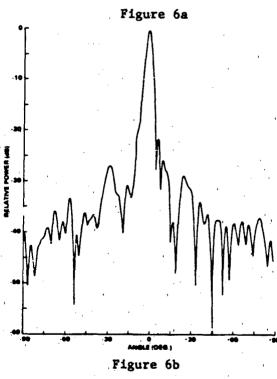


Figure 5





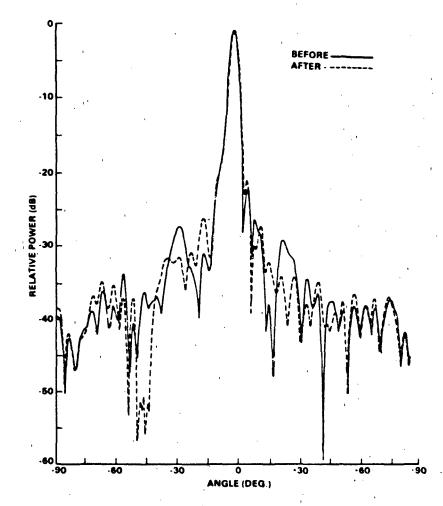


Figure 7

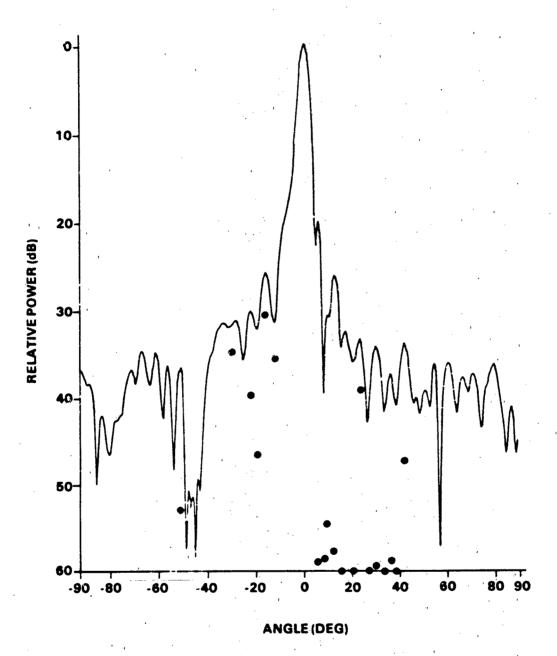
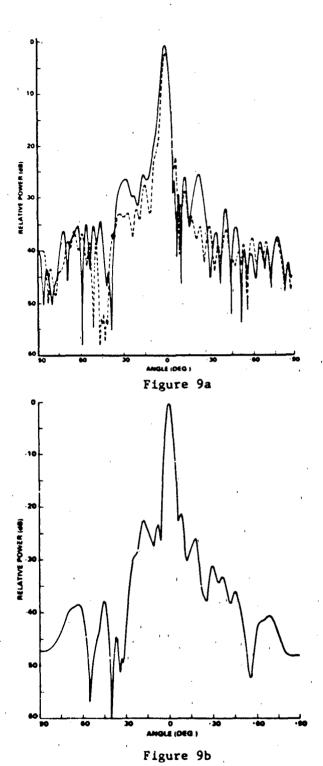


Figure 8

THE STATE OF THE S



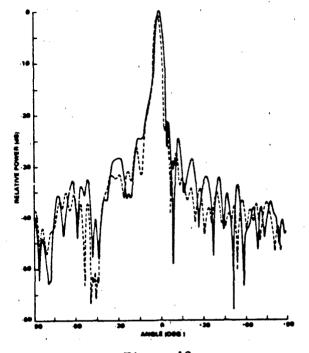


Figure 10a

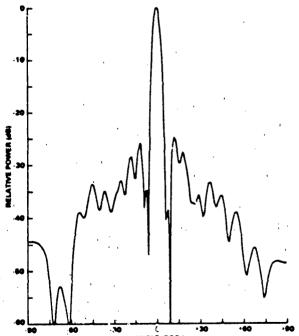


Figure 10b

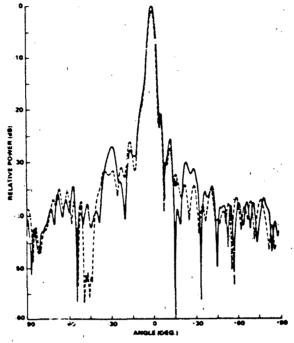


Figure lla

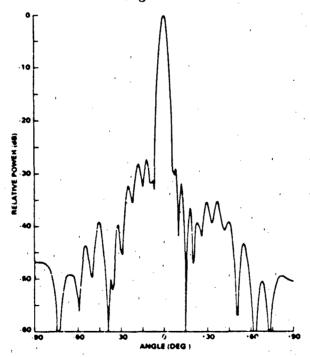
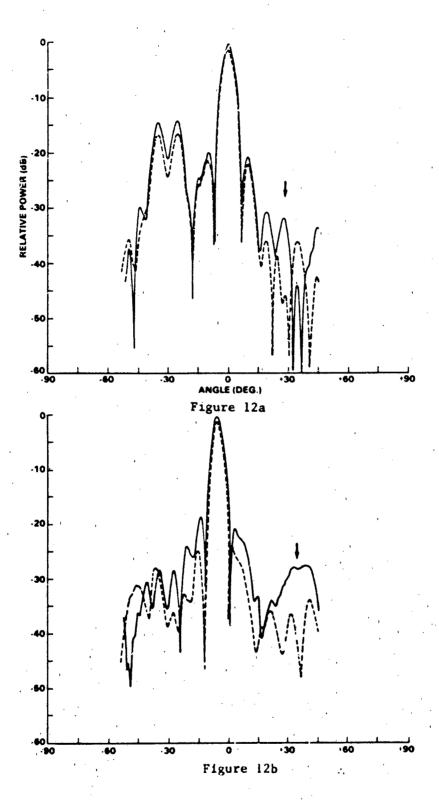


Figure 11b



NULL GENERATION BY PHASE PERTURBATIONS IN AN APERTURE

by
Michael D. Rudisill
and
Andrew J. Terzuoli

Air Force Institute of Technology Department of Electrical Engineering Wright-Patterson AFB OH 45433

NULL GENERATION BY PHASE PERTURBATIONS IN AN APERTURE

INTRODUCTION

This work was originated by Dr. Poirier and Daniel Jacavanco at RADC/EEC. Extrapolating from work on electrostatically controlled large reflector antennas (controlled in the sense of a perfect shape, i.e., parabolic, etc.) they theorized that by distortion of the reflector in the same manner adaptive nulling may be possible. Work by Havens (Havens, 1983) at AFIT showed this to be theoretically possible. However, the control problem of a perfect shape, let alone selective distortion, appears to be too burdensome for practical use.

In the summer of 1983 Jacavanco demonstrated it was possible to produce nulls in the pattern of a rigid reflector by mounting discs on the reflector dish and adjusting their distance off the diso. This method of null synthesis appears to offer a new flexibility to a highly efficient and widely used antenna system.

While the technique had been experimentally demonstrated, there was little or no theoretical basis for the mechanisms producing the nulls. Therefore, this study was undertaken at AFIT to attempt to develop theoretical background. Ideally this work will produce a means of predicting optimum configurations, bandwidths, etc.

APPROACH

Aperture integration was selected as the most straightforward method of analyzing the antenna system with discs
mounted on the dish. While it is well-known that this technique
is limited in effectiveness to the vicinity of the main beam,
it is in this area that null synthesis has been shown effective
and is of interest.

Equations for the electric field generated by an aperture as given by Stutzman and Thiele (Stutzman and Thiele, 1981) are,

$$E_{\theta} = j\beta \frac{e^{j\beta r}}{2\pi r} (P_{x} \cos \phi + P_{y} \sin \phi)$$
 (1)

$$E_{\phi} = j\beta \frac{e^{j\beta r}}{2\pi r} \cos\theta (P_{y} \cos\phi - P_{x} \sin\phi)$$
 (2)

where the P-values are given by integration of the aperture electric field (Stutzman and Thiele, 1981).

$$\bar{P} = \int_{0}^{2\pi} \int_{0}^{a} \bar{E}_{a} (\bar{r}') e^{j\beta r'} \sin\theta \cos(\phi - \phi') r' dr' d\phi'$$
 (3)

Since relative, not actual field strengths, are of interest, equations (1) and (2) are simplified.

$$E_{\odot} \sim (P_{x} \cos \phi + P_{y} \sin \phi)$$
 (4)

$$E_{\phi} \sim \cos\theta \ (P_{y} \cos\phi - P_{x} \sin\phi)$$
 (5)

To further simplify equations (4) and (5), the polarization is changed to a more convenient form—the fields that would be seen in the far-field by x— and y-oriented dipoles.

$$E_{x} = E_{\theta} \cos\theta \cos\phi - E_{\phi} \sin\phi$$
 (6)

$$E_{y} = E_{0} \cos\theta \sin\phi + E_{\phi} \cos\phi \tag{7}$$

By inserting equations (4) and (5) into equations (6) and (7) and squaring the electric field (to provide a power measure), we obtain:

$$|E_{i}|^{2} \sim \cos^{2}\theta \{(Re[P_{i}])^{2} + (Im[P_{i}])^{2}\} i = x,y$$
 (8)

The double integral in equation (3) presents a problem since the discs produce discontinuities in the phase of the aperture electric field. They prompt the use of numerical techniques to evaluate the integral. The method is taken from Abramowitz (Abramowitz and Stegun, 1972)

$$\iint f(x,y) dx dy = v \sum_{i=1}^{n} w_i f(x_i, y_i) + R$$
 (9)

where v is the area of the sections of the partitioned surface, the w_i 's are weighting functions given for a particular integration scheme, and R is the remainder term which will be approximated as zero. Again, since the v is a constant multiplier

on all terms and only relative numbers are of interest, it is dropped, yielding

$$\vec{P} \sim \sum_{i=1}^{n} w_i \vec{E}_a (r_i) e^{j\beta r_i \sin\Theta \cos(\phi - \phi_i)}$$
 (10)

To ease computer implementation, Euler's formula is used to break \overline{P} into real and imaginary parts.

$$Re[\bar{P}] \sim \sum_{i} w_{i} |\bar{E}_{a}(r_{i})| \cos(\beta r_{i} \sin\theta \cos(\phi - \phi_{i}) + \gamma_{i})$$
 (11)

Im[
$$\bar{P}$$
] ~ $\sum_{i} w_{i} | \bar{E}_{a}(r_{i}) | \sin(\beta r_{i} \sin \theta \cos(\phi - \phi_{i}) + \gamma_{i})$ (12) where

$$\bar{E}_{a}(r_{i}) = |\bar{E}_{a}(r_{i})| e^{j\gamma i}$$
(13)

Equations (11) and (12) are the basis for the integration scheme as implemented. Four variables of summation were used—the real and imaginary parts of P_X and the real and imaginary parts of P_Y —to sum over the aperture plane for a given Θ and Φ (far-field). These quantities, when used in equation (8), yield a quantity proportional to the magnitude of the electric field squared, which is normalized to the value obtained for $\Theta = \Phi = 0$, yielding a far-field power pattern point.

MODELING

The antenna modeled is a prime-focus parabolic reflector idealized with a point source at the focus producing a parabolically tapered aperture field. The feed is assumed to block a circular area (variable) in the middle of the aperture-essentially setting the electric field to zero. No direct radiation from the feed is considered.

The polarization of the aperture field assumes a linearly polarized feed with only the distortion induced by the reflector dish considered.

The disc's effect on the aperture field is modeled as a phase shift across a circular projection of the disc on the aperture field. No accounting is made for any amplitude variation in the field due to the different path lengths. The phase shifts for the aperture field are estimated two-dimensionally as shown in Figure 1 by computing the distance from F-D_i-A_i, and subtracting it from twice the focal distance of the dish.

Two approximations are made here worth mentioning. First, the ray tracing approach used does not take into account the actual geometrical optics path from the disc to the aperture plane. All rays reflected off the disc are assumed to travel on a path normal to the aperture plane—thus, the spreading from the disc is not accounted for.

Second, the disc model is two-dimensional and does not take into account the curvature of the disc in the third

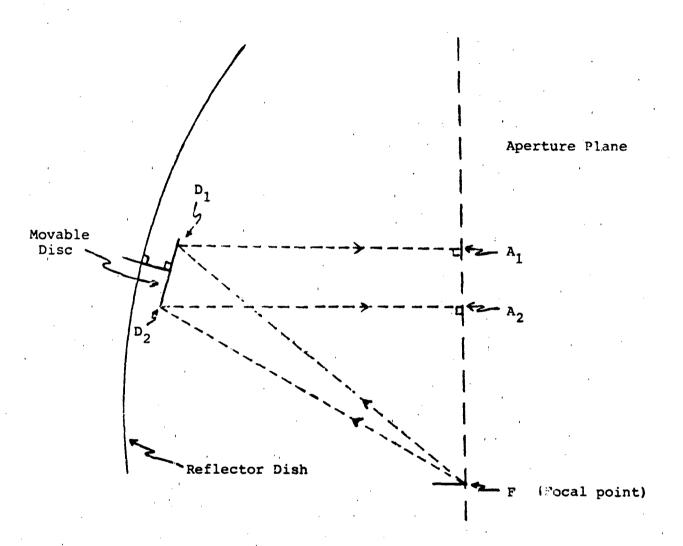


Figure 1--Disc Model

dimension. Thus, the phase shift has minor errors except on the radial line running through the center of the disc. In both cases it is assumed the errors introduced are minor for discs which are relatively small in relation to the dish.

RESULTS

This method of breaking down the aperture integral produces simplified equations that allow insight into the effects produced by the discs and methods to control these effects. Equation (8) shows that the copolarized pattern depends only on the P vector component of the same polarization. Thus, only two of the four variables summed over the aperture plane control the copolarized pattern strength. The two variables of interest are then

$$\left\{ \operatorname{Re}\left[P_{j}\right]\right\}_{i} = \left|E_{j}\left(r_{i}\right)\right| \cos\left(\beta r_{i} \sin\theta \cos\left(\phi - \phi_{i}\right) + \gamma_{i}\right) (14)$$

$$\{\operatorname{Im}[P_{j}]\}_{i} = |E_{j}(r_{i})| \sin(\beta r_{i} \sin\theta \cos(\phi - \phi_{i}) + \gamma_{i})$$
 (15)

where j is the copolarized unit vector and i references the points being summed. With no discs present let $\gamma_i = 0$ for all i and examine the magnitude of the P_i 's. The aperture electric field is assumed to be a function only of the radial position on the aperture plane. Letting radial position

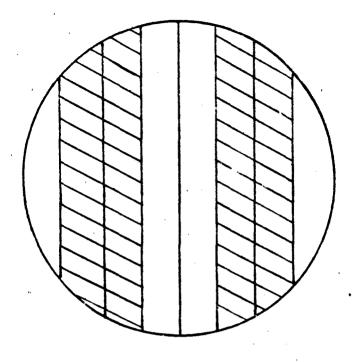
on the aperture plane (r_i) equal a variable k number of wavelengths and solving for the maxima, minima, and zeroes produces

$$k = \frac{n}{4 \sin \theta \cos (\phi - \phi_i)}$$
 $n=0,1,2,...$ (16)

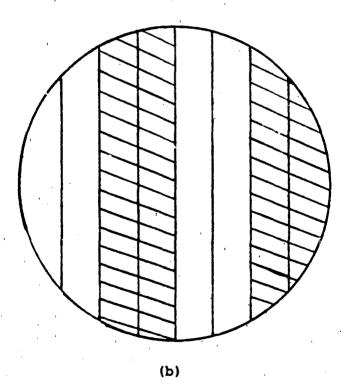
A plot of the lines of the maxima, minima and zeroes for the (a) cosine and (b) sine terms are shown for $\phi=0$ and $\theta=10^\circ$ in Figure 2. This shows that the imaginary part of the P_i's components are odd-symmetric about the center of the aperture p'ane. This results in the sum of the imaginary part of the P component equaling zero under all undisturbed conditions.

The real part of the P component therefore controls the pattern entirely in the undisturbed case. As ⁰ goes to zero, k goes to infinity essentially allowing the summing of the unmodulated electric field over the entire aperture plane. As ⁰ increases (from zero) the cosine term increasingly modulates the electric field until the positive and negative sections sum exactly to zero producing the first null. As ⁰ further increases, the negative sum of the P components now dominates and continues to increase until the maximum of the first sidelobe. (Figure 2 is approximately the maximum of the first sidelobe for aperture distribution shown.) The sum continues to oscillate alternating sign as ⁰ increases, producing the characteristic pattern. (Notice the cosine squared term in equation (8) has been neglected. However, its contribution is minimal in the ranges of interest [3 dB at 45°].)

では、中では、一つのは、一つのでは、一つのでは、一つのでは、一つのでは、一つのでは、一つのでは、一つのでは、一つのでは、一つのでは、一つのでは、一つのでは、一つのでは、一つのでは、一つのでは、一つのでは、



(a)



(Hatched areas are negative values)
Figure 2--Modulated P_i's

Using this simplified model the effects of the discs can be examined. The discs in the model produce a phase shift and it is easily seen how this may cause nulls. By locating the disc in a dominant zone (note the sidelobes are formed by alternately positive and negative sums of the P_i's) and adjusting it to produce one-half wavelength phase shift, the P_i's in the area affected by the disc will switch signs and, if the disc is exactly the right size, cause the sum of the real part of the P_i's to equal zero. Note, as an alternative to having an exact-sized disc, a larger disc with slightly less (or more) than exactly one-half wavelength phase shift will modulate the P_i's of the opposite sign still causing a zero sum.

The zeroing of the real part of the P_i's, however, creates another problem since the symmetry of the imaginary part of the P_i's has been destroyed—thus creating a non-zero sum. This explains why it requires two discs to produce a null in the pattern. In Jacavanco's original demonstration of this procedure he used two discs on the same side of center. However, this model seems to show optimum disc placement (in terms of using the smallest discs for minimal disturbance of the overall pattern) is symmetrically across the center of the dish. Using this placement the imaginary part of the P_i's regain their symmetry and thus once again sum to zero, producing a zero overall sum and a null in the pattern.

The above discussion overlooks one problem that is easily solved but requires mention. Even the simplified disc model

used in this model does not produce a constant phase shift over the area affected. (The same problem arises using oversized discs adjusted to less than one-half wavelength phase shift.) This lack of an exact one-half wavelength is not a major problem in the real part of the P_i sum. However, in the sum of the imaginary part of P_i's the lack of symmetry again prevents the nulling of the pattern. A solution is easily obtained by tweaking the position of the discs in opposite directions to zero out the imaginary part of the P_i's while maintaining a zero sum of the real part of the P_i's.

CONCLUSION

This model, while fairly simple, appears to explain the mechanism behind the nulling technique using discs. Many approximations have been made (ideal feed, discs' effects, etc.), and many items overlooked (feed supports, diffraction effects, etc.). For relatively large reflectors and small discs, these effects should be minimal.

It is not unexpected that the size of discs required to produce a null is related to the normal pattern power. However, that the placement of the discs has such a strong effect on required disc size (up to the point some positions are useless for nulling in some angular sectors while "optimum" for others) is rather surprising.

It should be noted also, however, that there is no optimum placement readily apparent for all angles. It is hoped,

with further study, to find usable placements and size to affect nulling over the entire pattern. If this can be done, and the theory shown experimentally correct, this would be a powerful technique in many applications.

BIBLIOGRAPHY

Abramowitz, Milton and Irene A. Stegun. <u>Handbook of Mathematical Functions</u> (Ninth Edition). New York: Dover Publications Inc., 1972.

Havens, Lt Douglas A. Pattern Nulling by Reflector Shaping. MS thesis, 83D-26. School of Engineering, Air Force Institute of Technology (AU), Wright-1 tterson AFB OH, December 1983.

Stutzman, Warren L. and Gary A. Thiele. Antenna Theory and Design. New York: John Wiley and Sons, Inc., 1981.

ANALYSIS OF THE CROSS-POLARIZATION PERFORMANCE OF ALTERNATIVE CSC-SQUARED DOUBLY CURVED REFLECTOR ANTENNA GEOMETRIES PRELIMINARY RESULTS

T. F. Carberry
The MITRE Corporation
Bedford, Massachusetts 01730

ABSTRACT

A study was initiated to analyze the cross-polarization properties of shaped beam doubly curved reflector types and to identify the design factors that control the cross-polarization level. These design factors were identified as: (1) the reflector surface geometry, (2) the feed position, and (3) the feed polarization properties. At present, significant results are only available on the first two factors.

The reflector surface geometries examined were threefold:
(1) the elevation angle strip geometry, (2) the horizontal strip geometry, and (3) the focal point strip geometry. Each strip geometry is formed by an intersecting plane and designed to collimate the rays in the transverse azimuth plane. There are different transforming actions of these reflector geometries on the feed illumination polarization characteristics. In general, vertical polarization produces poorer cross-polarization performance for each of these reflectors than does horizontal polarization. In particular, the focal point strip reflector produces a substantially worse performance than the other two reflector geometries.

The feed position of an offset shaped beam reflector is much more flexible than a paraboloid because the rays exit at wide angles and do not intercept the feed. This allows a much higher feed position that will yield significantly reduced cross-polarization.

The study, thus far, has not extensively examined feed types in detail; however, the study is continuing and will examine feed techniques that will result in lower cross-polarization.

1.0 <u>INTRODUCTION</u> — The cross-polarization component of an antenna is an important antenna performance parameter. Its importance is similar to the antenna sidelobe level. For example, the relative cross-polarization field component measures the vulnerability of the system to cross-polarized interfering signals. A relatively low cross-polarization level is necessary to prevent erroneous detections or jamming from cross-polarized signals.

Most of the literature on reflector antenna cross-polarization has been devoted to paraboloidal reflectors [1, 2]. Particular attention has been directed toward offset paraboloidal reflectors that eliminate feed blockage. However, offset paraboloidal geometries tend to significantly increase cross-polarization levels [3, 4, 5, 6].

Unfortunately, little data has been published on the crosspolarization performance of CSC-squared shaped-beam, doubly curved
reflector antennas. This is understandable since the use of paraboloidal reflectors is much more extensive than shaped-beam, doubly
curved reflectors, and the literature reflects this disparity.
Further, the shaped beam (vice the paraboloidal) reflector geometry
is much more complex and is designed to produce a principal polarization field distribution over a much wider angular sector in the
elevation plane. As a result, the reflector design also produces a
cross-polarization field distribution over the same angular sector.
However, the limited data available on this antenna's crosspolarization performance introduces substantial uncertainty concerning the vulnerability of the antenna to cross-polarized signals.

- 2.0 ANTENNA DESIGN FACTORS Both the principal and cross—polarization components of the far-field distribution of a CSC—squared, doubly curved reflector are basically a function of three antenna design factors: (1) the reflector surface geometry, (2) the feed position, and (3) the feed polarization characteristics.
- 2.1 <u>REFLECTOR SURFACE GEOMETRY</u> The design procedures of the shaped-beam, doubly curved reflector (figure 1) are well established. The reflector surface design is actually based on two reflector surface parameters: (1) the reflector central section, and (2) the reflector azimuth collimating strip. For design purposes, these two factors are assumed to independently determine the elevation plane pattern (in the x-z plane) and the azimuth plane

patterns (planes orthogonal to the x-z plane), respectively. The reflector radial dimension ρ , therefore, can be decomposed into two components (figure 1): (1) the central sector position vector $\rho_{\rm c}$, and (2) the strip position vector $\rho_{\rm c}$.

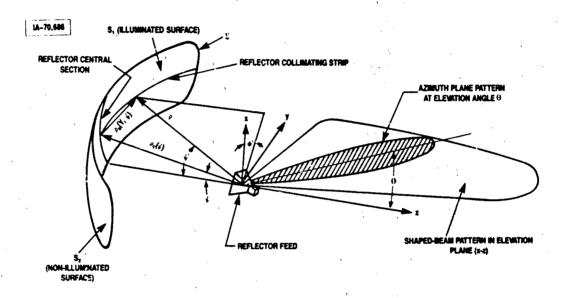


Figure 1. Basic Shaped-Beam, Doubly Curved Reflector Geometry and Far-Field Pattern Characteristics

The reflector central section is synthesized to properly shape the beam in the elevation plane by "spreading" the energy according to a CSC-squared power function. The central section design procedures are based on the principles of geometrical optics, conservation of energy, and differential geometry. These procedures are well described in the literature [7, 8]. Basically, the design procedures determine the central section radial dimension $\rho_{\rm C}$ as a function of the central section angle ψ . The central section radial dimension $\rho_{\rm C}$ can be expressed as

$$\rho_{c} = ix_{c} + kz_{c} \tag{1}$$

The x_c , z_c coordinates are simply (note $y_c = 0$):

$$x_{c} = \rho_{c} \sin \psi \tag{2a}$$

$$z_{c} = -\rho_{c} \cos \psi \tag{2b}$$

Using A. Brunner's [9] terminology, there are three possible types of reflector strip geometries defined by the collimating strip section used to focus the azimuth beam (figure 2); they are: (1) elevation angle strip geometry, (2) horizontal strip geometry, and (3) focal point strip geometry. The conventional technique is the elevation angle strip where the strip is formed by planes parallel to the direction of the elevation angle Q. This strip geometry is well described in the literature [7, 8, 11]. In this geometry, the strip forms a parabola in the intersecting plane defined by the elevation angle Θ (plane E_1). As noted by Brunner [9], this is not the only way to position the intersecting plane. For example, the intersecting plane could be horizontal (plane E_2) and generate a horizontal strip. The geometry of the strip is defined such that the rays reflected from the strip in the direction 9 will travel equal path lengths so that the wave in the direction 9 is a plane wave. Similarly, the intersecting plane could be also a plane through the focal point (plane E_2) generating a focal point strip. Both the horizontal strip geometry in plane E, and the focal point strip geometry in plane $\mathbf{E}_{\mathbf{q}}$ are ellipses. The advantage of the latter two geometries is that the reflector contour provides a more efficient surface area for typical feed illumination functions.

Since the three reflector geometries use the same central section geometry, the only difference is $\rho_{\rm S}$. Thus, the reflector strips' ${\bf x_S}$, ${\bf y_S}$, ${\bf z_S}$ coordinates are different for the three reflector strip geometries (see table 1). As shown, each set of coordinates is a function of y and ψ . The important design factor is the reflector depth factor $({\bf d}({\bf y},\psi))$ which varies with strip geometry.

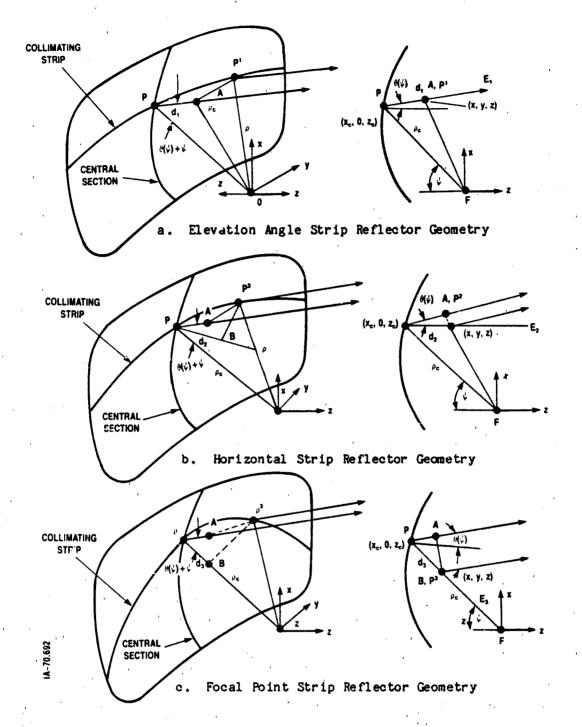


Figure 2. Three Shaped-Beam, Doubly Curved Reflector Geometries

2.2 <u>FEED POSITION</u> — The feed position of an offset paraboloid is restricted to avoid blocking the reflected rays emanating from the reflector. Blocking can increase both sidelobes and the crosspolarization level. This restricted geometry and the attendant

Table 1.

Xs. Ys. 2 Coordinate Expressions for Candidate Reflector Geometries

	HENLECTON DEPTH PARAMETER d(y,c)	$d(y,\psi) = \frac{y_s^2}{4_{\varphi_0}(\psi) \cos^2\left[-\frac{\beta}{2}\right]}$	$\begin{aligned} d(y,\psi) &= d_1(y,\psi) - d_2(y,\psi) \\ -d_1(y,\psi) &= \frac{\rho_1(\psi) \left[\cos\psi + \cos\theta(\psi)\right]}{\sin^2\theta(\psi)} \\ d_2(y,\psi) &= \frac{1}{\sin\theta(\psi)} \sqrt{\frac{\rho_2^{-2} \left[\cos\psi + \cos\theta\left(\psi\right)\right]^2}{\sin^2\theta(\psi_0)}} \end{aligned}$	$d(y, \psi) = d_1(y, \psi) - d_2(y, \psi)$ $d_1(y, \psi) = \rho_0(\psi) \frac{\{1 + \cos \beta\}}{\sin^2 \beta};$ $d_2(y, \psi) = \frac{1}{\sin \beta} \sqrt{\frac{\rho_0^2(\psi, \xi)\{1 + \cos \beta\}^2}{\sin^2 \beta} - \gamma_0^2}$
S	(? '4)*z	(/) soa (/) 'A)p	(A, v,)	+ d(y, ¢) sin _v
CARTESIAN COORDINATES	γ.	.	*	*
	(? 'A)*x	d(y . ¢) sin 6(¢)	•	- d(y, t) sin t
	REFLECTOR GEOMETRY TYPE	ELEVATION ANGLE STRIP	HORIZOMTAL STRIP	FOCAL POINT STRIP

MOTE: 3 = 4(2) + 1

geometric asymmetry also limits what cross-polarization level is achievable with an offset paraboloid (graph a in figure 3). However, the properly designed conventional "C-shaped" shaped-beam reflector forces those rays that could introduce blocking to exit the reflector at sufficiently wide angles (see graph b in figure 3) to avoid the blocking condition. As shown, this reflector type allows much greater flexibility in the position of the feed than is possible with an offset paraboloid. The feed position geometry that must be maintained to avoid blocking is illustrated in figure 4. Using ray theory and geometry, the condition to maintain no blocking based on ray theory is

の物質を含むできない。このでは、これののののない。これできなっているない。

$$\tan \theta = \frac{\Delta x - \rho_c \sin \psi}{\rho_c \cos \psi} \tag{3}$$

where $\triangle x$ is the distance between the passing ray and the feed along the x-axis. To avoid blocking $\triangle x>0$; thus

$$0 > -\psi \tag{4}$$

where θ = reflection angle (with respect with the z-axis) based on ray optics.

This condition cannot be achieved with a completely offset feed (e.g., the feed position corresponds to the same x-axis position as the bottom of the reflector). However, this condition can occur if the position of the feed moves up on the x axis.

2.3 <u>FEED POLARIZATION CHARACTERISTICS</u> — As noted by several authors [2, 4], the feed polarization characteristics have a dominant influence on the far-field cross-polarization characteristics of the reflector. In this initial effort, a simple ray theory model expressed in terms of the three orthogonal Cartesian coordinates is used to describe the feed polarization characteristics (see paragraph 3.3).

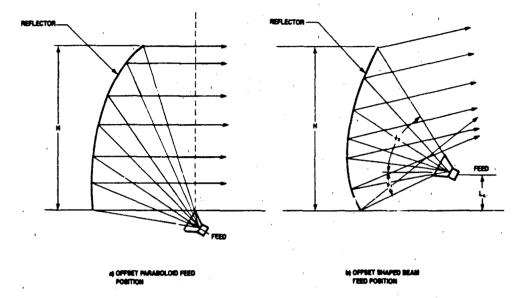


Figure 3. Feed Position Versus Reflector Type (No Blocking Condition)

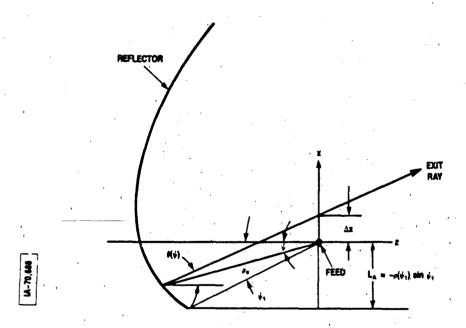


Figure 4. Feed Position Required to Avoid Feed Blocking for a Shaped-Beam Reflector

- 3.0 <u>REFLECTOR ANALYSIS PROCEDURE</u> This section describes an analysis procedure to calculate the radiation pattern performance from the shaped-beam, doubly curved reflector. There are a variety of methods that can be used to calculate the radiation pattern (e.g., the aperture plane method). Although it does not account for edge diffraction effects, the current distribution method using the physical optics approximation is a well-established procedure that yields accurate results near the main beam of the reflector antenna [16]. This procedure also accounts for cross-polarization due to axial (z-directed) current flows that are not accounted for in the aperture plane method. However, to accurately calculate the scattered field, the incident field as well as the reflector surface must also be adequately characterized.
- 3.1 <u>CALCULATING THE FAR-FIELD PATTERN</u> The radiation properties of an antenna can be expressed in terms of a field vector. A more convenient form, however, is to express the radiation pattern as a scalar function that is the dot product of a transverse unit vector and the field vector radiated from the antenna at that observation point (figure 5). Mathematically, the radiation field pattern (E) is expressed (using Silver's [8] notation):

$$\mathbf{E} = \mathbf{B} \, \widehat{\mathbf{1}}_{\alpha} \cdot \widehat{\mathbf{I}} \tag{5}$$

where

B = constant of proportionality

 \hat{i}_{α} = far-field transverse unit vector at observation point 0 (α refers to the defined angle associated with the observation point)

 \vec{I} = field vector at observation point 0

The field vector $(\vec{1})$ at the observation point can be expressed as a surface integral of the field contributions of the current distribution over the entire reflector surface.

$$\vec{I} = \iint_{S} [\vec{J}_{s} - \vec{J}_{s1} \cdot \hat{R}] \exp [+jk \vec{\rho} \cdot \hat{R}] dS \qquad (6)$$

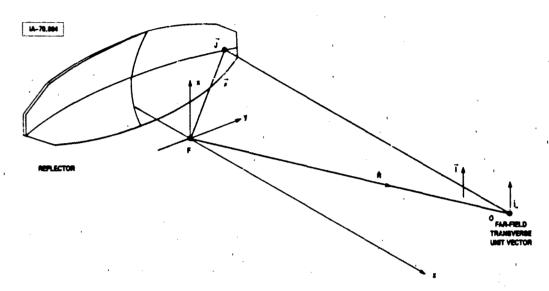


Figure 5. Generalized Far-Field Coordinate System and Field Vector Geometry

where

 \vec{J}_{s1} = current density vector distribution on reflector surface

 $j = \sqrt{-1}$

 $k = 2\pi/\lambda$

 $\lambda = wavelength$

 \hat{R} = far-field observation position unit vector

dS = reflector surface differential area

3.2 THE CURRENT DENSITY VECTOR — The current density vector can be accurately calculated by the physical optics approximation. The physical optics approximation is a method that calculates the induced currents on a metallic conducting surface forming a

reflector antenna from which the far-field radiation pattern can then be computed. The reflecting surface (see figure 1) is usually divided into two regions, S_1 and S_2 . Region S_1 is the region illuminated by an incident wave of known characteristics (e.g., amplitude, phase, and polarization). Region S_2 is defined as the shadow or nonilluminated region (assuming ray theory governs the properties of the illumination function). As shown in figure 1, S_2 is the rear or back of the reflector. The closed curve Σ separates S_1 from S_2 . The physical optics approximation for the induced current on the reflector surface S is:

$$\vec{J}_{S1} = 2 (\hat{n}_1 \times \vec{H}_{inc}) \text{ on } S_1$$
 (7a)

and -

$$\vec{J}_{s2} = 0 \text{ on } S_2 \tag{7b}$$

where

 \hat{n}_1 = unit normal vector on reflector surface S_1

 \vec{H}_{inc} = incident magnetic field vector

Thus, to proceed, it is necessary is to describe the incident field \vec{H}_{inc} and the reflector surface parameters (S₁, \sum , \hat{n}_1 and dS).

The physical optics theory employed in this analysis for a reflector antenna assumes the following conditions: (1) the reflector surface is relatively large in terms of wavelengths, (2) the reflector surface is a perfect smooth conductor with a radius of curvature exceeding 1 or 2 wavelengths, (3) one portion of the reflector does not shadow another, (4) interactions between reflector and source currents are negligible, (5) the currents at the shadow boundary are continuous, and (6) mutual coupling of surface currents is neglected. It should be noted that the physical optics approximation does not account for edge diffraction effects, blockage effects, feed spillover radiation, and actual currents on S2. Therefore, the procedure may be inaccurate for calculations substantially off the main

beam. Other techniques such as the geometrical theory of diffraction must then be used. However, for this application, the accuracy of the physical optics method is considered more than adequate.

3.3 <u>FEED POLARIZATION MODEL</u> — The feed polarization model is based on a geometrical optics theory model to calculate the current distribution on the reflector using the physical optics approximation.

The normalized incident magnetic field can be expressed as the following vector expression:

$$\vec{H}_{inc} = \frac{C G_f (\psi', \phi')^{1/2}}{\rho} [\hat{\rho} \times \hat{e}] \exp [-jk\rho]$$

$$C = 2 (\mu_0/\epsilon_0)^{1/4} (P_+/4\pi)^{1/2}$$
(8)

where

 P_{+} = total radiated power of the primary feed

 $G_f(\psi, \phi')^{1/2}$ = reflector feed illumination amplitude function (ψ, ϕ' are the primary feed field coordinates)

 ρ = radial dimension between feed phase center and reflector surface position (y, ψ)

and

This expression takes advantage of the fact that the incident magnetic field is orthogonal to the illumination electric field vector. The polarization of the geometric optics field is constant along a ray. The incident field polarization at the reflector surface can be calculated by specifying the characteristics of the incident wavefront and the polarization of the reflector feed.

Normally, the incident wavefront is assumed to be spherical so that

it is possible to express the polarization unit vector simply as [11, 12, 13, 14]:

$$\hat{\mathbf{e}} = \frac{\hat{\boldsymbol{\rho}} \times [\hat{\mathbf{e}}_{\mathbf{f}} \times \hat{\boldsymbol{\rho}}]}{|\hat{\boldsymbol{\rho}} \times [\hat{\mathbf{e}}_{\mathbf{f}} \times \hat{\boldsymbol{\rho}}]|}$$
(9)

This expression was derived by taking advantage of the fact that the polarization unit vector is orthogonal to the reflector position unit vector $\hat{\rho}$ and assumes that the feed polarization unit vector $\hat{\mathbf{e}}_{\mathbf{f}}$ is coplanar with the polarization unit vector. The feed polarization unit vector is normally expressed in terms of orthogonal linear polarization vectors as shown below

Combining each separately with equation (9), the polarization unit vector for each linear component can be determined.

In $\hat{e}_f = i$ (an x-directed or vertically polarized feed), then

$$\hat{e}_{v} = \frac{i(y^{2}+z^{2}) - jxy - kxz}{\rho \sqrt{y^{2} + z^{2}}}$$
(11)

If $\hat{e}_f = j$ (a y-directed or horizontally polarized feed), then

$$\hat{e}_{h} = \frac{-ixy + j(x^{2}+z^{2}) - kyz}{\rho \sqrt{x^{2} + z^{2}}}$$
 (12)

If $\hat{e}_f = k$ (a z-directed or longitudinally polarized feed), then

$$\hat{e}_{L} = \frac{-ixz - jyz + k(x^{2} + y^{2})}{\rho \sqrt{x^{2} + y^{2}}}$$
(13)

These feed unit vectors can be further combined to represent more complex feeds by proper weighting according to amplitude and phase (assuming the phase centers are the same). One simple geometry is the inclined feed (see figure 6) with the feed polarization vector $\hat{\mathbf{e}}_{\mathbf{f}}$ tilted in the x-z plane by the angle ψ_3 , along the x axis. The inclined feed polarization can be expressed for these conditions as:

$$\hat{e}_f = i \cos \psi_3 + k \sin \psi_3 \tag{14}$$

where ψ_3 represents the feed tilt angle with respect to the x-axis. As shown, an inclined polarization (x'-directed) feed introduces a longitudinal component along the z-axis. The polarization unit vector for an inclined feed with the polarization vector in the x-z plane is

$$\hat{e} = \frac{1}{\rho} \left\{ \frac{i(y^2 + z^2) - jxy - kyz}{\sqrt{y^2 + z^2}} \cos \psi_3 + \frac{-ixz - jyz + k(x^2 + y^2)}{\sqrt{x^2 + y^2}} \sin \psi_3 \right\} (15)$$

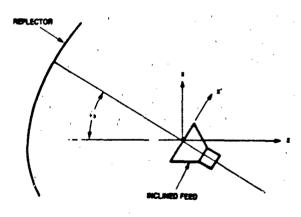


Figure 6. Inclined Feed Geometry

3.4 THE SURFACE NORMAL UNIT VECTOR/DIFFERENTIAL AREA — The remaining problem is to describe the reflector surface in terms of the normal unit vector $\hat{\mathbf{n}}$ and describing a differential area dS. To accomplish this, it is necessary to express the differential reflector position vector $d\vec{\rho}$ in terms of the independent but nonorthogonal coordinates y and ψ [11]. The differential equation relating $d\vec{\rho}$ to y and ψ is:

$$d\vec{\rho} = \frac{\partial \vec{P}}{\partial \psi} \quad d\psi + \frac{\partial \vec{P}}{\partial y} \quad dy$$
(16)

Letting
$$\vec{\tau}_{\psi} = \frac{\partial \vec{P}}{\partial \psi}$$
(17a)

and
$$\vec{\tau}_{y} = \frac{\partial \vec{P}}{\partial y}$$
(17b)
$$\vec{S}_{\psi} = \vec{\tau}_{\psi} \, d\psi$$
(18a)

and
$$\vec{S}_{y} = \vec{\tau}_{y} \, dy$$
(18b)

Then
$$d\vec{P} = \vec{\tau}_{\psi} \, d\psi + \vec{\tau}_{y} \, dy$$
(19)
$$= \vec{S}_{\psi} + \vec{S}_{y}$$

where \vec{S}_{ψ} and \vec{S}_{y} are the sides of the differential area dS which is an infinitesimal parallelogram, and $\vec{\tau}_{\psi}$ and $\vec{\tau}_{y}$ are designated as the surface tangential vectors. It is now a simple task to express the normal unit vector \hat{n} as:

$$\hat{\mathbf{n}} = \frac{\vec{\tau}_{\mathbf{y}} \times \vec{\tau}_{\mathbf{y}}}{|\vec{\tau}_{\mathbf{y}} \times \vec{\tau}_{\mathbf{y}}|} \tag{20}$$

The differential area dS can be expressed as

$$ds = |\vec{S}_{y} \times \vec{S}_{\psi}| = |\vec{\tau}_{y} \times \vec{\tau}_{\psi}| d\psi dy \qquad (21)$$

To derive the expressions for the reflector surface normal unit vector $\widehat{\mathbf{n}}$ and differential area dS, it is necessary to perform the vector operations in terms of an orthogonal coordinate system such as the Cartesian. This is quite simple since equations have already been derived that relate the Cartesian coordinate system to the \mathbf{y}, ψ curvilinear system; thus,

$$\vec{\tau}_{\psi} = \frac{\partial \rho}{\partial \psi} = \frac{1}{2} \frac{\partial x}{\partial \psi} + k \frac{\partial z}{\partial \psi} ; \qquad (22)$$

and
$$\vec{\tau}_y = \frac{\partial \rho}{\partial y} = i \frac{\partial x}{\partial y} + j + k \frac{\partial z}{\partial y}$$
 (23)

Thus
$$\hat{n} = \frac{i F_x + j F_y + k F_z}{\sqrt{F_x^2 + F_y^2 + F_z^2}}$$
 (24)

and
$$dS = \sqrt{F_x^2 + F_y^2 + F_z^2} d\psi dy$$
 (25)

where
$$F_{x} = \frac{\partial z}{\partial \psi}$$
; (26a)

$$\mathbf{F}_{\mathbf{y}} = \left(\frac{\partial \mathbf{x}}{\partial \psi}\right) \left(\frac{\partial \mathbf{z}}{\partial \mathbf{y}}\right) - \left(\frac{\partial \mathbf{x}}{\partial \mathbf{y}}\right) \left(\frac{\partial \mathbf{z}}{\partial \psi}\right) ; \tag{26b}$$

and
$$F_z = -\frac{\partial x}{\partial \psi}$$
 (26c)

but
$$\frac{\partial x}{\partial \psi} = \frac{\partial^{2} c}{\partial \psi} + \frac{\partial^{2} s}{\partial \psi}$$
; (27a)

$$\frac{\partial z}{\partial \psi} = \frac{\partial^2 c}{\partial \psi} + \frac{\partial^2 s}{\partial \psi} \quad ; \tag{27b}$$

$$\frac{\partial \mathbf{x}}{\partial \mathbf{v}} = \frac{\partial^{\mathbf{x}} \mathbf{s}}{\partial \mathbf{v}} \quad ; \tag{27c}$$

$$\frac{\partial y}{\partial y} = 1 \quad ; \tag{27d}$$

and
$$\frac{\partial z}{\partial y} = \frac{\partial^2 s}{\partial y}$$
 (27e)

The central section derivatives are listed in table 2. The central section partial derivatives are common to all three reflector geometries. The only change in the surface partial derivative is strip section partial derivatives. Table 3 presents the strip section partial derivatives.

3.5 THE FAR-FIELD PATTERN INTEGRAL -- Thus, equation (1) can now be reexpressed as a double integration or

$$E(\boldsymbol{\theta}, \boldsymbol{\phi}) = B \int_{-\frac{L_1}{2}}^{\frac{L_1}{2}} \psi_2(y) \\ - \frac{L_1}{2} \psi_1(y)$$
 (28)

 $J_{s1}(y, \psi)$ = current amplitude distribution on the reflector surface

W(Θ , ϕ ,y, ψ) = vector form factor

and $K(\Theta, \phi, y, \psi) = \text{phase factor}$

where $\psi_1(y)$ and $\psi_2(y)$ are the limits of integration of ψ along the reflector boundary \sum and L_1 is the maximum horizontal dimension of the reflector along the y axis.

Table 2
Reflector Central Section Derivatives

IA~70,687

$$\frac{\partial x}{\partial x} = 0$$

$$\frac{\partial z_c}{\partial y} = 0$$

$$\frac{\partial x_c}{\partial \psi} = \rho_c \cos \psi \left[1 + \tan \psi \tan \left(\frac{a}{2} \right) \right]$$

$$\frac{\partial z_c}{\partial \psi} = \rho_c \cos \psi \left[\tan \psi - \tan \left(\frac{t}{2} \right) \right]$$

3.5.1 <u>Far-Field Coordinate System</u>. The far-field coordinate system is also expressed in terms of the Cartesian system to perform the vector operations. The principal constraint on the observation

Table 3
Surface Derivative Expression for the Candidate Reflector Geometries

ASPLECTOR TYPE SUPPACE DEPARTIVE	BLEWITON ANGLE STRIP	MOREZONTAL STRIP	POCAL POINT STRIP
91 4. (y. +)	5 V (4) con ₃ (9 ₂ 5)	•	•
<u> </u>		- y aim² 0 (s) d _a (y, s)	-y um² 3 44 (y, 4)
94.	er" (1) com, (14,2) Jr. [Sp. (1)] res (14,2)	$\frac{\rho_{+}(\phi)}{\sin^{2}\theta(\phi)} \left\{ \left[\cos \phi + \cos \theta(\phi) \right] \sin \theta/2 - \left[\sin \phi + \sin \theta(\phi) \frac{\partial \theta(\phi)}{\partial \phi} \right] \right.$ $\left 2 \left[\cos \phi + \cos \theta(\phi) \frac{\partial \theta(\phi)}{\partial \phi} \right] \sin \theta(\phi) \right\}$	$\frac{A_1}{\sin^2 \beta} \left\{ (1 - \sin \beta) \left(1 + \frac{\partial B(\beta)}{\partial \beta} + \left(1 - \cos \beta \right) + \frac{\partial B(\beta)}{\partial \beta} \right) \right\}$ $\left\{ \tan \beta / 2 + 2 \sin \beta \cos \beta \left(1 + \frac{\partial B(\beta)}{\partial \beta} \right) \right\}$
<u>३५ ८</u> . श	•	d, (r, 4) ann θ (4) $\left[d, (r, 4) \frac{\partial}{\partial t} \theta + \frac{\partial}{\partial t} (r, 4) \frac{\partial}{\partial t} \theta + \frac{\partial}{\partial t} (r, 4) + \frac{\partial}{\partial t$	$ \frac{1}{\left\{d_{i}\left(y_{i},\delta\right) \sin \delta\right\}} \left\{d_{i}\left(y_{i},\delta\right) \left[d_{i}\left(y_{i},\delta\right) \cos \delta\right] + \left(1 + \frac{\partial \delta}{\partial \delta}\right) + \sin \delta \left[\frac{\partial d_{i}\left(y_{i},\delta\right)}{\partial \delta}\right] - d_{i}^{-1}\left(y_{i},\delta\right) \cos \delta \left[\left(1 + \frac{\partial d_{i}^{+}i}{\partial \delta}\right)\right] $
9x (r. 4)	+ apu 8 (4) (jul 63. 4)	•	- aim é ∂⊄(y, ψ)
91 914.19		,	
<u> </u>	- martet date. 43	∂4(t.4) ∂4	94 (v. c.)
<u>ð=(n. 6)</u>	4 (y. 4) (3 (4) 4) (4) 4	•	$\left\{ a_{i}(t) \left[1 + \tan t \tan dt \right] \right\}$ $- \left[\int d(t) dt + \tan t \frac{\partial d(t, t)}{\partial t} \right] \left\{ \cos t \right\}$
<u>94</u>	•	•	•
<u> 3247, 1)</u> 34	100 0 0 0 0 0 0 0 0 0 0 0 0 0 0 0 0 0 0	<u>ठेबस. स</u> ठे	$\left\{ \left[\begin{array}{cccc} \cos \varphi & - \cos \varphi \partial \varphi & \varphi & \varphi \\ - \left[d \left(y, \varphi \right) \log \varphi & - \frac{\partial d \left(y, \varphi \right)}{\partial \varphi} \right] \right\} & \cos \varphi \\ \end{array}$

point is that it remain on a spherical surface about the feed excitation point F so that |R| = constant. The far-field coordinate system was chosen to parallel the standard procedures used to measure the elevation and azimuth patterns of a shaped-beam, doubly curved reflector antenna. The elevation pattern is measured in the x-z plane (corresponding to $\phi = 0$ degrees) and azimuth planes are measured in planes perpendicular to the x-z plane at specified values of θ , as shown in figure 1. Clearly, the cross-polarization component should be defined with respect to these planes to facilitate comparison with measured data. The definition of cross-polarization is based on Ludwig's [15] third definition of cross-polarization which also parallels standard antennas range measurement practices.

Figure 7 illustrates and compares the conventional coordinate system and the modified system used in the calculations. The modified far-field coordinates can be expressed as [11]:

$$\hat{R} = i \cos \phi \sin \theta + j \sin \phi + k \cos \phi \cos \theta \qquad (29)$$

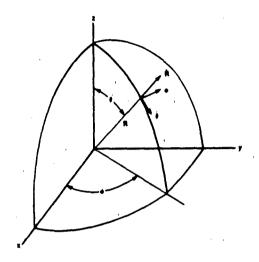
and
$$\hat{\mathbf{i}}_{\alpha} = \begin{cases} \hat{\mathbf{i}}_{\Phi} = \mathbf{i} \sin \phi \sin \theta + \mathbf{j} \cos \phi - \mathbf{k} \sin \phi \cos \theta & (30a) \\ \text{or} & \\ \hat{\mathbf{i}}_{\theta} = \mathbf{i} \cos \theta - \mathbf{k} \sin \theta & (30b) \end{cases}$$

3.5.2 <u>Vector Form Factor</u>. The vector form factor actually is a scalar quantity that includes all vector operations not included in the phase factor. The vector form factor includes the various vector parameters (the unit normal vector $\hat{\mathbf{n}}$, the illumination polarization unit vector $\hat{\mathbf{e}}$, and the far-field unit vector $\hat{\mathbf{i}}_{\alpha}$) that are incorporated in the integrand. Therefore, the vector form factor is:

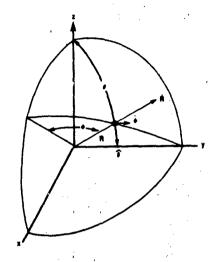
$$W(\boldsymbol{\theta}, \boldsymbol{\phi}, \mathbf{y}, \psi) = \hat{\mathbf{i}}_{\alpha}[\hat{\mathbf{n}} \times \hat{\boldsymbol{\rho}} \times \hat{\mathbf{e}}] | \vec{\tau}_{\mathbf{y}} \times \vec{\tau}_{\psi}|$$
 (31)

This equation must be separately defined for each feed model and far-field vector $\widehat{\mathbf{1}}_{\alpha}$.

IA-70,000



4 CONVENTIONAL SPHEREC/ COORDINATE SYSTEM



N) MODIFIED SPHERICAL COORDINATE SYSTEM (BASED ON STANDARD MEASUREMENT PROCEDURES)

Figure 7. Conventional and Modified Spherical Far-Field Coordinate Systems

The vector form factor can be expressed in six ways (Θ and Φ cut-patterns for three orthogonal feed polarizations): (1) Θ - vertical, (2) Θ - horizontal, (3) Φ - vertical, (4) Φ - horizontal, (5) Θ - longitudinal, and (6) Φ - longitudinal. Also, the vector form factor of a tilted feed is presented.

The 6 - vertical vector from factor is:

$$W_{\theta V} = -\frac{\left(yF_y + zF_z\right)\cos\theta + zF_x\sin\theta}{\sqrt{y^2 + z^2}}$$
 (32)

The 8 - horizontal vector form factor is:

$$W_{\theta h} = \frac{F_y}{\sqrt{y^2 + z^2}} \left[x \cos \theta - z \sin \theta \right]$$
 (33)

The ϕ - vertical vector form factor is:

$$W_{\phi V} = \{ [yF_y + zF_z] \sin \phi \sin \theta + F_x [y \cos \phi] - z \sin \phi \cos \theta] \} / \sqrt{y^2 + z^2}$$
(34)

and the ϕ - horizontal vector form factor is:

$$W_{\phi h} = -\{[x \sin \theta + z \cos \theta]\} F_y \sin \phi$$

$$+ [zF_z + xF_x] \cos \phi]\} / \sqrt{y^2 + z^2}$$
(35)

The 2 - longitudinal vector form factor is:

$$W_{\theta L} = \frac{xF_z \cos \theta + (xF_x + yF_y) \sin \theta}{\sqrt{x^2 + y^2}}$$
(36)

The ϕ -longitudinal vector form factor is:

$$W_{oL} = \frac{yF_z \cos \phi - xF_z \sin \phi \sin \theta + (xF_x + yF_y) \sin \phi \cos \theta}{\sqrt{\frac{2}{x} + y}}$$
(37)

The vector form factor of a feed tilted in the x-z plane by the angle ψ_3 with respect to z-axis is basically the weighted combination of the vertical vector form factor and the longitudinal vector form factor. Thus, the Θ -longitudinal vector form factor is:

$$W_{\theta incL} = W_{\theta V} \cos \psi_3 + W_{\theta L} \sin \psi_3 \tag{38}$$

and the ϕ -longitudinal vector form factor is:

$$W_{\phi incL} = W_{\phi v} \cos \psi_3 + W_{\phi L} \sin \psi_3$$
 (39)

3.5.3 Phase Factor Term. Since the far-field coordinate system has been defined, the phase factor term $K(\Theta, \phi, y, \psi)$ can now be expressed as:

$$K(\theta, \phi, y, \psi) = \exp \{-jk[\rho - x \cos \phi \sin \theta - y \sin \phi - z \cos \phi \cos \theta]\}$$
(40)

- 4.0 <u>COMPUTER RESULTS</u> The previous equations were programmed in BASIC on an HP-9826 computer. Several test cases (described below) were run.
- 4.1 ASSUMED ANTENNA PARAMETERS The reflector feed is assumed to be a rectangular horn with a pattern based on a rectangular aperture. Table 4 presents the assumed feed radiation characteristics for the y-polarized (horizontally polarized) feed and the x*-polarized (inclined or vertically polarized) feed. In all cases studied, the feed beam maximum was pointed toward the mid-point of the angular sector subtended by the reflector.

The basic parameters held constant during the calculations are:

$$H = 12\lambda$$
 reflector height $W = 24\lambda$ and width $(W = L_1)$ $\psi_2 - \psi_1 = 64^\circ$ (angular sector subtended by reflector in x-z plane)

Elevati in pattern - CSC² & from 4° to 40° (defines central section)

 $A_{\rm H}$ = 1.8 λ , $B_{\rm H}$ = 0.7 λ (horizontally polarized feed dimensions) $A_{\rm c}$ = 0.8 λ , $B_{\rm c}$ = 1.4 λ (vertically polarized feed dimensions)

Table 4
Assumed Reflector Feed Characteristics

[4-70,768]				
POLARIZATION UNIT YECTOR	ELECTRIC FIELD DISTRIBUTION	ASSUMED PATTERN FUNCTION		
ÿ .	$E_{o} \cos \frac{\pi x}{2A_{o}}$	$\frac{rE_{r}}{4} \left\{ \frac{\cos \left[\frac{2\tau A_{H}}{\lambda} \mu \right]}{1 - \left[\frac{4A_{H}}{\lambda} \mu \right]} \frac{\sin \left[\frac{2\tau B_{H}}{\lambda} r \right]}{\left[\frac{2\tau B_{H}}{\lambda} r \right]} \right\}$		
ř	E, coe	$\frac{\text{rE}_{\bullet}}{4} \left\{ \frac{\sin \left[\frac{2\tau A_{\bullet}}{\lambda} \mu \right]}{\left[\frac{2\tau A_{\bullet}}{\lambda} \mu \right]} \frac{\cos \left[\frac{2\tau B_{\bullet}}{\lambda} \gamma \right]}{1 - \left[\frac{4B_{\bullet}}{\lambda} \gamma \right]^{2}} \right\}$		

NOTE: $\mu = \sin \psi' \cos \phi$ $\phi = \sin \psi' \sin \phi'$ $\phi' = \tan^{-1} (x/y)$ $\psi' = -\cos^{-1} (x/y)$

4.2 THE CROSS-POLARIZATION PROBLEM — To illustrate, the principal and cross-polarization patterns were taken on an elevation angle strip reflector (H=12 λ and W=24 λ) excited with a vertically polarized feed completely offset (ψ_1 = 0°, ψ_2 = 64°, ψ_3 = 32°). The reflector central section was designed to shape the elevation patterns according to a CSC² function between 4° and 40°. Figure 8 presents the principal and cross-polarization patterns of this reflector. Graph a of figure 8 presents the elevation principal polarization pattern (ϕ = 0 degrees). Graph b of figure 8 presents azimuth cut principal polarization patterns at θ = 0°, 12°, 24°, and 36°. As expected, the beam width increases slightly and the first sidelobe relative amplitude tends to increase (with respect to the azimuth pattern beam peak) with elevation angle. Since the near-in

sidelobes are also a measure of vulnerability of the antenna to interfering signals, the peak sidelobe level is a useful measure to compare the cross-polarization level against. Clearly, to assure that the vulnerability of the antenna to cross-polarization interfering signals does not exceed that of principal polarized interfering signals, the cross-polarization level should not exceed the peak sidelobe level. As shown in graph a of figure 8, the relative cross-polarization patterns produce peak cross-polarization levels that may be substantially higher than the peak sidelobe.

4.3 <u>REFLECTOR/FEED POSITION GEOMETRIES</u> — Computer patterns were calculated for each reflector geometry discussed in section 2 with the feed position varied from completely offset ($L_a = 0$) to a position physically centered ($L_a = H/2$).

Figure 9 presents a comparison of the peak sidelobe and cross-polarization levels as a function of the elevation angle H and feed polarization (vertical and horizontal) for a feed in a completely offset position ($\psi_1 = 0^\circ$, $\psi_2 = 64^\circ$, and $\psi_3 = 32^\circ$). As shown, in most cases, the cross-polarization level exceeds the peak sidelobe level over most of the elevation sector of interest. In some cases the difference is in excess of 10 dB.

For a vertically polarized feed, the relative cross-polarization level increases with elevation angle. (This is the difference between the peak cross-polarization level and the elevation plane pattern gain at a specific elevation angle.) Also, a focal point strip reflector tends to produce significantly higher cross-polarization for a vertically polarized feed near the beam peak. Also, for a vertically polarized feed the relative cross-polarization level tends to be relatively constant over wide regions of the elevation sector. However, for all reflector types excited with a horizontally polarized feed, the peak sidelobe level increases in value as the elevation angle increases from $\theta = 0^{\circ}$ to the beam peak and then tends to decrease (or level off).

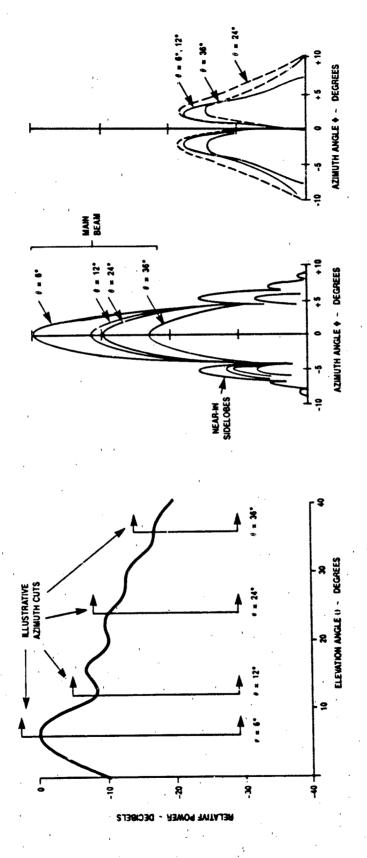


Figure 8. Illustrative Principal and Cross-Polarization Patterns from a Shaped-Beam Doubly Curved Reflector

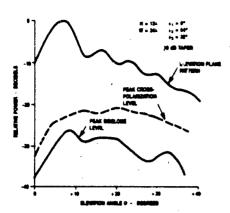
Azimuth Cut Gross-Polarization Patterns

. 0

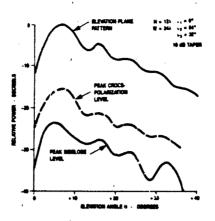
Azimuth Cut Principal Polarization Patterns

مُ

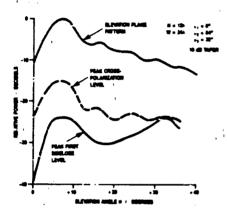
Elevation Principal Polarization Pattern



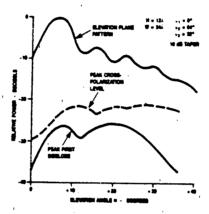
a. Elevation Strip Reflector, Vertically Polarized Feed



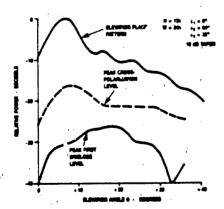
 Elevation Strip Reflector, Horizontally Polarized Feed



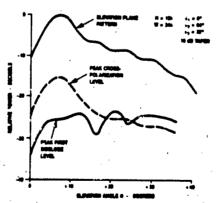
 d. Horizontal Strip Reflector, Vertically Polarized Feed



d. Horizontal Strip Reflector, Horizontally Polarized Feed



e. Focal Point Strip Reflector. Vertically Polarized Feed



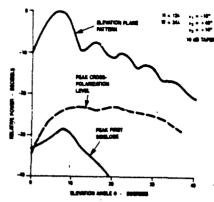
f. Focal Point Strip Reflector, Horizontally Polarized Feed

Figure 9. Comparison of the Cross-Polarization Characteristics for the Three Reflector Geometries for $\psi_1=0^\circ$, $\psi_2=64^\circ$, $\psi_3=32^\circ$ as a Function of Elevation Angles and Feed Polarization

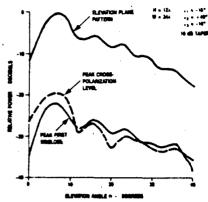
Figure 10 presents a similar comparison for the same reflector type but with the feed position moved up such that $\psi_{1}=-16^{\circ}$. $\psi_{2}=$ 48°, and $\psi_2 = +16^\circ$. The feed dimensions are the same as those used in figure 9. As shown, the cross-polarization characteristics are noticeably improved. For vertical polarization, the crosspolarization level over the elevation sector has similar shape characteristics but the relative level is reduced. (However, the peak sidelobe level also tends to be reduced.) For horizontal polarization, the effect is most significant since the cross-polarization level is often below the peak sidelobe level. Of interest are graphs d and f in figure 10, which illustrate that the peak sidelobes for both the horizontal strip and focal point strip reflectors tend to increase with elevation angle while the cross-polarization level continues to decrease. The elevation angle strip reflector, however, produces results where both the peak sidelobe and crosspolarization levels are comparable over a wide angular sector - a desirable condition.

Figure 11 presents a similar comparison for the three reflector types with the feed position moved further up such that $\psi_1=-32^\circ$, $\psi_2=+32^\circ$, $\psi_3=0^\circ$. Again, the feed dimensions are identical. As shown, for a vertically polarized feed (with the exception of the focal point strip reflector), the cross-polarization level continues to reduce. However, for the focal point strip reflector, the peak cross-polarization level increases substantially. For a horizon-tally polarized feed, the cross-polarization level decreases to values substantially below the peak sidelobe level.

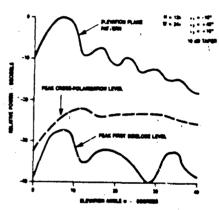
4.4 <u>FEED POLARIZATION CHARACTERISTICS</u> — For a paraboloid, it is well known that if the feed consists of a pair of cross electric and magnetic dipoles of equal strength, the induced currents combine to produce zero cross-polarization. While a shaped beam reflector is much more complex, it is believed that this technique of combining electric and magnetic radiating elements (but of unequal strengths)



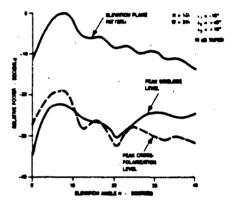
a. Elevation Strip Reflector, Vertically Polarized Feed



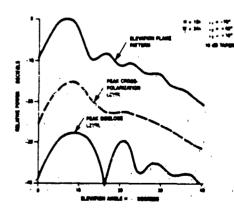
 Elevation Strip Reflector, Horizontally Polarized Feed



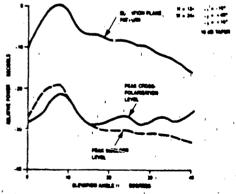
de la contraction de la contraction



d. Horizontal Strip Reflector, Horizontally Polarized Feed

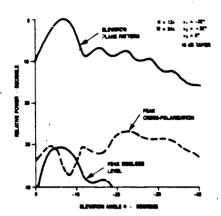


e. Focal Point Strip Reflector, Vertically Polarized Feed

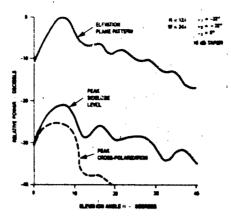


f. Focal Point Strip Reflector, Horizontally Polarized Feed

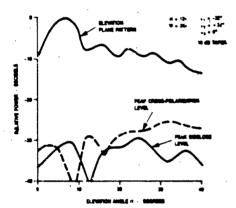
Figure 10. Comparison of the Cross-Polarization Characteristics for the Three Reflector Geometries for ψ_1 = 16°, ψ_2 = 48°, ψ_3 = 16° as a Function of Elevation Angles and Feed Polarization



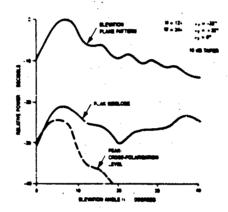
a. Elevation Strip Reflector, Vertically Polarized Feed



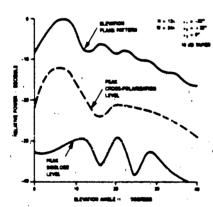
 Elevation Strip Reflector, Horizontally Polarized Feed



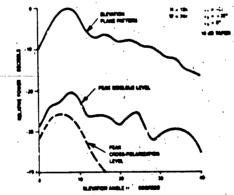
c. Horizontal Strip Reflector, Vertically Polarized Feed



d. Horizontal Strip Reflector. Horizontally Polarized Feed



e. Focal Point Strip Reflector, Vertically Polarized Feed



f. Focal Point Strip Reflector, Horizontally Polarized Feed

Figure 11. Comparison of the Cross-Polarization Characteristics for the Three Reflector Geometries for ψ_1 = 32°, ψ_2 = 32°, ψ_3 = 0° as a Function of Elevation Angles and Feed Polarization

can be adapted to the shaped-beam reflector. At present, an investigation is underway to explore this technique.

5.0 <u>SUMMARY AND CONCLUSIONS</u> — In this study, several design factors influencing the cross-polarization level were examined. For the reflector surface geometry, it was found that the cross-polarization performance for the three reflector geometries operating with vertical polarization was generally poorer than horizontal polarization for higher elevation angles. The focal point strip reflector tended to have significantly poorer cross-polarization performance for vertically polarized feeds. The more significant design factor appeared to be reflector feed position. As the feed position offset was reduced, the cross-polarization level was greatly reduced.

SPONSORSHIP -- Research reported in this paper was sponsored by the United States Air Force Electronic Systems Division, Hansoom Air Force Base, under contract number F19628-84-C-0001.

ACKNOWLEDGMENTS — The author would like to acknowledge the help and suggestions of D. Dettinger (D-17), K. Bernstein, D. Bleck, T. Stiling, and A. M. Sutcliffe (D-62), R. E. Clapp (D-86), J. C. Williamson (D-104) of MITRE, and C. Winter of Raytheon. Also, I would like to thank E. Lyon (D-62) for her substantial editorial help.

LIST OF REFERENCES

- 1. C. C. Cutler, "Parabolic Antenna Design for Microwave," Proceedings of the IRE, Vol. 35, Nov. 1947, pp. 1284-1294.
- 2. E. M. T. Jones, "Paraboloid Reflector and Hyperboloid Lens Antenna," IRE Transaction on Antennas and Propagation, Vol. AP-2, July 1954, pp. 119-127.
- 3. I. Koffman, "Feed Polarization for Parallel Currents in Reflectors Generated by Conic Sectors," IEEE Transactions on Antennas and Propagation, Vol. AP-14, June 1966, pp. 37-40.
- 4. T. S. Chu and R. H. Turrin, "Depolarization Properties of Offset Reflector Antennas," IEEE Trans. AP-21, no. 3, May 1973.
- 5. J. Dyk, C. T. W. van Diepenleek, E. J. Maanders, and L. F. G. Thurlings, "The Polarization Losses of Offset Paraboloid Antennas," IEEE Trans. AP-22, July 1974.
- 6. J. Jacobsen, "On the Cross-Polarization of Asymmetric Reflector Antennas for Satellite Applications," IEEE Trans. AP-25, March 1977.
- 7. A. Dunbar, "Calculation of Doubly Curved Reflectors for Shaped Beams," Proc. IRE, Vol. 36, Oct. 1948.
- 8. S. Silver, Microwave Antenna Theory and Design, McGraw-Hill Book Co., Inc., New York, 1949.
- 9. A. Brunner, "Possibilities of Dimensioning Doubly-Curved Reflector for Azimuth-Search Radar Antennas," IEEE Trans., Vol. AP-19, Jan. 1971.
- 10. V. Kerdemelidis, "A Study of Cross-Polarization Effects in Paraboloidal Antennas," California Institute of Technology, Antenna Laboratory Tech. Dept., No. 26, May 1966, AD 634153.
- 11. T. F. Carberry, "Analysis Theory for the Shaped-Beam Doubly Curved Reflector Antenna," IEEE Trans. AP-17, March 1969.
- 12. R. L. Pease, "Paraboloidal Reflector Patterns," M.I.T. Lincoln Lab. Tech. Report No. 184, August 5, 1958.
- 13. S. S. Sandler, "Paraboloidal Reflector Patterns for Off-Axis Feed," IRE Trans. Antennas and Propagation, Vol. AP-8, July 1960.
- 14. R. E. Collins and F. J. Zucker, Antenna Theory, Part 2, McGraw-Hill Book Co., Inc., New York, 1969, chap. 17, pp. 41-48.
- 15. A. C. Ludwig, "The Definition of Cross-Polarization," IEEE Trans. AP-21, Jan. 1973.
- 16. W. U. T. Rusch and P. D. Potter, "Analysis of Reflector Antennas!" Academic Press, 1970, New York.
- 17. A. W. Rudge, K. Milne, A. D. Olver, and P. Knight, "The Handbook of Antenna Design," Vol. I, Peter Peregrines Ltd., London, U.K., 1982.

PROBE CORRECTION FOR NEAR-FIELD ANTENNA MEASUREMENTS

Arthur D. Yaghjian
EM Techniques Branch
Electromagnetic Sciences Division
Rome Air Development Center
Hanscom AFB, MA 01731

ABSTRACT

To quote Kummer and Gillespie (Proc. IEEE, April, 1978), "The antenna measurements' problem is now of equal difficulty with that of design; now the antenna engineer often has to design the antenna as well as the method of measurement." In addition they state that "The near-field technique may well become accepted as the most accurate technique for the measurement of power gain and of patterns for antennas that can be accommodated by the measuring apparatus." However, in order to accurately determine the far fields of antennas from near-field measurements, one has to correct, in general, for the nonideal response of the measurement probe. In this paper we review planar, cylindrical, and spherical scanning; and show how probe correction can be introduced as a simple modification to near-field scanning with ideal dipole probes that measure the electric or magnetic field at a point. Data sampling spacing, efficient computational methods, and experimental errors involved with near-field measurements are also discussed.

OUTLINE OF PAPER

- 1. BRI'T HISTORY OF NEAR-FIELD SCANNING
 - 1.1 Early Experimental Period (No Probe Correction)
 - 1.2 First Probe-Corrected Theories
 - 1.3 Theory Put into Practice
 - 1.4 Technology Transfer
- 2. NEAR-FIELD THEORY
 - 2.1 Regions of the Near Field
 - 2.2 Scanning with Ideal Probes on Arbitrary Surfaces
 - 2.3 Scanning with Ideal Probes on Planar, Cylindrical, and Spherical Surfaces
 - 2.4 Probe Correction for Planar, Cylindrical, and Spherical Scanning
 - 2.5 Expressions for the Far Field
- 3. SAMPLING THEOREMS AND EFFICIENT METHODS OF COMPUTATION
 - 3.1 Sampling Theorems
 - 3.2 Efficient Methods of Computation
- 4. EXPERIMENTAL ERRORS
- 5. CONCLUSION

1. BRIEF HISTORY OF NEAR-FIELD SCANNING

The development of near-field scanning as a method for measuring antennas can be divided conveniently into four periods: the early experimental period with no probe correction (1950-1960), the period of the first probe-corrected theories (1961-1975), the period in which the first theories were put into practice (1965-1975), and the period of technology transfer (1975-1984) in which 35 or more near-field scanners were built throughout the world.

1.1 Early Experimental Period (No Probe Correction)

Probably the first near-field antenna scanner was the "automatic antenna wave-front plotter" built around 1950 by Ba ett and Barnes 1 of the Air Force Cambridge Research Center. Although they made no attempt to compute far-field patterns from their measured near-field data, Barrett and Barnes obtained full-size maps of the phase and amplitude variations in front of microwave antennas. Woonton measured the near rields of diffracting apertures and critically examined in his 1953 paper the assumption that the voltage induced in the probe is a measure of the electric field strength. Richmond and Tice³ in 1955 experimented with air and dielectric-filled, open-ended rectangular waveguide probes for measuring the near fields of microwave antennas, and compared calculated far fields with directly measured far fields. For an X-band cheese aerial, Kyle (1958) 4 compared the far-field pattern obtained directly on a far-field range with the far-field pattern computed from the near-field amplitude and phase as measured by an open-ended circular waveguide. In 1961 Clayton, Hollis, and Teegardin^{5,6} computed the principal far-field E-plane pattern for a 14-wavelength diameter reflector antenna from the amplitude and phase of the near-field distribution. They obtained good agreement with direct far-field measurements over the mainbeam and first few sidelobes.

1.2 First Probe-Corrected Theories

All of the experimental work of the early period assumed basically that the probe measured a rectangular component of the electric or magnetic vector in the near field. Some early theoretical work⁷⁻⁹ applied approximate correction factors in order to account for the finite size and near-field distance of the measurement probe. In 1961 Brown and $Jull^{10}$ gave a rigorous solution to the probe correction problem in two dimensions using cylindrical wave functions to expand the field of the test antenna but plane waves to characterize the probe. However, it wasn't until Kerns¹¹ reported his plane-wave analysis in 1963 that the first rigorous and complete solution to the probe correction problem in three dimensions became available. Kerns's NBS monograph 12, which provides a comprehensive treatment of the "Plane-Wave Scattering-Matrix Theory of Antennas and Antenna-Antenna Interactions", is the definitive work on the theory of planar near-field scanning.

Probe-compensated cylindrical near-field scanning was extended to three dimensions in 1973 by Leach and Paris 13 of the Georgia Institute of Technology (GIT). Characterizing the probe as well as the test antenna by cylindrical wave functions, they developed the theory, presented sampling criteria, and performed measurements on a slotted waveguide array to verify their tehenique. Later, Borgiotti 14 , using a plane-wave representation for the probe (as in the original paper of Brown and Jull 10), and Yaghjian 15 , using a uniform asymptotic expansion of the Hankel function, derived an approximate probe correction for cylindrical scanning that approaches the simplicity of the planar probe correction.

The probe-corrected transmission formula for near-field scanning in spherical coordinates was derived by Jensen 16 of the

Technical University of Denmark (TUD) in 1970. However, the transmission formula could not be "deconvolved" in practice to obtain the required spherical mode coefficients of the test antenna until Wacker's NBS report of 1975^{17} . In this report, he showed that the use of a circularly symmetric measurement probe allowed deconvolution through orthogonality of the spherical rotation functions with respect to (••). Wacker also proposed the use of a fast Fourier transform scheme to compute the problematic •• integrals. This scheme was later streamlined and made more efficient by Lewis and Larsen. An excellent account of probe-corrected spherical near-field antenna measurements at TUD may be found in Larsen's thesis.

Wood²¹ has developed an alternative spherical scanning technique using a Huygens probe that samples an assumed locally plane-wave field. Recently, Yaghjian²² has derived a simplified probe-corrected spherical transmission formula in terms of conventional vector spherical waves. This alternative transmission formula, which is free of rotational and translational addition functions, can be deconvolved by means of the familiar orthogonality of the vector spherical waves. Yaghjian also suggests a direct computation scheme for evaluating the pintegrations.

1.3 Theory Put into Practice

The first probe-corrected near-field measurements were conducted at the National Bureau of Standards²³ in 1965 using a lathe bed to scan on a plane in front of a 96 wavelength pyramidal horn radiating at a frequency of 47.7 GHz. For more than 10 years following, probe-corrected near-field scanning was confined to planar and cylindrical scanning at NBS²⁴⁻²⁶ and GIT,^{27,13,6} where near-field measurements began around 1970. During that period planar near-field scanning matured at these two laboratories to a fairly routine measurement procedure for directive antennas

operating at frequencies from less than 1 GHz to over 60 GHz. Sampling theorems were applied to determine data point spacing, automatic computer-controlled transport of the test antenna and probe was installed, lasers were used to accurately measure the position of the probe, and upper-bound theoretical as well as experimental and computer-simulated error analyses were performed. Table 1 lists some representative antennas that have been measured at NBS²⁸.

1.4 Technology Transfer

The development of near-field measurements seems to have anticipated the advent of specially designed antennas not well suited to measurement on conventional far-field ranges. During the first ten years of development, near-field antenna measurements were confined to the laboratories of NBS and GIT. The last ten years have seen a much wider interest that includes private industry, as the appeal, but more often the necessity of near-field techniques for measuring certain antennas has stimulated the construction of 35 or more near-field scanning facilities throughout the world. Figure 1 lists a few 3 these near-field facilities and their completion dates (second generation dates for NBS and GIT) along with a chart of their maximum dimension and frequency capability. 29 All the facilities listed in Figure 1 use the planar, cylindrical, or spherical scanning methods described above, except the Jet Propulsion Laboratory (JPL), 30 which takes planar near-field data on a polar grid rather than on the usual rectangular grid. Like cylindrical scanning, plane polar scanning requires the probe to move only on a single linear track. However, no convenient sampling theorem with uniform spacing, nor computer algorithm as efficient as the direct fast Fourier transform has been developed for the radial direction of plane-polar scanning. 31,32

It would be naive to think that the interest in and

proliferation of near-field measurement facilities has stemmed solely from an objective evaluation of the scientific merits of near-field techniques. The theory, measurements, and computer programming required to accurately characterize antennas by near-field scanning is considerably more extensive than for conventional far field measurements. Thus there has been a natural tendency to avoid near field techniques, often in spite of their advantages, whenever more familiar far-field techniques can be applied.

The recent interest in near-field measurements has been generated primarily by the development of modern, specially designed antennas that are not easily measured on conventional far field ranges. These antennas include electrically large antennas with Rayleigh distances too large for existing or available far-field ranges; physically large antennas which are difficult to rotate on conventional antenna mounts; array antennas with many elements that can be conveniently interrogated by near-field scanning; millimeter wave antennas that may experience high atmospheric noise and absorption, especially in inclement weather; antennas with complex far-field patterns for which extensive far-field amplitude (and possibly phase) data is required; delicate antennas that experience high stress and strain under certain rotations or changes in temperature and humidity. and that may require counter balancing and measurement in a controlled. environment; non-reciprocal antennas that must be measured in the transmitting mode and thus may produce excessive ground reflections on a far-field range; classified antennas that must be measured in a secure environment; HF aircraft antennas (3-30 MHz) whose image fields interfere with their free-space patterns being measured directly in the far field; and finally antennas with sidelobes too low to be accurately measured on conventional far field ranges. The possibility of measuring ultralow sidelooe

antennas using planar near-field measurements was discussed by $\operatorname{Grimm}^{33}$ at the Allerton Symposium of 1982.

2. NEAR-FIELD THEORY

A reasonable understanding of the theory of near-field measurements is a prerequisite to a successful near-field antenna measurements program. Although not everyone involved in near-field antenna measurements needs to be proficient in the theory, there should be at least one member of the team who gains a competent and versatile knowledge of the theoretical formulation on which the near-field measurements are based.

The references hereinbefore form a substantial bibliography from which planar, cylindrical, or spherical near-field theory can be studied. A few additional references may prove helpful. Kerns' "translation" 34 of the plane-wave scattering matrix theory of antennas to the measurement of acoustic transducers comprises a streamlined, pedagogical development of planar near-field scanning and extrapolation 35 techniques. The short papers by Kerns et al. in Electronics Letters 36,24 should also be consulted for a brief description of planar near-field analysis. The review paper 37 from GIT applies the Lorentz reciprocity theorem rather than a scattering-matrix approach to derive the probe-compensated planar transmission formula. Appel-Hansen³⁸ has recently given a useful review of the theory of probe-corrected planar, cylindrical, and spherical near-field measurements. He provides a unified vector spherical wave notation and adepts the source scattering matrix approach of Yaghjian. 15 Yaghjian 39 can also be referenced for methods to efficiently compute the mutual near-field coupling of two antennas arbitrarily oriented and separated in free space.

2.1 Regions of the Near Field

Figure 2 depicts the regions into which the external fields of a radiating antenna are commonly divided. The ancenna radiates into free space as a linear system with a single mode of

excitation and with the single-frequency time dependence of exp (ωt) . The antenna is assumed ordinary in the sense of not being an extraordinarily highly reactive radiator (such as a highly supergain antenna). Another example of a "super-reactive" antenna would be one formed by a number of multipoles located at a single point in space.

The far-field region extends to infinity, and is that region of space where the radial dependence of electric and magnetic fields behaves approximately as $\exp(ikr)/r$. The inner radius of the far field can be estimated from the general free-space integral for the vector potential and is usually set at $2D^2/\lambda + \lambda$ for nonsuper-reactive antennas. The added λ covers the possibility of the maximum dimension D of the antenna being smaller than a wavelength. For the mainbeam direction this "Rayleigh distance" can often be reduced. However, in the directions of nulls or very low sidelobes the far field may not accurately form until considerably larger distances are reached.

The free-space region from the surface of the antenna to the Rayleigh distance is referred to as the near-field region. It is divided into two subregions, the reactive and radiating near field. The reactive near-field region is commonly taken to extend about $\lambda/2\pi$ from the surface of the antenna, although experience with near-field measurements indicates that a distance of a wavelength (λ) or so would form a more reasonable outer boundary to the reactive near field.

The reactive near field can be defined in terms of planar, cylindrical, or spherical modes. However, a simpler, physically appealing, general method defines the reactive region of antennas directly from Poynting's theorem and the vector potential. One can show that the resistive and reactive parts of the input impedance of an antenna are proportional to the real and imaginary parts of the complex Poynting's vector integrated over

an arbitrary surface surrounding the antenna. Thus, wherever the electric and magnetic field vectors are predominantly out of phase, the Poynting vector will contribute mainly to the reactive part of the input impedance. Taking the curl of the vector potential integral once to get the magnetic field, and twice to get the electric field shows that the electric and magnetic fields tend to be predominantly out of phase in regions within a wavelength (λ) or so of the antenna. Beyond a distance of about a wavelength from nonsuper-reactive antenna, the electric and magnetic fields tend to propagate predominantly in phase, but, of course, do not exhibit $\exp(ikr)/r$ dependence until the far field is reached. This propagating region between the reactive near field and the Rayleigh distance is called the <u>radiating near field</u>.

Finally, the optical terms, "Fresnel and Fraunhofer regions," are sometimes used to characterize the fields of antennas. The term "Fraunhofer region" can be used synonymously with the far-field region, or to refer to the focal region of an antenna focused at a finite distance. The Fresnel region which extends from about $(D/2\lambda)^{\frac{1}{2}}D/2 + \lambda$ to the Rayleigh distance, is the region up to the far field in which a quadratic phase approximation can be used in the vector potential integral. The resnel region is a subregion of the radiating near-field region.

2.2 <u>Scanning with Ideal Probes on Arbitrary Surfaces</u>
Assume we had ideal probes that measured the electric and magnetic fields tangential to an arbitrary surface S enclosing

the test antenna, as shown in Figure 3. Then the fields outside S, and in particular the electric far field, is given by the vector Kirchhoff integral of the measured equivalent electric and magnetic currents, also shown in Figure 3. Although the vector Kirchhoff integral for the far field is fairly simple in form, it requires not only calibrated, ideal probes, but also the measurement of both the tangential electric and magnetic fields over the surface S. In addition, the integral generally takes a relatively large computer time compared to planar or cylindrical scanning (proportional to $(ka)^3$) to obtain one cut in the far-field pattern, where a is the radius of the sphere circumscribing the test antenna.

One can derive a modified vector Kirchhoff integral for the electric or magnetic field outside S in terms of the measured tangential electric field alone or the measured tangential magnetic field alone. Figure 4 gives the formal expression for the electric field outside S in terms of the measured electric field tangential to S and the dyadic Green's function G. However, G is impractical to find unless S supports orthogonal M and N vector wave functions. There are six coordinate systems that support M and N vector wave solutions, but just three of these the planar, cylindrical, and spherical - offer mechanically convenient scanning surfaces with simple orthogonal functions.

2.3 <u>Scanning with Ideal Probes on Planar, Cylindrical, and Spherical Surfaces</u>

The planar, cylindrical, and spherical scanning surfaces are pictured in Figure 5 along with the electric field represented by the complete set of M and N eigenfunctions. After the amplitude and phase of the tangential electric field is measured over the scanning surface S, one finds the unknown transmitting modal coefficients (T_m^A, T_m^M) of the antenna under test by means of the orthogonality integration given in Figure 5.

The specific eigenfunction expansions for planar, cylindrical, and spherical scanning, along with their inverse orthogonality integrations for the transmission coefficients are given in Figure 6. Again note that for each coordinate system, the desired transmission coefficients are determined by a straight-forward double integration of the measured tangential electric field over the scan surface. The cylindrical and spherical wave functions (M,N) shown in Figure 6 depend only upon p and 4 respectively. Their explicit expression in terms of Hankel functions and associated Legendre polynomials, respectively, can be deduced by comparison with similar expressions in references 15 and 22.

The ideal-probe planar formulas in Figure 6 as well as the probe-corrected planar formulas in Figure 8 apply to scanning in rectangular coordinates. Transmission formulas for plane-polar scanning may be found in references 30-32.

2.4 <u>Probe Correction for Planar, Cylindrical, and Spherical</u> Scanning

The nonprotering rected transission formulas and their inversions shown in Figure 6 merely involve the familiar planar, cylindrical, and spherical wave functions of traditional electromagnetic theory 41. Unfortunately, ideal probes that measure the electric or magnetic field at a point in the near field do not exist in practice. Thus, for accurate near-field measurements one must correct for the nonideal receiving response of the probe. For planar scanning, probe correction is necessary to obtain accurate values of the far field of the test antenna outside the mainbeam region, regardless of how far the probe is separated from the test antenna. With planar scanning the probe remains oriented in the same direction (usually parallel to the boresight direction of the test antenna), and thus samples the sidelobe field at an angle off the boresight direction of the

probe. Planar probe correction simply compensates for this off-boresight sampling by the probe of the plane waves radiated by the test antenna. For cylindrical scanning, the same argument can be applied in the axial scanning direction to explain why probe correction is necessary for cylindrical near-field measurements, regardless of the separation distance between the test and probe antennas.

For spherical scanning, the probe always points toward the test antenna, and thus probe correction becomes unnecessary if the scan radius becomes large enough. However, for spherical near-field measurements within a few diameters of the test antenna, probe correction is required to obtain accurate far-field patterns. Figure 7 shows the far-field pattern computed from unprobe-corrected spherical rear-field into taken at two scan radii from a 25 wavelength, X-band urray. A2 Comparison with the solid pattern obtained from probe-corrected planar near-field measurements shows that failur: to correct for the effect of the probe on spherical near-field data broadens the mainbeam and smooths out the sidelote. The broadening of the far-field mainbeam can be explained by the effective narrowing of the near-field beam by the nonideal probe receiving from further off its boresignt direction the further it gets from the center of the near-field beam. A similar handar of of the far-field pattern from effective near-field married occurs in the azimuthal patterns computed from uncorrected cylindrical near-field data as well. 43

The probe-corrected transmission formulas for planar, cylindrical, and spherical scanning can be found in the relevant references given herein. Reference 38 summarizes the probe-corrected transmission formulas for all three scanning geometries. Recently, a way has been found to express the probe-corrected transmission formulas for planar, cylindrical, and

spherical scanning as a simple modification of the nonprobe-corrected formulas. 44,22 By defining the vector output of a probe as its response in the two orthogonal orientations required for planar, cylindrical, or spherical near-field measurements, the probe-corrected formulas become similar in form to the uncorrected formulas of Figure 6. Specifically, these vector probe-corrected formulas shown in Figure 8 can be obtained from the ideal-probe formulas of Figure 6 by first replacing the measured tangential F-field with \overline{b}_{\bullet} , the vector response of the arbitrary probe, then vector multiplying the unknown transmission coefficients of the test antenna by the receiving coefficients of the probe. Once the receiving coefficients of the probe are obtained from the far fields of the probe, the probe-corrected near-field formulas reduce to the simplicity and familiarity of the uncorrected electric field formulas in planar, cylindrical, and spherical coordinate systems.

The only restrictive assumption in the theory leading to the probe-corrected formulas is that multiple reflections between the probe and test antennas are negligible. For spherical scanning, the rields of the probe are assumed to have first order azimuthal dependence only.

2.5 Expressions for the Far Field

After the transmission coefficients of the test antenna are computed from the double orthogonality integrals of the measured data (and probe correction is applied, if necessary), the amplitude and phase of the electric field outside the test antenna can be computed from its modal expansions given in Figure 6.

Usually, the far fields of the test antenna are of primary concern, and thus they are shown explicitly in Figure 9 for each of the three scanning geometries. The far fields are determined from the transmission coefficients of the test antenna directly for planar scanning, by a single summation for cylindrical

scanning, and by a double summation for spherical scanning. And, of course, the far-field patterns (co-polar and cross-polar), polarization (axial ratio, tilt angle, and sense), directivity and gain of the test antenna derive directly from the electric or magnetic far field. The gain and directivity functions obtained from near-field measurements can be used to determine the ohmic losses of antennas.

人の名称ののからのののは 私のないののでは はれのないののないない

3. SAMPLING THEOREMS AND EFFICIENT METHODS OF COMPUTATION

Richmond and Tice, in the earliest papers (of which I am aware) that computed the far-field pattern from near-field measurements (nonprobe-corrected), assumed separable near fields because as Richmond that states, "while the solution may be simple in principle, in practice the numerical computation is tedious and may require the use of large computers." Kyle also mentioned that computing the far field from the near-field data of electrically large antennas would be "difficult" on the computers available in 1958. These early statements of Richmond and Rice, and Kyle emphasize the important role that high speed computers, fast Fourier transforms, and rigorous sampling theorems have played in the development of near-field techniques.

3.1 Sampling Theorems

Before the far fields can be determined from the expressions in Figure 9, the transmission coefficients must be evaluated from the double integrals in Figure 8 (or Figure 6 for no probe correction) of the measured near-field data. Probably the simplest way to evaluate the integrals is to replace them by summations over constant increments in \$x\$Y, \$\$A\$\$, and \$\$A\$\$ for planar, cylindrical, and spherical measurements. Ordinarily this use of the elementary rectangular rule of integration would be an approximation that introduced computational errors unless the sample increments approached zero. Fortunately, the transmission coefficients can be shown to be bandlimited for

ordinary (nonsuper-reactive) antennas, and thus modern sampling theorems 45 can be applied to prove that the conversion of the integrals to summations introduces no error (or negligible error since real antennas are not quite perfectly bandlimited) if the sample increments are chosen less than a given finite value. Specifically, for planar scanning the T(A,A)eixe, becomes negligible a little beyond $k_1^2 \cdot k_2^2 = k_2^2$ and thus the sampling theorem yields the maximum data point spacing of $\Delta x = \Delta y = \lambda/2$. For cylindrical scanning the $T_{-}(r)$ are bandlimited by 2λ in Y and $2\lambda(\alpha+\lambda)$ in we to allow the sample spacing of $\Delta = \lambda/2$ or smaller than the bracketed number, that divides 27 into an integer number of divisions. For spherical scanning, the T__ are bandlimited by A(a+1) in both m and +n, to give identical angular sample increments of $\Delta \phi = \delta \phi : [\lambda/2(4 + \lambda)]$. Actually the sampling theorem applies only approximately to the direct - integration of spherical scanning because the limits of integration span π rather than $2\pi^{22}$. An alternative Fourier transform method has been developed by Wacker 17, Lewis 19, and Larsen 20 that avoids this extra, albeit slight, approximation.

Figure 10 summarizes the sampling criteria for the three conventional scanning surfaces as well as for plane—polar scanning. A question mark attends the sample spacing of $\[mu_2$ for the radial direction because no sampling theorem with uniform spacing has been derived for the radial functions of plane—polar scanning. The sampling theorem and Fourier transform have been applied indirectly to the radial integration but only for nonuniform sample spacing. 31,32

One of the attractive features of spherical scanning is that the angular sampling increments remain the same for all scan radii. Thus, as one scans further from the antenna the linear distance between data points becomes larger to keep the total required sample points at the fixed number $2(ka)^2$. Similarly the angular sampling increments of cylindrical and plane-polar scanning are independent of the scan radius. However, for the axial sampling of cylindrical scanning, the radial sampling of plane-polar scanning, and the xy rectangular sampling, the data point spacing must remain at $\lambda/2$ regardless of how large a separation distance between probe and test antenna in order to sample the rapid phase variation the probe encounters in the sidelobe region. Of course, if the far field is required only near the mainbeam direction, the sampling increments for all of the scan techniques can usually be increased without introducing serious aliasing errors.

3.2 Efficient Methods of Computation

Sampling theorems have converted the deconvolution integrals (shown in Figure 8 or 6) for the transmission coefficients to double summations and have provided convenient criteria for the data point spacing. (In practice, the infinite limits of integration in the planar and cylindrical cases are replaced by the finite limits of the scan surface.) For large intennas the plane rectangular summations take a computer time proportional to $(4a)^2$ for one cut (one 4a, or 4a,) in the far-field whether or not the fast fourier transform (FFT) is used. With the FFT the entire planar far field can be computed in a time proportional to $(4a)^2 \log_2 ka$. Similarly, the cylindrical summations take a computer time proportional to $(ka)^2$ for one azimuthal cut in the far field, and proportional to $(ka)^2 \log_2 ka$ for the entire far field using the FFT.

As Figure 9 shows, with spherical scanning all the transmission coefficients are required, in general, for just one cut in the far field. In addition, the double summations in Figure 9 and in Figure 8 for the transmission coefficients take a computer time proportional to (ka)³ whether summed directly²² or

using the FFT. 17,19,20 Similarly, the plane-polar computation of the transmission coefficients takes a computer time proportional to $(ka)^3$ using the Jacobi-Bessel functions 30 and proportional to $(ka)^2 \log_2 ka$ using the "quasi-fast Hankel transform" (FHT) 31,46 for one or more far-field cuts. The FHT requires nonuniform data spacing, however.

The computation times on a Cyber 750 for planar, cylindrical, and spherical scanning are displayed in Figure 11. All the computer times remain quite manageable even for electrically large antennas, except for spherical scanning and plane-polar scanning with uniformly spaced data points. Computer times for these two techniques quickly grow into the hours for antennas larger than 100 wavelengths in diameter. And, of course, on most mini-computers, the computations for any of the techniques would take considerably longer than on the Cyber 750.

In applying the FFT to conventional plane-rectangular measurements, one must consider the resolution one wants in the far-field pattern. A straightforward application of the FFT to near-field data taken at the usual $\lambda/2$ data point spacing specified by the sampling theorem generates output at points too widely spaced to smoothly resolve the far-field pattern. For single cuts in the far-field only a 1-dimensional FFT is required, and one can increase the resolution (i.e., decrease the distance between far-field points) merely by "zero-filling" the near-field data. Unfortunately, sufficient zero-filling of a 2-dimensional FFT that generates the entire far-field of an electrically large antenna may require more central memory than most computers provide. To obtain the complete highly-resolved pattern in such cases, one can resort to computing the discrete double Fourier transform directly in a time proportional to (ka)³, or if this computer time is prohibitive, one can use an off-line version of the 2-dimensional FFT. Off-line (mass-storage) versions of the

FFT are readily available or can be programmed straightforwardly starting with a 1-dimensional FFT algorithm. Typically, mass-storage versions of the FFT take an input/output time roughly equal to the central processing time. 47

4. EXPERIMENTAL ERRORS

The theory of near-field antenna measurements applies rigorously to linear antennas radiating or receiving in a single mode at a fixed frequency, and satisfying Maxwell's equations in free space. The antennas may be nonreciprocal and lossy, lossless, or "gainy." The only restrictive assumption involved in the theory of probe-corrected near-field measurements is that multiple reflections between the probe and test antennas are negligible. However, in practice experimental errors limit the accuracy of near-field techniques. In addition to the multiple reflections, the experimental measurements will introduce probe positioning errors, instrumentation errors, and for the planar and cylindrical scanning geometries, finite scan errors. Errors are also introduced by uncertainties in the far-field pattern of the probe and in the measurement of the insertion loss between the test antenna and probe when absolute gain is required. (If sample spacing and computer accuracy are adequate, aliasing and computational errors will be negligible compared to the experimental errors.)

Upper-bound error analyses 26, as well as computer simulations, 26b,48 have been performed for determining the accuracy of the far field obtained from planar near-field measurements. Computer simulations have also been performed for cylindrical 49 and spherical 16,50 near-field scanning, but an analytical treatment of upper-bound errors for near-field measurements on a cylinder and sphere remains outstanding.

The relative importance of the various near-field measurement errors upon the far field depends, of course, on the antenna under

test, the frequency of operation, the measurement facility, and the probe. However, the results of the planar upper-bound error analyses 26 show that for typical microwave antennas and planar near-field testing facilities, three or four sources of error dominate: finite scan area, z-position of the probe, receiver nonlinearities in measuring the near-field amplitude, and sometimes, multiple reflections.

The effects on the far field of limiting the planar measurements to a finite scan area are small for highly directive antennas well within the "solid angle" formed by the edges of the test antenna and the edges of the finite scan area. Outside this solid angle, the far fields cannot be relied upon with any confidence. Although for very highly tapered near fields this solid angle can be extended somewhat.

The z-position inaccuracies, i.e., the deviation from planarity of the probe transport over the scan area, can produce relatively large errors in the sidelobe levels of the far field. Variations in the z-position of the probe produce corresponding variations in the near-field phase. Thus, large errors in the sidelobes occur in the far-field directions corresponding to the predominant spacial frequencies of the deviations in z-position across the scan area. In the mainbeam direction, the effect of z-positioning of the probe is much less critical - the reduction in gain being given by 8/2, the familiar Ruze relation. 51,26aThe errors in the sidelobes caused by inaccurate z-positioning can be reduced by measuring the deviation of the probe from the scan. plane and correcting the near-field phase proportionately. 52 It should also be mentioned that receiver phase errors generally have a much smaller effect on the far field than phase errors caused by inaccurate z-positioning, because typical receiver phase errors are negligible at the maximum near-field amplitude and increase monotonically with decreasing amplitude. 26b

Receiver nonlinearities in the measurement of near-field amplitude, however, can cause significant errors in the mainbeam and sidelobes of the far fields. For example, a receiver nonlinearity of ± .02 dB/dB can produce several tenths of a dB error in gain, and a several dB error in a 35 dB sidelobe of a typical microwave reflector. Fortunately, these receiver amplitude errors can be greatly reduced by calibrating the receiver with a precision attenuator and applying the calibration curve to the near-field data.

The contribution to the output of the probe from the multiple reflections can be estimated by changing the separation distance between the probe and test antenna and recording the amplitude variations that occur in the received signal with a period of about $\lambda/2$. If multiple reflections prove significant, they may be reduced by the judicious use of absorbing material, by decreasing the size of the probe, by increasing the probe separation distance, by averaging the far fields computed from the near-field data taken on scan planes that are separated by a small fraction of a wavelength (say $\lambda/8$), or by using specially designed probes that filter the mainbeam and accentuate the sidelobes.

Finally, the upper-bound error formulas 26 should be applied with discretion. They are dependent upon underlying (usually explicitly stated) assumptions that are satisfied by most antennas and near-field measurement conditions, but which may be either violated or relaxed in certain circumstances. For example, it is well-known that phase errors introduced into the main near-field beam of directive antennas cause a reduction in the computed on-axis gain. However, this gain reduction applies to near-field beams of uniform phase and will not hold for antennas with variations in their phase if the phase errors occur in just the right places and with just the right values to eliminate the original phase variations. Although this conjunction of phase

variations is highly unlikely, its possibility of occurrence is revealed from an examination of the error analyses. ²⁶

When the underlying assumptions can be relaxed, lower upper-bounds can usually be obtained. For example, an estimate of the specific z-position errors for a particular measurement facility allows one to estimate their effect upon far-field sidelobes more accurately than with the general upper-bound expressions. ²⁶

5. CONCLUSION

The theoretical development of near-field antenna measurements extends from classical Maxwell's equations to the sophisticated use of modern sampling theorems. The near-field measurement system combines the traditional methods of far-field amplitude measurements with modern techniques for measuring phase, and for accurately monitoring and controlling the position of the probe and test antenna. The computation of the far field from the measured near-field data involves both conventional summation and highly efficient, two-dimensional FFT algorithms. In short, a successful near-field measurement program is founded upon this balanced triad of classical and modern electromagnetic theory, measurement, and computation.

REFERENCES

- 1. Barrett, R.M. and Barnes, M.H. (Jan. 1952) Automatic antenna wavefront plotter, Electronics 25: 120-125.
- 2. Woonton, G.A. (1953) On the measurement of diffraction fields, in <u>Proc. McGill Symposium on Microwave Optics</u> (AFCRC-TR-59-118(II): 347-350.
- 3.a) Richmond, J.H. and Tice, T.E. (April 1955) Probes for microwave near-field measurements, IRE Trans. Microwave Theory and Techniques MTT-3: 32-34.
 - b) Richmond, J.H. (July 1955) Simplified calculation of antenna patterns with application to radome problems, ibid: 9-12.
- 4. Kyle, R.F. (July 1958) Far-field radiation of a cheese aerial Electronic & Radio Engineer 35: 260-262.
- 5. Clayton, L., Jr., Hollis, J. S. and Teegardin, H.H. (Oct. 1961) A wide frequency range microwave phase-amplitude measuring system, in Abstracts of the 11th Annual USAF Symp. on Antenna Research and Development, Univ. of Illinois.
- 6. Johnson, R.C., Ecker, H.A. and Hollis, J.S. (Dec. 1973)
 Determination of far-field antenna patterns from near-field
 measurements, Proc. IEEE 61: 1668-1694.
- 7. Polk, C. (Jan. 1956) Optimal Fresnel-zone gain of a rectangular aperture, IRE Trans. Antennas Propagat. AP-4: 65-69.
- 8. Bates, R.H.T. and Elliott, J. (Mar. 1956) The determination of the true sidelobe level of long broadside arrays from rediation-pattern measurements in the Fresnel region, Proc. IEE Monograph No. 169R: 307-312.
- 9. Brown, J. (Feb. 1958) A theoretical analysis of some errors in aerial measurements, Proc. IEE Monograph No. 285R: 343-351.
- 10. Brown, J. and Jull, E.V. (Nov. 1961) The prediction of aerial radiation patterns from near-field measurements, Proc. IEE 108B: 635-644.
- 11. Kerns, D.M. (Apr.-May 1963) Analytical techniques for the correction of near-field antenna measurements made with an arbitrary but known measuring antenna, in Abstracts of

URSI-IRE Meeting, Washington, D.C., 6-7.

- 12. Kerns, D.M. (June 1981) Plane-Wave Scattering-Matrix Theory of Antennas and Antenna-Antenna Interactions, NBS Monograph 162, US Gov. Printing Office, Washington, D.C.
- 13. Leach, W.M., Jr. and Paris. D.T. (July 1973)

 Probe-compensated near-field measurements on a cylinder,
 IEEE Trans. Antennas Propagat. AP-21: 435-445.
- 14. Borgiotti, G.V. (July 1978) Integral equation formulation for probe corrected far-field reconstruction from measurements on a cylinder, IEEE Trans. Antennas Propagat. AP-26: 572-578.
- 15. Yaghjian, A.D. (Sept. 1977) Near-Field Antenna Measurements on a Cylindrical Surface: A Source Scattering Matrix Formulation, NBS Tech. Note 696.
- 16. Jensen, F. (1970) Electromagnetic near-field far-field correlations, Ph.D. dissertation, Tech. Univ. Demmark.
- 17. Wacker, P.F. (June 1975) Non-Planar Near-Field Measurements: Spherical Scanning, NBSIR 75-809.
- 18. Ricardi, L.J. and Barrows, M.L. (June 1972) A recurrence technique for expanding a function in spherical harmonics, IEEE Trans. Computers C-21: 583-585.
- 19. Lewis, R.L. (Oct. 1976) Highly efficient processing for near-field spherical scanning data reduction, in <u>Digest of AP-S Int. Symp.</u>, Amherst, MA., 251-254.
- 20.a) Larsen, F.H. (July 1977) Probe correction of spherical near-field measurements, Electron. Lett. 13: 393-395.
 - b) Larsen, F.H. (Dec. 1930) <u>Probe-Corrected Spherical</u>
 <u>Near-Field Antenna Measurements</u>, Tech. Univ. Denmark Report
 <u>LD36</u>.
- 21. Wood, P.J. (1977) The prediction of antenna characteristics from spherical near-field measurements-Parts I and II, theory and experimental verification, Marconi Review 30: 42-68 and 117-155.
- 22. Yaghjian, A.D. (Mar. 1984) Simplified approach to probe-corrected spherical near-field scanning, Electron. Lett. 20: 195-196.

- 23. Baird, R.C. (1966) Antenna measurements with arbitrary probes at arbitrary distances, in <u>High Frequency and Microwave Field Strength Precision Measurement Seminar</u>, NBS Report 9229.
- 24. Baird, R.C., Newell, A.C., Wacker, P.F. and Kerns, D.M. (May 1970) Recent experimental results in near-field antenna measurements, Electron. Lett. 6:349-351.
- 25. Newell, A.C. and Crawford, M.L. (July 1974) Planar
 Near-Field Measurements on High Performance Array Antennas,
 NBSIR 74-380.
- 26.a) Yaghjian, A.D. (Oct. 1975) <u>Upper-Bound Errors in Far-Field</u>
 Antenna Parameters Determined from Planar Near-Field
 Measurements, Part I: Analysis, NBS Tach. Note 667.
 - b) Newell, A.C. (July 1975) , Part II: Analysis and Computer Simulation, NBS Short Course Notes, Boulder, CO.
- 27. Joy, E.B. and Paris, D.T. (May 1972) Spatial sampling and filtering in near-field measurements, IEEE Trans. Antennas Prop.gat. AP-20: 253-261; also 1970 Ph.D. Dissertation, Georgia Institute of Technology.
- 28. Newell, A.C. (1984) Private communication.
- 29. Sharp, R.G. (1983) Near-field measur ment facility plans at Lewis Research Center, in NASA Conference Publication 2269, Pt 2: 899-921
- 30. Rahmat-Samii, Y., Galindo-Isreal, V. and Mittra, R. (Mar. 1980) A plane-polar approach for far-field construction from near-field measurements, IEEE Trans. Antennas Propagat. AP-28: 016-230.
- 31. Stubenrauch, C.F. (1980) <u>Planar Near-Field Scanning in Polar Coordinates: A Feasibility Study</u>, NBS report to sponsor No. SR-723-73-80.
- 32. Wacker, P.F. and Severyns, R. (April 1983) Near-field analysis and measurement: plane polar scanning, in IEE Conference Publication No.219, Pt. 1., 105-107.
- 33. Grimm, K.R. (Jan. 1983) Ultralow sidelobe planar near-field measurement study, in Proc. 1982 Antenna Applications Symposium (RADC-TR-82-339), Hanscom AFB, MA., 663-682.
- 34. Kerns, D.M. (Feb. 1975) Scattering matrix description and

- near-field measurements of electroacoustic transducers, J. Acoust. Soc. Am. 57:497-507.
- 35. Newell, A.C., Baird, R.C. and Wacker, P.F. (July 1973)
 Accurate measurement of antenna gain and polarization at
 reduced distances by an extrapolation technique, IEEE Trans.
 Antennas Propagat. AP-21: 418-431.
- 36.a) Kerns, D.M. (May 1970) Correction of near-field antenna measurements made with an arbitrary but known measuring antenna, Electron. Lett. 6:346-347.
 - b) Kerns, D.M. (May 1970) New method of gain measurement using two identical antennas, ibid: 348-349.
 - c) Kerns, D.M. and Newell, A.C. (Feb. 1971) Determination of both polarization and power gain by a generalized 3-antenna measurement method, ibid.7: 68-70.
- 37. Paris, D.T. Leach, W.M., Jr. and Joy, E.B. (May 1978) Basic theory of probe-compensated near-field measurements, IEEE Trans. Antennas Propagat. AP-26: 373-379.
- 38. Appel-Hansen, J. (1982) Antenna measurements, in <u>The Handbook of Antenna Design, Vol.1</u>, Peter Pevegrinus, London, ch.8.
- 39. Yaghjian, A.D. (Jan. 1982) Efficient computation of antenna coupling and fields within the near-field region, IFEE Trans. Antennas Propagat. AP-30, 113-128.
- 40. Morse, P.M. and Feshbach, H. (1953) Methods of Theoretical Physics, McGraw-Hill, New York, ch. 13.
- 41. Stratton, J.A. (1941) <u>Electromagnetic Theory</u>, McGraw-Hill, New York.
- 42. Newell, A.C. and Repjar, A. (June 1977) Results of spherical near-field measurements on narrow-beam antennas, in <u>Digest of Int. Symp. Antennas and Propagation</u>, Stanford CA, 382-385.
- 43. Stubenrauch, C.F. and Newell, A.C. (Nov. 1980) Some recent near-field antenna measurements at NES, Microwave Journal 23: 37-42.
- 44. Yaghjian, A.D. (May 1984) Near-field antenna measurements. Paper presented at the Boston Chapter of the IEEE Antennas and Propagation Society, Lexington, MA.

- 45. Oppenheim, A.V. and Schaffer, R.W. (1975) <u>Digital Signal</u>
 <u>Processing</u>, Prentice-Hall, Englewood Cliffs, N.J., ch. 3.
- 46. Siegman, A.E. (July 1977) Quasi fast Hankel transform, Optics Letters 1:13-15.
- 47. Repjar, A. (1984) Private communication.
- 48.a) Rodrique, G.P., Joy, E.B. and Burns, C.P. (Aug. 1973) An Investigation of the Accuracy of Far-Field Radiation Patterns Determined from Near-Field Measurements, Georgia Institute of Technology Report.
 - b) Joy, E.B. (June 1977) Maximum near field measurement error specification, in <u>Digest of Int. Symp. Antennas and Propagation</u>, Stanford, CA., 390-393.
- 49. Chang, W., Fasold, D. and Fischer, C.P. (Jan. 1984) A new near-field test facility for large spacecraft antennas, in Abstracts of National Radio Science Meeting, Boulder, CO., p. 3.
- 50. Jensen, F. (Nov. 1978) Computer simulations as a design tool in near-field testing, IEE Conference Publication No. 169, Pt. 1, 111-114.
- 51. Ruze, John (April 1966) Antenna tolerance theory—a review, Proc. IEEE 54: 633-640.
- 52. Joy, E.B. and Wilson, R.E. (Oct.1982) A simplified technique for probe position error compensation in planar surface near-field measurements, in Proc. AMTA Meeting, 12.1-12.10.

		MAJOR DIMENSION	
ANTENNA TYPE	FREQUENCY (GHz)	IN WAVELENGTH	GAIN (DB)
HORN LENS	48.0	90	47.0
CONICAL HORN (JPL)	8.0		22.08
CASSEGRAIN REFLECTOR	60.0	91	45.5
LENS ARRAY (CONSTRAINED LENS)	9.2	- 23	34.0
PHASED ARRAY (VOLPHASE)	8.4	17	21.5
PHASED ARRAY	7.5	. 15	30.5
DIPOLE ARRAY	1.4	5	20.3
FAN BEAM RADAR (LINEAR % CIRCULAR POLARIZATION)	9.5	58	30.0
KU-BAND REFLECTOR	14.5	60	42.0
KU-BAND ARRAY (PENCIL & FAN EEAM)	17.00	50	40.0
SHAPED BEAM, C.P. (ARRAY FED REFLECTOR	4.0	20	27.5
MICROSTRIP ARRAY	1.5	27	30.Ò
PARABOLIC REFLECTION	1.5-18	15-183	26-47
COMPACT RANGE REFLECTOR	18 2 .55	285 a 870	~ 60.0

Table 1. List of some representative antennas measured on NBS near-field facility.

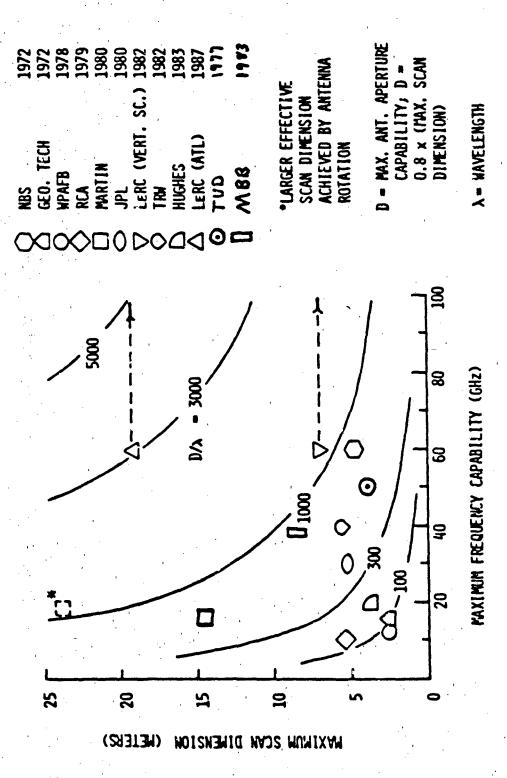


Figure 1. Chart of a few existing near-field facilities.

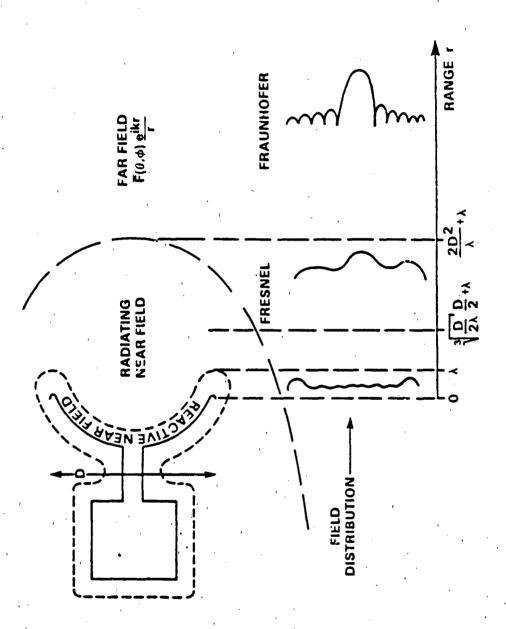
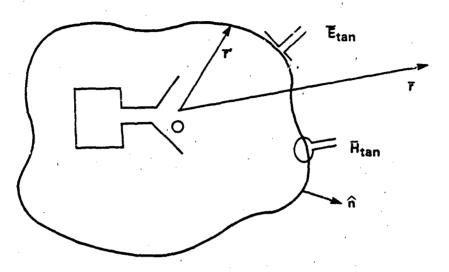


Figure 2. Regions of the external fields of ordinary, radiating antennas.



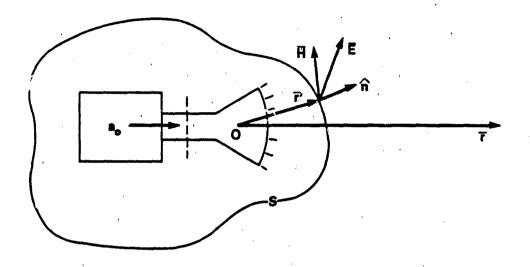
VECTOR KIRCHHOFF INTEGRAL

$$\vec{E}(\vec{r}) = \frac{-ike^{ikr}}{4\pi r} \hat{e}_r \times \oint (\vec{R}_m + Z_0 \hat{e}_r \times R_0) e^{-ik\hat{e}_r \cdot \vec{r}'} dS'$$

$$r \rightarrow \infty$$

$$\vec{K}_0 = \hat{n} \times \vec{H} \qquad \vec{K}_m = -\hat{n} \times \vec{E}$$

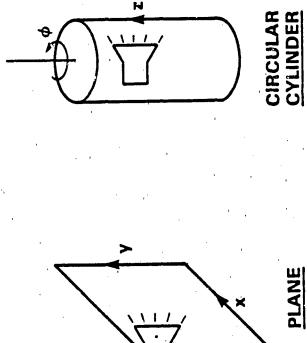
Figure 3. Scanning with ideal probes on arbitrary surfaces.

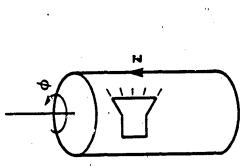


 $\overline{E}(r) = \oint i\omega \mu_0 [\widehat{n} \times \overline{E}(r)] \cdot \overline{G}(r,r) dS'$

G IS IMPRACTICAL TO FIND UNLESS S SUPPORTS
ORTHOGONAL M AND N EIGENFUNCTIONS

Figure 4. Modified vector Kirchhoff integral in terms of the tangential E-field alone.





SPHERE

 $\vec{E}(\vec{r}) = \sum' T_m^E \vec{M}_m(\vec{r}) + T_m^M \vec{N}_m(\vec{r})$

ORTHOGONALITY OF M AND N YIELDS:

 $T_{m}^{E} = \int [\bar{N}_{m}^{*}(\bar{r}) \times E(\bar{r})] \cdot \hat{n} dS; T_{m}^{M} = -\int [\bar{M}_{m}^{*}(\bar{r}) \times E(\bar{r})] \cdot \hat{n} dS$

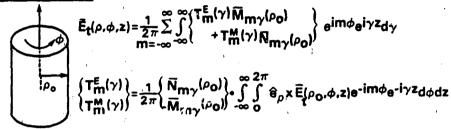
Figure 5. Scanning with ideal probes on planar, cylindri-cal, or spherical surfaces. (The symbol ∑ denotes integration as well as summation.)

$$\frac{\text{PLANAR}}{\text{YA}} = \frac{1}{2\pi} \int_{-\infty-\infty}^{\infty} \overline{T}_{t}(k_{x},k_{y})e^{i\gamma z}e^{ik_{x}x_{t}ik_{y}y}dk_{x}dk_{y}$$

$$z$$

$$\overline{T}_{t}(k_{x},k_{y}) = \frac{e^{i\gamma z_{0}}}{2\pi} \int_{-\infty-\infty}^{\infty} \overline{E}_{t}(x,y,z_{0})e^{-ik_{x}x_{0}-ik_{y}y}dxdy$$

CYLINDRICAL:



SPHERICAL:

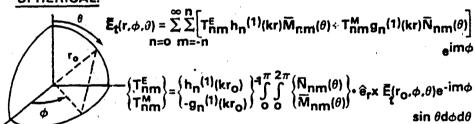


Figure 6. Specific expressions for planar, cylindrical, and spherical scanning with ideal probes

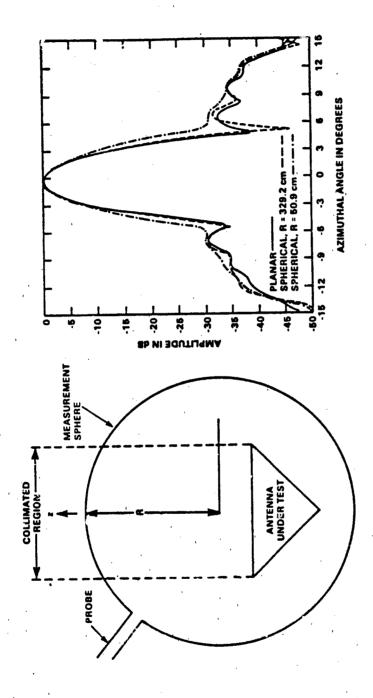


Figure 7. Effect of probe correction in spherical near-field measurements.

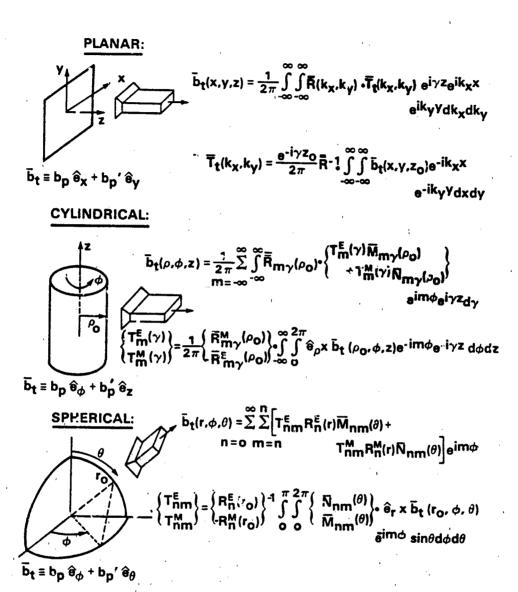
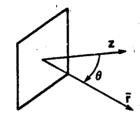


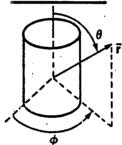
Figure 8. Probe-corrected formulas for vector response $(\overline{\mathbf{b}}_{\mathbf{t}})$ of the probe.

PLANAR:



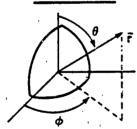
 $\overline{E}(r,\theta,\phi) = \frac{-ik\theta ikr}{r} \cos \theta \cdot \overline{f}(\sin \theta \cos \phi, \sin \theta \sin \phi)$

CYLINDRICAL:

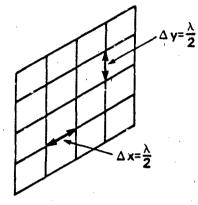


 $\bar{\mathbf{E}}(\mathbf{r},\theta,\phi) = \frac{-2k\mathbf{e}^{i\mathbf{k}\mathbf{r}}}{\mathbf{r}}\sin\theta\sum_{i=-\infty}^{\infty}(-i)^{m}\left[\mathbf{T}_{\mathbf{m}}^{\mathbf{E}}(\mathbf{k}\mathbf{c}\mathbf{o}\mathbf{s}\theta)\hat{\mathbf{e}}_{\phi}\right]$ $-i\;\mathbf{T}_{\mathbf{m}}^{\mathbf{M}}(\mathbf{k}\mathbf{c}\mathbf{o}\mathbf{s}\theta)\hat{\mathbf{e}}_{\theta}$

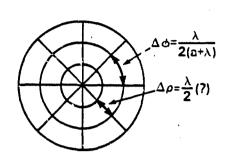
SPHERICAL:



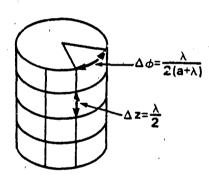
$$\begin{split} \vec{E}(r,\theta,\phi) &= \frac{-ie^{ikr}}{r} \sum_{n=0}^{\infty} \sum_{m=0}^{n} (-i)^{n} \left[T_{nm}^{E} \vec{M}_{nm}(\theta) + T_{nm}^{M} \vec{N}_{nm}(\theta) \right] e^{im\phi} \\ , \end{split}$$



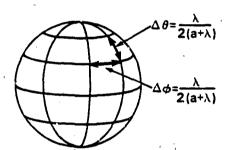
PLANE RECTANGULAR



PLANE FCLAR



CYLINDRICAL



SPHERICAL

Figure 10. Sample spacing for scanning on a plane, cylinder, and sphere.

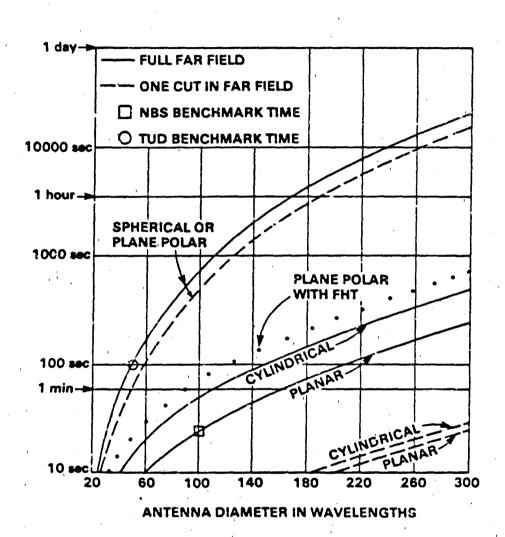


Figure 11. CPU time for near-field to far-field transformation on Cyber 750.



Technology Service Corporation

Washington Division: 962 Wayne Avenue, Silver Spring, Maryland 20910 Phone. [301] 565-2970

Ref: TSC-W41-241/cad A3155K

Optimum Probe Design for Near Field Scanning of UltraLow Sidelobe Antennas

Prepared by:

Kenneth R. Grimm
Technology Service Corporation
Washington Division

Prepared for:

1984 Antenna Applications Symposium Allerton Park, Illinois September 19-21, 1984

ABSTRACT

An innovative technique has been developed for accurately measuring very low sidelube antenna patterns by the method of planar near field probing. The technique relies on a new probe design which has a pattern null in the direction of the test antenna's steered beam direction. Simulations of the near field measurement process using such a probe show that -60dB peak sidelobes will be accurately measured (within established bounds) when the calibrated near field dynamic range does not exceed 40 dB. The desireable property of the new probe is its ability to "spatially filter" the test antenna's spectrum by reduced sensitivity to main beam ray paths. In this way, measurement errors which usually increase with decreasing near field signal level are minimized. The new probe is also theorized to have improved immunity to probe/array multipath. Plans to use the new probe on a modified planar scanner during tests with the AWACS array at the National Bureau of Standards will be described.*

^{*}Work reported herein is being performed as part of an on-going exploratory development for the Office of Naval Research under contract NCOO14-83-C-0671. The Planar Near Field Scanner at the National Bureau of Standards has been provided as a government-furnished facility for this investigation under the Defense Small Business Advanced Technology (DESAT) program, phase II.

1.0 INTRODUCTION

Planar Near Field (PNF) scanning continues to be widely used for efficient and convenient pattern testing of large microwave antennas. However, new requirements to measure very low sidelobe level patterns has forced designers of PNF facilities to include sophisticated and expensive calibration techniques and instruments within their facilities. This paper describes a new probing technique which is capable of minimizing the effects of most NF measurement errors which are known to degrade the desired far field (FF) sidelobe pattern. A NF probe has been designed and built to point a single pattern null in the direction of the test antenna's mainbeam. Simulations of NF data acquired with the new probe, Fourier transformed and then probe-corrected, show the resulting FF sidelobe spectrum to be more accurately measured than with a standard probe. Actual tests with the new probe when measuring the AWACS array antenna are presently under way.

2.0 PROBE COMPENSATED NEAR FIELD MEASUREMENTS

Many good references exist which describe probe compensation processing for near field scanning on planes, cylinders, and spheres [1,2,3]. For planar scanning, Kerns first showed that the probe may be considered to be a spatial filter whose weighting effects in the NF measurement plane can be compensated (removed) in the spectral domain only if the probe's FF pattern were adequately known a priori [4]. In this paper, we use the formulation of Paris who applied a reciprocity relation to define the voltage response of a simple probe, receiving in the NF of a test antenna (see Figure 1) [5]. If measurements are made on the NF surface S₁, then by reciprocity the radiated plane wave spectra of the probe and test antenna are Fourier related to the probe's voltage response when it is located at an arbitrary NF sampling point, by:

$$V(x_{0}, y_{0}, z_{0}) = \int \int (k_{z} \overline{A}. \overline{B} e^{-jk_{z} z_{0}}) e^{-j(k_{x} x_{0} + k_{y} y_{0})} dk_{x} dk_{y}$$
 (1)

Here \overline{A} is the vector plane wave spectrum of the test antenna which we seek, \overline{B} is the probe's spectrum known by independent measurement, and both are evaluated at wavenumbers:

Figure 1. Planar Near Field Scanning Geometry

$$k_x = k \sin \theta \cos \phi$$

 $k_y = k \sin \theta \sin \phi$
 $k_z = \sqrt{k^2 - k_x^2 - k_y^2}$
 $k_z = \frac{2\pi}{\lambda}$

The goal of NF measurements then is to adequately acquire $V(x_0,y_0,z_0)$ on a plane of sufficient extent, and perform an inversion calculation of equation (1) from the measured voltages. The Fourier inversion yields the probe/antenna coupling product, written as:

$$\overline{A} \cdot \overline{B} (k_x, k_y) = \frac{1}{(2\pi)^2} \int_{-\infty}^{\infty} V(x_0, y_0, z_0) e^{+j(k_x x_0 + k_y y_0 + k_z z_0)} dx_0 dy_0$$
 (2)

Equation (2) shows that an ideal probe (one for which $\overline{8}(k_x,k_y)=1$ for all k_x,k_y) will yield straightforwardly the desired test antenna spectral amplitude function $\overline{A}(k_x,k_y)$ with no probe compensation. However, all other probes (all real probes) impart a complex weighting to \overline{A} which if known a priori, can be removed (compensated) in equation (2) by division. The final result is then used to find any desired field property (near or far) of the test antenna. For example, once $A_{x,y}(k_x,k_y)$ is known, the FF spherical components can be straightforwardly calculated as:

$$E_{s} \sim 2\pi j k \frac{e^{-jkr}}{r} \left[\Lambda_{x} \cos \phi + A_{y} \sin \phi \right]$$

$$E_{s} \sim 2\pi j k \frac{e^{-jkr}}{r} \cos \theta \left[\Lambda_{x} \sin \phi - \Lambda_{y} \cos \phi \right]$$
(3)

The probe of course, also imparts a polarization weighting which is being tacitly ignored herein, but does not compromise the result of this development.

3.0 OPTIMUM PROBES

The concept of an optimum probe was introduced by Huddleston at Georgia Institute of Technology in 1978 [6]. He observed that by probing only over a limited extent in the x, y, directions (Figure 1), the measured wave number spectrum \tilde{A} would be an aliased version of the actual test antenna spectrum \tilde{A} . This finite-scan length limitation had of course been previously recognized and adequately reported [7], but here Huddleston was attempting to find a "best" probe pattern for \tilde{B} , so that the unavoidable spectral aliasing in \tilde{A} might be minimized. He formed a mean square error criterion for "bestness" of \tilde{A} by requiring that:

$$\iint_{-\infty} |\overline{A}(k_x, k_y) - \widetilde{A}(k_x, k_y)|^2 dk_x dk_y \text{ be a minimum}$$
 (4)

where $\tilde{A}(k_x, k_y)$ is the measurement estimate of the true spectrum $\overline{A}(k_x, k_y)$. The measurement estimate is given by:

$$\widehat{A}(k_x k_y) = \overline{A}(k_x k_y) \cdot \overline{B}(k_x k_y) \star \overline{P}_{\overline{I}}(k_x k_y)$$
 (5)

with $P_{T}(k_{x},k_{y})$ being the Fourier transform of the step function sampling window,

$$p_{t}(x,y) = \begin{cases} 1 & |x| \le x_{\text{max}}, |y| \le y_{\text{max}} \\ 0 & \text{otherwise} \end{cases}$$

Huddleston concluded that the optimum NF probe would minimize the FF error in A because its NF voltage response is most concentrated over the finite scan area.

4.0 OPTIMUM PROBES FOR LOW SIDELOBE TESTING

In 1982 Grimm reinterpreted Huddleston's mean square error criterion [8]. He reasoned that if a probe pattern could be found which concentrated its NF voltage response in a way which minimized the mean square measurement error only over specified regions in the A spectrum, then this new probe would be optimum in a weighted mean square error sense. By selecting the weighting

function to discriminate against the mainbeam spectral wavenumbers, it was predicted that the usually very low level sidelobe region would have enhanced measurement accuarcy in the NF. Of course, the discrimination property of the new probe could also be expected to introduce uncertainty in and around the FF main beam region, but this region could always be accurately measured in a second test with a standard probe.

The "bestness" criterion for an optimum low sidelobe NF probe then becomes:

for
$$\iint_{-\infty}^{\infty} |W(k_x, k_y)| [\overline{A}(k_x, k_y) - \widetilde{A}(k_x, k_y)]|^2 dk_x dk_y \text{ be a minimum}$$

$$W(k_x, k_y) = \begin{cases} 1 & k_0 \le |k_x, k_y| \le k_{\text{max}} \text{ (sidelobes)} \\ 0 & 0 \le |k_x, k_y| < k_0 \text{ (mainlobe)} \end{cases}$$
(6)

In equation (6) k_0 is the wavenumber limit (first zero) for the mainbeam, and k_{max} is the maximum wavenumber allowed by NF measurement. $W(k_x,k_y)$ is essentially a mainbeam wavefilter. Such a probe filter can not be practically realized, however a useful approximation has been designed and built as shown in Figure 2. The new probe is a 2-element linear array of WR-284 waveguide elements. The element voltages are combined in a 4-port 180° hybrid coupler, producing both Σ and Δ NF voltage responses in the probe output ports. The transform of the Δ port voltage implements the filter of equation (6) only approximately. Approximation errors will be due to probe:

- null depth limitations
- null pointing inaccuracies
- null shape variations.

The effect of these approximations and the overall sidelobe measurement accuracy improvement is described next by simulation.

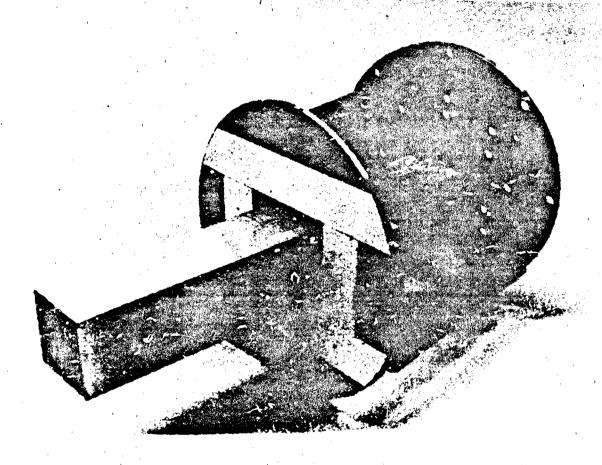


Figure 2. Two-Element Array Probe Built in WR-284
Waveguide. The 180 Hybrid Combines the
Element Voltages to Implement an Approximate
Mainbeam Wavefilter During Planar Near Field
Scanning of Ultralow Sidelobe Antennas.

5.0 SIMULATION

A computer study was performed which implements equation (1) to simulate NF measurement plane voltages generated by arbitrary probes in tests with arbitrarily low sidelobe antennas [9]. For the optimum probe, the simulation computes a measurement estimate of an error-free spectrum as:

$$\overline{A(k_x, k_y)} = \overline{A(k_x, k_y)} \cdot \overline{B(k_x, k_y)} \cdot \overline{W(k_x, k_y)} \star \overline{P_T(k_x, k_y)}$$
 (7)

When sufficient scan length is available, the sampling window transform $P_{-}(k_{_{\rm X}},k_{_{\rm Y}})$ becomes unity and the product $\overline{B} \cdot \overline{W}$ describes an optimum probe pattern which completely filters (attenuates) the mainbeam wavenumbers. Practical probe patterns which approximate the optimum filter are achieved using the new 2-element probe array.

Figure 11 is a block diagram of the simulation. For any probe type, both a reference test array spectrum $\overline{A}(k_\chi)$ and the specified probe spectrum $\overline{B}(k_\chi)$ are first generated. Then the coupling product $\overline{A} \cdot \overline{B}$ is formed and transformed for the simulated error-free NF voltages. These voltages are then numerically corrupted to simulate measurement inaccuracies due to RF instrumentation, multipath, and positioning error limitations. Finally the corrupted voltage set is retransformed by equation (2) and probe corrected to yield $\overline{A}(k_\chi, k_y)$, the measurement estimate of $\overline{A}(k_\chi, k_y)$. Comparing \overline{A} and \overline{A} then demonstrates the "bestness" of the new probe to measure low sidelobes accurately as described in the results.

6.0 SIMULATION RESULTS

The results of this section confirm that the optimum NF probe (in simulation) offers improved sidelobe measurement accuracy. The new probe operates to transform the sidelobe spectrum of an arbitrarily low sidelobe antenna into an "effective" pattern whose peak sidelobes have been artificially increased by the probe.* These increased peaks are then measured with improved accuracy as shown, and finally reported at the correct relative level following standard probe compensation processing.

by an amount equal to the probe null depth.

The observation of significance is that \underline{all} sources of NF measurement error are minimized by this probe because the effect of these errors are directly proportional to the far field pattern level of interest. In essence, it is the coupling product $\overline{A} \cdot \overline{B}$ which is being measured. Improvement in \widetilde{A} is achieved only following probe compensation.

6.1 Single-element W/G Probe

Figure 3 shows a reference array pattern $\overline{A}(k_\chi)$ which would be radiated by a 44 λ linear test array of point sources separated by .5 λ . The elements support a Taylor 50 dB sidelobe illumination for \overline{n} = 10. The pattern has been generated at 256 equally spaced k_χ increments. Overlayed on the array pattern is a simple cosine-response probe pattern $\overline{B}(k_\chi)$ normalized to the array's peak gain. This model for \overline{B} simulates the pattern from a commonly used open-ended waveguide (W/G) probe. The coupling product pattern $\overline{A} \cdot \overline{B}$ for this pair is shown in Figure 4. The complex weighting of the probe only slightly attenuates the mainbeam gain at its 9.6° (k_χ = 149) steering angle, as well as causing the roll off over the outer sidelobes as expected. Figure 5 shows the simulated NF measurement plane voltage computed from equation (2) for this coupling product. The NF phase displays the expected steering gradient of 46°/ λ for a probe z-separation of 3 λ . NF samples are assumed to be spaced by .32 λ .

The simulated error-free NF voltages in Figure 5 are then perturbed to model random and systematic NF measurement errors which usually increase with decreasing relative amplitude. The perturbed voltage set is finally retransformed and probe-corrected to yield the FF measurement estimate $\tilde{A}(k_X)$ for this probe type. Figure 6 overlays the \tilde{A} and \tilde{A} spectra. It can be seen that large sidelobe errors have been introduced in \tilde{A} when measured by the simple open-ended W/G probe subject to NF amplitude dependent measurement errors. Details of measurement corruption model is contained in [9].

Frequency-dependent beam steering is always expected from a travelling wave test antenna.

Figure 3. Simulated Reference Array Pattern for a 44% Linear Taylor -50 dB Sidelobe Design. The Overlay Shows a Standard Probe Pattern for a Single Open-ended Waveguide.

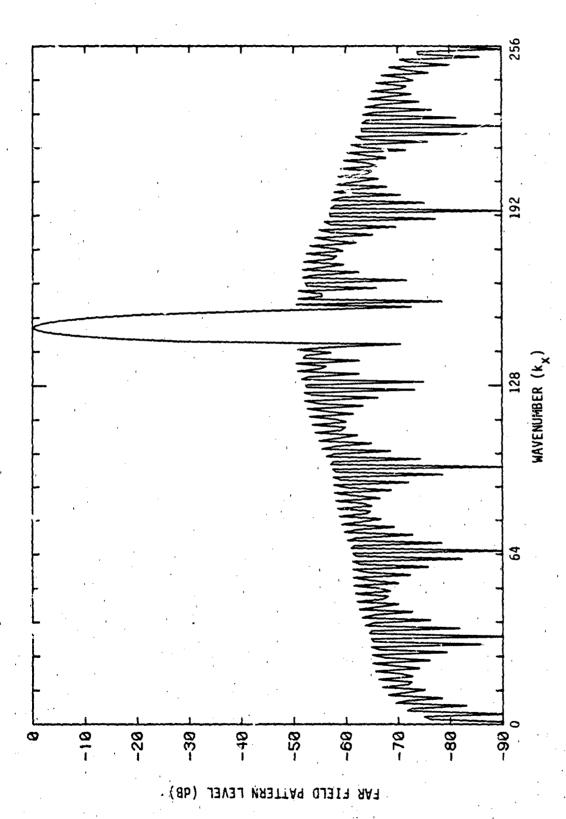


Figure 4. Coupling Product Pattern A · B for the Probe and Reference Spectrum in Figure 3.

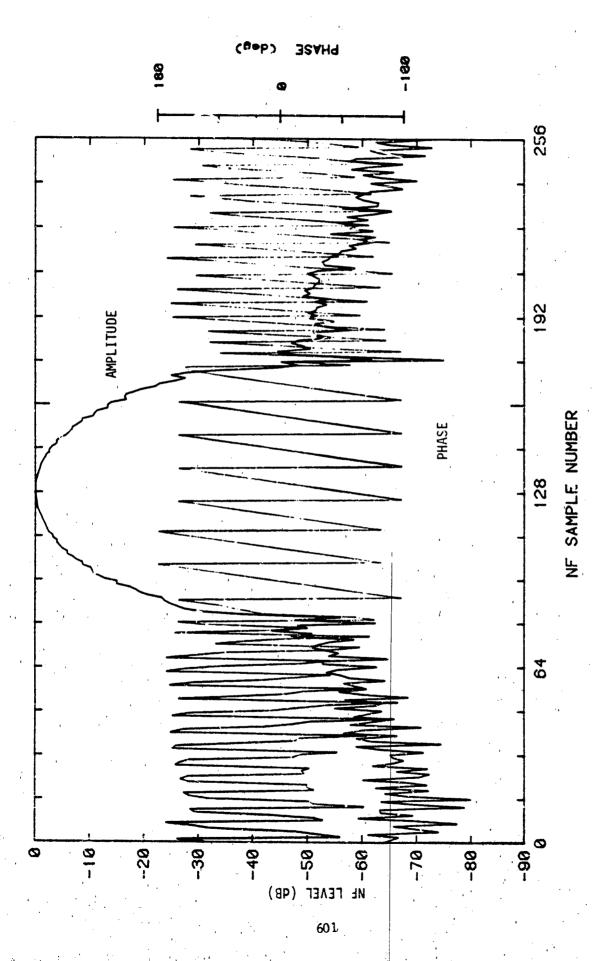
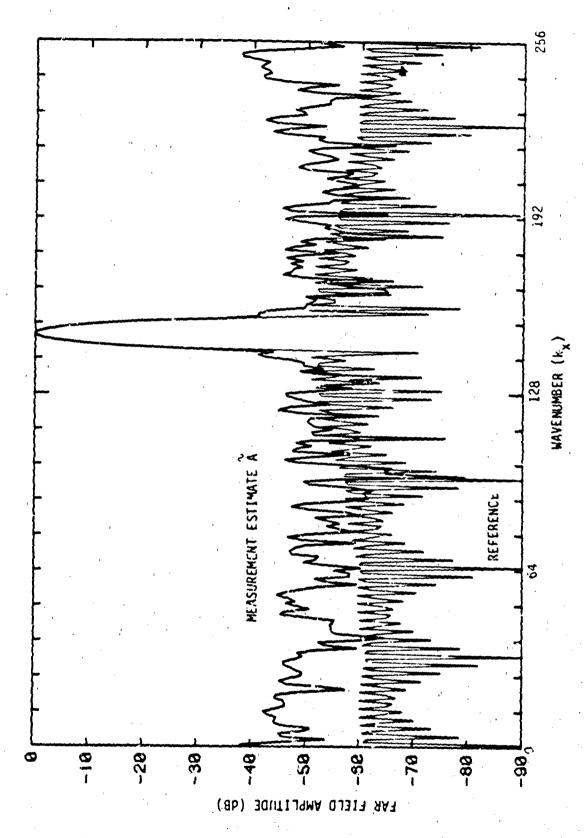


Figure 5. Simulated NF Measurement Plane Voltage for the Coupling Product Pattern of Figure 4. the NF Phase Slope of $46^{\circ}/\lambda$ is due to FF Å Beam Steering of 9.6



igure 6. Overlay Comparison of the Reference Pattern A (light curve) for a 44x Taylor Linear Array Design and its Measurement Estimate A Using a Standard Single Element Open-Ended Wayeouide NF Probe

6.2 <u>Two-element W/G Array Probe</u>

The same sequence is repeated, but now using the new 2-element W/S probe operating in the Δ mode. Figure 7 again shows the reference spectrum $\overline{\mathcal{A}}(\mathsf{k_x})$ overlayed with probe FF amplitude and phase patterns radiated by two different Δ probes, each having an element spacing as annotated. The coupling product pattern for $\overline{A}(k_{\downarrow})$ with the probe having .5% spaced elements is shown in Figure 8. Notice that this new probe attenuates mainbeam wavenumbers by at least 25 dB, has caused the mainbeam to split into two lobes, and has imposed an envelope weighting over the whole sidelobe spectrum. The voltage transform of this coupling product pattern simulates the exacted NF probe voltage, as shown in Figure 9. The dynamic range of the NF voltage amplitude is reduced by 20 dB compared with Figure 5, and higher frequency amplitude variations are more prominent. Again the $46^{\circ}/\lambda$ beam steering gradient in the NF phase is preserved over the high energy NF region, but a 1800 phase shift has also occurred as expected at the center sample in the scan. These error-free NF voltages are then perturbed exactly as was done for the open-ended W/G probe, retransformed, and probe corrected to yield a new measurement estimate,

improvement in the sidelobe region is apparent when compared with the Figure 6 results, and is summarized in Table 1.

Table 1. Sidelobe Level Measurement Accuracy Comparison,

n en	Measured SLL (dB) Ref SLL (dB)				
Probe Type	peak	RMS	peak	RMS	Figure #
1. Open-ended W/G	- 38.0	-51.3	-50.0	-57.9	6
 Two element Δ (.5λ spacing) 	-45.0	-57.0	-50.0	-57.9	10

These results pertain to a probe perfectly consteered with the test antenna's mainbeam pointing direction, and having a null at least as deep as the sidelobe ratio for the test antenna.

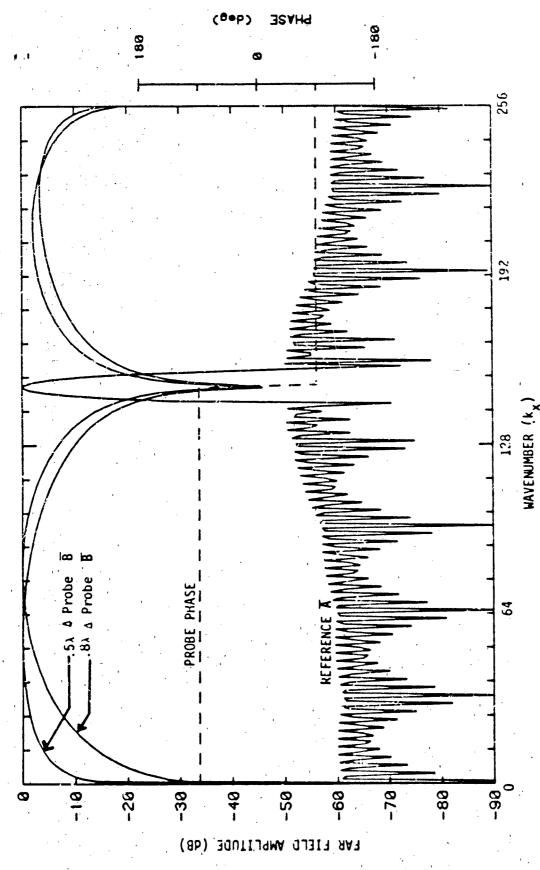


Figure 7. Simulated Reference Array Pattern for a 44% Linear Taylor -50 dB Sidelobe Design with Overlays Showing two A Probe Patters Steered to to 9.60. The A Probes Have Element Spacings as Annotated.

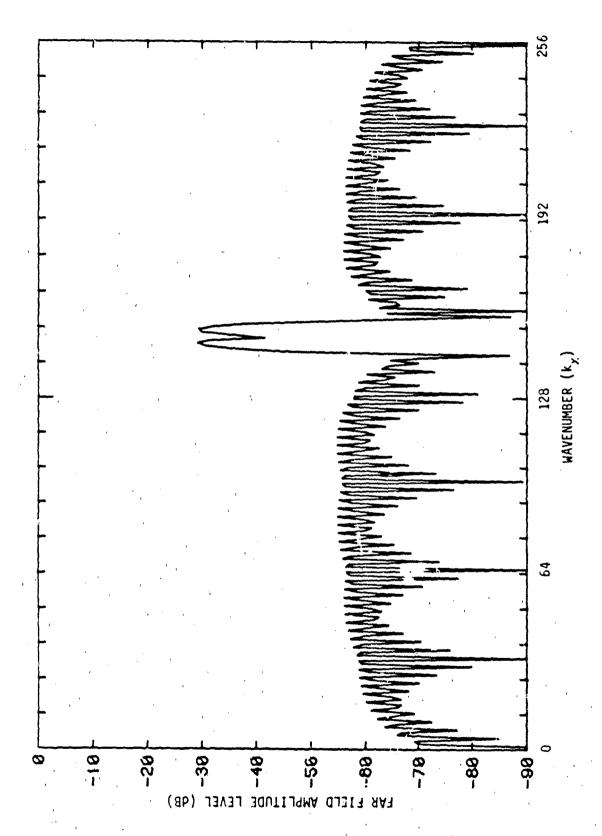


Figure 8. Coupling Product Pattern $A \cdot B$ for the Δ Probe (.5) Element Spacing) and the Reference Spectrum of Figure 7.

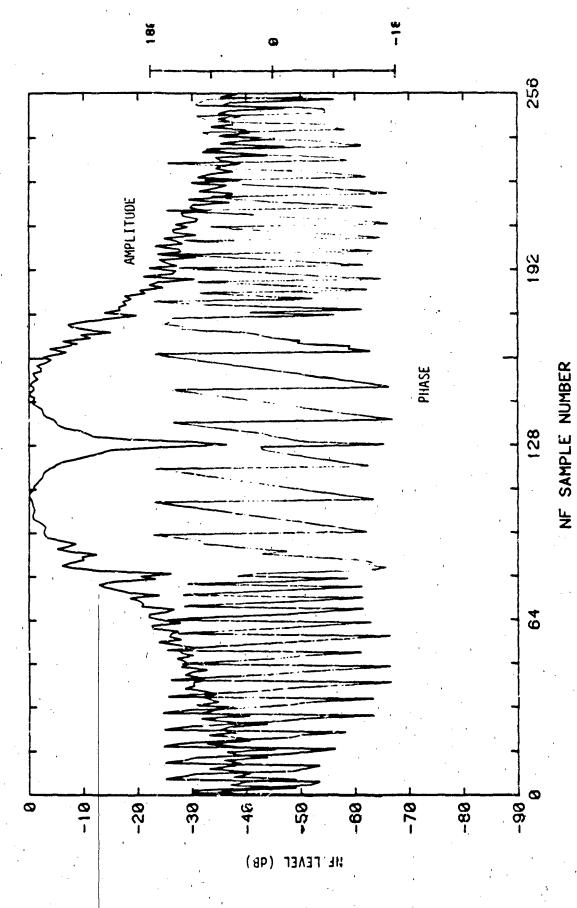


Figure 9. Simulated NF Measur-ment Plane Voltage for the Coupling Product of Figure 8. The Phase Slope of 46/ is due to A Beam Steering

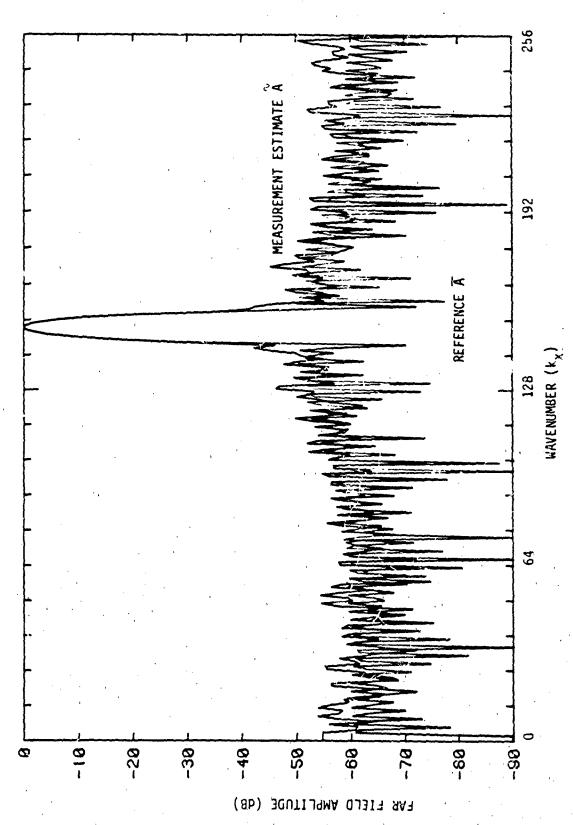


Figure 10. Overlay Comparison of the Reference Array Pattern A (light curve) for a 44x Taylor Linear -50 dB design and its Measurement Estimate A using the Simulated Optimum Probe Having Element Spacing of .5x.

7.0 LOW SIDELOBE TESTING EXPERIMENT

An experiment is presently underway which will evaluate the utility of the new probe to measure very low level reference pattern sidelobes, and will confirm the simulation results of section 5. The planar NF scanner at the National Bureau of Standards in Boulder has been modified to accept the very long AWACS array as sketched in Figure 12. As shown, the 7.6m array will be scanned in sections by translating the array mount laterally in front of the fixed scanner whose maximum horizontal scan dimension is only 3.85 m. Then the sectioned data is merged and processed as if a single sufficiently large scanner were used. This procedure was originally demonstrated under Air Force sponsorship in 1977 [10], and has been shown to be accurate, providing the initial alignment tolerances can be maintained after translation.

NF probing tests will then be conducted using both a standard and a new 2-port Δ pattern probe. FF pattern results will be compared from NF tests with the two probes. Intentionally introduced NF scan errors are expected to produce measurable sidelobe errors at predicted levels (\leq - 50 dB peak) when probed with the standard probe. However, the new \angle probe is expected to discriminate against these intentional NF errors and minimize the mean square error criterion in equation (6).

Additional NF tests are also planned in order to co. ify the validity of known measurement error models which are used to predict expected FF error due to NF sources including positioning error, sample density and extent, and multipath. Test methods and expected results will be described during the presentation.

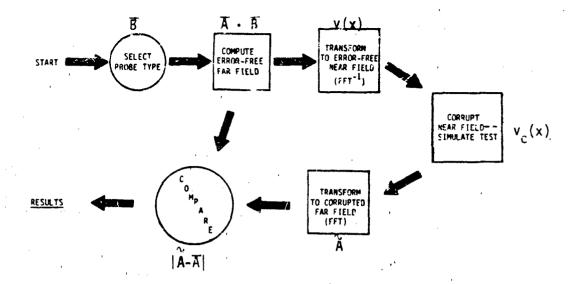


Figure 11. Simulation Flow for Evaluating the Effectiveness of Near Field Probe Patterns

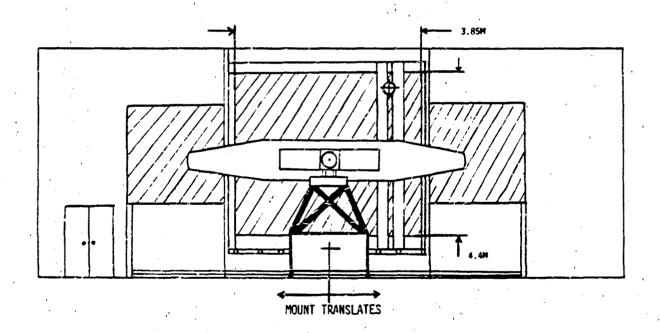


Figure 12. Sketch of Planar Near Field Scanning Facility at National Bureau of Standards

8.0 CONCLUSION

An on-going state-of-the-art planar near field testing demonstration has been described. Its successful completion will establish the fundamental accuracy limits for this testing method when attempting to measure very low level sidelobes from large microwave arrays. A new 2-element probe array has been developed which approximates an optimum probe by spatially filtering the test antenna's mainbeam wavenumbers. Simulations show that such filtering reduces the effect of all NF measurement errors with increase with decreasing NF amplitude. Results of tests should be available in late 1984.

9.0 REFERENCES

- 1. "Non-Pianar Near Field Measurements: Spherical Scanning," <u>AFAL TR-75-38</u>, by Paul F. Wacker, National Bureau of Standards, DDC AD# A012295, May 1975.
- 2. "A Qualitative Survey of Near-Field Measurements," NBSIR 79-1602, Paul F. Wacker, June 1979.
- 3. "Near Field Antenna Measurement on a Cylindrical Surface: A Source Scattering-Matrix Formulation," NBS Technical Note 696, Arthur Yaghjian, Sept 1977.
- 4. "Correction of Near Field Antenna Measurements Made with an Arbitrary but Known Measuring Antenna," by D. Kerns, <u>Electronics Letters</u>, <u>Vol 6 No. 11</u>, May 1970.
- 5. Joy, E. B. and Paris, D. T. "Spatial Sampling and Filtering in Near Field Measurements," IEEE Trans on Ant. and Propagat., Vol AP-20, May 1972.
- 6. "Optimum Probes for Near Field Antenna Measurements on a Plane," PhD. Dissertation, University Microfilms International, #7823710, G. K. Huddleston, August 1978.
- 7. "Planar Near Field Measurements on High Performance Array Antennas," NBSIR 74-380, A. Newell, M.Crawford, July 1974.
- 8. "Ultralow Sidelobe Planar Near Field Measurement Study," K. Grimm, 1982 Allerton Antenna Applications Symposium, Sept 1982.
- 9. "Optimum Near Field Probe Pattern Effectiveness Simulation Part 2: Software Implementation and Preliminary Results," by R. Lawrence, TSC Technical Memo W55-39/rev, May 1984.
- 10. "Flight Line Antenna Pattern Measurements," Allerton Symposium on Antenna Applications, by G. Kirchhoff, B. McKeever, J. Osborn, Sept 1977.

CASE STUDY OF SAMPLE SPACING IN PLANAR NEAR-FIELD MEASUREMENT OF HIGH GAIN ANTENNAS

R. J. Acosta and R. Q. Lee
National Aeronautics and Space Administration
Lewis Research Center
Cleveland, Ohio 44135

INTRODUCTION

The near-field measurement technique has been used extensively for electrically large antennas which can not be easily tested on a far-field range. In reconstructing the far-field antenna patterns from the near-field measurements, a planar configuration may be used with a computation based on the Fast Fourier Transform (FFT). The near-field data are generally sampled over a planar grid at the Nyquist sampling rate of $\lambda_{\rm O}/2$ spacing or less. For electrically large antennas, sampling at the Nyquist rate requires long data acquisition times over which significant system electronic drift may occur. Furthermore, the computer capacity may limit the largest size of the data set. Special data filtering techniques for large data sets have been reported (ref. 1). However, these techniques still require sampling at $\lambda_{\rm O}/2$ spacing.

E. B. Joy (ref. 2) discussed how the sampling spacing may be increased through the use of a priori information on the antenna under test. In this paper, the criterion of sample spacing greater than $\lambda_0/2$ is examined and demonstrated using data obtained with an offset Cassegrain configuration.

FORMULATION

It is well known that the electric field may be represented as a plane wave spectrum (ref. 3)

$$\overline{E}(x,y,z) = \frac{1}{4\pi^2} \iint_{-\infty}^{\infty} \overline{F}(K_x,K_y) e^{-j\overline{K} \bullet \overline{r}} dK_x dK_y$$

where

$$\vec{K} = K_x \hat{x} + K_y \hat{y} + (K_0^2 - K_x^2 - K_y^2)^{1/2} \hat{z}$$

$$K_0 = 2\pi/\lambda_0$$

 $\vec{F}(K_x,K_y)$ is the wave-number spectrum function which may be expressed as the Fourier transform of the aperture field, $\vec{E}(x,y,o)$, in the x-y plane as follows:

$$F(K_x,K_y) = \iint_S E(x,y,o) e^{jK_x x + jK_y y} dxdy$$

As $\tilde{\gamma}$ tends to infinity, as asymptotic value of $\tilde{E}(x,y,z)$ may be found by the method of steepest descent, namely,

$$E(\bar{r}) \sim \frac{jK_{G}\cos\theta}{2\pi r} e^{jK_{O}} F(K_{O}\sin\theta\cos\phi, K_{O}\sin\theta\sin\phi)$$

For plane wave propagating away from the aperture plane at z=o, the propagation constant in the z direction is

$$K_{z} = \left(K_{0}^{2} - K_{x}^{2} - K_{y}^{2}\right)^{1/2} \geq 0$$

Thus, radiating modes exist only in the visible region of the real k-space defined by

$$K_x^2 + K_y^2 \leq K_o^2$$

while evanescent modes exist in its complement space. According to the Nyquist sampling theorem, a function whose spectrum exists and is nonvanishing over finite region of wave-number space may be exactly reproduced from its sample values taken on a periodic lattice at a rate of at least two times the maximum frequency, or in terms of wave number, $2k_{max}$. Since the maximum wave-numbers k_{max} and k_{max} which define the boundary of the visible k_{max} space is $24/\lambda_0$, the Nyquist sample spacing is given by

or .

$$\Delta x \leq \lambda_0/2$$

Similarly,

For a broad spectrum, the radiated power extends over the entire visible region and a sample spacing of $\lambda_0/2$ is required. However, for high gain antennas such as large reflector systems used on communication satellites at geosynchronous orbit, most of the spectral components are concentrated in the central region of the visible space. Consequently, data acquisition at a sample rate greater $\lambda_0/2$ is possible.

If only the spectrum within the region bounded by $(\pm K_x, \pm K_y)$ is of significance, the sample spacing may then be increased by k_x /K and k_y /K where k_x and k_y /K k_y . That is

$$\Delta x = \pi/K_{x}$$

$$\Delta y = \pi/K_y$$

where $K_{\mathbf{x}} \leftarrow K_{\mathbf{x}}$ and $K_{\mathbf{y}} \leftarrow K_{\mathbf{y}}$ and $K_{\mathbf{y}} \leftarrow K_{\mathbf{y}}$ and $K_{\mathbf{y}} \leftarrow K_{\mathbf{y}}$

By expressing the wave-number, k_{max} , in spherical coordinate, i.e., $k_{\text{max}} = 2\pi/\lambda \quad \sin \theta \quad , \text{ the maximum elevation angle of coverage,}$

 $heta_{ ext{max}}$, as a function of sample spacing, Δ , can be computed from

$$\theta_{\text{max}} = \sin^{-1} (\lambda_{\Omega}/2\Delta)$$

For illustration, a few computations of $\theta_{m\in X}$ versus Δ are tabulated below

$$\frac{\Delta}{\Theta_{\text{max}}} = \frac{\lambda_{\text{o}}/2}{90^{\circ}} \frac{\lambda_{\text{o}}}{30^{\circ}} \frac{2\lambda_{\text{o}}}{15^{\circ}} \frac{3\lambda_{\text{o}}}{10^{\circ}} \frac{5\lambda_{\text{o}}}{3^{\circ}} \frac{20\lambda_{\text{o}}}{3^{\circ}}$$

As indicated above when the sample spacing is increased, only a small angular sector of the far-field can be accurately computed by the FFT. For antennas with broader beams sample spacings approaching λ /2 are required.

DISCUSSION AND RESULT

The effects of sampling at greater than the Nyquist rate were studied experimentally for a dual offset Cassegrain Configuration designed by TRW for NASA Lewis Research Center (ref. 4). The main reflector is parabolic with the following characteristics:

Dish diameter = 257.89 $\lambda_{\rm c}$

Focal length = $318.74 \lambda_{0}$

Offset length = 135.51 λ_{Λ}

Centerfrequency t = 28.5 GHz ($\lambda_0 = 1.05 \text{ cm}$)

The reflector is illuminated by a linearly polarized feed at the focus with a 18 db edge taper. The hyperboloidal subreflector has a magnification factor of z. The antenna was tested with the planar near-field range currently in operation at the NASA Lewis Research Center, Near-field Centerline data were acquired at $\lambda_0/2$ spacing. The radiation patterns were reconstructed from the centerline near-field data set with a one-dimensional FFT algorithm. For sample spacing greater than $\lambda_0/2$ appropriate subsects were selected from the original data set. The effects of the sample spacings are illustrated in the antenna patterns shown in figures 1(a) to (e).

This antenna patterns showed no perceptible changes from data taken at 0.5, 1, and $2\lambda_0$ spacing. Sidelobe degradation starts to occur at approximately $4\lambda_0$ spacing. The main beam is slightly modified by a sample spacing of up to $8\lambda_0$. For antennas used in space communication application where the beam widths are in the order of 0.3° are often desired, a good choice of sample spacing will be between 2 to $4\lambda_0$.

Spectrum characteristics with cut-off power levels at -30, -40, and -50 dB are shown in figures 2(a) to (c). These spectrum plots were obtained with near-field data taken at a λ /2 spacing. As shown, spectral components with higher cut-off power level occupies a smaller visible region of the K-space, and thus a smaller wave number limit K_x and K_y . This corresponds to sample spacing greater than λ /2.

Figures 3(a) to (c) compares far-field antenna pattern from near-field data taken at $\lambda_0/2$ spacing (dotted line) and spacings implied by the spectrum cut-off plots (solid line). From these figures we can conclude that neglecting data below -40 dB is consistent with sample spacing.

In general, desired pattern accuracy, desired angular range, and available instrumentation dynamic range must be taken into consideration when selecting sample spacing.

ACKNOWLEDGEMENT

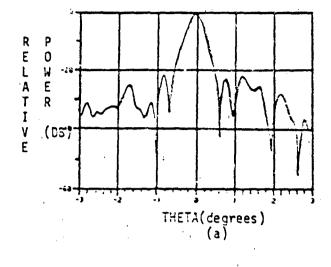
The authors want to express their gratitude to R. Zakrajsek and R. Kunaih for providing the near-field data measurements and to Dr. C. Raquet for his helpful suggestions.

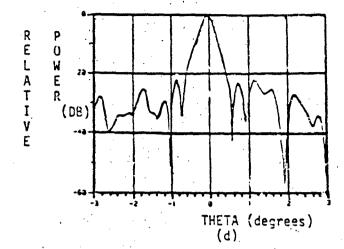
KEFERENCES

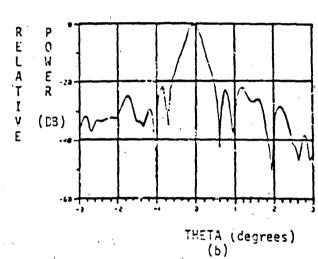
- E. B. Joy and D. T. Paris, "Spatial Sampling and Filtering in Near-Field Measurements," IEEE Trans. AP-20, F253, May 1972.
- 2. E. B. Joy "Spatial Sampling and Filtering in Near-Field Measurements".

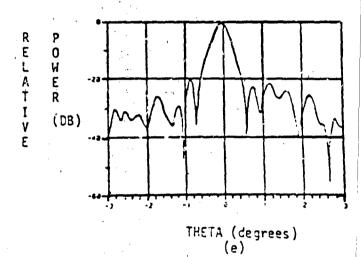
 Ph.D. Thesis (1970), University Microfilms.
- 3. H. C. Booker and P. C. Clemmow, 'The Concept of an Angular Spectrum of Plane Waves and its Relation to that of Polar Diagram and Aperture Distribution," Proc. Inst. Elec. Eng., Vol. 97, pt III; P11-17, 1950.

4. NASA Report CR 174543, 30/20 GHz "Multiple Beam Antenna for Space Communication Satellites," TRW Final Report. (Contract No. NAS3-22499).









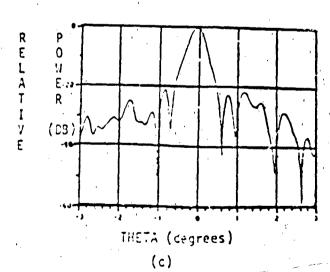
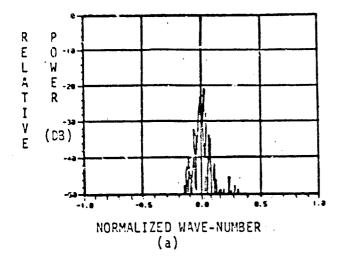
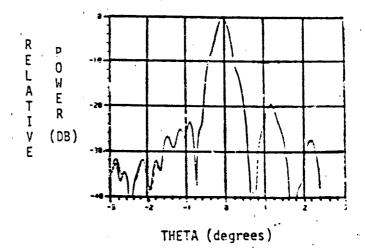


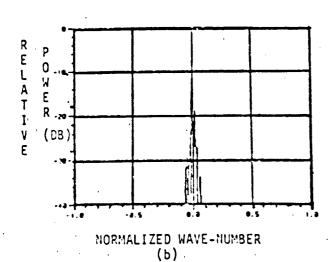
FIGURE 1. RELATIVE POWER PATTERN
ASTA FUNCTION OF
ELEVATION ANGLE FOR
DIFFERENT SAMPLE SPACING

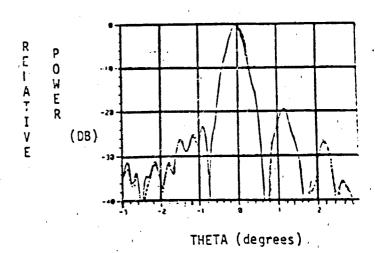
(a) $\lambda_0/2$, b) λ_0 , c) $2\lambda_0$, d) $4\lambda_0$, e) $8\lambda_0$

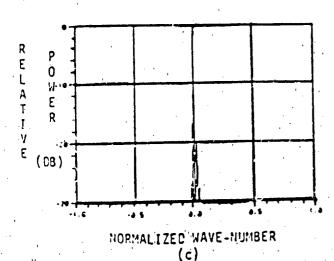
FIGURE 3 RELATIVE POWER PATTERN
AS A FUNCTION OF ELECATION
ANGLE

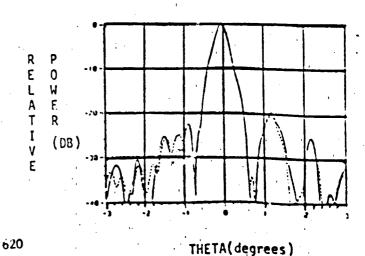












Comparison of Measured and Calculate & Mutual Coupling in the Near Field Between Microsses Antennas

Carl F. Stubenrauch and Michael H. Francis
National Bureau of Standards
Boulder, Colorado 80303

Measurements of near-field mutual coupling were performed between two moderate sized microwave antenns and compared to coupling calculated using recently developed computer programs. Required input data for the programs are the complex far-field radiation patterns of the antennas and various geometrical factors describing the relative positions and orientations of the two ancennas. Experimentally determined and calculated coupling as a function of both transverse displacement and separation agree closely except for a constant offset observed in some cases.

Key words: co-sited antennas, coupling loss, far fields, mutual coupling, near fields.

1. Introduction

Recent theoretical work at the National Bureau of Standards has led to the development of computer programs which can efficiently calculate the coupling loss between two antennas regardless of their separation. Thus near-field as well as far-field coupling may be calculated.

The required data for the calculation are the far-field patterns (amplitude and phase) for the two antennas, and the geometrical factors which define the relative orientations and separation of the two antennas.

Two computer programs have been developed which calculate the coupling loss, b'_0/a_0 , between two antennas as a function of transverse displacement and as a function of radial displacement. b'_0 is the amplitude of the wave emerging from the waveguide feed of the receiving antenna and a_0 is the amplitude of the wave incident in the waveguide feed of the transmitting antenna, as illustrated in figure 1. The program CUPLNF, which calculates coupling versus transverse displacement, was documented previously². Program CUPLZ, for coupling versus longitudinal displacement, is discussed in¹.

It is the purpose of this study to compare coupling losses measured for a variety of geometrical situations to the corresponding losses calculated using the computer programs. Measurements were performed using the NBS near-field scanner and data were obtained for both transverse and radial displacements. Far-field patterns used in the calculation of coupling loss were obtained from transformed planar near-field measurements³.

2. Description of Measurement Procedure

In order to experimentally verify the coupling formulation, coupling between two pairs of antennas was measured. The first antenna was a 1.2 meter paraboloidal reflector antenna having a power gain of approximately 30 dB and a half-power beamwidth of 4.5°. The second antenna was a 25-element microstrip array having a power gain of approximately 22 dB and a half-power beamwidth of 15°. Most of the coupling measurements were performed on this antenna pair. Some preliminary tests were also performed to measure the coupling between the reflector antenna and an openended section of WR187 waveguide of the type which is often used as the probe antenna in near-field measurements.

Far-field radiation patterns necessary for the calculation of near-field coupling were obtained from probe-corrected near-field measurements on the reflector and array antennas. The far-field pattern of the open-ended waveguide was measured directly.

The region over which a valid far-field pattern is obtained using near-field techniques is determined by the aperture size and scan areas as was shown by the error analysis of Yaghjian⁴ and the experimental work of Newell and Crawford³. From this work it can be demonstrated that the patterns for the antennas used are valid to an angle of approximately 60° off boresight for the reflector antenna and 77° off boresight for the array antenna. The waveguide probe pattern is valid over the entire forward hemisphere.

Measurements were performed at the NBS near-field measurement facility which allows precise adjustment and determination of the relative orientation of the two antennas. The reflector antenna was mounted on a rotator which allowed rotation of the antenna about a vertical axis. This rotator was mounted on a movable cart which travels on a pair of precision rails which are aligned to be perpendicular to the plane of the near-field scanner thus allowing variation of the separation distance between the two antennas.

The second antenna, either the microstrip array or the waveguide probe, was mounted on the x-y positioner of the NBS near-field scanner. The antennas were carefully aligned so that the relationship between the coordinate systems in which the far-field patterns of the antennas were obtained and the common coordinate system could be accurately determined. Two wedges were also employed in mounting the array antenna which allowed it to be rotated by angles of 21.6° and 30.3° about a vertical axis.

In all cases, the polarization vectors for the antennas were parallel and oriented in the y-direction. The current versions of the coupling programs only calculate coupling due to a single component of the far field of each antenna. Hence, one can only calculate meaningful coupling values for coupling where the polarization vectors are parallel. Because of this limitation, coupling measurements were only made for cases where the antennas were oriented with their nominal polarization vectors parallel.

The measurements were performed for coupling loss as a function of x and y position for various values of θ_T and θ_R , where θ_T and θ_R are the angles by which the transmitting or receiving antenna boresight direction is rotated with respect to the common coordinate system as illustrated in figure 2. Measurements were also performed for coupling as a function of separation for various values of θ_T and θ_R . The comparison between measured and calculated coupling will be discussed in section 3 for transverse displacement and in section 4 for longitudinal displacement.

3. Coupling Loss Versus Transverse Displacement

We summarize here the major result of the mathematical development in order to be able to discuss the results. It has been shown by Yaghjian^{1,2} that the coupling between two antennas, neglecting multiple reflections, is given by,

$$\frac{a_0'(\underline{R})}{a_0} = -C' \iint_{K < k} \frac{\underline{f}(\underline{k}) \cdot \underline{f}'(-\underline{k})e^{i\gamma d} e^{i\underline{K} \cdot \underline{R}}}{\gamma} d\underline{K}$$
 (1)

where C' is a constant which includes the mismatch correction and \underline{f} and \underline{f}' are the free space, far electric field radiation pattern of the transmitting and receiving antennas respectively. The

propagation vector is $\underline{k} = k_x \hat{e}_x + k_y \hat{e}_y \pm \gamma \hat{e}_z = \underline{K} \pm \gamma \hat{e}_z$. $|k| = 2\pi/\lambda$ with λ the wavelength. The location of the receiving antenna in the common coordinate system is $\underline{r} = \underline{R} + d \hat{e}_z$. The $e^{-i\omega t}$ time convention is employed throughout.

Yaghjian has also shown that, for most cases, the integration range may be limited to $|K/k| < (D_T + D_R)/d$ where D_T and D_R are the diameters of the smallest spheres circumscribing the radiating part of each antenna (including feeds, struts, edges and all other parts of the antennas which radiate or affect the reception significantly). This restriction of the integration limits amounts to making use of the fact that only those rays which originate from a point on one antenna and actually intersect a part of the other antenna take part in the interaction. range should give good results for $|R| < (D_T + D_R)$. restriction of the integration range also has the effect of artificially bandlimiting the integrand so that the sampling theorem may be applied in order to convert the integration to a summation. Two parameters, XLIM and BFAC, control the actual integration range and increment employed in the program. actual integration range is

$$\frac{K_{\text{max}}}{K} = \left(\frac{D_T + D_R}{d}\right) \circ XLIM . \tag{2}$$

The actual increment value is

$$\frac{\Delta k_{x}}{k} = \frac{\Delta k_{y}}{k} = \frac{d}{(D_{T} + D_{R}) \cdot XLIM} \cdot \frac{1}{BFAC} . \tag{3}$$

We also note that $K_{\mbox{ma}\,\mbox{x}}/k$ is never allowed to exceed 0.9 in the program.

Numerous measurements were performed to investigate the technique under a variety of circumstances⁵. In this paper, however, we only present the results for a limited number of cases. As will be seen, agreement between measured and calculated coupling loss was generally good. The one case where a severe discrepancy was noted will be shown and discussed. In addition, we will illustrate the effect of changing the integration limit and the increment on the results of the calculation.

For each case, we present a plot of measured and calculated coupling loss for a transverse displacement in the x or y direction. In all cases, rotations are about the y (vertical) axis. Polarization of each antenna is nominally vertical. Rotations were limited to \pm 30° for both the array and reflector antennas because rotation to angles greater than this would require a large angular segment of radiation pattern which could not be determined from the near-field measurements.

It is noted that the magnitude of the measured, compared to the calculated curves, seems to diverge slowly as the antennas are turned so that their boresight direction deviates from the z-axis in the common coordinate system. In almost every case, the experimentally determined coupling is larger than the calculated coupling. The average discrepancy is approximately 1 dB with a maximum observed discrepancy of 3 dB. A number of possible causes of the discrepancy have been investigated including errors in the program, improper normalization, and erroneous insertion loss measurement at the reference point. However, these possible sources of error are not large enough to account for the observed discrepancy.

In figures 3 through 6, three cases of measured and calculated coupling loss are illustrated for transverse displacement of the microstrip antenna. The first two show good agreement between the experimentally and theoretically obtained The first case illustrates the situation where the losses. boresight directions of the two antennas are parallel to each other and the z-coordinate of the common coordinate system. As is to be expected, the pattern is quite symmetrical with relatively little structure. Figure 4 illustrates a case where each antenna is steered with its boresight direction away from the common coordinate system z-axis. The peaks in the coupling occur where the main beam of one of the two antennas approximately faces the center of the other antenna. Good agreement is observed to coupling level below -45 dB.

Figure 5 illustrates the only example of poor agreement in the cases studied. We note that in this case, the coupling level is extremely low (< -50 dB). In this case, the effect of the coupling through the cross-polarized components may be significant and it should no longer be neglected. In fact, agreement at these levels in other cases may be fortuitous. We do note that while the shape of the measured and calculated patterns are dissimilar, that the levels are comparable indicating that the cross-polarized coupling is of the same magnitude as the co-polarized coupling.

As is discussed previously, the coupling calculation should give good results for $|R| < (D_T + D_R)$ (= 1.4 meters for our case). The calculated coupling is generally good to this distance.

Finally, in figure 6, we illustrate the effect of changing XLIM and BFAC. In all previously presented results, calculations were performed with XLIM = BFAC = 2. In this figure we see the results for values of XLIM and BFAC equal to 1 and 2. These results are typical of those obtained for the other cases. The agreement between the various curves is very good up to a transverse displacement of about 1 meter. Beyond 1 meter, the various examples diverge with the best result, as expected, being for XLIM and BFAC both set to 2. We see that the results for XLIM = 1, BFAC = 2, and XLIM = 2, BFAC = 1 are essentially identical. This indicates that the size of the increment is more important than the range of the integral since for these two cases the

increment is the same, but the limit is larger for the second case as can be seen from equations 2 and 3.

4. Coupling Loss Versus Separation

As for the transverse case, we begin by briefly reviewing the mathematical results relating to the calculation of coupling versus longitudinal displacement. As has been discussed by Yaghjian¹ the calculation may not be completed by simply performing the γ transform of (1) because the necessary increment size requires impractical array sizes and computation time. However, the coupling loss satisfies the scalar wave equation, and, as a result, can be expressed in terms of spherical wave functions. Further, since the choice of the polar axis is arbitrary, the longitudinal axis may be chosen as the polar axis with the resulting simplified expression for the coupling:

$$\frac{b_0'(d)}{a_0} = \sum_{n=0}^{\infty} B_n h_n^{(1)}(kd), \quad d > (D_T + D_R)/2$$
 (4)

where we have

$$B_{n} = \frac{(2n+1)}{2} (i)^{n} \int_{0}^{\pi} \int_{0}^{2\pi} \underline{f}' \cdot \underline{f} P_{n}(\cos\theta_{0}) \sin\theta_{0} d\phi_{0} d\theta_{0}.$$
 (5)

The spherical Hankel function of the first kind, $h_n^{(1)}$ represents outgoing waves with the chosen time convention and $P_n(\cos\theta)$ is the Legendre polynomial.

A program, CUPLZ, was written to calculate the coupling loss between two antennas as a function of longitudinal displacement employing the above theory. The calculated coupling obtained from this program was compared to the experimentally obtained results.

In figures 7 and 8 we show comparisons between measured coupling loss and the loss calculated using CUPLZ. In both cases, the loss was measured for a separation range of 1 to 4 meters. The measured curves (dotted) indicate the envelope of the measured loss pattern. The measurements exhibit a rapid oscillation due to multiple reflections between the antennas, an effect not treated in the theory. As may be seen, the agreement between the measured and calculated curves is good with the exception of an offset, which is similar to that observed in the transverse displacement case.

6. Corclusions

It has been shown that the programs CUPLNF and CUPLZ give good results for predicting the coupling between two antennas in the near-field region. In particular, patterns for displacements in the transverse direction and the longitudinal direction show excellent agreement except when the coupling level is very low

(> 45 dB). If it is desired to predict coupling to very low levels, or for the more general case where the antenna polarization vectors are not parallel, it will be necessary to include both polarization components of the far field. For some situations, a constant offset was observed, however, it is not great enough to affect the utility of the programs for electromagnetic compatibility purposes.

The authors wish to thank Dr. Arthur D. Yaghjian and Allen C. Newell of NBS for many helpful discussions, and Douglas P. Kremer and Douglas T. Tamura for performing the measurements. The support of Dr. Ramon C. Baird of NBS is also appreciated. The work was partially supported by the Electromagnetic Compatibility Analysis Center of the Department of Defense.

7. References

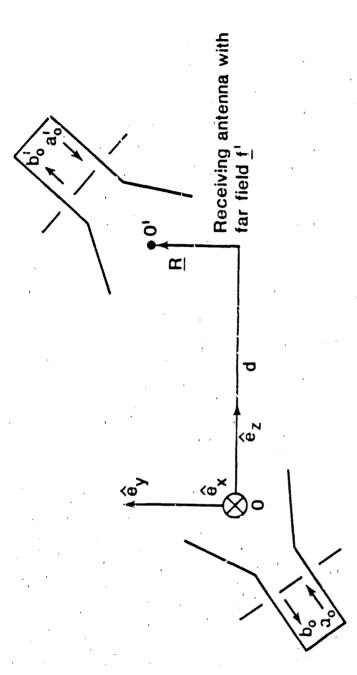
- Yaghjian, A. D. (1982) Efficient computation of antenna coupling and fields within the near-field region, <u>IEEE Trans.</u> <u>Antennas Propag.</u>, AP-30, 113-128.
- Stubenrauch, C. F.; Yaghjian, A. D. (1981) <u>Determination of mutual coupling between co-sited microwave antennas and calculation of near-zone electric field.</u> Nat. Bur. Stand. (U.S.), NBSIR 80-1630.
- 3. Newell A. C.: Crawford, M. L. (1974) <u>Planar near-field</u>

 measurements on high performance array antennas. Nat. Bur.

 Stand. (U.S.), NBSIR 74-380.
- 4. Yaghjian, A. D. (1975) <u>Upper-bound errors in far-field antenna</u>

 parameters determined from planar near-field measurements,

 Part 1: Aralysis. Nat. Bur. Stand. (U.S.), Tech. Note 667.
- 5. Stubenrauch, C. F. and Francis, M. H. (1984) Comparison of Measured and Calculated Mutual Coupling in the Near (1984) Between Microwave Antennas, Nat. Bur. Stand. (U.S.) NBSIR 84-3010.



Transmitting antenna with far field t

Figure 1. Schematic of two arbitrarily oriented and separated antennas. Coupling loss is $b_0'(R,d)/a_0$. For transverse displacement, d is held constant; for radial displacement, R=0.

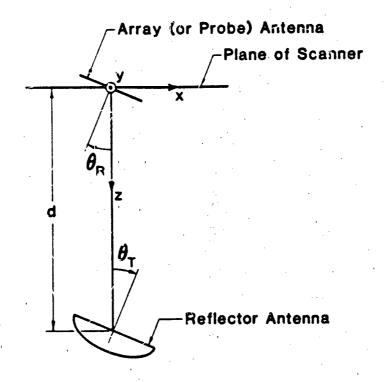


Figure 2. Definition of simplified coordinate systems for mutual coupling measurements.

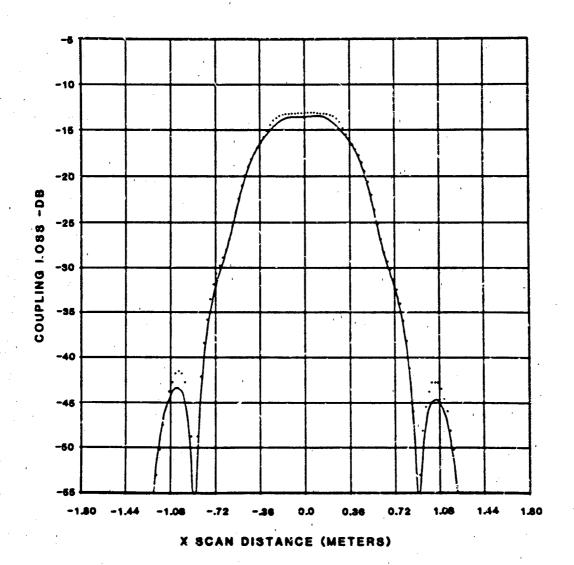


Figure 3. Comparison of measured and calculated coupling loss between reflector and microstrip array antennas. x-scan, $\theta_T = 0^\circ$, $\theta_R = 0^\circ$, d = 3.0 meters. Solid curve - calculated pattern, dotted curve - measured pattern.

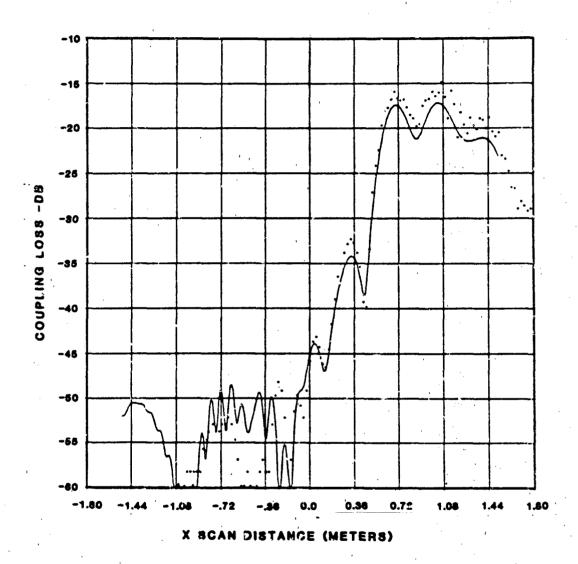


Figure 4. Comparison of measured and calculated coupling loss between reflector and microstrip array antennas. x-scan, θ_T = -30°, θ_R = -21.6°, d = 2.0 meters. Solid curve - calculated pattern, dotted curve - measured pattern.

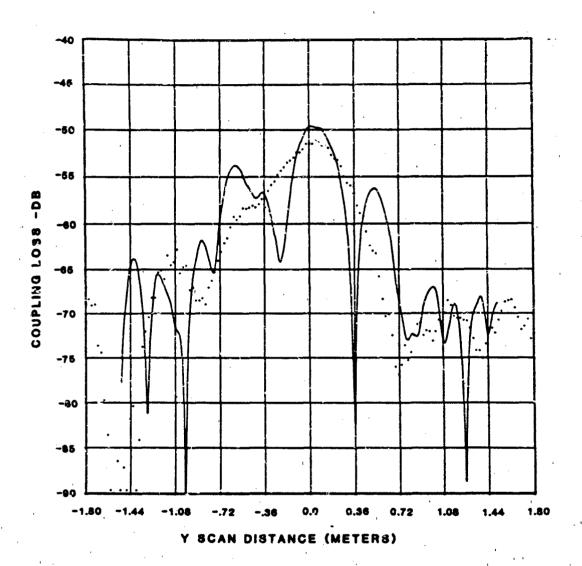


Figure 5. Comparison of measured and calculated coupling loss between reflector and microstrip array antennas. y-scan, θ_T = -20°, θ_R = -21.6°, d = 4.0 meters. Solid curve - calculated pattern, dotted curve - measured pattern.

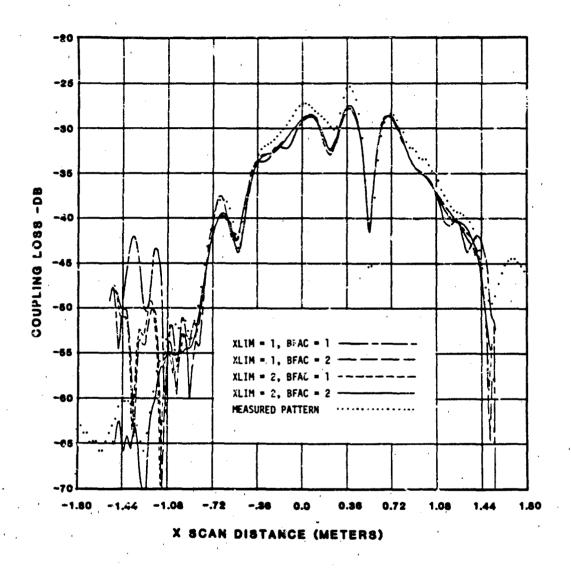


Figure 6. Comparison of coupling losses calculated using various values of the parameters XLIM and BFAC to measured losses. x-scan, $\theta_T \approx 0^\circ$, $\theta_R \approx -21.6^\circ$, d = 3.0 meters.

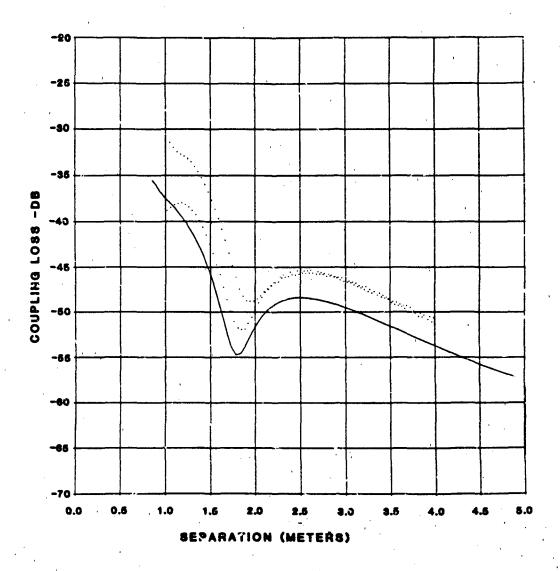


Figure 7. Comparison of measured and calculated coupling loss vs. separation between reflector and microstrip array antennas. $\theta_T = 20^\circ$, $\theta_R = -21.6^\circ$. Solid curve - calculated pattern, dotted lines indicate the envelope of the measured coupling loss.

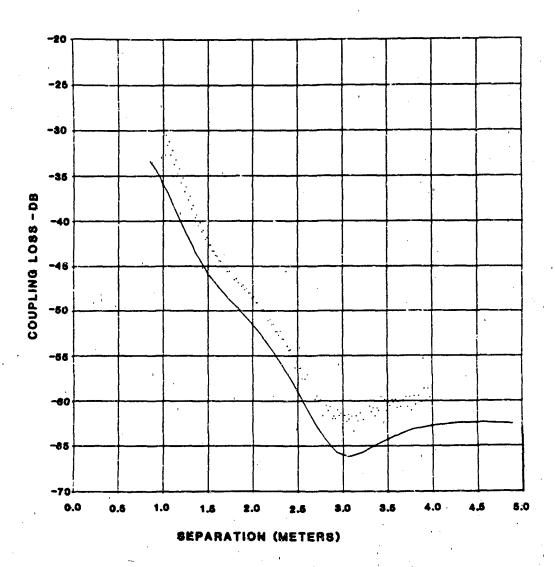


Figure 8. Comparison of measured and calculated coupling loss vs. separation between reflector and microstrip array antennas. $g_{\rm T} = 30^{\circ}$, $g_{\rm R} = -21.6^{\circ}$. Solid curve - calculated pattern, dotted lines indicate the envelope of the measured coupling loss.

PREDICTION OF LOW SIDELOBE ANTENNA PERFORMANCE IN THE PRESENCE OF LARGE SCATTERERS USING RF FIELD PROBE TECHNIQUES

J. Wojtowicz, R. Konapelsky, J. Havrilla, R. Vogelsang and K. Ramsey

September 19-21, 1984

Prepared For

1984 Antenna Applications Symposim
University of Illinois
Urbana, Illinois

Ву

Westinghouse Electric Corporation

Systems Development Divisions

Baltimore, Maryland

Modern airborne radar systems that demand narrow beamwidths and low delobes require large antenna apertures. As the antennas become larger and delobe requirements tighter, the effects of scattering from the aircraft ructure becomes more pronounced and the resulting antenna performance can come quite degraded. It would therefore be useful to know beforehand what fect the aircraft will have on the performance of the antenna. A brute ree method of obtaining this information would be to build and mount a full ale antenna on the plane, but this would be quite expensive due to the high st of fabricating the antenna. This paper presents a more practical isurement scheme using a full scale model of the plan and a field probe sembly.

The field probe track assembly is mounted on the aircraft in the same cation as the proposed radar antenna. With a RF signal source in the fareld, the field probe is moved over the whole area of the antenna aperture i data is taken at each point corresponding to a radiating element cation. These complex data points are then processed along with the coretical antenna aperture distribution to obtain a predicted actual antenna catern in the presence of the aircraft.

Experimental Setup

The investigation described in this paper was conducted at the stinghouse Ridge Road Antenna Range in Baltimore, Md. The range used was a 10 ft, elevated X-Band range, with a large 3-axis positioner mounted on the of a 4-story building.

The hull of a government surplus airplane was obtained and mounted upside m on the 3-axis positioner. The upside down mounting provided better less to the proposed antenna mounting site which was under the forward part the fuselage and off to one side. This configuration also helped eliminate wanted reflections from the positioner itself (See figure 1).

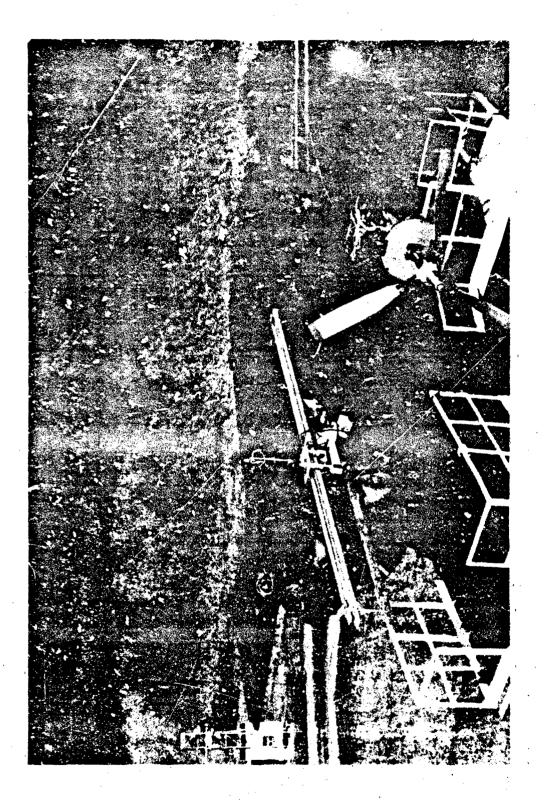


Figure 1. Mounting Configuration

The field probe assembly used was a Scientific Atlanta field probe with a 39-foot track and a servo controlled carriage that could be moved along the full length of the track. The assembly was mounted on the plane such that the field probe element would completely sweep through the proposed antenna aperture, which was approximately 15 ft long by 16 in. high. In order to reduce the number of data points that needed to be taken, a vertical slotted waveguide stick that completely covered the height of the aperture was used as the field probe element. This reduced the data taking and processing from a two dimensional case to a one dimensional case (See figure 2).

Extreme care was taken in the mounting of the field probe to insure that the track was as straight as possible and that the carriage and field probe element experienced little "wobble" as they moved down the track. Sturdy mounting structures and optical alignment techniques were employed. A piece of absorber was attached to the back of the stick to reduce backlobe reflections.

Figure 3 shows the block diagram for the experimental setup. The APC norm is a reference horn for the receiver that allows it to lock onto the correct frequency. Channel A is the measured data from the field probe and channel B is the reference signal for the measurement. The high speed RF switch continuously switches between these two channels at a high rate. The computer reads three values from the receiver. The first is the amplitude of A, the second is the amplitude of B, and the third is the difference in phase between A and B. The computer also reads the position of the field probe from the field probe controller.

The procedure for obtaining a set of data is as follows. First the field probe track must be aligned perpendicular to the range axis. This is accomplished by positioning the field probe at one end of the track and then slowly moving it while monitoring the phase on the pattern recorder. If the track is misaligned, the phase response will have a slope proportionate to the misalignment (See figure 4). The position of the track is adjusted using the lower azimuth table until the phase response is a straight line, at which point the track is boresighted.

Figure 2. Field Probe Element

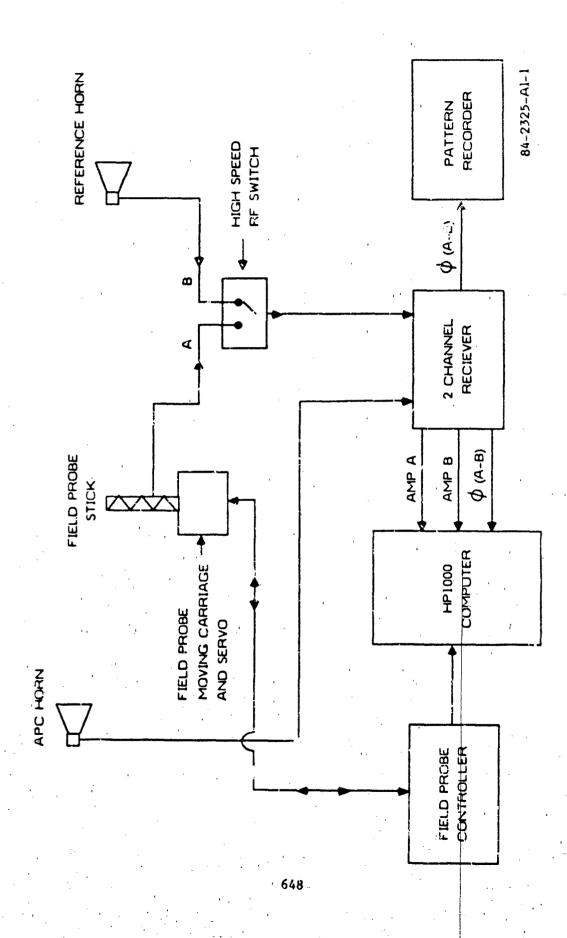


Fig. re 3. Experiment Block Diagram

ではれたがく タインスト あっている (Andrews Control of Andrews Co

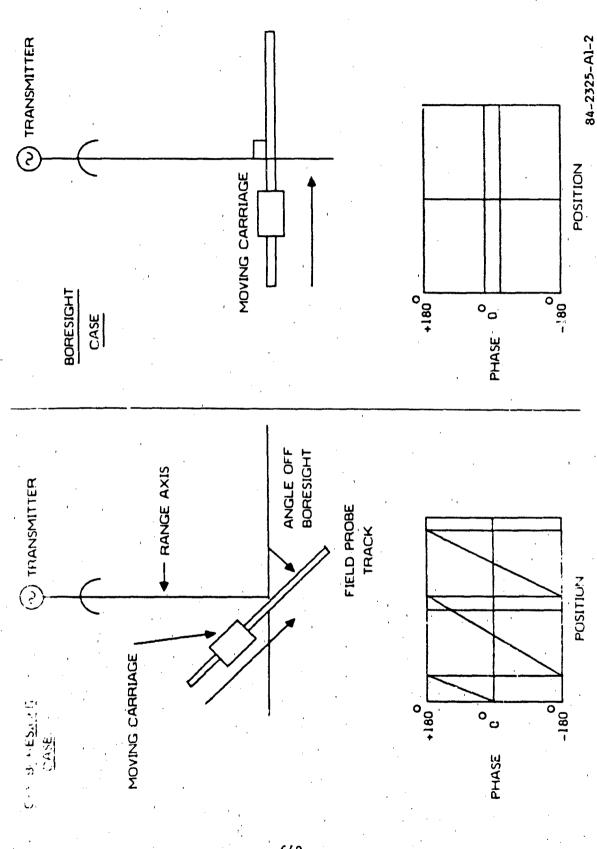


Figure 4. Boresighting

Once the field probe assembly is boresighted, the probe is once again positioned at one end of the track, and then slowly moved down toward the other end. The computer continuously monitors the position of the probe and once the probe reaches the position of the first radiating element of the antenna it takes ten reads of the three receiver values. The average of these ten reads is then stored along with the appropriate probe position. This process is repeated for each radiating position. During the run, the phase data is monitored on the pattern recorder. If a malfunction should occur in the setup during a run such as the receiver losing lock, this could be detected by a larger "glitch" in the phase and the run could immediately be stopped. Once a data run has been completed the data is stored on a disc.

After a sufficient amount of data is taken, it can then be processed. The processed data is to be presented in three ways. The first is a plot of the amplitude of the scattering data versus probe position. This information is obtained by taking the difference of the amplitude of channels A and B. The second is a plot of the phase versus probe position. The third way is in the format of a far field antenna pattern. The amplitude and phase of the scattering information is multiplied by a typical theoretical amplitude distribution and then processed using a Fast Fourier Transform (FFT). If desired, the aperture weights can be further modified by a random complex multiplier, prior to the FFT, to simulate aperture errors due to fabrication and aperture phase tuning. A typical example of a set of processed data is shown in figure 5.

During the early part of the experiment a high frequency ripple was noticed in the measured phase data. After a careful investigation, it was determined that the major cause of this ripple was due to field probe wobble. Most of this effect was removed by mechanical adjustments to the probe assembly. To further remedy this situation, a software filter was developed that used an averaging technique to smooth out this high frequency ripple. Figure 6 shows the same set of data filtered and unfiltered. The corresponding far field patterns are shown in figure 7.

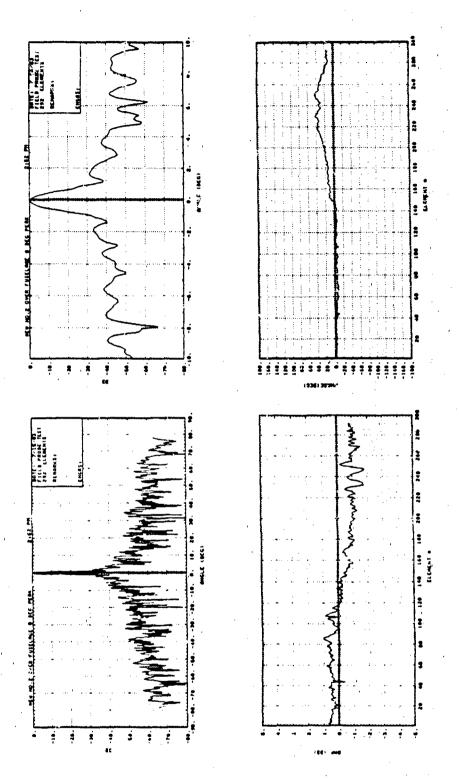


Figure 5. Example of Processed Data

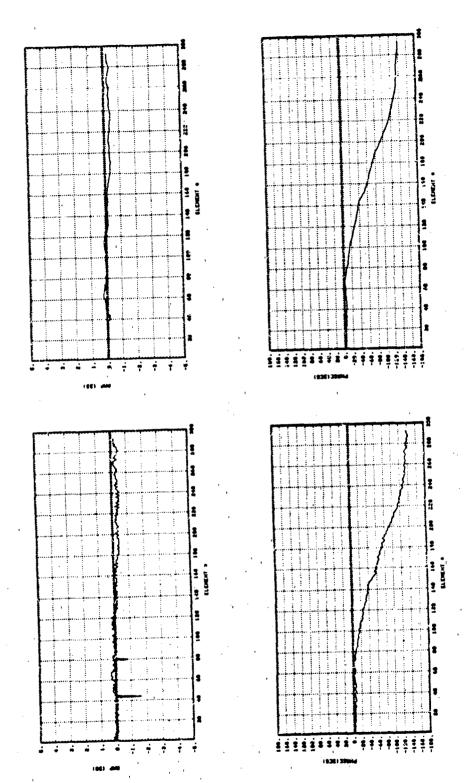


Figure 6. Effects of Filtering

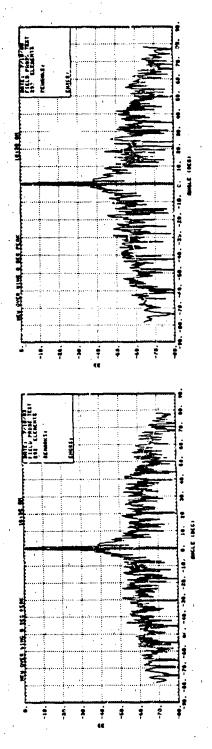


Figure 7. Far Field Patterns of Filtered and Unfiltered Data

3. Data

Data was taken for two basic aircraft/antenna geometeries. The first was for the case of the antenna looking out directly over the wing, and the second was for the case of looking across the fuselage. These two cases are shown schematically in figure 8 and will be referred to from now on as over the wing, and over the fuselage.

The effects of mechanical elevation scanning were simulated as shown in figure 9. First the airplane is tilted to some angle using the 3-axis positioner, and then the field prope element is mechanically boresighted using a level. Positive angles correspond to looking into the aircraft and negative angles correspond to looking away.

The effects of electronic azimuth scanning were also investigated. Figure 10 illustrates the geometry used to simulate this condition. The airplane was simply rotated to some angle relative to the range axis using the positioner. Due to the broad beamwidth in the azimuth plane of the field probe element, reboresighting of the element was only necessary for angles greater than 40 degrees. In order to make the phase plots more readable for these cases, the derivative of the phase was plotted instead of the actual phase, which would have consisted of a series of ramps. Positive angles correspond to the antenna scanning toward the front of the plane and negative angles correspond to scanning toward the tail.

Scattering off a fuel tank was also investigated by actually attaching a wing tank to the plane as shown in figure 11.

In order to obtain a reference set of data that is essentially free of aircraft effects, the probe was placed in the over the wing configuration and the plane tilted down -25°. This gave the field probe a clear line of sight view of the transmitter over the full length of travel. This data is shown in figure 12. For all of the data presented in this paper, a 60 dB Tachebyscheff distribution was used as the theoretical autenna distribution with added random errors of 0.15 dB RMS amplitude and 1° RMS phase. This ultra low

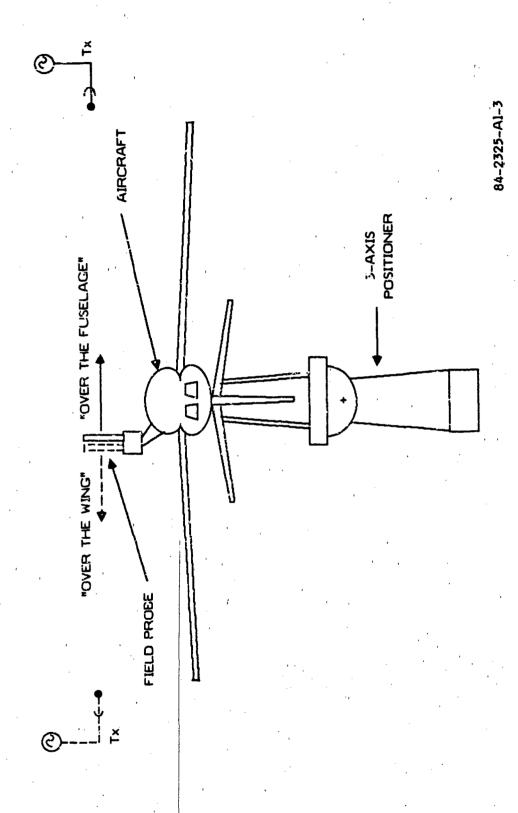


Figure 8. Field Probe Test Setup

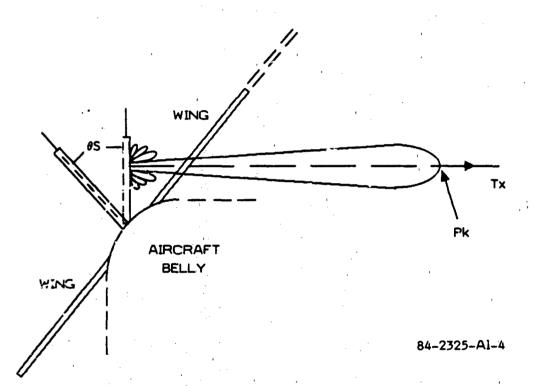
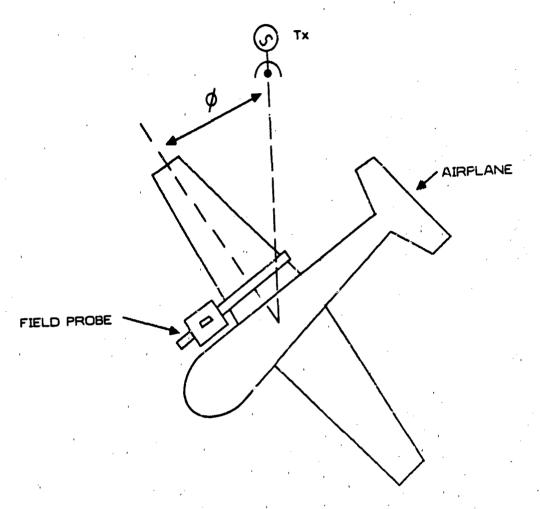


Figure 9. Elevation Scan.



84-2325-Al-5

Figure 10. Azimuth Scan.

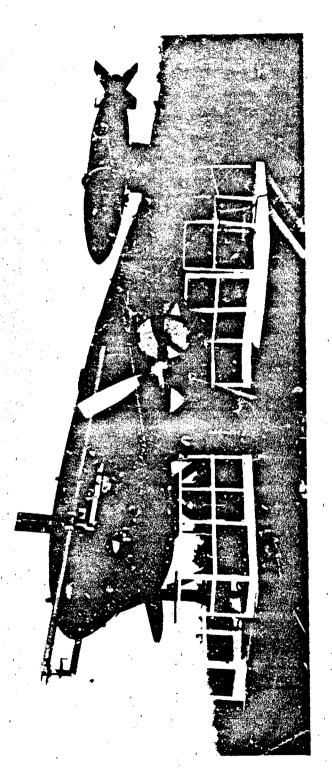


Figure 11. Wing Tank Position

sidelobe distribution was used so that scattering effects could be readily observed. Figure 12 indicates that all far out sidelobes are below 50 dB. The close in sidelobes are higher due to the phase fall off shown. This fall off was due to a twist in the probe track which could not be corrected during the experiment without significant additional expense.

Figures 13 and 14 present data for the two basic configurations of over the wing and over the fuselage. Both cases are for 0° elevation and 0° azimuth. The amplitude scattering is slightly greater for the fuselage case due to a slight blockage by the fuselage.

Figure 15 shows the results for a case of severe blockage. The probe is setup to look over the wing with the fuel tank in place. The azimuth scan angle is -40 degrees and the elevation angle is +15 degrees. The blockage effects of the wing and tank are very evident.

4. Conclusions

The conclusion that can be drawn from the data presented here is that the basic setup and instrumentation is quite clean and accurate. This is evidenced by the 50 dB peak far out sidelobes measured in the reference setup. The first few close in sidelobes are somewhat higher due to experimental errors caused by carriage "webble" and twists in the track itself.

Improvements in the setup can be made to improve close in sidelobe performance. These improvements would include mechanical adjustments to the probe assembly, and carriage to remove wobble and twists. Consideration must be given however to the fact that good close in sidelobes are hard to obtain in the manufacturing of low sidelobe antennas and therefore the performance demonstrated in this paper may be surficient.

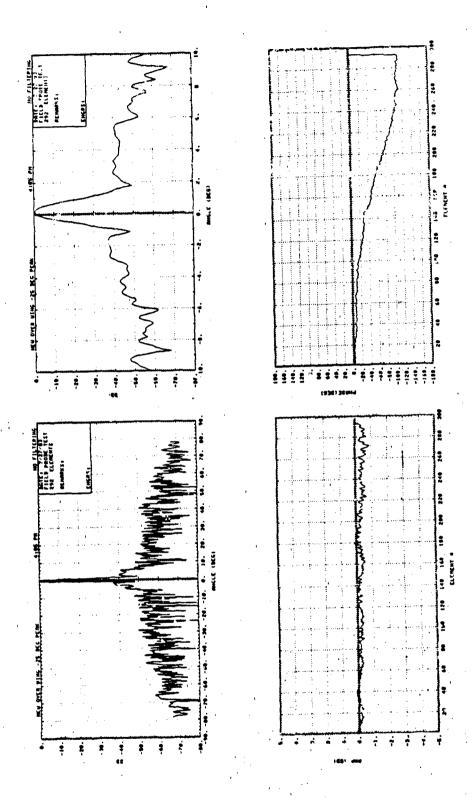


Figure 12. Field Probe Clear of Airplane

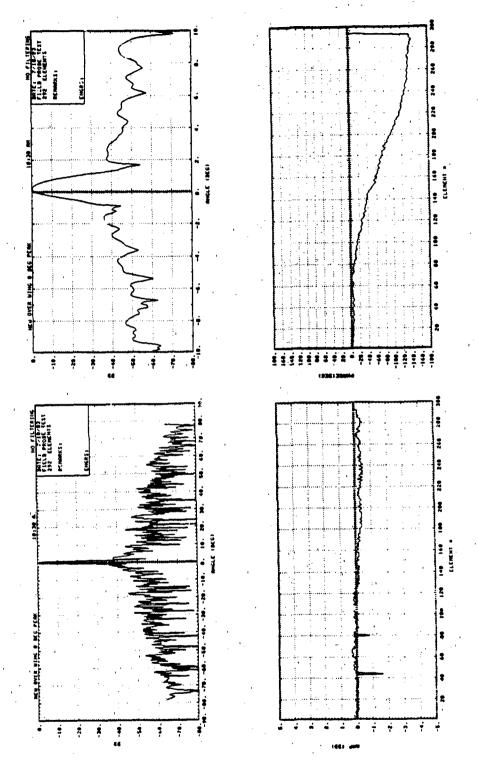


Figure 13. Over Wing

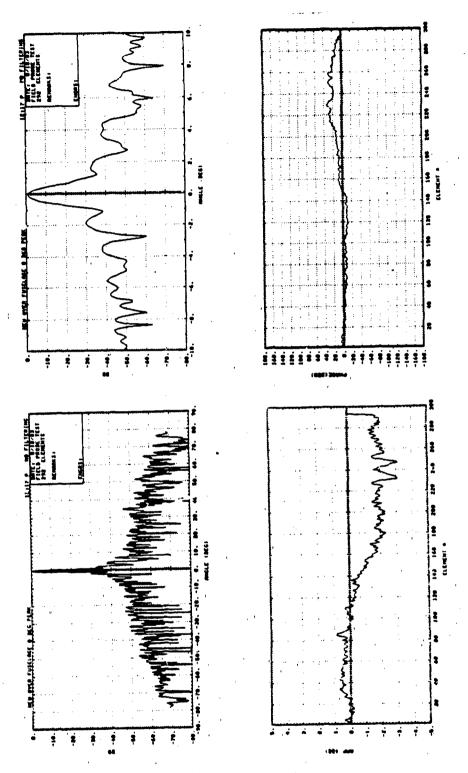


Figure 14. Over Fuselage

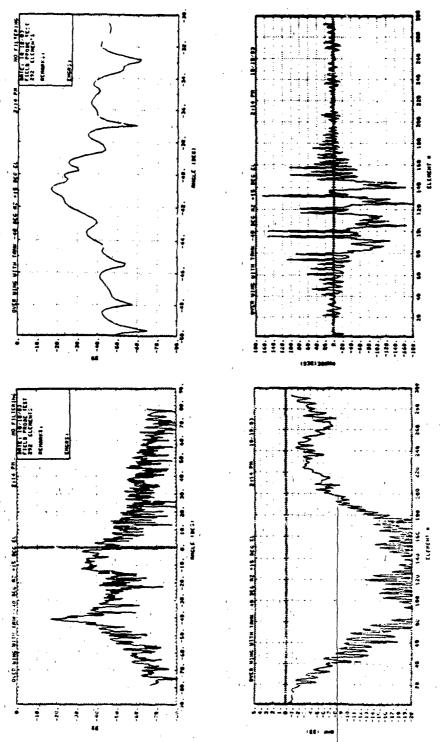


Figure 15. Over Wing With Wing Tank - 40°Az, +15° EI

EXTENSION OF PLANE-WAVE SCATTERING-MATRIX THEORY OF ANTENNA - ANTENNA INTERACTIONS TO THREE ANTENNAS: A NEAR-FIELD RADAR CROSS SECTION CONCEPT

Michael A. Dinallo
The BDM Corporation
1801 Randolph Road, S.E.
Albuquerque, New Mexico 87106

1. Abstract

This paper presents a three-antenna plane-wave scatteringmatrix (PWSM) formulation and a formal solution. An example will be demonstrated in which two of the three antennas are electromagnetically identical (the transmitter and receiver) and the third (the scatterer) has arbitrary electromagnetic properties. A reduced reflection integral-matrix will be discussed which describes the transmit, scatter, receive (TSR) interaction. antenna scatterer spectral tensor Greens function is identified. In this formulation the transmit spectrum will be scattered by the third arbitrary antenna (target) and this scattered spectrum may be considered to have originated from a transmitting antenna. Near-field antenna measurement techniques are applicable which determine the electric (scattered) field spectral density function. 1 , 3 If a second deconvolution is applied, a transmit probe corrected spectral density function or scattering tensor can be determined in principle. In either case, a near- or farelectric field can be calculated and a radar cross section determined.

2. Introduction

The successful results that near-field antenna measurement techniques have achieved in determining far-field antenna patterns encourage the idea that perhaps similar techniques may be applied to determine a target's far-field radar cross-section (RCS) based upon near- scattered field measurements. that a target's far-field RCS can be determined from nearscattered field measurements is considered here as a near-field Planar scanning near-field antenna measurement is RCS concept. theoretically substantiated using the twc-antenna, plane-wave scattering-matrix (PWSM) formulation. 2 Since determining an RCS requires a transmit probe, a target, and a receive probe, extending the PWSM formulation to include three antennas was chosen for investigating the feasibility of a near-field RCS concept. This paper presents a three-antenna PWSM formulation. discusses some of the results, and shows how this formulation substantiales the near-field RCS concept.

In the following section, the theory and definitions associated with the PWSM fomulation are stated.² This is followed by a section on the three-antenna PWSM equations and a general solution. A specific solution for the RCS problem (TSR interaction) is then presented in section 5. The paper closes by stating conclusions and identifying future efforts related to this topic.

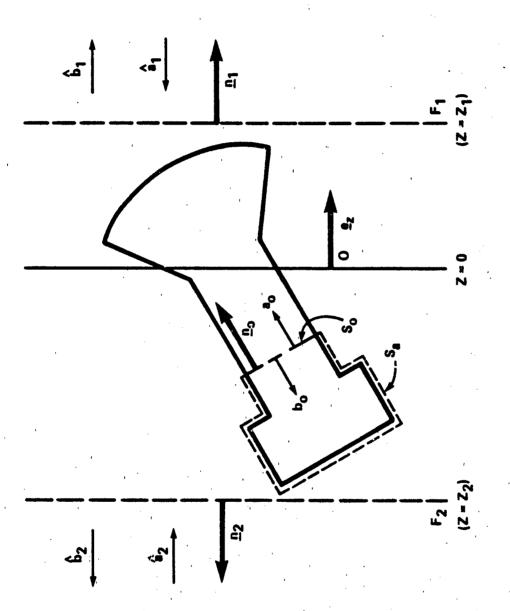
3. Background

The FWSM formulation of antennas depends upon the plane-wave representation of an electromagnetic field. Beginning with plane-wave solutions to Maxwell's equations in a rectangular xyz coordinate system in free space, solutions for \tilde{E} and \tilde{H} can be constructed from elementary plane-waves. Referring to figure 1, an antenna system bounded by two planar surfaces F_1 and F_2 , which are transverse to the z-axis direction (\hat{e}_z) , can have corresponding \tilde{E} and \tilde{H} field solutions in the form of weighed-sums of planewaves traveling to the right and left on either side of the antenna. Specifically,

$$\vec{E}_{qt}(\vec{r}) = \frac{1}{2\pi} \int \sum_{m} \left[b_{q}(m,\vec{K}) e^{\frac{1}{2}i\gamma x} + a_{q}(m,\vec{K}) e^{\frac{1}{2}i\gamma x} \right] \hat{\kappa}_{m} e^{i\vec{K} \cdot \vec{R}} d\vec{K} \qquad (1-a)$$

$$\vec{\mathbf{g}}_{\mathbf{q}g}(\vec{r}) = \frac{1}{2\pi} \int_{-m}^{\infty} \left[\mathbf{b}_{\mathbf{q}}(\mathbf{m},\vec{K}) \mathbf{e}^{\frac{1}{2}\mathbf{i}\gamma\mathbf{z}} - \mathbf{a}_{\mathbf{q}}(\mathbf{m},\vec{K}) \mathbf{e}^{\frac{1}{2}\mathbf{i}\gamma\mathbf{z}} \right] \hat{\mathbf{n}}_{\mathbf{q}} \mathbf{x} \hat{\mathbf{x}}_{\mathbf{m}} \mathbf{n}_{\mathbf{m}}(\vec{K}) \mathbf{e}^{\mathbf{i}\vec{K}\cdot\vec{R}} d\vec{K} \tag{1-b}$$

where the following sign conventions and definitions apply: q takes on values of 1 or 2 which correspond to the right (F_1) or left (F_2) side of the antenna, respectively; also, q values of 1 or 2 dictate use of the upper or lower sign respectively, found with the z-dependent exponentials; the subscript t denotes the transverse components $(\omega.r.t.\ \hat{e}_z)$; m takes on values of 1 and 2 which correspond to TM and TE polarizations respectively; the transverse vectors \vec{k} and \vec{k} and the transverse unit vector \vec{k}_m and \vec{k} are defined in (1-c); \vec{n}_q is the unit outward normal to \vec{k}_q ;



Some Notation for Plane-Wave Scattering-Matrix Description of Antennas

 $\eta_m(\vec{K})$ are the TM and TE wave admittances; $b_q(m,\vec{K})$ and $a_q(m,\vec{K})$ are the continuous spectral (angular) density functions for emergent and incident (relative to $\hat{\eta}_q$ and F_q) plane-waves, respectively. Finally, an $e^{-i\omega t}$ time dependence is used.

$$\vec{k} = k_{x}\hat{e}_{x} + k_{y}\hat{e}_{y} + k_{z}\hat{e}_{z} \qquad ; \qquad \vec{r} = r_{x}\hat{e}_{x} + r_{y}\hat{e}_{y} + r_{z}\hat{e}_{z}$$

$$\vec{R} = k_{x}\hat{e}_{x} + k_{y}\hat{e}_{y} \qquad ; \qquad \vec{R} = r_{x}\hat{e}_{x} + r_{y}\hat{e}_{y}$$

$$k_{z} = \pm\sqrt{k^{2} - R^{2}} = \pm\gamma \qquad ; \qquad \hat{\kappa}_{1} = \vec{K}/|\vec{K}| \qquad (1-c)$$

$$k^{2} = \omega^{2}\epsilon_{0}\mu_{0} \qquad ; \qquad \hat{\kappa}_{2} = \hat{e}_{x} \times \hat{\kappa}_{1}$$

The remaining component of \bar{E} and \bar{H} (\hat{e}_Z) can be obtained by using the fact that each elementary plane-wave is orthogonal to \bar{k} , i.e., $\bar{k} \cdot \bar{E}$ (or \bar{H}) = 0. This is referred to as transversality in reference 1.

Expressions for $b_q(m,\bar{K})$ and $a_q(m,\bar{K})$ are obtained by inverting (1-a,-b).

$$b_{\mathbf{q}}(\mathbf{m},\vec{\mathbf{g}}) = \frac{e^{+i\gamma\mathbf{g}}}{4\pi} \hat{\mathbf{e}}_{\mathbf{m}} \cdot \int \left\{ \vec{\mathbf{g}}_{\mathbf{q}}(\vec{\mathbf{g}},z) + \mathbf{n}_{\mathbf{m}}^{-1} \vec{\mathbf{g}}_{\mathbf{q}}(\vec{\mathbf{g}},z) \times \hat{\mathbf{n}}_{\mathbf{q}} \right\} e^{-i\vec{\mathbf{g}}\cdot\vec{\mathbf{g}}} d\vec{\mathbf{g}} \quad (2-a)$$

$$\mathbf{a}_{\mathbf{q}}(\mathbf{m}, \widehat{\mathbf{R}}) = \frac{e^{\pm i\gamma z}}{4\pi} \hat{\kappa}_{\mathbf{m}}. \quad \int \left\{ \widehat{\mathbf{E}}_{\mathbf{q}}(\widehat{\mathbf{R}}, z) - \mathbf{n}_{\mathbf{m}}^{-1} \widehat{\mathbf{E}}_{\mathbf{q}}(\widehat{\mathbf{R}}, z) \times \widehat{\mathbf{n}}_{\mathbf{q}} \right\} e^{-i\widehat{\mathbf{R}} \cdot \widehat{\mathbf{R}}} d\widehat{\mathbf{R}} \quad (2-b)$$

Note from (2) that a knowledge of \vec{E} and \vec{H} in the transverse plane \vec{R} is sufficient to determine the spectral density functions and therefore \vec{E} and \vec{H} anywhere \vec{I} using (1-a,-b) and transversality.

I If E and H are determined in a transverse plane which excludes evanescent modes, application of (1-a,-b) in the reactive nearfield would be erroneous. Therefore, constraints used in (2) become restrictions in (1-a,-b).

These equations and definitions show now the spectral density functions are related to the \bar{E} and \bar{H} field. The spectral density functions are also used explicitly in the scattering-matrix fomulation of antenna characteristics and in fact will be defined in terms of the scattering parameters. Therefore, the dependence of \bar{E} and \bar{H} upon the scattering-matrix parameters will be made apparent. Also, these equations will be used to derive a set of joining-equations for the three-antenna formulation which relates the incident spectral density functions of one antenna to the emergent spectral density functions of another antenna.

The scattering matrix parameters will now be defined in conjunction with the spectral density functions $a_q(m,\bar{K})$ and $b_q(m,\bar{K})$. Since an antenna is an imperfect receiver, an incident electromagnetic wave with the corresponding incident spectral density function $a_p(n,\bar{L})$ will be scattered. The subscript p accounts for the fact that the incident spectral density function can impinge upon the antenna from the right side (p=1) or the left side (p=2). For each particular transverse incident vector \bar{L} and a particular polarization n any scattered direction \bar{K} and polarization m is, in general, possible and may be in either the forward or backward direction (q = 1 or 2). The emergent spectral density function $b_q(m,\bar{K})$ is then dependent upon the incident wave by the following equation:

$$b_{\mathbf{q}}(\mathbf{m}, \tilde{\mathbf{K}}) = \sum_{\mathbf{p}} \int_{\bar{\mathbf{L}}} \sum_{\mathbf{n}} S_{\mathbf{p}}(\mathbf{m}, \tilde{\mathbf{K}}; \mathbf{n}, \bar{\mathbf{L}}) a_{\mathbf{p}}(\mathbf{n}, \tilde{\mathbf{K}}) d\bar{\mathbf{L}}$$
(3)

where $S_{qp}(m,\bar{K};n,\bar{L})$ is an element of a dyadic scattering tensor. If the antenna is in an active (transmit) mode then $b_q(m,\bar{X})$ will have an additional spectral contribution which is the product of the antenna waveguide feed modal amplitude a_0 and the antenna transmitting 'spectral) characteristics $S_{qo}(m,\bar{K})$. To complete the scattering-matrix description of the antenna characteristics, the antenna waveguide feed emergent modal amplitude b_0 will be due to two factors: the product of a_0 and the antenna waveguide impedance mismatch S_{oo} ; and the product of the incident wave spectral amplitude $a_p(n,\bar{K})$ and the antenna receiving spectral characteristics $S_{oq}(m,\bar{K})$. The antenna scattering-matrix equations can now be written as:

$$b_{o} = S_{oo} a_{o} + \sum_{p} \int_{\vec{L}} S_{op}(n,\vec{L}) a_{p}(n,\vec{L}) d\vec{L}$$

$$b_{q}(m,\vec{R}) = S_{qo}(m,\vec{R}) a_{o} + \sum_{p} \int_{\vec{L}} S_{qp}(m,\vec{R};n,\vec{L}) a_{p}(n,\vec{L}) d\vec{L}$$

$$(4)$$

Each of the scattering parameters can be vectorized by using the TM and TE unit vectors $\hat{\kappa}_1$ and $\hat{\kappa}_2$. The invariance of (4) with respect to the choice of coordinates in the transverse plane should be noted. All of the necessary antenna scattering parameters and formulations have been stated. The three antenna scattering equations will now be considered.

4. Three-Antenna Formulation

Figure 2 shows the three-antenna configuration to be studied. A superscript will be added to all of the PWSM parameters to indicate the antenna to which a parameter corresponds (1, 2, or 3). Antennas 1 and 2 are located in the same transverse plane. Each antenna will have its own relative coordinate system and therefore its own relative incident and emergent spectral density functions.

Antenna 1 of figure 2 will be the reference. The other antennas will have corresponding incident and emergent spectral density functions relative to antenna 1. These relations (joining-equations) are developed using the geometry in figure 2, equations (2) and the uniqueness or \bar{E} and \bar{H} at any physical point. These joining-equations are:

$$\bar{a}_1^2 = \bar{\pi} \bar{a}_1^1; \quad \bar{b}_1^2 = \bar{\pi} \bar{b}_1^1; \quad \bar{\pi} = \bar{I} e^{i\vec{K}\cdot\vec{Q}}; \quad \bar{\pi}^{-1} = \bar{I} e^{-i\vec{K}\cdot\vec{Q}}$$
 (5-a)

$$\bar{b}_{2}^{3} = \bar{T}_{-1}\bar{a}_{1}^{1} = \bar{T}_{-2}\bar{a}_{1}^{2} ; \quad \bar{a}_{2}^{3} = \bar{T}_{+1}\bar{b}_{1}^{1} = \bar{T}_{+2}\bar{b}^{2}$$
 (5-b)

$$\vec{T}_{-1} = \vec{T} e^{i\vec{k}^{+} \cdot \vec{r}_{1}}$$
(5-c)

- n Thurn Antonna Crattoring Configuration

where $\bar{1}$ is the 2 x 2 identity matrix and the \bar{a} and \bar{b} spectral density function vectors have two components, one for each polarization, TM and TE (i.e., $\hat{\kappa}_1$ and $\hat{\kappa}_2$). Similarly, using vector-operator notation the three-antenna coupled scattering equations are:

These scattering equations are coupled due to the mutual interactions of antenna 1 and 2. Note that the subscripts on the vector or tensor quantities refer to the right or left side of a

particular antenna as defined under (2). This being understood, the subscripts on \bar{a} and \bar{b} will now be suppressed. The mutual receive parameters, \bar{S}_{01}^{12} and \bar{S}_{01}^{21} , account for the presence of a second antenna in the transverse plane located at $z_1=z_2=0$ of figure 2.

Two mutual interactions are possible. The first is one antenna transmitting in an active mode and the second antenna directly receiving this primary radiation. This interaction is encountered in antenna array theory and can be accounted for in S_{00} as an active input impedance. The second interaction is due to radiation being scattered from one antenna and received by the second. This is explicitly accounted for in the scattering equations as the mutual receive parameters \bar{S}_{01}^{12} and \bar{S}_{01}^{21} . The mutual receive parameter \bar{S}_{01}^{12} is due to \bar{a}^2 being scattered from antenna 2 and received by antenna 1.

Using the two-antenna solution (located on the same transverse plane) and (5-a), \tilde{S}_{01}^{12} can be expressed as:

$$\vec{s}_{01}^{12} = \vec{s}_{01}^1 \quad \bar{\vec{T}}^{-1} \quad \bar{\vec{s}}_{11}^2$$
 (7)

Similarly, the mutual receive parameter \tilde{s}_{01}^{21} can be expressed as:

$$\bar{s}_{01}^{21} = \bar{s}_{02}^{2} \bar{\bar{T}} \bar{\bar{s}}_{11}^{1}$$
 (8)

The mutual transmittances \bar{S}_{10}^{12} and \bar{S}_{10}^{21} account for primary radiation being transmitted from one antenna, transformed (or propagated) to another antenna reference, and scattered. As in (7) and (8), \bar{S}_{10}^{12} can be expressed as:

$$\bar{s}_{10}^{12} = (\bar{1} + \bar{s}_{11}^1) \bar{T}^{-1} \bar{s}_{10}^2$$
 (9)

Similarly, \tilde{S}_{10}^{21} can be expressed as:

$$\bar{s}_{10}^{21} = (\bar{1} + \bar{s}_{11}^2) \bar{T} \bar{s}_{10}^1$$
 (10)

The final parameters to be defined under (6) are the mutual scattering parameters $S_{11}^{=12}$ and $S_{11}^{=21}$. Mutual scattering accounts for one antenna scattering radiation, transformed to another antenna reference. These are expressed as in (11) and (12).

$$\vec{S}_{11}^{12} = \vec{T}^{-1} \, \vec{S}_{11}^{2} \tag{11}$$

$$\bar{S}_{11}^{21} = \bar{T} \bar{S}_{11}^{1}$$
 (12)

The mutual transmit and scattering parameters are necessary for \bar{b}^1 or \bar{b}^2 to separately represent all interactions or processes contributing to rightward-traveling spectral radiation. A formal solution to (6) can be derived where the antenna wave guide feed emergent modal amplitudes b_0 are written in terms of the antenna wave guide feed exiting amplitudes a_0 . Using (5) and (7) - (12) in (6) the following matrix solution can be obtained:

$$\begin{pmatrix} b_0^1 \\ b_0^2 \\ b_0^3 \end{pmatrix} = \begin{pmatrix} M_{11} & M_{12} & M_{13} \\ M_{21} & M_{22} & M_{23} \\ M_{31} & M_{32} & M_{33} \end{pmatrix} \begin{pmatrix} a_0^1 \\ a_0^2 \\ a_0^2 \end{pmatrix}$$
(13)

$$\mathbf{M}_{11} = \mathbf{S}_{00}^{1} + \bar{\mathbf{S}}_{01}^{1}(\bar{\mathbf{I}} + \bar{\mathbf{R}}_{11}^{2}) (\bar{\mathbf{I}} - \bar{\mathbf{R}}_{11}^{13} (\bar{\mathbf{S}}_{11}^{1} + \bar{\mathbf{R}}_{11}^{2}))^{-1} \bar{\mathbf{R}}_{22}^{13} \bar{\mathbf{S}}_{10}^{1}$$
 (13-a)

$$\mathbf{H}_{12} = \bar{\mathbf{S}}_{01}^{1} (\bar{\mathbf{I}} + \bar{\mathbf{R}}_{11}^{2}) (\bar{\mathbf{I}} - \bar{\mathbf{R}}_{22}^{13} (\bar{\mathbf{S}}_{11}^{1} + \bar{\mathbf{R}}_{11}^{2}))^{-1} \quad \bar{\mathbf{R}}_{22}^{13} \, \bar{\mathbf{S}}_{10}^{12}$$
(13-b)

$$\mathbf{H}_{13} = \bar{\mathbf{S}}_{01}^{1} (\bar{\mathbf{I}} + \bar{\mathbf{R}}_{11}^{2}) (\bar{\mathbf{I}} - \bar{\mathbf{R}}_{22}^{13} (\bar{\mathbf{S}}_{11}^{1} + \bar{\mathbf{R}}_{11}^{2}))^{-1} \quad \bar{\mathbf{A}}_{-1}^{-1} \bar{\mathbf{S}}_{20}^{3}$$
(13-c)

$$\mathbf{H}_{21} = \bar{\mathbf{S}}_{01}^{2}(\bar{\mathbf{I}} + \bar{\mathbf{R}}_{11}^{1}) (\bar{\mathbf{I}} - \bar{\mathbf{R}}_{22}^{23} (\bar{\mathbf{S}}_{11}^{2} + \bar{\mathbf{R}}_{11}^{1}))^{-1} \bar{\mathbf{R}}_{22}^{23} \bar{\mathbf{S}}_{10}^{21}$$
(13-d)

$$\mathbf{H}_{22} = \mathbf{S}_{00}^{2} + \bar{\mathbf{S}}_{01}^{2} (\bar{\mathbf{I}} + \bar{\mathbf{R}}_{11}^{1}) (\bar{\mathbf{I}} - \mathbf{R}_{22}^{23} (\bar{\mathbf{S}}_{11}^{2} + \bar{\mathbf{R}}_{11}^{1}))^{-1} \bar{\mathbf{R}}_{22}^{23} \bar{\mathbf{S}}_{10}^{2}$$
 (13-e)

$$\kappa_{23} = \bar{s}_{01}^{2} (\bar{I} + \bar{R}_{11}^{1}) (\bar{I} - \bar{R}_{22}^{23} (\bar{s}_{11}^{2} + \bar{R}_{11}^{1}))^{-1} \bar{T}_{-2}^{-1} \bar{s}_{20}^{3}$$
 (13-f)

$$\mathbf{M}_{31} = \mathbf{\bar{s}}_{02}^{3} \left[\mathbf{\bar{I}} - \mathbf{\bar{R}}_{11}^{3} \mathbf{\bar{S}}_{22}^{3} \right]^{-1} \mathbf{\bar{T}}_{+1} \mathbf{\bar{s}}_{10}^{1}$$
 (13-g)

$$\mathbf{M}_{32} = \bar{\mathbf{S}}_{02}^{3} \left[\bar{\mathbf{I}} - \bar{\mathbf{R}}_{11}^{3} \, \bar{\mathbf{S}}_{22}^{3} \right]^{-1} \, \bar{\mathbf{T}}_{+1}^{1} \, \bar{\mathbf{S}}_{10}^{12} \tag{13-h}$$

$$\mathbf{M}_{33} = \mathbf{S}_{00}^{3} + \bar{\mathbf{S}}_{02}^{3} \left[\bar{\mathbf{I}} - \bar{\mathbf{R}}_{22}^{3} \, \bar{\mathbf{S}}_{22}^{3} \right]^{-1} \, \bar{\mathbf{R}}_{11}^{3} \, \bar{\mathbf{S}}_{20}^{3} \tag{13-1}$$

where the following 2×2 matrices R are given by:

$$\bar{g}_{11}^{1} = \bar{T}\bar{g}_{11}^{1}\bar{T}^{-1}; \qquad \bar{g}_{11}^{2} = \bar{T}^{-1}\bar{g}_{11}^{2}\bar{T}; \qquad \bar{g}_{11}^{3} = \bar{T}_{+1}(\bar{g}_{11}^{1} + \bar{g}_{11}^{2}) \; \bar{T}_{-1}^{-1}$$

$$\bar{g}_{12}^{13} = \bar{T}_{-1}^{-1} \; \bar{g}_{22}^{3} \; \bar{T}_{+1}; \qquad \bar{g}_{22}^{23} = \bar{T}_{-2}^{-1} \; \bar{g}_{22}^{3} \bar{T}_{+2}$$
(14)

The R matrices represent transformations of the scattering parameters among the antennas. The expressions contained in (13) account for the following interactions: direct transmit and receive (zero-order); transmit, scatter and receive (TSR)

(first-order); and higher order scattering among the three antennas. In obtaining (13) expressions for \bar{a}^1 , \bar{b}^1 , \bar{a}^2 , \bar{b}^2 , and \bar{a}^3 , \bar{b}^3 are found which can be used in (2) for explicitly representing the corresponding \bar{E} and \bar{H} fields.

5. Transmit-Scatter-Receive Interaction: The Radar Problem

for simulating the radar problem, let antenna 1 transmit, antenna 3 be passively scattering radiation, and antenna 2 be operating in the receiving mode. Further, let antennas 1 and 2 have identical characteristics (as defined under (3) and (4)) denoted by

$$\bar{s}_{01}^1 = \bar{s}_{01}^2 = \bar{r}_{01}^2$$
, $\bar{s}_{10}^1 = \bar{s}_{10}^2 = \bar{r}_{10}^2$, $\bar{s}_{11}^1 = \bar{s}_{11}^2 = \bar{r}_{11}^2$ (15)

If mutual scattering between antennas 1 and 2 is assummed negligible, then since $a_0^2 = a_0^3 = 0$, b_0^2 from (13) becomes:

$$b_0^2 = \bar{I}_{01} [\bar{I} - \bar{R}_{22}^{23} \bar{I}_{11}^{21}]^{-1} \bar{R}_{22}^{23} \bar{I}_{10}^{21} a_0^1$$
 (16)

Considering the first reflection to be dominant and subsequent reflections to be negligible. (16) can be further reduced to:

$$b_0^2 = \bar{I}_{01} \bar{T}_{-2}^{-1} \bar{S}_{22}^3 \bar{T}_{+1} \bar{I}_{10}^1 a_0^1$$
 (17)

In explicit integral form, (17) can be written as

$$b_0^2(\vec{r}_1,\vec{r}_1) = a_0^1 \int [\vec{I}_{01}(\vec{R})e^{-i\vec{k}-\vec{r}_2}] \int \vec{S}_{22}^3(\vec{R},\vec{L}) \cdot \vec{I}_{10}(\vec{L})e^{i\vec{k}-\vec{r}_1} d\vec{L} d\vec{R}$$
receiving right to left spectral transmitting left to dyadic Greens characteristics right propagation function

and is a reduced reflection integral. If multiple reflections are considered significant, (18) can be used as a first approximation to b_0^2 , and using an appropriate iterative technique b_0^2 may be evaluated in principle if (16) is convergent. For this latter class of problems it may be possible to evaluate the full "unreduced" form for b_0^2 ($a_0^2 = a_0^3 = 0$) as written in (13-d).

The reduced reflection integral (18) mathematically describes a TSR interaction which is the radar problem. To make apparent the similarity of (18) with the transmission integral (reference 1) let

$$\vec{\mathbf{I}}_{10}(\vec{\mathbf{r}}_1,\vec{\mathbf{K}}) = \int \vec{\mathbf{S}}_{22}^3 (\vec{\mathbf{K}},\vec{\mathbf{L}}) \cdot \vec{\mathbf{I}}_{10}(\vec{\mathbf{L}}) e^{i\vec{\mathbf{L}} \cdot \vec{\mathbf{r}}} \mathbf{1} d\vec{\mathbf{L}}$$
(19)

Then (18) becomes:

$$b_0^2 (\bar{r}_1, \bar{r}_2) = a_0^1 \int \bar{I}_{01}(\bar{R}) \cdot \bar{I}_{10}(\bar{r}_1, \bar{R}) e^{-i\bar{R} \cdot \bar{r}_2} d\bar{R}$$
 (20)

which is indeed a transmission integral. The transmit antenna has a spectral radiation pattern $\vec{I}_{10}(\vec{r}_1,\vec{k})$ which differs from that defined under (3) only by the \vec{r}_1 dependence. The scattering dyadic \vec{S}_{22}^3 represents any scattering target and the scattered field can be considered to have originated from an antenna. As a result, near-field antenna measurement techniques are applicable (reference 2). Denote the coupling-product by

$$D(\vec{K}, \vec{r}_1) = \vec{I}_{01}(\vec{K}) \cdot \vec{I}_{10}(\vec{r}_1, \vec{K})$$
 (21)

Deconvolution of (21) allows $D(\bar{K},\bar{r}_1)$ to be expressed as:

$$D(\bar{K}, \bar{r}_1) = \frac{1}{4\pi^2 a_0^1} \int b_0^2 (\bar{r}_1, \bar{r}_2) e^{i\bar{K}\cdot\bar{r}_2} d\bar{R}_2 \qquad (22)$$

Since for planar near-field antenna measurment techniques b_0^2 represents sampled data in the transverse \bar{R}_2 plane, $D(\bar{K},\bar{r}_1)$ can

be empirically determined, and $\bar{I}_{10}(\bar{K},\bar{r}_1)$ can be computed and receive probe corrected via (21). A far-electric field can then be calculated and an RCS evaluated although it will generally be transmit probe dependent. If a plane-wave is incident upon the target then $\bar{I}_{10}(\bar{K},\bar{r}_1)$ will not be transmit probe dependent, and the far-electric field can be calculated and an RCS determined. However, even if $\bar{I}_{10}(\bar{K},\bar{r}_1)$ is transmit probe dependent a second deconvolution can be performed upon (19) and $\bar{S}_{22}^3(\bar{K},\bar{L})$ evaluated. $\bar{S}_{22}^3(\bar{K},\bar{L})$ is the most essential parameter in the PWSM formulation of the RCS problem since it describes the scattering properties of the target.

Defining

$$\vec{Q} = (\vec{K}, \vec{L}) = \vec{S}_{22}(\vec{K}, \vec{L}) \cdot \vec{I}_{10}(\vec{L})$$
 (23)

as a scattering product, a second deconvolution can be written as

$$\bar{Q}(\vec{K}, \bar{L}) = \frac{1}{4\pi^2} \int \bar{I}'_{10}(\vec{K}, \bar{r}_1) e^{-i\vec{k}\cdot\vec{r}_1} d\vec{R}_1 \qquad (24)$$

An explicit set of equations, assuming TM(x) and TE(y) polarization, can be written as:

$$Q_{x}(\vec{R}, \vec{L}) = I_{10x}(\vec{L}) S_{22}^{3}(x, \vec{K}; x, \vec{L}) + I_{10y}(\vec{L}) S_{22}^{3}(x, \vec{K}; y, \vec{L})$$

$$Q_{y}(\vec{K}, \vec{L}) = I_{10x}(\vec{L}) S_{22}^{3}(y, \vec{K}; x, \vec{L}) + I_{10y}(\vec{L}) S_{22}^{3}(y, \vec{K}; y, \vec{L})$$
(25)

If the transmitter is rotated and (20) through (25) resolved, S_{22}^3 can be determined. Once known, S_{22}^3 can be used in the reflection integral (18) allowing b_0^2 to be calculated for any incident field, and an RCS can be determined in the near- or far-field.

6. Discussion

The TSR interaction is compactly expressed in the reducedreflection integral (18). This integral describes a transmitted radiation pattern which is propagated to a target and scattered. from this interaction is another, re-transmitted radiation pattern. This target radiation pattern is determined by evaluating and summing the scattering-product (23) for all The target radiation pattern is then incident directions. propagated to and received by a probe antenna which also has a particular pattern (or angular spectrum). The first deconvolution (22) allows the coupling-product (21) to be evaluated, which in turn enables the transmit-target pattern to be determined and receive probe corrected. A second deconvolution (24) allows the scattering-product to be evaluated which in turn enables the dyadic scattering tensor element to be determined and transmitprobe corrected.

The scattering tensor element S^3_{22} (m,K;n,L) is a quantity which enforces the electromagnetic boundary conditions to be satisfied for any of the incident field directions L and polarizations n. This enforcement of the boundary conditions is dependent upon the target geometry and electromagnetic

constitutive parameters σ , μ and ϵ . As such, the dyadic scattering tensor element is a significant quantity for the radar problem since it inherently contains the target geometry and electromagnetic constitutive parameters. Since the scattering tensor is independent of transmit and receive probes it can be used as a classification parameter for various targets and may also be used for calculating a measured RCS using any set of probes, in the near- or far-field.

A final note to be mentioned is that if the first deconvolution required an N x N array of data, then the second deconvolution would require an $(N \times N)^2$ array for determining S_{22}^3 $(m,\bar{K};n,\bar{L})$. Efficient data acquisition and processing schemes are needed to minimize computation memory and time requirements.

7. Conclusion

A three-antenna PWSM formulation has been presented and a solution formally obtained. The radar problem or TSR interaction is a special case of the three-antenna problem. A transmission integral was obtained (20) which is similar to the one obtained in reference 1. This substantiates using near-field antenna measurement techniques for measuring the near-scattered field of a target. The scattered field transmission pattern can be determined and probe corrected as in the near-field antenna measurements. A near- or far-field electric field and corresponding RCS can then be calculated. This RCS will in general be probedependent. However, applying the second deconvilution (24)

allows the scattering-product to be evaluated and the target scattering parameters determined and transmit probe corrected. Using an arbitrary incident field, a near- or far-field electric field and the corresponding RCS can be calculated.

Future efforts include the following topics:

- 1. Analytically calculating the dyadic scattering tensor elements from known scattered field solutions.
- Performing a similar three-antenna analysis with one of the antennas located in a plane mutually orthogonal to the other two.
- 3. Determining how to simulate a "near-field" plane-wave and thus avoid a full second deconvolution.
- 4. Fully utilizing a given near-field measurement dataset, including simulating with software other incident field directions.

Acknowledgements

Supported Under Contract F08635-83-C-0286

References

Newell, A. C. and Crawford, M. L. (1974) <u>Planar Near-Field</u>
 <u>Measurements on High Performance Array Antennas</u>,
 NBSIR 74-380, National Bureau of Standards.

- Kerns, D. M. (1981) <u>Plane-Wave Scattering-Matrix Theory of</u>
 Antennas and Antenna-Antenna Interactions, Monograph
 No. 162, National Bureau of Standards.
- 3. Joy, E. B. and Paris, D. T. (1972) Spatial sampling and filtering in near-field measurements, in <u>IEEE Trans.</u>
 Antenna Propag., Vol. AP-20, pp. 253-261.

MISSION of Rome Air Development Center

RADC plans and executes research, development, test and selected acquisition programs in support of Command, Control, Communications and Intelligence (C³I) activities. Technical and engineering support within areas of competence is provided to ESD Program Offices (POs) and other ESD elements to perform effective acquisition of C³I systems. The areas of technical competence include communications, command and control, battle management, information processing, surveillance sensors, intelligence data collection and handling, solid state sciences, electromagnetics, and propagation, and electronic, maintainability,

and compatibility.

FILMED

5-85

DTIC